INITIAL COLLECTION EFFICIENCY
FOR GLASS FILTER MEDIA

Prof.Dr.Rafa H.Alsuhaili   **Dr.Awatif Soaded   A. alsaqqar**   **Nawar Omran Ali Nasser**

College of Engineering   **College of Engineering**   **College of Engineering**

University of Baghdad   **University of Baghdad**   **University of Baghdad**

ABSTRACT

This study investigated the ability of using crushed glass solid wastes in water filtration by using a pilot plant, constructed in Al-Wathba water treatment plant in Baghdad. Different depths and different grain sizes of crushed glass were used as mono and dual media with sand and porcelaniate in the filtration process. The mathematical model by Tufenkji and Elimelech was used to evaluate the initial collection efficiency η of these filters. The results indicated that the collection efficiency varied inversely with the filtration rate. For the mono media filters the theoretical ηth values were more than the practical values ηprac calculated from the experimental work. In the glass filter ηprac was obtained by multiplying ηth by a factor 0.945 where this factor was 0.714 for the sand filter. All the dual filters showed that ηth was less than ηprac. Whereas the dual filter 35cm porcelanite and 35cm glass showed the highest collection efficiency. To obtain ηprac in the dual filter glass and sand, ηth is multiplied by **1.374**, as for the dual filters porcelanite and glass the factor was **1.168** and **1.204**.

الخلاصه:

Tufenkji and Elimelech   .

0,945

0,714

35   35

1,204   1,168   1,374

.

KEY WORDS: Filtration, Dual filters, Crushed glass, Initial collection efficiency, Models.

INTRODUCTION

Glass can be crushed to meet different gradation specifications which allow it to be used in such filters. Because glass is amorphous and has no internal crystal structure, the particles are homogenous and have no grain boundaries. This gives glass more resistance to break down through filtration and backwashing cycles. Furthermore, the lack of grain boundaries minimizes cracks where bacteria can lodge and resist flushing in backwashing. Glass particles have a slight negative charge on their surface, which tends to hold onto fine particles during the filtration cycle. Upon backwashing, this weak charge apparently releases these fine particles to the effluent thereby contributing to a better filtration process. Theoretically, one could see that less washing water is required, owing to the better permeability in glass filters (CWC, 1997).

Glass is a product of the super-cooling of a melted liquid mixture consisting primarily of sand (silicon dioxide and sodium carbonate) to a rigid condition. This material does not crystallize; and when the glass is crushed to a size similar to natural sand, it exhibits properties of an aggregate material. Coarse angular material is effective in trapping dirt and impurities in the filters for water treatment and offers a greater filtration power than sand. Glass grains are less porous and do not saturate itself compared to traditional sand (do not form a cake in the filter) (Opta Minerals Inc., 2008).

INITIAL COLLECTION EFFICIENCY η_o

The performance of a filter is expressed in terms of the single collector (grain of the filter media) efficiency (η_s) which is defined as the ratio between the quantities of particles in contact with the collector and the flow rate. There are two theoretical methods for calculating the particles deposition rate on the collectors from the flowing suspension, the Lagrangian and Eulerian methods. The Lagrangian method describes the trajectory of the particle approaching the collector which is governed by Newton's second law, while Eulerian method describes the particles concentration in time and space. The trajectory analysis is limited to non Brownian particles as it can not include the effect of diffusion .In the Eulerian approach, the difficulty of accounting for Brownian effects is eliminated. (Jegathesan, 2007). The total amount of mass particles that a filter can retain will depend on the initial collection efficiency η_o , the determination of the initial collection efficiency η_o is important in predicting the performance of a clean bed filter, which can be calculated by the following equation (Jagatheesan, 2007)

$$[Ce/Ci]=\exp[(-3/2)\times(1-\varepsilon)\times\alpha\,\eta_o\times L/a_c] \qquad (1)$$

where
Ci =Influent particle concentration into the filter (mg/l)
Ce =Effluent particle concentration from the filter (mg/l)
L=Depth of filter (m)
ε =Porosity
η_o = Initial Collection Efficiency
a_c =Radius of the filter grain(m)
α =Is The ratio between the number of contacts which succeeded in producing adhesion and the number of

collisions which occur between suspended particles and the filter grain.Ideally , α is equal to unity in a completely destabilized system.

Equation 1 provides the basis for determining η_o from the results of the experimental work (Yongwon and Tien,1989).

The basic mechanisms for transporting particles to a single collector are:

Interception

Particles remaining centered on the streamlines, that pass through the collector surface by a distance of half or less than the particle diameter will contact the collector and will be intercepted. For laminar flow, spherical particles and spherical collectors, particle transport by interception is given by the following expression (Yao et al., 1971):

$$\eta_I = (d_p / d_c) \qquad (2)$$

Where:

η_I =Transport efficiency due to interception (dimensionless)

d_p= Particle diameter (m)

d_c= Filter grain diameter (m)

Inertia

In general as fluid streamlines curve around the collector, particles can deviate from the streamline and continue downward to contact the collector due to inertial forces. Inertia is important in air filtration systems, but is insignificant in water filtration and collection efficiency. Inertia force has been ignored as it is difficult to calculate, and require numerical solutions for determination.

Sedimentation

Particles with density significantly greater than water tend to deviate from fluid streamlines due to gravitational forces. The collector efficiency (as a result of gravity) has shown to be the ratio of stokes settling velocity to the superficial velocity (Yao et al., 1971) as shown in the expression:

$$\eta_g = [(\rho_P - \rho) d_P{}^2 g]/[18 \mu U_s]$$

$$(3)$$

η_g =Transport efficiency due to gravity (dimensionless)

g=Gravitional acceleration,m/s^2

U_s = Settling velocity (m/s)

μ, ρ =Water viscosity(kg/m.s), water density(kg/m^3) respectively

ρ_p d_P =Particle density(kg/m^3), particle diameter(m) respectively

Diffusion

Particles are influenced by Brownian motion and will deviate from the fluid streamlines due to diffusion. The transport efficiency due to diffusion is given by the following expression (Levich, 1962):

$$\eta_{pe} = U_s d_c / D_{BM} \qquad (4)$$

$$D_{BM} = C_s KT/3\pi\mu d_P \qquad (5)$$

η_{pe} =Transport efficiency due to diffusion (related to the Peclet number)

U_s = Superficial velocity (m/s)

d_c =Filter-grain diameter(m)

D_{BM}=Brownian diffusivity

C_s =Cunningham s correction factor

C_s =1+ Kn[1.257+0.4 exp (-1.1/Kn)]

$$(6)$$

$Kn=0.06 \mu/(d_p /2)$

K = Boltzmann constant, 1.381×10^{-23} j/k

T=Absolute temperature, K (273 +C).

d_p =Particle diameter(m)

μ= water viscosity (kg/m.s)

Different models were developed to describe the performance of the filtration process in water treatment.

Yao et al.,1971 developed a model based on an isolated single collector in a uniform flow field . The accumulation of particles in the filter is the product of the total number of collector and the accumulation of particles on one single collectors. They developed a filtration coefficient related to η and α taking in to account porosity, particle size, and depth of the filter.   The Yao filtration model may under estimate the number of collisions between particles and collectors when compared to experimental data . Several attempts were performed to refine the Yao model by using different flow regimes or adding more transport mechanisms. Rajagopalan and Tien (1976) developed a fundamental depth filtration .This model correlates to the experimental data more significantly than other models and it is considered more accurate (Logan et al., 1995). Rajagopalan and Tien presented an approximate expression of the initial collector efficiency, η_o, as in the following expression:

$\eta_o =1.5 A_s(1-\varepsilon)^{2/3} N_R^2[2/3 N_{Lo}^{1/8} N_R^{-1.8}+$
$2.25*10^{-3} N_G^{1.2} N_R^{-2.4}$
$+4(1- \varepsilon)^{2/3} A_s^{1/3} N_{pe}^{-2/3}$ (7)

Where:

η_o =Initial collector efficiency

A_s= Porosity function (dimensionless)

$N_R= \eta_I$ (dimensionless)

$N_G=\eta_G$ (dimensionless)

N_{PE}: Peclet number defined as Us dc/D_{BM}

N_{Lo}= London force parameter, defined as H/(9 $\pi \mu a_p^2$ Us

H = Hamaker constant describing Van der Waals forces. Its value ranges from 10^{-19} to 10^{-20} J

a_p = radius of partical

The RT model can be used to demonstrate the effect of specifying filter media with a low uniformity coefficient.

Bai and Tien in 1996 developed a correlation for the initial filter coefficient under unfavorable surface interactions. By applying Bukingham π theory,α is shown to be a function of eleven dimensionless parameters. Further, by conducting partial regression analysis to available experimental data, only four of the eleven dimensionless parameters were found to exert strong influence on α.

$\alpha =10^{-0.2.9949}(N_{Lo})^{0.8495}(N_{E1})^{-0.2676}(N_{E2})^{3.8328}(N_{DL})^{1.6776}$
(8)

where, N_{Lo} is the London number, N_{E1} first electrokinetic parameter, N_{E2} second electrokinetic parameter and N_{DL} is the double layer force parameter.

Cushing and Lawler in 1998 presented an expression based on their respective trajectory calculation results. The expression is:

$(\eta_s)_o =0.029 N_{Lo}^{0.012} N_R^{0.023}$
$+0.48 N_G^{1.8} N_R^{-0.38}$ (9)

The correlations of Tufenkji and Elimelech in 2004 were based on the numerical solution of

140

the convective diffusion equation and gave the following expression (Tien and Ramarao, 2007)

$(\eta_s)_o = 2.3644\ A_s^{1/3}\ N_R^{-0.029} N_{Lo}^{0.052}\ N_{PE}^{-0.633} + 0.5306\ A_s\ N_R^{1.675}\ N_{LO}^{0.125} +$

$0.2167\ N_R^{-0.187}\ N_G^{1.11} N_{PE}^{0.053}\ N_{LO}^{0.053}$

$$(10)$$

Where $N_R < 0.02$

EXPERIMENTAL WORK

A pilot plant was constructed in Al wathba WTP to test the filtration processes using crushed glass as mono and dual filter media. The plant consisted of three filtration columns of a diameter 10cm and height 150cm to hold 70cm filter media. The influent to these filters was the effluent from the sedimentation tank in the plant (the same water flowing to the existing rapid sand filters). The sets of experimental runs were performed on different types of filters as shown in figures 1 and 2. Filter No.2 in the two sets is the sand filter with the same media used in the plant. The filtration rates of each filter in the pilot unit were maintained as the same rates of the filters used in the plant; on a constant rate basis (Kawamura ,2000). The filtration runs were carried out at filtration rates 5, 10 and 15 m/hr. Samples of the influent and effluent were collected for turbidity measurements at certain time intervals during each run.

THE THEORETICAL INITIAL COLLECTION EFFICIENCY FOR EACH FILTER

The mathematical model suggested by Tufenkji and Elimelech (Tien and Ramarao, 2007) was used to determine the initial collection efficiency as follows: The model is:

$(\eta_s)_o = 2.3644\ A_s^{1/3}\ N_R^{-0.029} N_{Lo}^{0.052}\ N_{PE}^{-0.633} + 0.5306\ A_s\ N_R^{1.675}\ N_{LO}^{0.125} + 0.2167$

$N_R^{-0.187}\ N_G^{1.11} N_{PE}^{0.053}\ N_{LO}^{0.053}$

$$(11)$$

Where $N_R < 0.02$

$(\eta_s)_o$ = Initial collector efficiency for single collector

A_s = Porous function which is Happels parameter defined as $2(1-p^5)/w$

$P = (1-\varepsilon)^{1/3}$

$$(12)$$

$w = 2-3p+3p^5-2p^6$

$$(13)$$

N_R: Interception parameter, defined as d_p / d_c

N_{LO}: London force parameter, defined as $H/(9\pi\mu\ a_p^2\ Us)$ (14)

N_{PE}: Peclet number defined as $Us\ d_c /(D_{BM})$

$$(15)$$

N_G: Gravitational parameter, defined as $[\ (\rho_p - \rho)\ d_p^2 g]/(18\ \mu Us)$ (16)

The values of initial collection efficiencies obtained from the mathematical model were compared with the practical values obtained from the equation:

$C_e / C_i = \exp[(-3/4)(1-\varepsilon)\ \alpha\ \eta o\ L/\ a_C]$

$$(17)$$

Where :

C_e and C_i are the effluent and influent concentrations respectively.

The theoretical initial efficiency was determined by applying this model (equation 10) for the filters in Set No.1 and Set No.2, representing the different types of filters of the pilot plant.

The practical initial efficiency was calculated using equation 17. the results are shown in tables 1 to 6 for each filter in the two sets at different flow rates 5,10 and 15 m/hr, taking in to accounts the variation in temperature during the period of the experimental work.

RESULTS AND DISCUSSION

The results in tables 1 to 6 show that ηth and ηprac decreases as the filtration rate increases. Increasing the filtration rate will increase the hydraulic shear force which tends to push the suspended particles deeper in the filter and may carry them out by the effluent. Also high velocities in the pores will lead to higher scour effects on the deposited particles (Cleasby et al.,1992).

For the mono media filters in the two sets the values of ηth were more than ηprac . In sand filters ηprac could be obtained by multiplying ηth by a factor 0.714 for set No.1 and by a factor 0.55 for set No.2, this difference may be due to the variation in temperature. Where the measurement of set No.1 were in a colder climate 10-15 C and for set No.2 20 C. The factor for the glass filter was 0.945.

All the dual filters show that ηth is less than ηprac. Filter No.1 in set No.2 showed the higher collection efficiency than the other two dual filters.

The higher percentage of coarse grains per unit filter depth leads to low numbers of filter media grains per m^2 which will cause a significant reduction in the total surface area of filter media in a unit area so a clear reduction in the removal of suspended solids indicated here as the collection efficiency (Letterman,1987). For the dual filter glass and sand No.3 in set No.1, ηth is multiplies by 1.374 to obtain ηprac. For dual filters glass and porcelanite in set No.2 ηth is multiplied by 1.168 for filter No.1 and by 1.204 for filter No.3

CONCLUSIONS

The collection efficiency varied inversely with the filtration rate. For the mono media filters the theoretical values were more than the practical values calculated from the experimental work. In the glass filter ηprac is obtained by multiplying ηth by a factor 0.945 where this factor was o.714 and 0.55 for the sand filters. All the dual filters showed that ηth was less than ηprac. Whereas the dual filter 35cm porcelanite and 35cm glass showed the highest collection efficiency.

To obtain ηprac in the dual filter glass and sand, ηth is multiplied by 1.374, as for the dual filters porcelanite and glass the factors was 1.168 and 1.204.

REFERENCES

Cleasby,J.L.,Sindt, G.L., Watson, D.A. and Buumann, E.R., 1992, "Design and Operation Guidelines for Optimization of High Rate Filtration Process ", AWWA Research Foundation. Deriver Company.

CWC, 1997,"Crushed Glass as a Filter Medium for The onsite Treatment of Wastewater", final report, Clean Washington

Center, A Division of The Pacific Northwest Economic Region
.

Jegatheesan, V. and S.Vigneswaran, 2007, "Mathematical Modeling of Deep Bed Filtration", Environmental Engineering Group, Faculty of Engineering, University of Technology Sydney, Australia.

Kawamura, S., 2000," "Integrated Design and Operation of Water Treatment Facilities", John Wiley and Sons, New York.

Levich, V.G., 1962, " Physical-Chemical Hydrodynamics", Prentice Hall, Engllewood Cliffs, N.J.

Letterman, R.D.,1987, "An Overview of Filtration ". AWWA,Vol.79,No.12,26.

Logan, B. E., Jewett, D. G., Arnold, R.G., Bouwer, E.J., and O Melia, C.R., 1995, "Clarification of Clean-Bed Filtration Models", J.   Environ. Eng.,121,12,869-873.

Opta Minerals Inc., 2008,"Glass Material Description and its Related",
 www.optaminerals.com

Rajagopalan,R. And Tien,C., 1976,"Trajectory Analysis of Deep Bed Filtration With Soher in Cell Porous Media Model",AIChEJ.,22,3,523-533.

Tien ,C., and Ramarao, B. V., 2007,"Granular Filtration of Aerosols and Hydrosols", First edition, Elsevier Ltd.

Yao K.M., Habibian, M.T., and O Melia, C. R., 1971,"Water and Waste Water Filtration: Concepts and Applications", Environ. Sci. Technol.,5,11,1105-1112.

Yongwon J.S. Walata, and Tien C.,1989, "Experimental Determination of The Initial Collection Efficiency Of Granular Beds In The Inertial-Impaction-Dominated Region", Department of Chemical Engineering and Materials Science, Syracuse University, Syracuse.
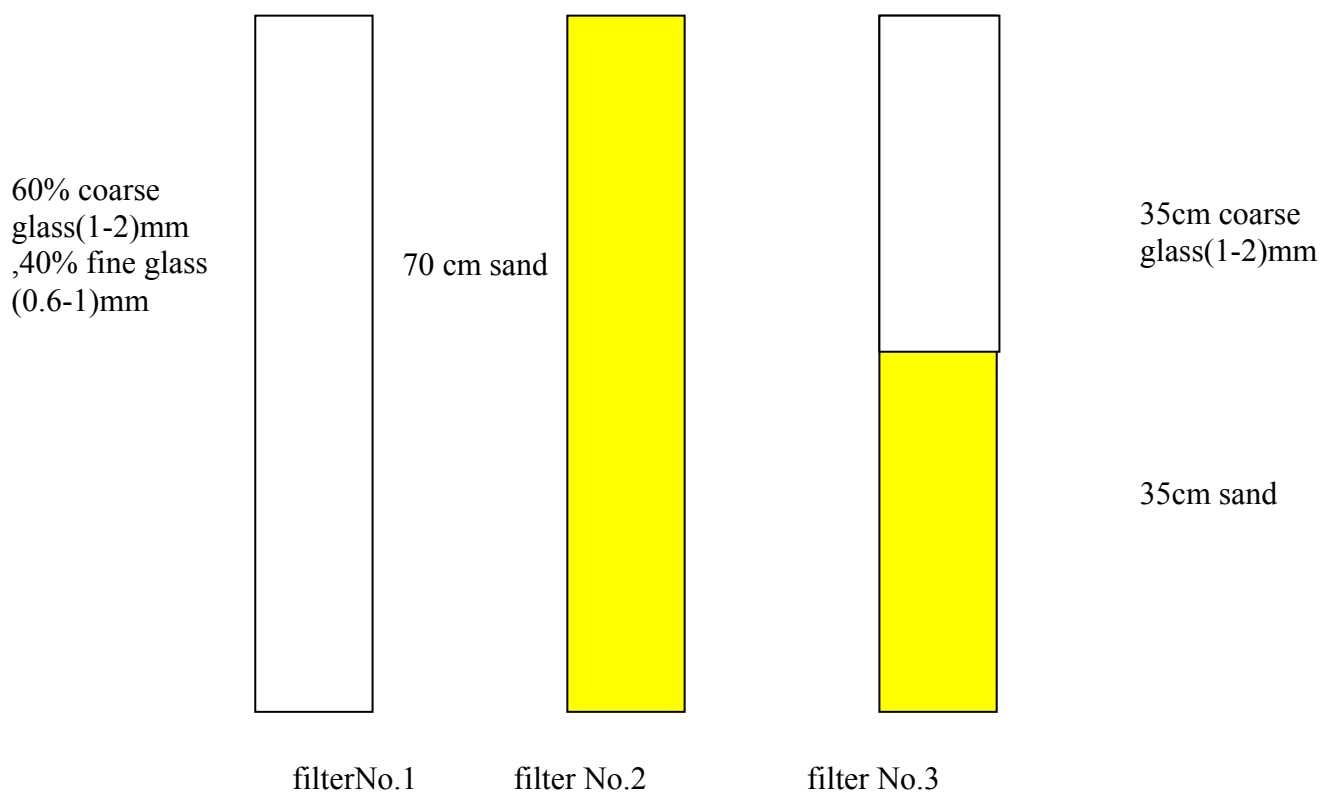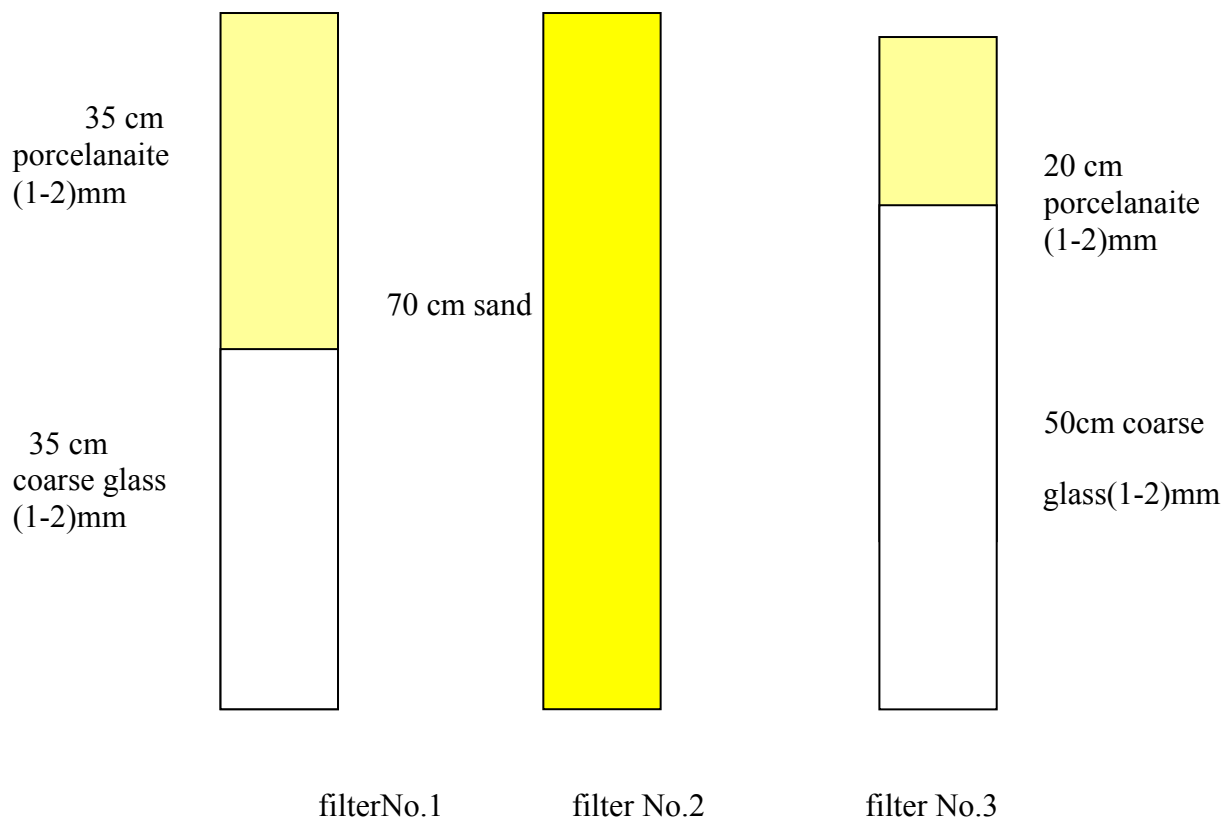
60% coarse glass(1-2)mm ,40% fine glass (0.6-1)mm

70 cm sand

35cm coarse glass(1-2)mm

35cm sand

filterNo.1   filter No.2   filter No.3

Figure 1 Set No.1

35 cm porcelanaite (1-2)mm

35 cm coarse glass (1-2)mm

70 cm sand

20 cm porcelanaite (1-2)mm

50cm coarse glass(1-2)mm

filterNo.1   filter No.2   filter No.3

Figure 2 Set No.2

Table 1 Results of Set No. 1, Filter No. 1

Parameters	Filtration Rates		
U_s	5m/hr	10m/hr	15m/hr
T	11^oC	13^oC	15^oC
ε	37%	37%	37%
p	0.825	0.825	0.825
w	0.04	0.04	0.04
A_s	30.891	30.891	30.891
N_R	$4.629*10^{-3}$	$4.629*10^{-3}$	$4.629*10^{-3}$
N_{Lo}	$3.117*10^{-7}$	$1.665*10^{-7}$	$1.192*10^{-7}$
D_{BM}	$6.554*10^{-14}$	$7.053*10^{-14}$	$7.626*10^{-14}$
N_{pe}	22886787	42535091	59008655
N_G	0.0134	$7.174*10^{-3}$	$5.136*10^{-3}$
E	81.458	82.664	67.208
$\eta_{th}*$	$3.61*10^{-3}$	$3.38*10^{-3}$	$2.20*10^{-3}$
$\eta_{prac}**$	$3.48*10^{-3}$	$3.20*10^{-3}$	$2.04*10^{-3}$

Table 2 Results of Set No. 1, Filter No. 2

Parameters	Filtration Rates		
U_s	5m/hr	10m/hr	15m/hr
T	11^oC	13^oC	15^oC
ε	37%	37%	37%
p	0.857	0.857	0.857
w	0.023	0.023	0.023
A_s	23.379	23.379	23.379
N_R	$4.784*10^{-3}$	$4.784*10^{-3}$	$4.784*10^{-3}$
N_{Lo}	$3.117*10^{-7}$	$1.665*10^{-7}$	$1.192*10^{-7}$
D_{BM}	$6.554*10^{-14}$	$7.053*10^{-14}$	$7.626*10^{-14}$
N_{pe}	22145085	41156639	57096337
N_G	0.0134	$7.174*10^{-3}$	$5.136*10^{-3}$
E	80.209	75.177	75.433
$\eta_{th}*$	$5.76*10^{-3}$	$2.99*10^{-3}$	$2.20*10^{-3}$
$\eta_{prac}**$	$2.55*10^{-3}$	$2.19*10^{-3}$	$2.13*10^{-3}$

$\eta_{th}*$ Theoretical efficiency calculated by equation 11
$\eta_{prac}**$Practical efficiency calculated by equation 17

Table 3 Results of Set No. 1, Filter No. 3

Parameters	Filtration Rates		
U_s	5m/hr	10m/hr	15m/hr
T	11 ^{o}C	13 ^{o}C	15 ^{o}C
ε	41%	41%	41%
p	0.838	0.838	0.838
w	0.033	0.033	0.033
A_s	17.78	17.78	17.78
N_R	$3.929*10^{-3}$	$3.929*10^{-3}$	$3.929*10^{-3}$
N_{Lo}	$3.117*10^{-7}$	$1.665*10^{-7}$	$1.192*10^{-7}$
D_{BM}	$6.554*10^{-14}$	$7.053*10^{-14}$	$7.626*10^{-14}$
N_{pe}	26955549	50096885	57096337
N_G	0.0134	$7.174*10^{-3}$	$5.136*10^{-3}$
E	84.508	84.772	81.289
η_{th}*	$3.06*10^{-3}$	$3.01*10^{-3}$	$2.10*10^{-3}$
η_{prac}**	$3.82*10^{-3}$	$3.78*10^{-3}$	$3.40*10^{-3}$

Table 4 Results of Set No. 2, Filter No. 1

Parameters	Filtration Rates		
U_s	5m/hr	10m/hr	15m/hr
T	20 ^{o}C	22 ^{o}C	20 ^{o}C
ε	57.5%	57.5%	57.5%
p	0.752	0.752	0.752
w	0.104	0.104	0.104
A_s	14.606	14.606	14.606
N_R	$3.333*10^{-3}$	$3.333*10^{-3}$	$3.333*10^{-3}$
N_{Lo}	$4.074*10^{-7}$	$2.155*10^{-7}$	$1.358*10^{-7}$
D_{BM}	$8.58*10^{-14}$	$9.415*10^{-14}$	$8.837*10^{-14}$
N_{pe}	24281274	42535091	70725359
N_G	0.0175	$9.293*10^{-3}$	$5.853*10^{-3}$
E	81.029	72.256	64.271
η_{th}*	$6.13*10^{-3}$	$4.01*10^{-3}$	$2.41*10^{-3}$
η_{prac}**	$6.26*10^{-3}$	$4.30*10^{-3}$	$3.40*10^{-3}$

Table 5 Results of Set No. 2, Filter No. 2

Parameters	Filtration Rates		
U_s	5m/hr	10m/hr	15m/hr
T	$20\,^{o}C$	$22\,^{o}C$	$20\,^{o}C$
ε	37%	37%	37%
P	0.857	0.857	0.857
w	0.023	0.023	0.023
A_s	23.379	23.379	23.379
N_R	$4.784*10^{-3}$	$4.784*10^{-3}$	$4.784*10^{-3}$
N_{Lo}	$4.074*10^{-7}$	$2.155*10^{-7}$	$1.358*10^{-7}$
D_{BM}	$8.58*10^{-14}$	$9.415*10^{-14}$	$8.837*10^{-14}$
N_{pe}	16915954	30831416	49272000
N_G	0.0175	$9.293*10^{-3}$	$5.853*10^{-3}$
E	87.349	74.750	49.997
$\eta_{th}*$	$4.94*10^{-3}$	$3.91*10^{-3}$	$2.43*10^{-3}$
$\eta_{prac}**$	$3.24*10^{-3}$	$2.16*10^{-3}$	$1.08*10^{-3}$

Table 6 Results of Set No. 2, Filter No. 3

Parameters	Filtration Rates		
U_s	5m/hr	10m/hr	15m/hr
T	$20\,^{o}C$	$22\,^{o}C$	$20\,^{o}C$
ε	52.1%	52.1%	52.1%
p	0.782	0.782	0.782
w	0.074	0.074	0.074
A_s	19.123	19.123	19.123
N_R	$3.333*10^{-3}$	$3.333*10^{-3}$	$3.333*10^{-3}$
N_{Lo}	$4.074*10^{-7}$	$2.155*10^{-7}$	$1.358*10^{-7}$
D_{BM}	$8.58*10^{-14}$	$9.415*10-^{14}$	$8.837*10^{-14}$
N_{pe}	24281274	44255620	70725359
N_G	0.0175	$9.293*10^{-3}$	$5.853*10^{-3}$
E	87.317	76.188	73.633
$\eta_{th}*$	$6.01*10^{-3}$	$4.09*10^{-3}$	$2.49*10^{-3}$
$\eta_{prac}**$	$6.15*10^{-3}$	$4.07*10^{-3}$	$3.97*10^{-3}$

Adaptive Coded Modulation for OFDM System

Assist. Prof. Dr. Serkout N. Abdullah   **Zainab Mageed Abid**
sar_abd2000@yahoo.com   zainab.mageed@yahoo.com

Abstract

This paper studies the adaptive coded modulation for coded OFDM system using punctured convolutional code, channel estimation, equalization and SNR estimation. The channel estimation based on block type pilot arrangement is performed by sending pilots at every sub carrier and using this estimation for a specific number of following symbols. Signal to noise ratio is estimated at receiver and then transmitted to the transmitter through feedback channel ,the transmitter according to the estimated SNR select appropriate modulation scheme and coding rate which maintain constant bit error rate lower than the requested BER. Simulation results show that better performance is confirmed for target bit error rate (BER) of (10^{-3}) as compared to conventional modulation schemes, the convolutional coded modulation offers a SNR gains of 5 dB compared to uncoded state at BER of 10^{-3}. The proposed adaptive OFDM scheme maintains fixed BER under changing channel conditions.

<div dir="rtl">

الخلاصة

في هذه المقالة تم دراسة منظومة التقسيم المتعدد المتعامد للتردد متعددة السرعة ومتكيفة و مرمزة باستخدام نوع الترميز Punctured Convolutional و تخمين وتعديل القناة وتخمين نسبة الإشارة إلى الضوضاء.تم دراسة طريقة لتخمين جودة القناة تسمى Block تعتمد على إرسال معلومات معروفة لدى المستلم على كل الترددات وهي ملائمة للقناة التي تتغير حالتها ببطء و طريقة لتخمين نسبة الإشارة إلى الضوضاء، يتم قياس مستوى الإشارة إلى الضوضاء في جهة الاستلام وإعادة إرسالها إلى المرسل من خلال قناة التغذية العكسية المثالية اعتمادا على مستوى الإشارة إلى الضوضاء يقوم المرسل باختيار الأسلوب المناسب للاتصال الذي يتضمن وحدة تضمين مرمزة تحقق نسبة خطا محددة مسبقا على أن لا يتجاوز عتبة نسبة الخطأ المطلوبة. لقد أظهرت النتائج العملية عند نسبة خطا 10^{-3} أداء جيد لهذه المنظومة مقارنة بمنظومة التضمين المر مز الغير متكيف وكذلك التضمين المر مز أعطى تحسن ل SNR قدره 5 dB مقارنة بالتضمين الغير مر مز. هذه المنظومة تحقق نسبة خطا ثابتة تحت ظروف القناة المتغيرة.

</div>

Key words: OFDM, adaptive, SNR estimation, convolutional code, channel estimation

Assist. Prof. Dr. Serkout N. Abdullah
Zainab Mageed Abid

Adaptive Coded Modulation for OFDM System

INTRODUCTION

The idea of adaptive modulation and coding (AMC) is to dynamically change the modulation and coding scheme in subsequent frames with the objective of adapting the overall throughput or power to the channel condition. In fact, when employing orthogonal frequency division multiplexing (OFDM) over a spectrally shaped channel the occurrence of bit errors is normally concentrated in a set of severely faded sub carriers, which should be excluded from data transmission. On the other hand, the frequency domain fading, while impairing the signal-to-noise ratio of some sub-carriers, may improve others above the average signal-to-noise ratio. Hence, the potential loss of throughput due to the exclusion of faded sub carriers can be mitigated by using higher order modulation modes on the sub-carriers exhibiting higher signal-to-noise ratio. In addition, other system parameters, such as the coding rate of error correction coding schemes, can be adapted at the transmitter according to the channel frequency response [**Benvenuto and Tosato, 2004**].

ADAPTIVE CODING AND MODULATION

The main concept of adaptive coding and modulation is to maintain a constant performance by varying transmitted power level, modulation scheme, coding rate or any combination of these schemes .This allows us to vary the data rate without sacrificing BER performance .Since in land mobile communication systems , the local mean value of the received signal level varies due to the fading channel, Adaptive coding and modulation is an effective way to achieve high data rates and it has proved to be a bandwidth efficient technology to transmit multimedia information over mobile wireless channels. It can be described as follows:

$$\text{Modulation mode} = (\begin{array}{ll} M_1 & cq < I_1 \\ M_2 & I_1 < cq < I_2 \\ . \\ . \\ . \\ M_n & I_{n-1} < cq) \end{array} \quad (1)$$

Where M_1, M_2... M_n, are n different modulation modes varying from lower multi-level modulation to higher multilevel modulation with increasing order. cq is the estimated channel quality expressed in terms of the signal-to-noise ratio (SNR) of the mobile wireless channel, I_1, I_2,….., I_{n-1} are the switching thresholds between different modulation modes.

The selection of modulation mode for the next transmission heavily depends on the current channel quality estimation. If the channel quality can be measured accurately, ideal switching between different modes is available. The system could have the highest performance under such circumstances, if the switching thresholds are selected carefully. In other words, in the scenario of no channel quality estimation error, the effectiveness of the adaptive modulation system will be decided mainly by the selection of the switching thresholds [**Long and Lo, 2003**].

Modulation scheme and coding rate are the most common parameters used in adaptive modulation. Basic guidelines for efficient usage of these parameters

are as follows **[Sampei and Harada, 2007]:**

1) Modulation Scheme Control: Modulation scheme control is the only technique to enhance the upper limit of spectral efficiency in terms of bit/s/Hz in single-input and single-output systems. However, if only the modulation scheme is used as a controllable modulation parameter MP, its dynamic range is not so wide. Table(1) summarizes theoretically obtained required energy per symbol to noise spectral density E_s/N_o to satisfy a required BER (BER_{req}) for each modulation scheme under additive white Gaussian noise (AWGN) conditions, where Gray mapping is assumed and no channel coding is employed. When all the modulation schemes in this table are selectable, the system's dynamic range is about 16 dB. On the other hand, when a channel is in a flat Rayleigh fading condition, the system's dynamic range is more than 20 dB, which is wider than that covered by an adaptively controlled modulation scheme. One solution to this problem is to introduce a non transmission mode as one of the selectable MPs and to choose this mode when the received signal level is too low to guarantee transmission of even a binary phase-shift keying (BPSK).

In this case, however, the ratio of the non transmission time period (outage probability) increases as the average received signal level decreases.

2) Coding Rate Control: When coding rate control is introduced to adaptive modulation schemes, because the required E_s/N_o for a specific BER can be lowered, one can have more chance to use higher user rates compared to non coding rate controlled systems under the same received signal level; thus, coding rate control enhances average system throughput. Moreover, the coding rate control has another advantage; one can reduce the required signal-to-noise power ratio (SNR) or SINR gap between adjacent MP modes, because an arbitrary number of coding rates can be prepared by a combination of punctured codes and regular bit puncturing.

The rules which follow to Choose MP Set are:
1. List all the possible combinations of modulation Schemes and coding rates, and sort these combinations of MPs in the order of the required SNR or SINR.
2. If there are several MP sets that can achieve the same spectral efficiency, a set with the lowest required SNR is chosen.
3. If there are several MP sets located very closely in the required SNR, some of them can be removed.

In Figure (1), the curves from left to right represent the BER of QPSK, 16QAM, 64QAM and 256-QAM in AWGN channel, respectively. In order to decide the proper switching levels from this plot, operating point, or

Assist. Prof. Dr. Serkout N. Abdullah
Zainab Mageed Abid

Adaptive Coded Modulation for OFDM System

desired BER must be decided. In this study, BER of (10^{-3}) is used as operating point. This means that the system will try and keep a BER lower than (10^{-3}) with the most spectrally efficient modulation scheme whenever possible. At this point spectral efficiency should be defined as the number of information bits encoded on a modulated transmission symbol. For example, QPSK has a spectral efficiency of 2 bits per symbol, 16 QAM has 4 bits per symbol, 64 QAM has 6 bits per symbol and 256 QAM has 8 bits per symbol.

THE ADAPTIVE OFDM SYSTEM

The proposed adaptive OFDM system used in the test is shown in Figure (2). The system consists of a transmitter, a receiver and a Rayleigh communication channel .The transmitter codes the input data by the convolutional coder that is efficient in the multipath fading channel. The convolutional coder uses the code rate (R=1/2) and the constraint length (k=7). The encoded data are punctured to generate high code rates from a mother code rate of 1/2, the coded serial bit sequences are converted to the parallel bit sequences and then modulated. The OFDM time signal is generated by an inverse FFT and is transmitted over the Rayleigh fading channel after the cyclic extension has been inserted. Doppler frequency is assumed to be 5Hz (slow flat fading). In the receiver side, the received signal is serial to parallel converted and passed to a FFT operator, which converts the signal hack to the frequency domain. This frequency domain signal is coherently demodulated. Then the binary data is decoded by the Viterbi hard decoding

algorithm. The simulation parameters are listed in Table (2)

The system is operating at a sampling rate of 20MHz. It uses 64-point FFT. The OFDM symbol duration worth's 66 sample where 64 is for data while 2 is cyclic prefix . This corresponds to efficiency of (0.96). Using different modulation schemes combined with puncturing of the convolutional encoder, 5 different data rate are defined. Data rate is a function of the modulation (QPSK, 16-QAM, 64-QAM and 256-QAM) and the code rate. The data rate is calculated using,

$$\text{Data rate} = (\text{bits}_{carrier} * N_{carriers} * CR) / T_{OFDM}$$
(2)

Where $\text{bits}_{carrier}$ is the number of bits per carrier, i.e. 2 for QPSK, $N_{carriers}$ is the number of subcarriers with information, CR is the code rate and T_{OFDM} is the OFDM symbol duration. The frame length is variable consists of fixed number of pilot symbols N_p and variable number of data symbols N_d.

SIGNAL TO NOISE RATIO ESTIMATION

The adaptive modulation scheme needs the accurate information of the multipath channel and estimates the SNR value by measuring the quantity of noise among the received signal. There have been two methods of measuring the quantity of noise among the received signal that passed through the channel. The first method uses the

previously known pilot symbol as the reference signal that is speedy and stable measuring method. The second method uses the demodulated signal as the reference signal and has the BER value sufficiently low for the accurate measurement of the SNR. Therefore, the pilot symbol is not necessary. SNR estimation algorithm is shown in Fig. (3).

The SNR value is computed by comparison between the received signal power and the noise power that $<|x|^2>$ is the received signal power and $<|y|^2>$ is the noise power **[Chu, Park and etc, 2007].**

CHANNEL ESTIMATION

Channel estimation can be achieved by transmitting pilot OFDM symbol as a preamble. The channel estimation can be performed by either inserting pilot tones into all of the subcarriers of OFDM symbols with a specific period or inserting pilot tones into each OFDM symbol.

The first one, block type pilot channel estimation, has been developed under the assumption of slow fading channel. This assumes that the channel transfer function is not changing very rapidly. The estimation of the channel for this block-type pilot arrangement can be based on Least Square (LS) or Minimum Mean-Square (MMSE). The later, the comb-type pilot channel estimation has been introduced to satisfy the need for equalizing when the channel changes even in one OFDM block. The comb-type pilot channel estimation consists of algorithms to estimate the channel at pilot frequencies and to interpolate the channel. The interpolation of the

channel for comb-type based channel estimation depends on linear interpolation.

Assuming P is the transmitted pilot data, the received signal after FFT is:

$$Y(k) = H(k)P(k) + W(k) \qquad (3)$$

Where w (k) is the noise components, and since, the pilot data is known at the receiver, then the simplest way to estimate the channel is by dividing the received signal by the known pilot:

$$\hat{H}(k)=Y(k)/P(k) \qquad (4)$$

Where $\hat{H}$ (k) is the estimate of the channel, and without noise, this gives the correct estimation. When noise is present, there could be an error [**Omran, 2007**].

RESULTS

Figure (4) shows the estimator's performance in all modulation schemes, the SNR estimator works well with QPSK modulation. As shown in Figure (4) , for M-QAM modulation at low SNR, the estimate is not good. This is because at low SNR, there are a greater number of symbol errors that occur. Those symbols are the input to the estimator. The more reliable the symbol information is, the better the SNR estimate is for QAM schemes. This is why the estimates are better at high SNR.

The levels in table (3) are concluded in the following way: At an operating BER of (10^{-3}), there is no modulation scheme that gives the desired

Assist. Prof. Dr. Serkout N. Abdullah
Zainab Mageed Abid

Adaptive Coded Modulation for OFDM System

performance at an SNR below 6.8 dB. Therefore, 1/2 QPSK is chosen as it is the most robust. Between 6.8 and 12.5 dB, there is only one scheme that gives performance below (10^{-3}), and that is 1/2 QPSK. Between 12.5 and 15.5 dB, 1/2 16-QAM gives the desired BER at a better spectral efficiency than 1/2 QPSK. Between 15.5 and 23dB, 3/4 16- QAM gives the desired BER at a better spectral efficiency than 1/2 16-QAM. Between 23 and 30 dB, 3/4 64-QAM gives the desired BER at a better spectral efficiency than 3/4 16-QAM. And at SNR higher than 30dB, 256-QAM gives the best spectral efficiency while providing the desired BER performance.

In Figure (7), the performance of adaptive coded modulation begins by overlapping the QPSK curve. It is analogous to the spectral efficiency curve, as QPSK is the primary transmission mode used in low SNR. However, as the SNR is increased to 13 dB, we see an interesting result. The performance of adaptive coded modulation begins to improve beyond what QPSK can provide.

Consider a channel that has a deep fade. Options here are to use one of five modulation modes, which differ in spectral efficiency and robustness. If the fading considered to be extremely deep, perhaps half of all bits will be in error. Here, it is advantageous to send fewer bits because the total number of errors will be decreased, which influences bit error rates much more than total number of bits sent. When the channel is not in a fade, then many bits are wanted to be sent. In this situation, The BER is lowered by increasing the number of bits sent

because errors become less frequent. It is the combination of these two principles that allows the BER performance of adaptive systems to be more robust than static systems while simultaneously providing better spectral efficiency at most ranges of SNR.

In Figure (8), a plot of the spectral efficiency of adaptive coded modulation versus SNR in dB. Here, spectral efficiency will be defined to be the number of bits sent per modulation symbol.
Note that at low SNR, the system achieves 2 bits per symbol, as QPSK is primarily used. However, as the SNR increases, the throughput also improve steadily, which indicates that more spectrally efficient transmission mode is beginning to use.

The curve begins to level out at close to 30 dB, as 256QAM becomes the transmission mode used most often and QPSK is rarely used. As SNR improves, the system is more able to choose more efficient transmission mode.

CONCLUSION

The main conclusions drawn from this study are:
1. The ACM scheme enhances the performance of the OFDM wireless communication system since it combines two adaptive schemes based on modulation and coding. The results show that the ACM scheme adjusts effectively to the channel environment because it allocates (1/2 QPSK) to the decreasing SNR value and (1/2 16-

QAM, 3/4 16-QAM, 3/4 64-QAM and 3/4 256-QAM) to the increasing SNR value.

2. When channel has deep fade one of five modulation modes which differ in spectral efficiency and robustness is used, if fading is extremely deep half of all bits will be in error, it is advantageous to send fewer bits because the total number of errors will be decreased. When channel is not in a fade many bits are send, In this situation BER is lowered by increasing the number of bits sent because errors are small. It is the combination of these two principles that allows the BER performance of adaptive system to be more robust than static system.

3. The ACM system provides better spectral efficiency at most ranges of SNR, at low SNR, the system achieves 2 bits per symbol, as QPSK is primarily used. However, as the SNR increases, the throughput also improve steadily, which indicates that more spectrally efficient transmission mode is used.

4. The concept of adaptive modulation optimizes the bandwidth efficiency for wireless communications without excessive complexity.

REFERENCES

Buthaina Mosa Omran ,"IMPROVEMENT TECHNIQUES FOR SATELLITE DIGITAL VIDEO BROADCASTING USING OFDM", P.HD. Thesis, in electronic and communication engineering, University of Baghdad, 2007.

F.Y. Long and K.T. Lo ,"Measurements for performance degradation of adaptive modulation scheme caused by channel quality estimation error" IEE, Proceeding Communication Vol 150, No. 2, April 2003.

Fernando H. Gregorio,"802.11a - OFDM PHY Coding and Interleaving", Helsinki University of Technology.

Hyung Suk Chu, Byung Su Park and Chong Koo An ,"Wireless Image Transmission based on Adaptive OFDM System",IEEE, 2007.

Nevio Benvenuto and Filippo Tosato, "On the selection Of Adaptive Modulation and Coding Modes Over OFDM", IEEE Communications Society, 2004.

Seiichi Sampei and Hiroshi Harada, "System Design Issues and Performance Evaluations for Adaptive Modulation in New Wireless Access Systems", Proceedings of the IEEE, Vol. 95, No. 12, December 2007.

Sinem Coleri, Mustafa Ergen, Anuj Puri, and Ahmad Bahai , "Channel Estimation Techniques Based on Pilot Arrangement in OFDM Systems", IEEE Transactions On Broadcasting, VOL. 48, NO. 3, September 2002.

LIST OF ABBREVIATIONS:

ACM   : Adaptive Coded Modulation

AWGN   : Additive Wight Gaussian Noise

BER   : Bit Error Rate

LS   : Least Square

MMSE   : Minimum Mean Square Error

OFDM   : Orthogonal Frequency Division Multiplexing

QAM   : Quadrature Amplitude Modulation

QPSK   : Quadrature Phase Shift Keying

SNR   : Signal to Noise Ratio

Table 1 Theoretical Required E_s/N_o to Satisfy a BER_{req} under AWGN Conditions

BER_{req}	BPSK	QPSK	16QAM	64QAM
10^{-2}	4.3dB	7.3dB	13.9 dB	19.6 dB
10^{-3}	6.8dB	9.8dB	16.5 dB	22.6 dB
10^{-4}	8.4dB	11.4dB	18.2 dB	24.3 dB
10^{-5}	9.6dB	12.6dB	19.4 dB	25.6 dB

Table 2 simulation parameters

Sampling rate	20 MHz
Number of FFT points	64
Number of carriers ($N_{carriers}$)	64
No. of input serial bits	100 000 bit
OFDM symbol period (T_{OFDM})	3.3 μs (66 sample)
Cyclic prefix	0.1 μs (2 sample)
FFT symbol period	3.2 μs (64 sample)
Data rate	19, 32,48,72,96 Mbps
Modulation scheme	QPSK, 16QAM, 64QAM, 256QAM
Demodulation	Coherent detection
Coding	Convolutional coding (Rate=1/2, constraint length=7) with Puncturing (3/4)
Fading	Slow flat fading
Doppler frequency	5 Hz
Channel	One path(AWGN+ Rayleigh fading)

Table 3 Transmission modes with convolutionaly coded modulation in AWGN channel

	Mode 1	Mode 2	Mode 3	Mode 4	Mode 5
Modulation	QPSK	16-QAM	16-QAM	64-QAM	256-QAM
Coding rate	1/2	1/2	3/4	3/4	3/4
Rate (bits/symbol)	1	2	3	4.5	6
SNR (dB) at BER=10^{-3}	6.8	12.5	15.5	23	29

Table 4 Transmission modes with convolutionaly coded modulation in Rayleigh fading

	Mode 1	Mode 2	Mode 3	Mode 4	Mode 5
Modulation	QPSK	16-QAM	16-QAM	64-QAM	256-QAM
Coding rate	1/2	1/2	3/4	3/4	3/4
Rate (bits/symbol)	1	2	3	4.5	6
SNR (dB) at BER=10^{-3}	7.5	13	16	24	30

channel,   fd =5 HZ
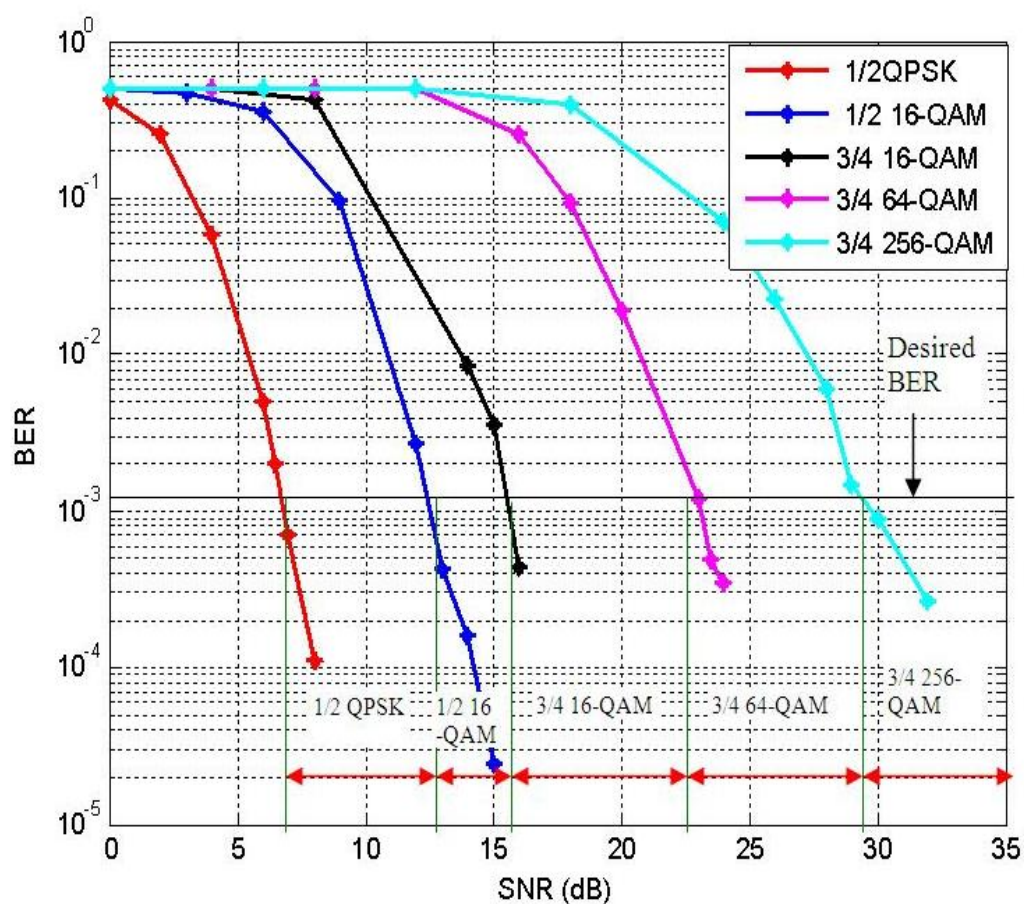
Fig. 1 BER Performance of coded OFDM in AWGN

157
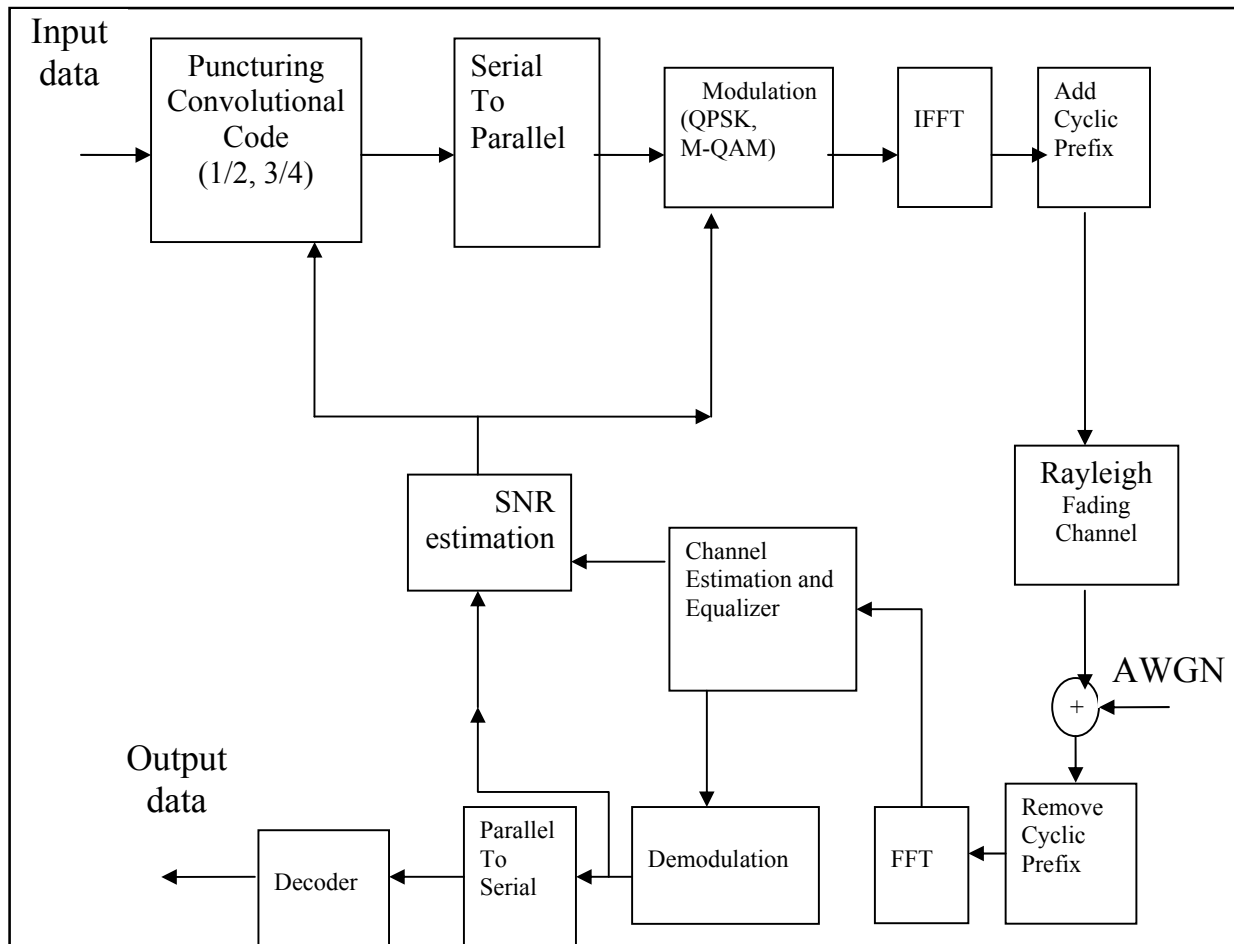
Fig. 2 Adaptive OFDM System Block Diagram

158
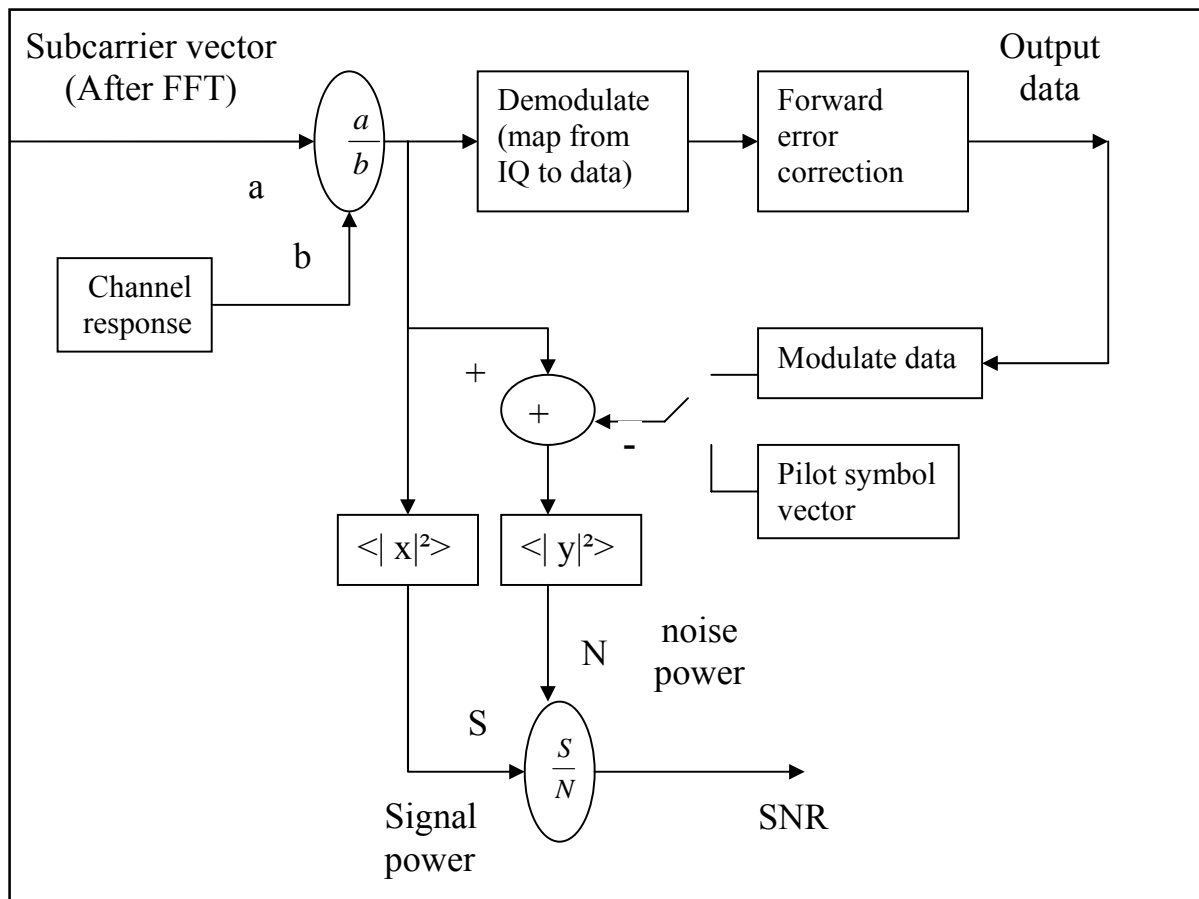
Fig. 3 SNR estimation algorithm
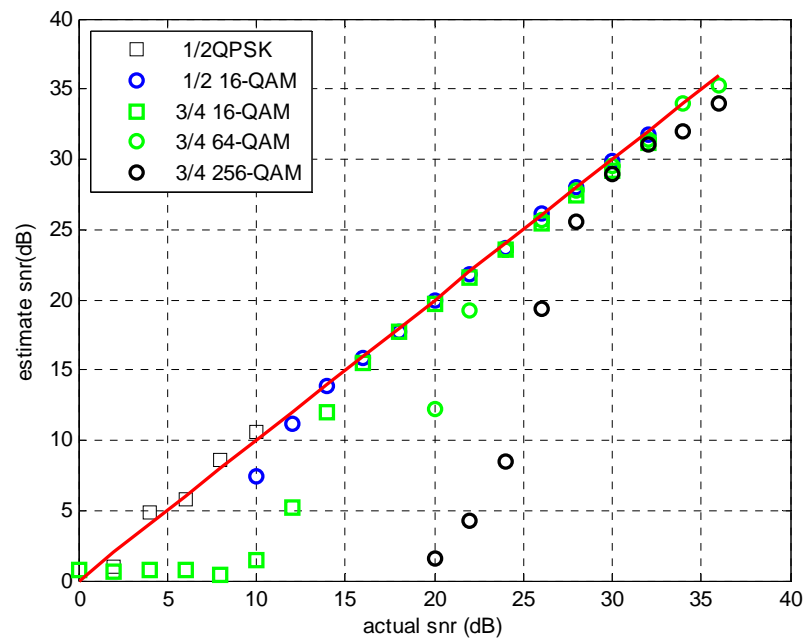
Fig. 4 SNR Estimation for all modulation schemes
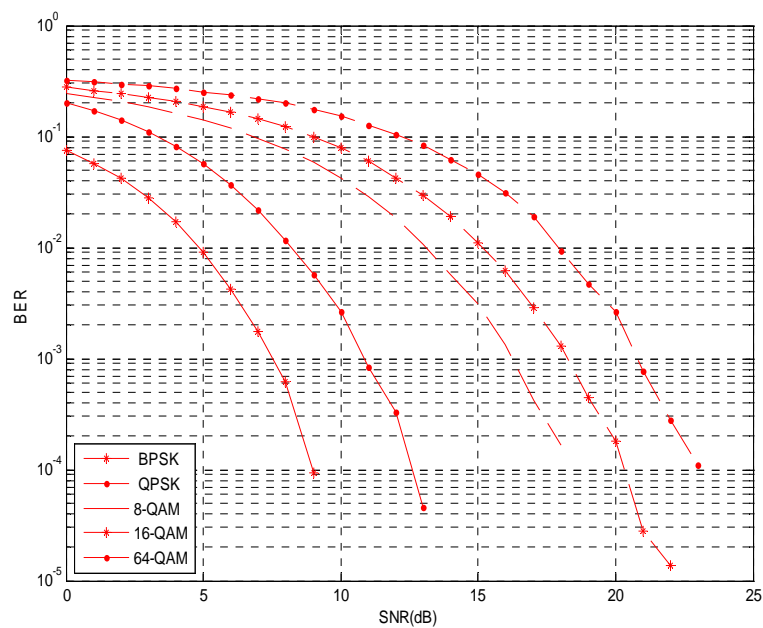
Fig. 5 BER performance of an un-coded OFDM system operating in an AWGN channel with different modulation schemes
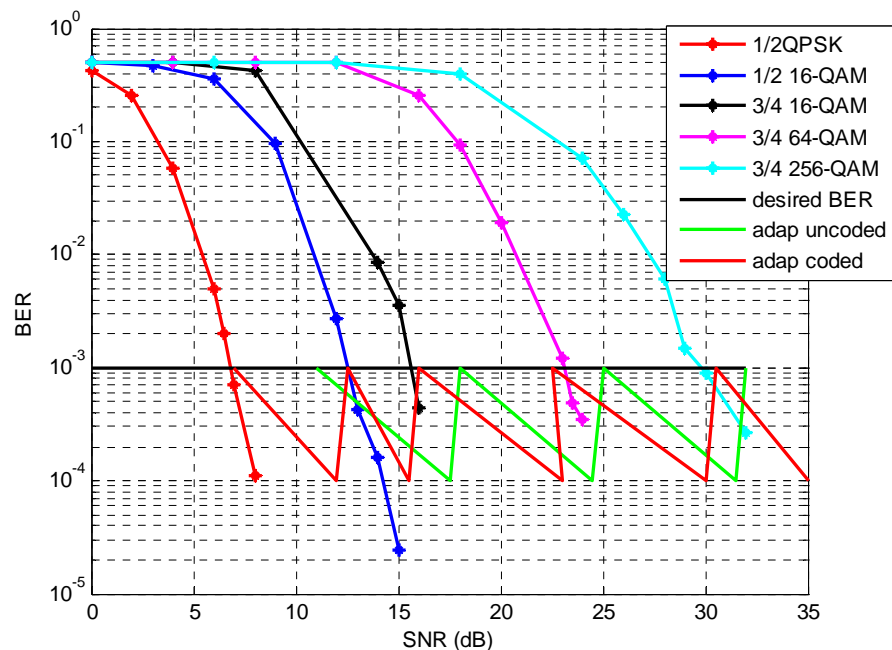
Fig. 6 BER Performance of Adaptive coded Modulation in AWGN
Channel with practical SNR estimation
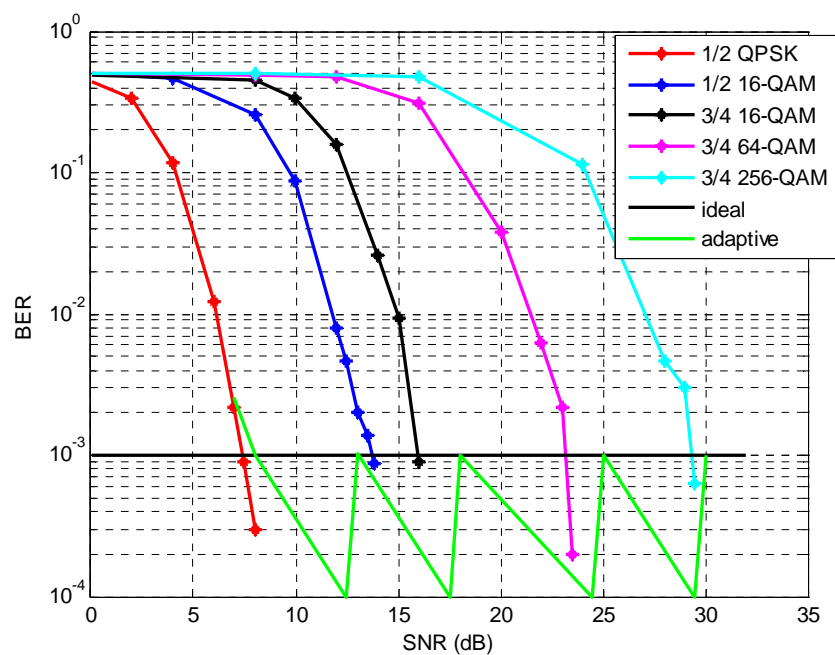
Fig. 7 BER Performance of Adaptive coded Modulation in Rayleigh
fading channel with practical SNR estimation
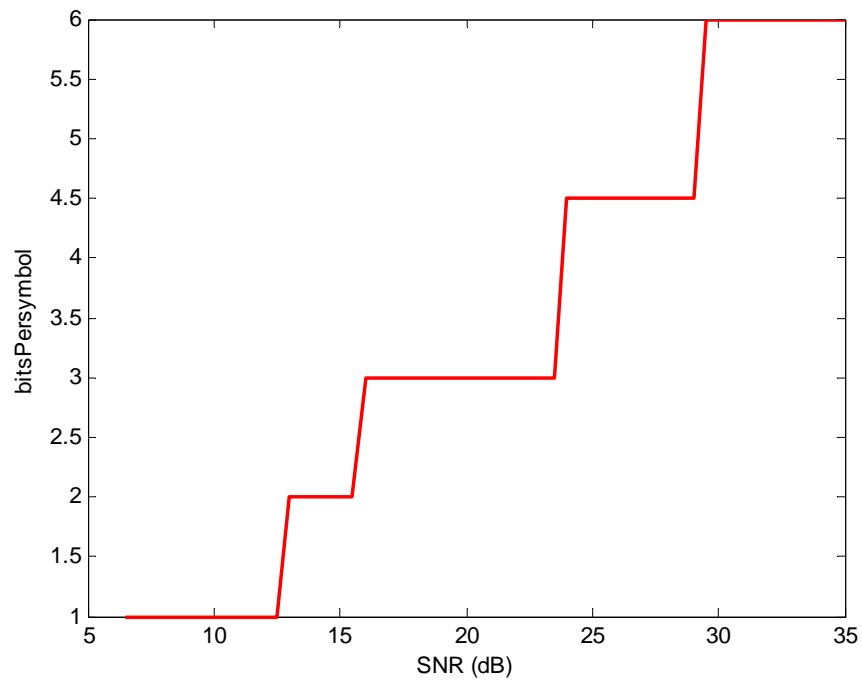
Fig. 8 Spectral Efficiency for Adaptive coded Modulation vs.
SNR for a Rayleigh channel

FLUTTER SPEED LIMITS OF SUBSONIC WINGS

Prof. Dr. Muhsin J. Jweeg	Ass. Prof. Dr. Shokat Al-Tornachi	Eng. Tariq Samir Talib
College of Engineering	College of Engineering	College of Engineering
Al-Nahrain University	University of Technology	University of Technology

BSTRACT

   Flutter is a phenomenon resulting from the interaction between aerodynamic and structural dynamic forces and may lead to a destructive instability. The aerodynamic forces on an oscillating airfoil combination of two independent degrees of freedom have been determined. The problem resolves itself into the solution of certain definite integrals, which have been identified as Theodorsen functions. The theory, being based on potential flow and the Kutta condition, is fundamentally equivalent to the conventional wing-section theory relating to the steady case. The mechanism of aerodynamic instability has been analyzed in detail. An exact solution, involving potential flow and the adoption of the Kutta condition, has been analyzed in detail. The solution is of a simple form and is expressed by means of an auxiliary parameter K. The use of finite element modeling technique and unsteady aerodynamic modeling with the V-G method for flutter speed prediction was used on a fixed rectangular and tapered wing to determine the flutter speed boundaries. To build the wing the Ansys 5.4 program was used and the extract values were substituted in the Matlab program which is designed to determine the flutter speed and then predicted the various effects on flutter speed. The program gave us approximately identical results to the results of the referred researches. The following wing design parameters were investigated skin shell thickness, material properties, cross section area for beams, and changing altitude. Results of these calculations indicate that structural mode shape variation plays a significant role in the determination of wing flutter boundary.

الخلاصة

الـرفرفـة (الأرتجـاج) هـي الظاهـرة الـتي تنتـج مـن التداخـل بيـن القـوى الدينـاهوائيـة ودينـاميكيـة الهيـكل مـما يـؤدي الى حـالـة من عـدم الاستقرار وبالتـالي تدميـر وتحطم الجنـاح. تحسـب القـوى الدينـاهوائيـة لمقطع جنـاح مهتـز لـه درجتان مـن الحـريـة باستخدام نظـريـة ثيودرسن(Theodorsen function)، حيـث إن المسألة تحـل باستخـدام التكـامـل المحدد. ويعتمـد أسـاس هذه دالة على التدفـق الكامن (potential flow) وعلى شرط كوتـا (Kutta condition) ، والتي تكون أسـاسا مكافئـاً لنظريـة مقاطع الأجنحـة للحـالـة الثابتـة. حيث يتم تحليـل الآليـة الدينـاهوائيـة الغير مستقرة بشكل مفصـل. الحـل الحقيقي يتضمن التدفـق و تبني شـرط كوتـا وتحليـله بشكل مفصـل. يمكن تمثيل الحـل باستخدام العـامـل المسـاعد (K) (auxiliary parametric). لحسـاب حـدود سـرعـة الـرفرفـة على الجنـاح المستدق والجنـاح المستطيـل حيث تم استخدام تقنية العنـاصـر المحددة و النمـوذج الدينـاهوائي الغير مستقر مـع طـريـقة السـرعـة-عامل التضاؤل (V-g) (velocity - damping method) للتنبـؤ بسـرعـة الـرفرفـة بـاستخـدام بـرنـامـج (ANSYS 5.4) تم بنـاء الجنـاح والقيم المستخـرجـة التي تستخدم في بـرنـامـج الـ(MATLAB) الذي صمم لحسـاب سـرعـة الـرفرفـة. ومنـه التنبـؤ بالمتغيـرات المؤثـرة على سـرعـة الـرفرفـة.حيث إن البرنـامـج أعطى نتـائج مطـابقـة تقريبـاً إلى نتـائج البحوث المشـار إليها. تم بحث المتغيـرات التصميمية التالية للجناح سمك متغير للغلاف ومادة متغيرة ومساحة مقطع متغيرة لقطع التقوية وارتفاع متغير. اوضحت النتائج بان تغير النسق للهيكل يلعب دورا مهما في حساب سرعة الرفرفة.

KEY WORKS: **Flutter, V-g Method, Wings.**

Prof. Dr. Muhsin J. Jweeg
Ass. Prof. Dr. Shokat Al-Tornachi
Eng. Tariq Samir Talib

FLUTTER SPEED LIMITS OF SUBSONIC WINGS

INTRODUCTION

The problem of oscillating airfoils has been an important subject of unsteady aerodynamics because of its close link with flutter analysis. The sustained oscillation is a boundary between convergent and divergent motions. Hence, the speed thus obtained is the critical speed, above which flutter occurs.

(Sadeghi, 2003); developed a code for the computation of three-dimensional aeroelastic problems such as wing flutter. **(Bala Krishnan 2003)**; Investigated the initial mathematical theory of aeroelasticity centered on the canonical problem of the flutter boundary instability endemic to aircraft that limits attainable speed in the subsonic regime. **(Massimo Bianchin 2003)**; Studied a methodology to merge state-space time domain realizations of a complete numerical aeroservoelastic model with flight mechanics equations

UNSTEADY AERODYNAMIC FORCES OF THE TYPICAL SECTION MODEL:-

The unsteady aerodynamic forces are calculated based on the linearized thin - airfoil .In this section, Theodorsen's approach will be summarized and the flutter analysis will be conducted based on his approach **(Theodore Theodorsen 1935)**.

In Theodorsen's approach, aerodynamic surfaces are modeled by flat plates. Theodorsen assumes that the flat airfoil is oscillating about the shear center (elastic axis) and unsteady flow is composed of two components, (a) non – circulatory flow which can be expressed through the sources and sinks and (b) circulatory flow related to the flat vorticity surface extending from trailing edge to infinity. For each flow component, he obtained the velocity potential and then calculated the pressure using Bernoulli's theory.

The Non-circulatory Flow:-

By using Joukoweski's conformal transformation **(Theodore Theodorsen 1935)**, the airfoil can be mapped onto a circle. The velocity potential of a source (ε) on a circle (x_1, y_1) can be expressed as:

$$\varphi = \frac{\varepsilon}{4\pi} Ln\left[(x - x_1)^2 + (y - y_1)^2\right]$$

Similarly, the velocity potential is due to a source (2ε) at on circle (x_1, y_1) and a sink (-2ε) at on circle $(x_1, -y_1)$.

$$\varphi = \frac{\varepsilon}{2\pi} Ln\left[\frac{(x - x_1)^2 + (y - y_1)^2}{(x - x_1)^2 + (y + y_1)^2}\right]$$

(1)

Since ($y = \sqrt{1 - x^2}$), the velocity potential is a function of (x) only.
The downward displacement of the airfoil can be written as

$$z = h + \alpha(x - ab)$$

Then, up-wash will be

$$w_a(x,t) = -\left[\frac{\partial z}{\partial t} + V\frac{\partial Z}{\partial x}\right] =$$

$$-\left[\dot{h} + \dot{\alpha}(x - ab)\right] - V\alpha$$

Therefore, the velocity potential due to pitch angle (α) will be

$$\varphi_\alpha = b\int_{-1}^{1} \frac{-V\alpha}{2\pi} Ln\left[\frac{(x - x_1)^2 + (y - y_1)^2}{(x - x_1)^2 + (y + y_1)^2}\right] dx_1 = V\alpha b\sqrt{1 - x^2}$$

(2)

Similarly, velocity potentials due to plunge motion, ($\dot{h}$) and angular velocity, ($\dot{\alpha}$) are respectively expressed as:

$$\varphi_h = \dot{h}b\sqrt{1 - x^2} \qquad \varphi_\alpha = \dot{\alpha}b^2\left(\frac{x}{2} - a\right)\sqrt{1 - x^2}$$

The total velocity potential due to non-circulatory flow becomes:

$$\varphi_{NC} = \varphi_\alpha + \varphi_h + \varphi_{\dot\alpha}$$

$$= V\alpha b\sqrt{1-x^2} + \dot{h}b\sqrt{1-x^2} + \dot\alpha b^2(\frac{x}{2}-a)\sqrt{1-x^2}$$

$$(3)$$

By Bernoulli theorem, the pressure is obtained as follows:

$$\Delta p = -2\rho\left(\frac{\partial\varphi}{\partial t} + V\frac{\partial\varphi}{\partial x}\right) = -2\rho\frac{\partial\varphi}{\partial t} = -2\rho\,\dot\varphi$$

$$(4)$$

And the force (positive downward) and the pitching moment (positive nose-up) about the elastic axis will be expressed as:-

$$F_{NC} = b\int_{-1}^{1}\Delta p\,dx = -2\rho b\int_{-1}^{1}\dot\varphi\,dx$$

$$\equiv -\pi\rho b^2\left(\ddot{h} + V\dot\alpha - ba\ddot\alpha\right)$$

$$(5)$$

$$M_{NC} = b\int_{-1}^{1}\Delta p(x-a)b\,dx = -2\rho b^2\int_{-1}^{1}\frac{\partial\varphi}{\partial t}(x-a)dx$$

$$\equiv \pi\rho b^2\left(V\dot{h} + ba\ddot{h} + V\dot\alpha^2 - b^2\left(\frac{1}{8}+a^2\right)\ddot\alpha\right)$$

$$(6)$$

The Circulatory Flow:-
        To satisfy the Kutta condition, Theodorsen employs a bound vortex distribution over the airfoil and a vortex over the airfoil wake.

In order to consider wake, assume a bound vortex $(\Delta\Gamma = \gamma\,dx)$ at (X_o), and a shed vortex $(-\Delta\Gamma)$ at (X_o).
Then, the velocity potential due to vortex is

$$\Delta\varphi_\Gamma = \frac{\Delta\Gamma}{2\pi}\left[\tan^{-1}\frac{Y}{X-X_o} - \tan^{-1}\frac{Y}{X-1/X_o}\right]$$

$$= -\frac{\Delta\Gamma}{2\pi}\tan^{-1}\left[\frac{(X_o-1/X_o)Y}{X^2-X(X_o+1/X_o)+Y^2+1}\right]$$

Define $(X_o + 1/X_o = 2x_o)$,   and
$(X = x, y = \sqrt{1-x^2})$
Then,

$$X_o = x_o + \sqrt{x_o^2-1}$$

$$1/X_o = \frac{1}{x_o+\sqrt{x_o^2-1}} = x_o - \sqrt{x_o^2-1}$$

The velocity potential can be expressed as

$$\Delta\varphi_\Gamma = -\frac{\Delta\Gamma}{2\pi}\tan^{-1}\left[\frac{\sqrt{1-x^2}(2\sqrt{x_o^2-1})}{x^2-x(2x_o)+(1-x^2)+1}\right]$$

$$= -\frac{\Delta\Gamma}{2\pi}\tan^{-1}\left[\frac{\sqrt{1-x^2}\sqrt{x_o^2-1}}{x^2-xx_o}\right]$$

$$(7)$$

Where

$$-1 \le x \le 1, \quad 1 \le x_o \le \infty$$

It is to be noted that the vortex is moving away from the airfoil with velocity of (V). Therefore, by Bernoulli theorem, the pressure due to the vortex is

$$\Delta p = -2\rho\left(\frac{\partial\Delta\varphi_\Gamma}{\partial t} + V\frac{\partial\Delta\varphi_\Gamma}{\partial x}\right)$$

Where:

$$\frac{2\pi}{\Delta\Gamma}\frac{\partial\Delta\varphi_\Gamma}{\partial x} = -\frac{\partial}{\partial x}\left[\tan^{-1}\left[\frac{\sqrt{1-x^2}\sqrt{x_o^2-1}}{1-xx_o}\right]\right]$$

$$= \frac{\sqrt{x_o^2-1}}{\sqrt{1-x^2}}\frac{1}{x_o-x}$$

Prof. Dr. Muhsin J. Jweeg
Ass. Prof. Dr. Shokat Al-Tornachi
Eng. Tariq Samir Talib

$$\frac{2\pi}{\Delta\Gamma}\frac{\partial\Delta\varphi_\Gamma}{\partial x_o} = \frac{\sqrt{1-x^2}}{\sqrt{x_o^2-1}}\frac{1}{x_o-x}$$

The pressure at (X) due to the vortex at (x_o) is

$$\Delta p_\Gamma = -2\rho\frac{\Delta\Gamma}{2\pi}V\left[\frac{\sqrt{x_o^2-1}}{\sqrt{1-x^2}}+\frac{\sqrt{1-x^2}}{x_o^2-1}\right]\frac{1}{x_o-x}$$

$$= -\rho V\frac{\Delta\Gamma}{2\pi}\left[\frac{x_o^2-x^2}{\sqrt{1-x^2}\sqrt{x_o^2-1}}\right]\frac{1}{x_o-x}$$

(8)

$$= -\rho V\frac{\Delta\Gamma}{2\pi}\frac{x_o+x}{\sqrt{1-x^2}\sqrt{x_o^2-1}}$$

The force on the whole airfoil due to a vortex at (x_o) will be

$$\Delta F_\Gamma = b\int_{-1}^{1}\Delta p_\Gamma dx$$

$$= -\rho V b\frac{x_o}{\sqrt{x_o^2-1}}\Delta\Gamma, 1\le x_o\le\infty$$

The total force can be calculated by integrating with respect to (x_o)

$$F_\Gamma = \int\Delta F_\Gamma$$

$$= -\rho V b\int_{-1}^{\infty}\frac{x_o}{\sqrt{x_o^2-1}}\gamma dx_o$$

Similarly,

$$\Delta M_\Gamma = b^2\int_{-1}^{1}\Delta p_\Gamma(x-a)dx, 1\le x_o\le\infty$$

$$M_\Gamma = \int\Delta M_\Gamma$$

$$= -\rho V b^2\int_{1}^{\infty}\left[\frac{1}{2}\sqrt{\frac{x_o+1}{x_o-1}}-\left(a+\frac{1}{2}\right)\frac{x_o}{\sqrt{x_o^2-1}}\right]\gamma dx$$

(10)

It has to be noted that the force and moment are functions of vortex strength (γ). By applying Kutta condition at trailing edge the vortex strength can be determined. The total

velocity potential is:

$$\varphi_{total} = \varphi_\Gamma + \varphi_\alpha + \varphi_{\dot{h}} + \varphi_{\dot{\alpha}}$$

$$= \varphi_\Gamma + V\alpha b\sqrt{1-x^2} + \dot{h}b\sqrt{1-x} + \dot{\alpha}b^2(\frac{x}{2}-a)\sqrt{1-x^2}$$

By applying the Kutta condition, the following equation is obtained:

$$\frac{\partial\varphi_\Gamma}{\partial x} + \frac{V\alpha b(-x)}{\sqrt{1-x^2}} + \frac{\dot{h}b(-x)}{\sqrt{1-x^2}} + \frac{1}{2}\dot{\alpha}b^2\sqrt{1-x^2}$$

$$+ \frac{\dot{\alpha}b^2(\frac{x}{2}-a)(-x)}{\sqrt{1-x^2}} =$$

Finite. At (x=1)   Therefore,

$$\left[\sqrt{1-x^2}\frac{\partial\varphi_\Gamma}{\partial x}\right]_{x=1} + \left\{-V\alpha b - \dot{h}b - \dot{\alpha}b^2(\frac{1}{2}-a)\right\} = 0$$

Since

$$\frac{\partial\varphi_\Gamma}{\partial x} = \frac{\Delta\Gamma}{2\pi}\frac{\sqrt{x_0^2-1}}{\sqrt{1-x^2}}\frac{1}{x_o-x}$$

The following expression is obtained from the above equation.

$$\left[\sqrt{1-x^2}\frac{\partial\varphi_\Gamma}{\partial x}\right]_{x=1} = \int\frac{\Delta\Gamma}{2\pi}\frac{\sqrt{x_o-1}}{x_o-1}$$

$$= \frac{b}{2\pi}\int_{1}^{\infty}\frac{\sqrt{x_o^2-1}}{x_o-1}\gamma dx_o$$

$$= V\alpha b + \dot{h}b + \dot{\alpha}b^2\left(\frac{1}{2}-a\right)$$

Define

$$\frac{1}{2\pi}\int\frac{\sqrt{x_o^2-1}}{x_o-1}\gamma dx_o = V\alpha + \dot{h} + \dot{\alpha}b\left(\frac{1}{2}-a\right) \equiv Q$$

Then, the total force and moment on the airfoil will be as follows:

$$F_\Gamma = -\rho V b\int\frac{x_o}{\sqrt{x_o^2-1}}\gamma dx_o$$

$$= - 2\pi\rho \quad VbQ \quad \frac{\int_1^\infty \frac{x_o}{\sqrt{x_o^2 - 1}}\gamma\, dx_o}{\int_1^\infty \frac{\sqrt{x_o + 1}}{\sqrt{x_o - 1}}\gamma\, dx_o}$$

$$M_\Gamma = -\rho Vb^2 \int_1^\infty \left[\frac{1}{2}\sqrt{\frac{x_o+1}{x_o-1}} - \left(a+\frac{1}{2}\right)\frac{x_o}{\sqrt{x_o^2-1}}\right]\gamma dx_o$$

$$= -2\pi\rho \, VbCQ$$

$$= -2\pi\rho Vb^2 Q\left[\frac{1}{2} - C\left(a+\frac{1}{2}\right)\right]$$

(11)

Where (c) is the Theodorsen function, and is defined as

$$C = \frac{\int_1^\infty \frac{x_o}{\sqrt{x_o^2-1}}\gamma dx_o}{\int_1^\infty \frac{\sqrt{x_o+1}}{\sqrt{x_o-1}}\gamma dx_o}$$

Assume that the airfoil has a simple harmonic motion

$$\gamma = \gamma_o e^{i\left[k\left(\frac{s}{b}-x_o\right)+\varphi\right]} = \gamma_o e^{i[\omega t - kx_o + \varphi]}$$

$$k = \frac{\omega b}{V} = \omega t$$

Where $s = Vt$

Then, Theodorsen function is expressed as

$$C = \frac{\int_1^\infty \frac{x_o}{\sqrt{x_o^2-1}}\gamma_o e^{i\omega t}e^{-ikx_o}e^{i\varphi}dx_o}{\int \frac{\sqrt{x_o+1}}{\sqrt{x_o-1}}e^{-ikx_o}dx_o}$$

$$= \frac{\int_1^\infty \frac{x_o}{\sqrt{x_o^2-1}}e^{-ikx_o}dx_o}{\int_1^\infty \frac{\sqrt{x_o+1}}{\sqrt{x_o-1}}e^{-ikx_o}dx_o}$$

(12)

The Theodorsen function is frequently replaced by simple algebraic approximation as follows:-

$$C(k) = 0.5 + \frac{0.0075}{0.0455 + ik} + \frac{0.10055}{0.3 + ik}$$

(13)

The total force and moment resulting from the noncirculatory and circulatory flows are expressed as:

$$F_\Gamma = -\pi\rho b^2\left[\ddot{h} + V\dot{\alpha} - ba\ddot{\alpha}\right] - 2\pi\rho VbQC(k)$$

$$M = \pi\rho b^2\left[ba\ddot{h} - Vb\left(\frac{1}{2}-a\right)\dot{\alpha} - b^2\left(\frac{1}{8}+a^2\right)\ddot{\alpha}\right] + 2\pi\rho Vb^2\left(a+\frac{1}{2}\right)QC(k)$$

Where

$$Q = V\alpha + \dot{h} + \dot{\alpha}b\left(\frac{1}{2}-a\right)$$

If a quasi-steady aerodynamic is assumed (The aerodynamic characteristics of an airfoil whose motion consists of variable linear and angular motions are equal, at any instant of time, to the characteristics of the same airfoil moving with constant linear and angular velocities equal to actual instantaneous values.), then C (k) becomes (1), and the force and moment will be

$$F_{QS} = -\pi\rho b^2\left[\ddot{h} + V\dot{\alpha} - ba\ddot{\alpha}\right] - 2\pi\rho Vb\left[V\alpha + \dot{h} + \dot{\alpha}b\left(\frac{1}{2}-a\right)\right]$$

$$M_{QS} = \pi\rho b^2\left[ba\ddot{h} - Vb\left(\frac{1}{2}-a\right)\dot{\alpha} - b^2\left(\frac{1}{8}+a\right)\ddot{\alpha}\right] + 2\pi\rho Vb^2\left(a+\frac{1}{2}\right)\left[V\alpha + \dot{h} + \alpha b\left(\frac{1}{2}-a\right)\right]$$

(14)

3. Flutter Equation Of The Typical Section Model.

Equation of Motion:-
   Consider the typical section shown in **Fig. (3).**

   The model has a translation spring with stiffness (k_h) and torsion spring, with stiffness (k_T). These springs are attached to the airfoil at the shear center. Therefore, it is two degrees of freedom model (h, α). And (h) is measured at the shear center (elastic axis).
The downward displacement of any other point on the airfoil is

$$z = h + x\alpha$$

Where (x) is a distance measured from the shear center.
The strain energy and the kinetic energy are respectively given by

$$U = \frac{1}{2}K_T\alpha^2 + \frac{1}{2}K_h h^2$$

Prof. Dr. Muhsin J. Jweeg
Ass. Prof. Dr. Shokat Al-Tornachi
Eng. Tariq Samir Talib

FLUTTER SPEED LIMITS OF SUBSONIC WINGS

$$T = \frac{1}{2}\int \rho \dot{z}^2 \, dx$$

where (ρ) is the mass per unite length of the airfoil.

$$T = \frac{1}{2}\left(\dot{h}^2 \int \rho \, dx + 2\dot{h}\dot{\alpha}\int \rho x \, dx + \dot{\alpha}^2 \int \rho x^2 \, dx \right)$$

Define the following.

Mass $\quad (m = \int \rho \, dx)$

The second moment of inertia of the airfoil about shear center,

$$I_\alpha = \int \rho x^2 \, dx = m r_\alpha^2$$

The first moment of inertia of the airfoil about shear center,

$$S_\alpha = \int \rho x \, dx = m x_\alpha$$

Where (r_α) is the radius of gyration and (x_α) is a distance from the coordinate to the mass center.

Then, the kinetic energy can be written as follows:

$$T = \frac{1}{2}m\dot{h}^2 + mx_\alpha \dot{h}\dot{\alpha} + \frac{1}{2}I_\alpha \dot{\alpha}^2$$

The virtual work due to the unsteady aerodynamic forces is

$$\delta W_\alpha = \int \Delta p \, \delta z \, dx = \int \Delta p \{\delta h + x \delta \alpha\} dx = Q_h \delta h + Q_\alpha \delta \alpha$$

Where the force (Q_h) is positive downward and moment (Q_α) is positive nose-up.

Lagrange's equations provide the equation of motion of the airfoil.

$$\frac{d}{dt}\left(\frac{\partial (T-U)}{\partial \dot{q}} \right) - \frac{\partial (T-U)}{\partial q} = Q_q$$

$$\begin{bmatrix} m & mx_\alpha \\ mx_\alpha & mr_\alpha^2 \end{bmatrix}\begin{Bmatrix} \ddot{h} \\ \ddot{\alpha} \end{Bmatrix} + \begin{bmatrix} K_h & 0 \\ 0 & K_T \end{bmatrix}\begin{Bmatrix} h \\ \alpha \end{Bmatrix} = \begin{Bmatrix} Q_h \\ Q_\alpha \end{Bmatrix} = \begin{Bmatrix} f \\ m \end{Bmatrix}$$

where $q = h, \alpha$

$$\begin{bmatrix} 1 & \bar{x}_\alpha \\ \bar{x}_\alpha & \bar{r}_\alpha \end{bmatrix}\begin{Bmatrix} \ddot{h}/b \\ \ddot{\alpha} \end{Bmatrix} + \begin{bmatrix} \omega_h^2 & 0 \\ 0 & \omega_\alpha^2 \bar{r}_\alpha^2 \end{bmatrix}\begin{Bmatrix} h/b \\ \alpha \end{Bmatrix} = \begin{Bmatrix} F/mb \\ M/mb^2 \end{Bmatrix}$$

where

$$\omega_h^2 = K_h/m, \omega_\alpha^2 = K_T/I_\alpha, \bar{x}_\theta = x_\alpha/b, \bar{r}_\alpha = r_\alpha/b.$$

The harmonic motions ($h = h_o e^{i\omega t}$)

and ($\alpha = \alpha_o e^{i\omega t}$) assumed the equations of motion will be:-

$$-\omega^2 \begin{bmatrix} 1 & \bar{x}_\alpha \\ \bar{x}_\alpha & \bar{x}_\alpha^2 \end{bmatrix}\begin{Bmatrix} h/b \\ \alpha \end{Bmatrix} + \begin{bmatrix} \omega_h^2 & 0 \\ 0 & \omega_\alpha^2 \bar{r}_\alpha^2 \end{bmatrix}\begin{Bmatrix} h/b \\ \alpha \end{Bmatrix} = \begin{Bmatrix} F/mb \\ M/mb^2 \end{Bmatrix}$$

The unsteady aerodynamic force and moment are:

$$F = -\pi \rho b^2 \left[\ddot{h} + V\dot{\alpha} - ba\ddot{\alpha} \right] -$$

$$2\pi \rho V b C(k) \left[V\alpha + \dot{h} + b\left(\frac{1}{2} - a\right)\dot{\alpha} \right]$$

$$= \pi \rho b^3 \omega^2 \left[\frac{h}{b}\left(1 - i2C\frac{1}{k}\right) + \alpha \left(-a - i\frac{1}{k} - 2C\frac{1}{k^2} - 2i\left(\frac{1}{2} - a\right)\frac{C}{k}\right) \right]$$

$$= \pi \rho b^3 \omega^2 \left[\frac{h}{b}L_h + \alpha\left(L_\alpha - \left(\frac{1}{2} + a\right)L_h\right) \right]$$

Where the reduce frequency is ($k = \dfrac{\omega b}{V}$), and

$$L_h = 1 - i2C\frac{1}{k}, \quad L_\alpha = \frac{1}{2} - i\frac{1+2C}{k} - \frac{2C}{k^2}$$

Similarly,

$$M = \pi \rho b^4 \omega^2 \left[\left\{ M_h - \left(\frac{1}{2} + a\right)L_h \right\}\frac{h}{b} + \left\{ M_\alpha - \left(\frac{1}{2} + a\right)(L_\alpha + M_h) + \left(\frac{1}{2+a}\right)^2 L_h \right\}\alpha \right]$$

Where

$$M_h = \frac{1}{2}, M_\alpha = \frac{3}{8} - i\frac{1}{k}$$

Then, the equation of motion can be rewritten as:

$$-\omega^2 \begin{bmatrix} 1 & \bar{x}_\alpha \\ \bar{x}_\alpha & \bar{r}_\alpha^2 \end{bmatrix} \begin{Bmatrix} h/b \\ \alpha \end{Bmatrix} + \begin{bmatrix} \omega_h^2 & 0 \\ 0 & \omega_\alpha^2 \bar{r}_\alpha^2 \end{bmatrix} \begin{Bmatrix} h/b \\ \alpha \end{Bmatrix}$$

$$= \frac{\omega^2}{\mu} \begin{bmatrix} L_h & L_\alpha - \left(\frac{1}{2}+a\right) L_h \\ M_h - \left(\frac{1}{2}+a\right) L_h & M_\alpha - \left(\frac{1}{2}+a\right)(L_\alpha + M_h) + \left(\frac{1}{2}+a\right)^2 L_h \end{bmatrix} \begin{Bmatrix} h/b \\ \alpha \end{Bmatrix}$$

(15)

where the mass ratio is defined as:

$\mu = \dfrac{m}{\pi \rho b^2}$), (m) is the airfoil mass per unit length.

Define ($\Omega^2 = \dfrac{\omega^2}{\omega_\alpha^2}$) and ($R^2 = \dfrac{\omega_h^2}{\omega_\alpha^2}$), then

$$-\Omega^2 \begin{bmatrix} 1 & \bar{x}_\alpha \\ \bar{x}_\alpha & \bar{r}_\alpha^2 \end{bmatrix} \begin{Bmatrix} h/b \\ \alpha \end{Bmatrix} + \begin{bmatrix} R^2 & 0 \\ 0 & \bar{r}_\alpha^2 \end{bmatrix} \begin{Bmatrix} h/b \\ \alpha \end{Bmatrix}$$

$$= \frac{\Omega^2}{\mu} \begin{bmatrix} L_h & L_\alpha - \left(\frac{1}{2}+a\right) L_h \\ M_h - \left(\frac{1}{2}+a\right) L_h & M_\alpha - \left(\frac{1}{2}+a\right)(L_\alpha + M_h) + \left(\frac{1}{2}+a\right)^2 L_h \end{bmatrix} \begin{Bmatrix} h/b \\ \alpha \end{Bmatrix}$$

V-G METHOD FOR FLUTTER ANALYSIS:-

The above flutter equation is expressed in the following matrix form.

$$[K_{ij}] \begin{Bmatrix} h/b \\ \alpha \end{Bmatrix} = \Omega^2 [A_{ij} + M_{ij}] \begin{Bmatrix} h/b \\ \alpha \end{Bmatrix}$$

Where (K_{ij}) is the stiffness matrix, (M_{ij}) mass matrix, and (A_{ij}) is the aerodynamic matrix. Note that the aerodynamic is function of the reduced frequency, (k).
V-g method assumes first the artificial structure damping, (g).

$$[K_{ij}] = (1 + ig)[K_{ij}]$$

This artificial damping indicates the required damping for the harmonic motion. The eigenvalue of the equation of motion represents a point on the flutter boundary if the corresponding value of (g) equals the assumed value of (g).

For a given reduced frequency, ($k = \dfrac{\omega b}{V}$) will be a complex eigenvalue problem.

$$\frac{(1+ig)}{\Omega^2}[K_{ij}] \begin{Bmatrix} h/b \\ \alpha \end{Bmatrix} = [A_{ij} + M_{ij}] \begin{Bmatrix} h/b \\ \alpha \end{Bmatrix} \quad (16)$$

The Eigen value is:-

$$\lambda = \frac{1 + ig}{\Omega^2}$$

From this eigenvalue:

$$\frac{1}{\lambda_{Re}} = \frac{\omega_i^2}{\omega_\alpha^2}$$

$$g = \frac{\lambda_{Im}}{\lambda_{Re}}$$

ANSYS ANALYSIS OF WING MODEL:-

The wing model analysis in the Ansys program is by using the suitable element for the work. The (Shell 93) may be used for skin and the spar web and the (Beam 4) (3D elastic beam) is used for the stiffeners in the isotropic case

FLUTTER PROGRAM: -

The combination between the (ANSYS 5.4) and the (MATLAB 7.0) is employed. The program is solved by using the Theodorsen's theory with velocity damping (V-g) method.
The inputs of program for the wings model are:
1. From (ANSYS 5.4) the natural frequencies are taken.
2. The static unbalance, frequency ratio, mass ratio, radius of gyration and non-dimensional location of airfoil elastic axis.
3. Density of air at any altitude.

And the outputs of program are:
1- The bending and torsional mode shapes for both rectangular and tapered wings as shown in Figures a to d.

169

Prof. Dr. Muhsin J. Jweeg
Ass. Prof. Dr. Shokat Al-Tornachi
Eng. Tariq Samir Talib

FLUTTER SPEED LIMITS OF SUBSONIC WINGS

2- The relation between the non-dimensional parameter (1/k) with structural damping.
3- Calculation of the flutter speed.

RESULTS AND DISCUSSIONS:-

RESULTS OF COMPARISON: -

By using analytical and numerical solution for the case where (μ=60, r_α = 0.4, x_α = 0.2, a = -0.3) it is found that the results in the work are approximately equal to the results in references as shown table 1.The following parameter are to be investigated

Effect of the Changing Wing Skin Thickness

The shell thickness is one of the main important variables in the wing design; therefore the effect of variation thickness from (0.001m) to (0.0035m) was studied in the reduced frequency, flutter speed and mass for two types of wing (rectangular wing and straight-tapered wing).

Rectangular Wing

Table (2) shows the shell thickness effects on the vibration modes. For the configuration (3x5) with area (A=44mm^2) and thickness (0.001m) the first two natural frequencies are equal to (20.016 HZ, 101.15 HZ), with mass (8.231kg), **Figs. (5)** and **(6)** show the reduced frequency ($\frac{1}{k} = \frac{V_f}{b \omega_\alpha}$ =1.66) and frequency ratio ($\frac{\omega_f}{\omega_\alpha}$ =0.351). For these values (ω_f =35.503HZ, V_f=474.751m/sec). But when the thickness increases to (0.0035m) the first two natural frequencies are equal to (19.489HZ, 108.7HZ) with mass (20.704kg), **Figs. (15)** and **(16)** show the reduced frequency ($\frac{1}{k} = \frac{V_f}{b \omega_\alpha}$ =2.66) and frequency ratio ($\frac{\omega_f}{\omega_\alpha}$ =0.322) and (ω_f =35.0014HZ, V_f =817.115m/s). From **Figs (7), (8) (9), (10) (11), (12) (13)** and **(14)** it is found that the reduced frequency is increased while the frequency ratio decreases therefore; the flutter speed is increased with thickness i.e. mass increases and the effect of thickness on the flutter speed is under investigation.

Tapered Wing

Table (3) shows that the effects of thickness are high on the flutter speed. For thickness (0.001m) the first two natural frequencies are equal to (31.807HZ, 128.22 HZ), with mass (7.4752kg) and **Figs. (17)** and **(18)** show the reduced frequency ($\frac{1}{k} = \frac{V_f}{b \omega_\alpha}$ =2.97) and frequency ratio ($\frac{\omega_f}{\omega_\alpha}$ =0.416) and (ω_f =53.33HZ, V_f =765.671m/s). And for thickness (0.0035m) the first two natural frequencies are equal to (32.446HZ, 138.75HZ), with mass (18.721kg), **Figs. (27)** and **(28)** show the reduced frequency ($\frac{1}{k} = \frac{V_f}{b \omega_\alpha}$ =4.956) and frequency ratio ($\frac{\omega_f}{\omega_\alpha}$ =0.396) and (ω_f =54.945HZ, V_f =1381.891m/s). **Figs (19), (20), (21), (22), (23), (24), (25)** and **(26)** show the thickness effect on flutter speed for taper wing type.

From the static solution **(Mechanical and Electrical Systems, Operation Manual, Boeing Commercial Airplane Company 1984)**. the optimum thickness is taken for the wings (0.001m) for rectangular wing and (0.003m) for tapered wing.

EFFECT OF THE USED MATERIAL

One of the important and necessary factors in the wing design is the material that is used. The material chosen gives the high resistance with little weight (high resistance to weight ratio). Therefore, three types of materials to build the wing structure are tested in this work.

Rectangular Wing:-

From **Table (4)** the (adv. Aluminum) is used in the wing design. For configuration (3x5) with thickness equal to (0.001m) the first two natural frequencies are equal to (21.20HZ,

107.49HZ) with mass (8.5437kg) and **Figs**. **(29)** and **(30)** show the reduced frequency $(\frac{1}{k}=\frac{V_f}{b\,\omega_\alpha}=1.688)$ and frequency ratio $(\frac{\omega_f}{\omega_\alpha}=0.337)$ and $(\omega_f =36.22HZ,\ V_f =513.018m/s)$. And for the same thickness for (7075-T6) the first two natural frequencies are equal to (20.016 HZ, 101.15 HZ), with mass (8.231kg) and **Figs. (5)** and **(6)** show the reduced frequency $(\frac{1}{k}=\frac{V_f}{b\,\omega_\alpha}=1.66)$ and frequency ratio $(\frac{\omega_f}{\omega_\alpha}=0.351)$. For these values $(\omega_f =35.503HZ,\ V_f =474.751m/sec)$. From **Table (5)** and for the same thickness when using the (Ti6A14V) the first two natural frequencies are equal to (19.825HZ, 101.21HZ) with mass (13.02 kg). **Figs. (33)** and **(34)** show the reduced frequency $(\frac{1}{k}=\frac{V_f}{b\,\omega_\alpha}=2.044)$ and frequency ratio $(\frac{\omega_f}{\omega_\alpha}=0.327)$ and $(\omega_f =33.095HZ,\ V_f =584.624m/s)$. From above it is clear that the effects of the materials (7075-T6) and (Adv.Aluminum) are approximately equal in angular flutter frequency but the difference in the flutter speed is equal to (7.45%) using the same mass. But when using (Ti6A14V) the angular flutter frequency is less than the (7075-T6) and (Adv.Aluminum) while the flutter speed is greater with high value of mass. The percentage between (Ti6A14V) and (7075-T6) is equal to (18.7%), and (Ti6A14V), (Adv.Aluminum) is equal to (12.2%). The percentages differ because of the wing mass difference.

TAPERED WING

From **Table (6)**,and when using the (adv. Aluminum) in the wing design with changing thickness, it is seen that for configuration (3x5) with thickness equal to (0.003m) the first two natural frequencies are equal to (34.306HZ, 146.07HZ) with mass (17.098kg), **Figs. (31)** and **(32)** show the

reduced frequency $(\frac{1}{k}=\frac{V_f}{b\,\omega_\alpha}=4.769)$ and frequency ratio $(\frac{\omega_f}{\omega_\alpha}=0.429)$ and $(\omega_f =62.66HZ,\ V_f =1399.903m/s)$. And for the same thickness for (7075-T6) the first two natural frequencies are equal to (32.387HZ, 137.75HZ), with mass (16.472kg), **Figs. (13)** and **(14)** show the reduced frequency $(\frac{1}{k}=\frac{V_f}{b\omega_\alpha}=4.675)$ and frequency ratio $(\frac{\omega_f}{\omega_\alpha}=0.421)$ and $(\omega_f =57.992HZ,\ V_f =1294.144m/sec)$. From **Table (7)** and for the same thickness when using the (Ti6A14V) the first two natural frequencies are equal to (32.07HZ, 136.88HZ) with mass (26.055kg), **Figs. (35)** and **(36)** show the reduced frequency $(\frac{1}{k}=\frac{V_f}{b\omega_\alpha}=5.79)$ and frequency ratio $(\frac{\omega_f}{\omega_\alpha}=0.405)$ and $(\omega_f =55.436HZ,\ V_f =1592.679m/s)$. From above, it is found that the effects of the materials (7075-T6) and (Adv.Aluminum) are different in angular flutter frequency but the flutter speed difference percentage is equal to (7.5%) with the same mass approximately. But when using (Ti6A14V) it is found that the angular flutter frequency is less than the (7075-T6) and (Adv.Aluminum) while the flutter speed is greater with high value for mass. The percentage difference between (Ti6A14V) and (7075-T6) is equal to (18.7%) and (Ti6A14V) (Adv.Aluminum) is equal to (12.2%). These differences are because of the wing mass difference.

From above, the material (7075-T6) is recommended for both wings rectangular and taper because it gives good results for flutter speed and angular flutter frequency with little mass.

Figs. (1) and **(2)** show the bending and torsion mode shapes and the corresponding deformations of the material, type (7075-T6) in configuration (3x5) and shell thickness (0.001m) with beam cross section area of

Prof. Dr. Muhsin J. Jweeg
Ass. Prof. Dr. Shokat Al-Tornachi
Eng. Tariq Samir Talib

FLUTTER SPEED LIMITS OF SUBSONIC WINGS

$(44\text{x}10^{-6}\text{m}^2)$. These deformations are due to free vibration in the rectangular wing. **Figs. (3)** and **(4)** show the bending and torsion mode shapes and the corresponding deformations of the material, type (7075-T6) in configuration (3x5) and shell thickness (0.003m) with beam cross section area of $(44\text{x}10^{-6}\text{m}^2)$. These deformations are due to free vibration of the tapered wing.

CONCLUSIONS

From the results achieved in this work the following points may be concluded.

Increase of radius of gyration (r_α) tends to increase the flutter speed especially for higher mass ratio. The static unbalance (x_α) increases (the distance between the rotation center and center of gravity) the flutter speed decreases because of the strong coupling between heaving and pitching motion.

- The flutter speed is sensitive to the ratio of uncoupling natural frequencies, where the increasing of the frequency ratio increases the flutter speed and the flutter speed has a minimum near $(\dfrac{\omega_h}{\omega_\alpha}=1)$. With structure damping omitted the typical section model is neutrally stable until $(V = V_f)$ for $(V = V_f)$ the bending and torsion frequencies merge and for $(V > V_f)$ the system is unstable.
- With including structure damping (g) for small (V) all values of structure damping (g) are stable and flutter speed is sufficiently large (V) where structure damping (g) changes its sign from negative to positive.
- The higher wing aspect ratio decreases the flutter speed, while the increasing of the taper ratio increases the flutter speed. The flutter speed changes linearly with the altitude and it is increased with increasing the altitude. Flutter prevention can be summarized by adding mass or redistribute mass so that $(x_\alpha < 0)$ mass balance, increases torsional stiffness i.e. increase (ω_α),

Increasing or decreasing $(\dfrac{\omega_h}{\omega_\alpha})$ if it is near one (for fixed ω_α), adding damping to the structure and require the aircraft to be flown below its critical mach number.

REFERENCES:-

- Bala Krishnan A.V. (2003), Toward a Mathematical Theory of Aero elasticity Flight Systems Research Center. UCLA.
- Darrol Stinton. (1989), The Design of the Aeroplane. Bsp. Professional Books Oxford, England.

- Massimo Bianchin, Giuseppe Quarantay, Paolo Mantegazza. (2003), State Space Reduced Order Models for Static Aeroelasticity and Flight Mechanics of Flexible Aircrafts. Department of Engineering, Milano. Italy.

- Mechanical and Electrical Systems (1984). Operation Manual, Boeing Commercial Airplane Company.

- Sadeghi M., Yangy S., Liuz F., Tsaix H. M. (2003), Parallel Computation of Wing Flutter with a Coupled Navier-Stokes/CSD Method. AIAA 1347.

- Theodore Theodorsen. (1935), General Theory of Aerodynamic Instability and the Mechanism of Flutter. NACA Report No.496.

- Ueda T. and Dowell E. H. (1984), Flutter Analysis Using Nonlinear Aerodynamic Force. J. of Aircraft, Vol.12, No.2.

- Yang T. Y. (1980), Flutter Analysis of a NACA 64A006 Airfoil in Small Disturbance Transonic Flow. J. of Aircraft, Vol.17.

Symbols:-

Symbol	Definition	Unit
Aij	Aerodynamic matrix	-
A	Area of element	m2
a	Non-dimensional location of airfoil elastic axis	-
b	Semi chord of the wing	m
C	Theodorsen function	-
Cr	Wing root chord	m
Ct	Wing tip chord	m
[D]	Elasticity matrix	-
E	Modulus of elasticity	Gpa
F	Total force	N
F(k)	Real part of Theodorsen function	-
FNC	Force due to non-circularity flow	N
FΓ	Force due to vortex	N

Symbol	Definition	Unit
Lα	Aerodynamic coefficient	-
M	Total moment	N.m
MNC	moment due to non-circularity flow	N.m
Mh	Aerodynamic coefficient	-
Mij	Mass matrix	-
Mα	Aerodynamic coefficient	-
MΓ	moment due to vortex	N.m
m	Mass of wing	Kg
[N]	Shape function matrix	-
p	Pressure	N/m²
ΔpΓ	Pressure due to vortex	N/m2
R	Frequency ratio	-
rα	Radius of gyration	m
Sα	First moment of inertia	kg.m
s	The distance from the vortex element to the airfoil	m
T	Kinetic energy	N.m

Symbol	Definition	Unit
t	time	sec
U	Strain energy	N.m
V	Velocity of air	m/s
Wα	Up-wash velocity of the airfoil	m/s
δWα	Virtual work due to unsteady aerodynamic forces	N.m
x	The distance measured from the shear center	m
xα	The center of gravity distance of the wing	m
α	Angle of attack	Degree
$\dot{\alpha}$	Angular velocity	rad/s
$\ddot{\alpha}$	Angular acceleration	rad/s2
ε	Source intensity	m2/s
γ	Function of the distance from the first vortex element	-
φ	Velocity potential	m/s

Symbol	Definition	Unit
φα	Velocity potential due to pitch angle	m/s
φ_h	Velocity potential due to plunger motion	m/s
φ_α	Velocity potential due to angular velocity	m/s
φNC	Velocity potential due to non circularity	m/s
φΓ	Velocity potential due to vortex	m/s
φtotal	Total Velocity potential	m/s
Γ	Bound vortex and shed vortex	
ρ	Air and material density	kg/m3
ωh	Bending frequency	Hz
ωα	Torsion frequency	Hz
Ω	Frequency ratio	-
μ	Mass ratio	-
λ	Eigen value	-

Prof. Dr. Muhsin J. Jweeg
Ass. Prof. Dr. Shokat Al-Tornachi
Eng. Tariq Samir Talib

FLUTTER SPEED LIMITS OF SUBSONIC WINGS

Symbol	Definition	Unit
G(k)	Imaginary part of Theodorsen function	-
g	Structural damping	-
H	Altitude	km
h	Te Vertical coordinate of the axis of rotation	m
$\dot{h}$	Plunger motion	m/s
$\ddot{h}$	Plunger acceleration	m/s2
Iα	Second moment of inertia about shear center	kg.m2
i	$\sqrt{-1}$	-
[Ke]	Element stiffness matrix	-
Kij	stiffness matrix	-
Kh	Stiffness for translation spring	N/m
Kα	Stiffness for tensional spring	N/m
k	Reduced frequency	-
Lh	Aerodynamic coefficient	-
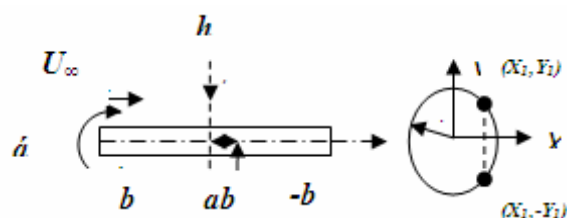
Fig. a. Flat airfoil and the transformed circle [4]
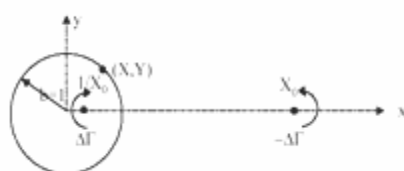
Fig. b. Circle in circulatory flow (**Theodore Theodorsen 1935**).
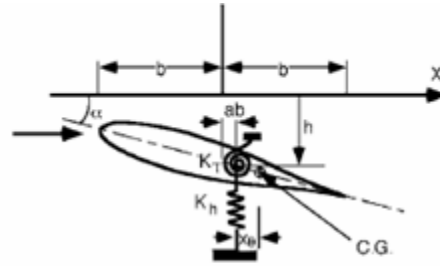
Fig. C. Typical section model

Table. 1 Results of the flutter speed parameter comparison.

Results of present work for flutter	Results of ref.[5],[6]
$\dfrac{V_f}{b\,\omega_\alpha} = 3.327$	$\dfrac{V_f}{b\,\omega_\alpha} = 3.69$ [5] $\dfrac{V_f}{b\,\omega_\alpha} = 3.89$ [6]

RECTANGULAR WING
Material: - cast-aluminum (7075-T6).

Table. 2 .Shell thickness variation for rectangular wing.

case	Thickness (m).	Mass (Kg).	Mode 1 (Hz).	Mode2 (Hz).	$R = \dfrac{\omega_h}{\omega_\alpha}$	I_α
1	0.001	8.231	20.016	101.15	0.197	0.1157
2	0.0015	10.726	19.82	104.75	0.189	0.1576
3	0.002	13.22	19.69	106.54	0.184	0.1995
4	0.0025	15.715	19.6	107.57	0.182	0.2414
5	0.003	18.21	19.536	108.24	0.180	0.2832
6	0.0035	20.704	19.489	108.70	0.179	0.3251

Prof. Dr. Muhsin J. Jweeg
Ass. Prof. Dr. Shokat Al-Tornachi
Eng. Tariq Samir Talib

FLUTTER SPEED LIMITS OF SUBSONIC WINGS

TAPERED WING

Material: - cast-aluminum (7075-T6).

Table. 3. Shell thickness variation for tapered wing.

case	Thickness (m).	Mass (Kg).	Mode 1 (Hz).	Mode 2 (Hz).	$R = \frac{\omega_h}{\omega_\alpha}$	I_α
1	0.001	7.4752	31.807	128.22	0.248	0.1111
2	0.0015	9.7244	32.066	132.33	0.242	0.1546
3	0.002	11.974	32.214	134.72	0.239	0.1981
4	0.0025	14.223	32.313	136.45	0.237	0.2416
5	0.003	16.472	32.387	137.75	0.235	0.285
6	0.0035	18.721	32.446	138.75	0.233	0.328

RECTANGULAR WING

Material: - cast-aluminum (Adv.Aluminum).

Table 4 .Effect of (Adv.Alum) shell thickness variation for rectangular wing.

case	Thickness (m).	Mass (Kg).	Mode 1 (Hz).	Mode 2 (Hz).	$R = \frac{\omega_h}{\omega_\alpha}$	I_α
7	0.001	8.5437	21.204	107.49	0.197	0.1201
8	0.0015	11.133	20.994	111.25	0.188	0.1636
9	0.002	13.723	20.856	113.11	0.184	0.2071
10	0.0025	16.312	20.760	114.19	0.182	0.2505
11	0.003	18.902	20.691	114.87	0.180	0.2940
12	0.0035	21.491	20.641	115.34	0.178	0.3375

RECTANGULAR WING

Material: - cast-aluminum (Ti6A14V).

Table 5. Effect of (Ti6A14V) Shell thickness variation for rectangular wing.

case	Thickness (m)	Mass (Kg).	Mode 1 (Hz).	Mode2 (Hz).	$R = \frac{\omega}{\omega_k}$	I_α
13	0.001	13.02	19.825	101.21	0.195	0.1831
14	0.0015	16.966	19.625	104.63	0.187	0.2493
15	0.002	20.912	19.494	106.29	0.183	0.3155
16	0.0025	24.858	19.403	107.24	0.181	0.3818
17	0.003	28.804	19.338	107.84	0.179	0.4480
18	0.0035	32.75	19.29	108.25	0.178	0.5143

TAPERED WING

Material: - cast-aluminum (Adv.Aluminum).

Table. 6 .Effect of (Adv.Alum) shell thickness variation for tapered wing.

Case	Thickness (m).	Mass (Kg).	Mode 1 (Hz).	Mode2 (Hz).	$R = \dfrac{\omega_t}{\omega_b}$	I_α
7	0.001	7.7593	33.679	136.01	0.247	0.1153
8	0.0015	10.094	33.969	140.35	0.242	0.1605
9	0.002	12.429	34.124	142.87	0.238	0.2057
10	0.0025	14.763	34.229	144.69	0.236	0.2508
11	0.003	17.098	34.306	146.07	0.234	0.2960
12	0.0035	19.433	34.368	147.12	0.233	0.3412

TAPERED WING

Material:- cast-aluminum (Ti6A14V).

Table. 7. Effect of (Ti6A14V) Shell thickness variation for tapered wing.

case	Thickness (m).	Mass (Kg).	Mode 1 (Hz).	Mode2 (Hz).	$R = \dfrac{\omega_t}{\omega_b}$	I_α
13	0.001	11.824	31.512	127.54	0.247	0.1757
14	0.0015	15.382	31.761	131.57	0.241	0.2446
15	0.002	18.940	31.903	133.91	0.238	0.3134
16	0.0025	22.497	31.999	135.60	0.235	0.3822
17	0.003	26.055	32.07	136.88	0.234	0.4511
18	0.0035	29.613	32.126	137.86	0.233	0.5199
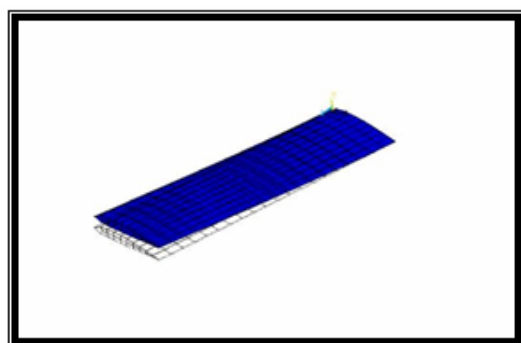
Fig. 1 Bending mode shape for rectangular wing
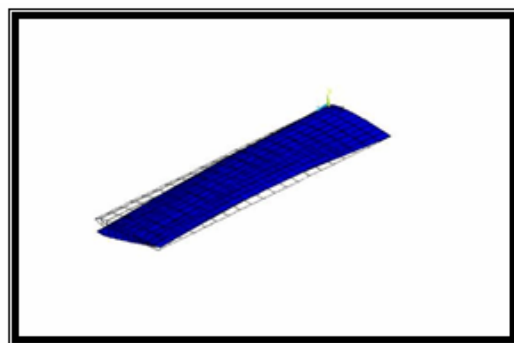
Fig. 2 Torsional mode shape for rectangular wing

Prof. Dr. Muhsin J. Jweeg
Ass. Prof. Dr. Shokat Al-Tornachi
Eng. Tariq Samir Talib

FLUTTER SPEED LIMITS OF SUBSONIC WINGS
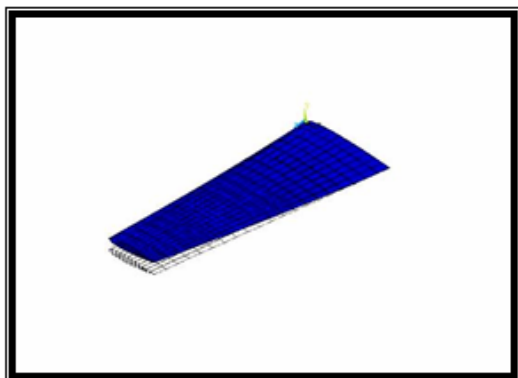
Fig. 3 Bending mode shape for tapered wing
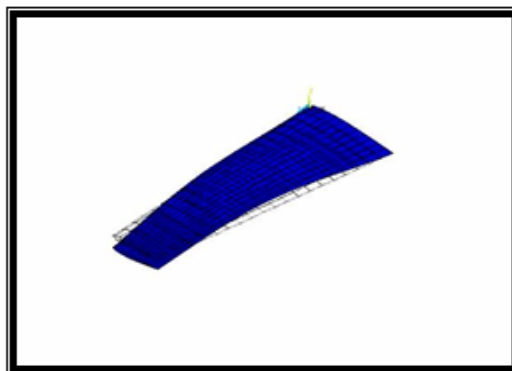
Fig. 4 Torsional mode shape for tapered wing

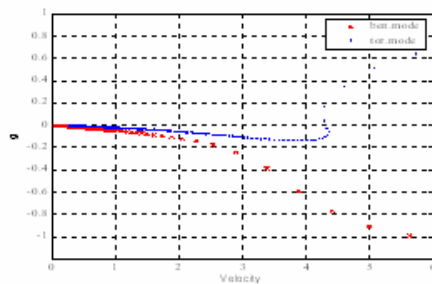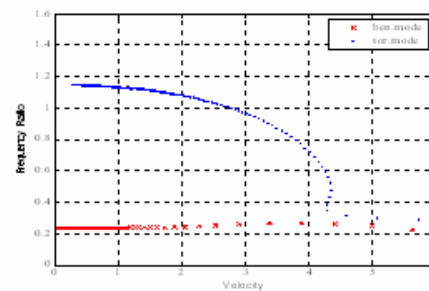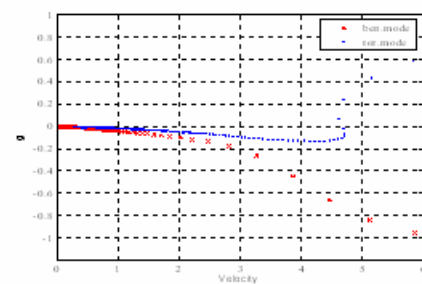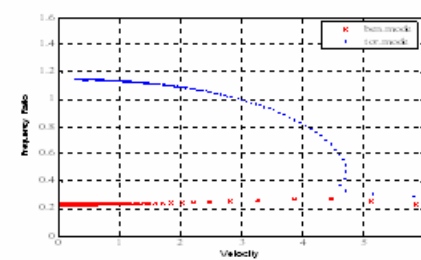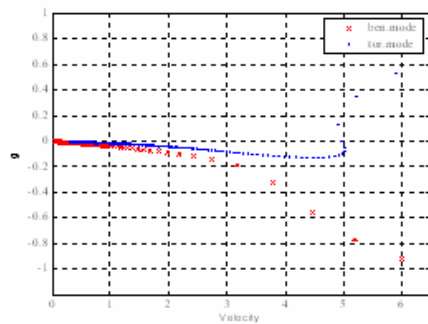**Rectangular Wing**: - Figures below show the shell thickness variation.
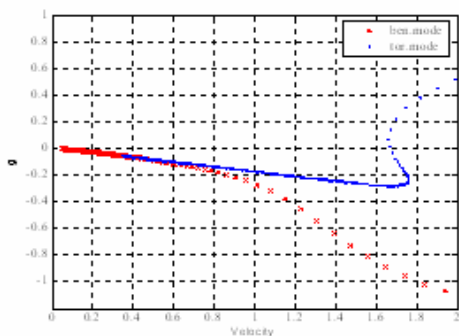
Fig. 5. The relation between non-dimensional parameter 1/k and damping ratio.
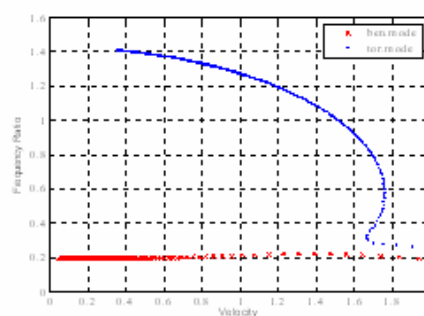
Fig. 6. The relation between the non-dimensional parameter 1/k and frequency
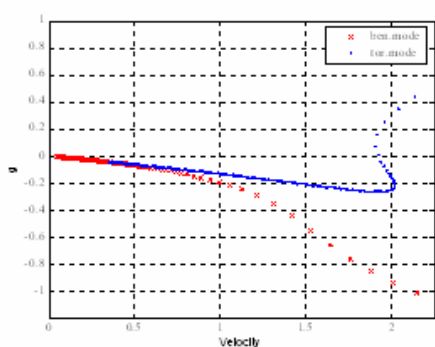
Fig. 7. The relation between non-dimensional parameter 1/k and damping ratio
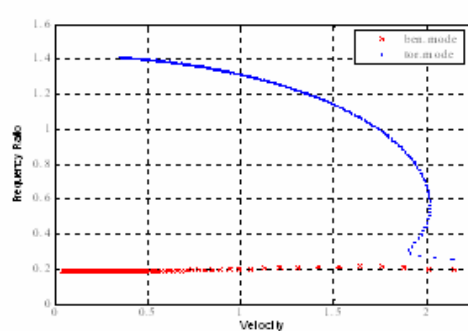
Fig. 8. The relation between the non-dimensional parameter 1/k and frequency ratio.
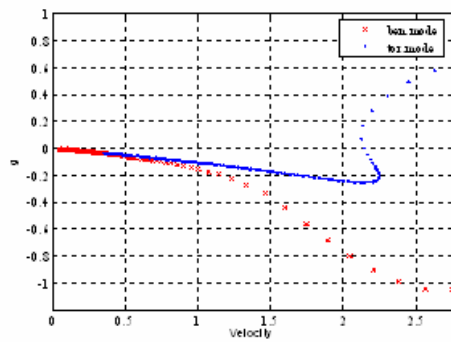
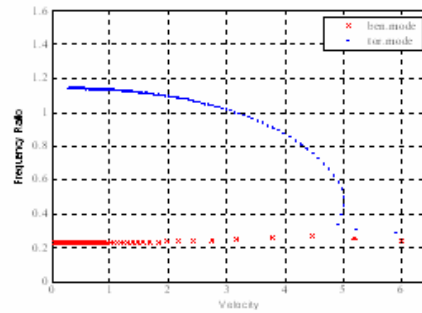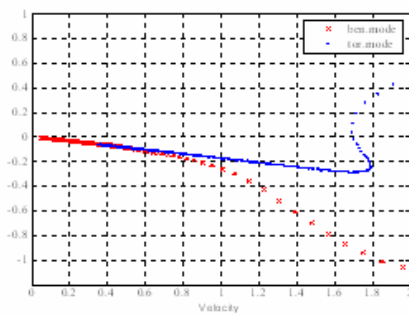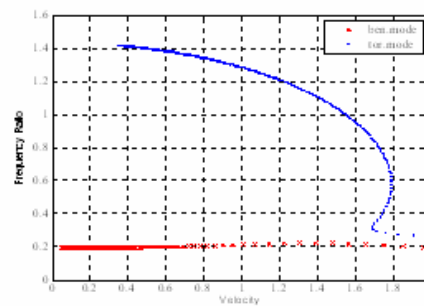Fig. 9. The relation between non-dimensional parameter 1/k and damping ratio.
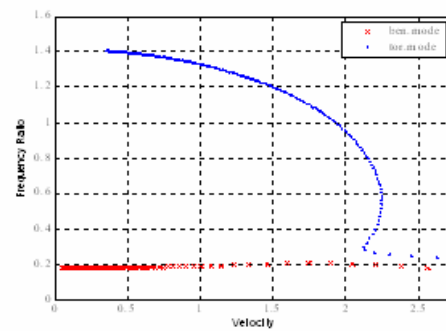
Fig. 10. The relation between the non-dimensional parameter 1/k and frequency ratio.
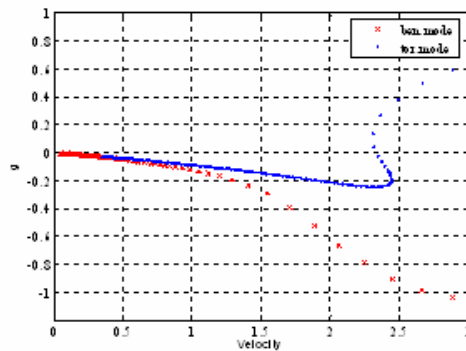
Fig. 11 .The relation between non-dimensional parameter 1/k and damping ratio.
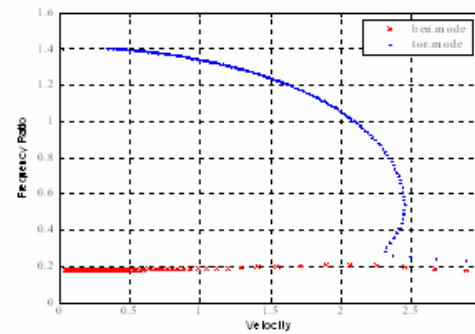
Fig. 12. The relation between the non-dimensional parameter 1/k and frequency ratio.
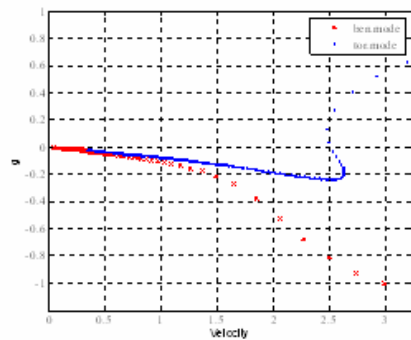
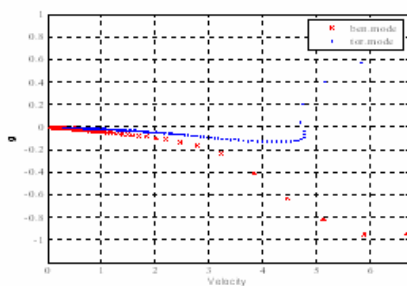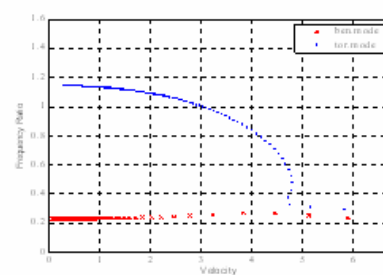

Fig. 13 .The relation between non-dimensional parameter 1/k and damping ratio.
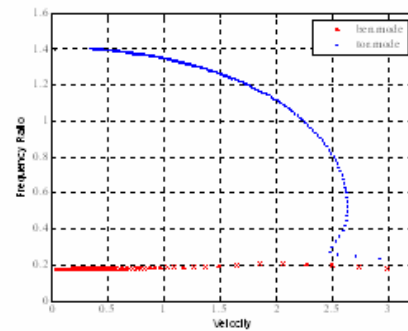
Fig. 14. The relation between the non-dimensional parameter 1/k and frequency ratio.

179

Prof. Dr. Muhsin J. Jweeg
Ass. Prof. Dr. Shokat Al-Tornachi
Eng. Tariq Samir Talib

FLUTTER SPEED LIMITS OF SUBSONIC WINGS
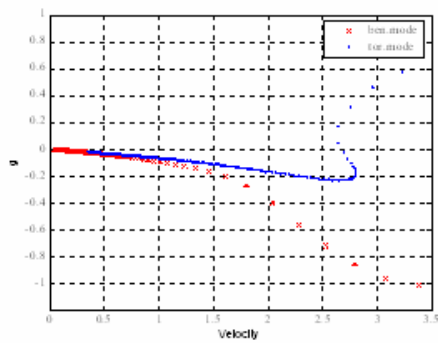
Fig. 15 . The relation between non-dimensional parameter 1/k and damping ratio.
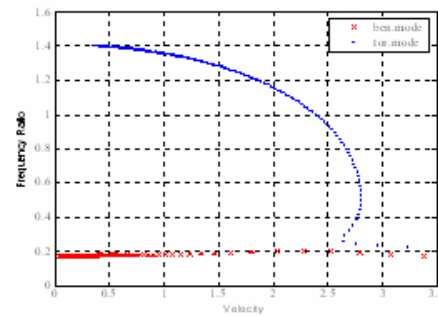
Fig. 16 . The relation between the non-dimensional parameter 1/k and frequency ratio.

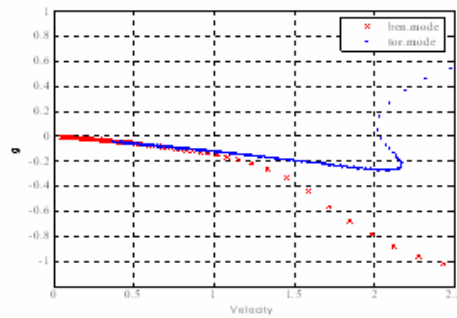**Tapered wing:-** Figures below show the shell thickness variation.
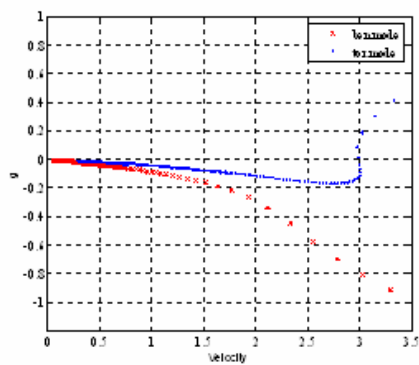
Fig. 17. The relation between non-dimensional parameter 1/k and damping ratio.
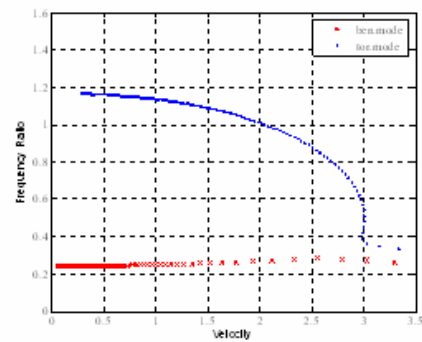
Fig. 18. The relation between the non-dimensional parameter 1/k and frequency ratio.
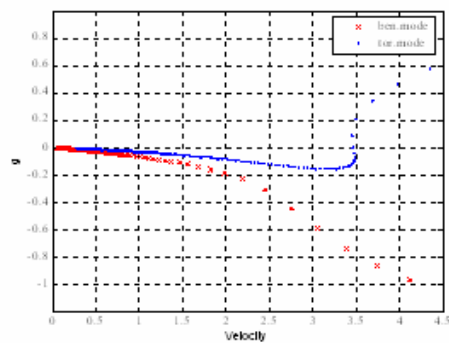
Fig. 19. The relation between non-dimensional parameter 1/k and damping ratio.
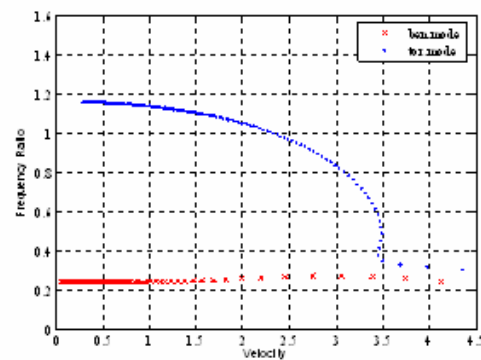
Fig. 20. The relation between the non-dimensional parameter 1/k and frequency ratio.
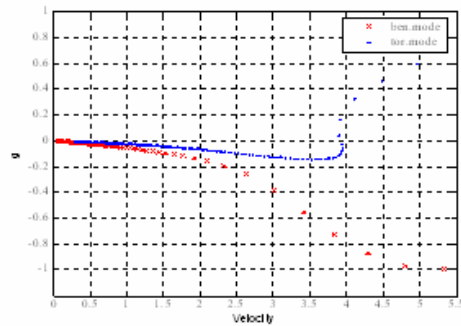
Fig. 21. The relation between non-dimensional parameter 1/k and damping ratio.
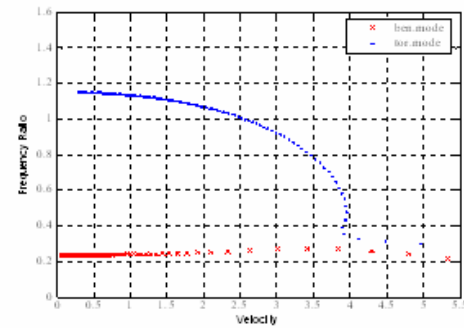
Fig. 22. The relation between the non-dimensional parameter 1/k and frequency ratio.
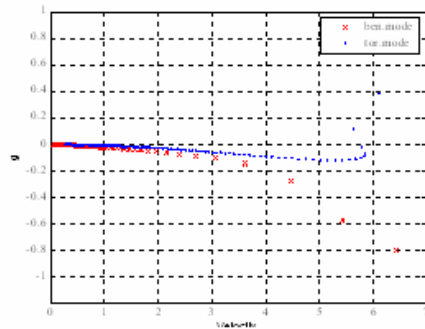
Fig. 23. The relation between non-imensional parameter 1/k and damping ratio.

Fig. 24. The relation between the non-dimensional parameter 1/k and frequency ratio.

Fig. 25. The relation between non-dimensional parameter 1/k and damping ratio.

Fig. 26 . The relation between the non-dimensional parameter 1/k and frequency ratio.

181

Prof. Dr. Muhsin J. Jweeg
Ass. Prof. Dr. Shokat Al-Tornachi
Eng. Tariq Samir Talib

FLUTTER SPEED LIMITS OF SUBSONIC WINGS

Fig. 27. The relation between non-dimensional parameter 1/k and damping ratio.

Fig. 28. The relation between the non-dimensional parameter 1/k and frequency ratio.

Rectangular wing:- The (Adv.Aluminum) effect with thickness=(0.001m).

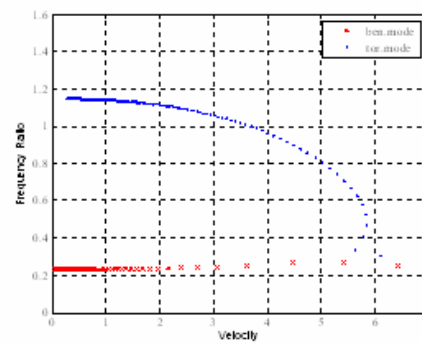**Fig. 29.** The relation between non-dimensional parameter 1/k and damping ratio.

Fig. 30. The relation between the non-dimensional parameter 1/k and frequency ratio.

Fig. 31. The relation between non-dimensional parameter 1/k and damping ratio.

Fig. 32. The relation between the non-dimensional parameter 1/k and frequency ratio.

Rectangular Wing: - The (Ti6A14V) effect with thickness= (0.001m).

Fig. 33. The relation between non-dimensional parameter 1/k and damping ratio.
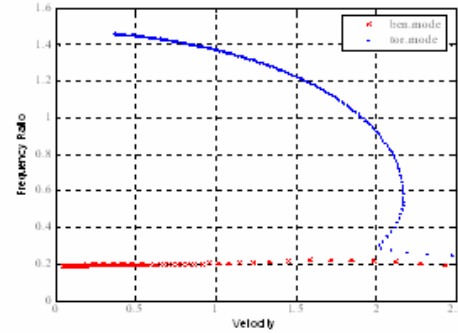
Fig. 34. The relation between the non-dimensional parameter 1/k and frequency ratio

Tapered Wing: - The (Ti6A14V) effect with thickness= (0.003m).

Fig. 35. The relation between non-dimensional parameter 1/k and damping ratio.

Fig. 36. The relation between the non-dimensional parameter 1/k and frequency ratio.

183

AXIAL FAN BEARING SYSTEM VIBRATION ANALYSIS

Dr. Assim H Yousif   Dr. Muawafak A Tawfik   Dr. wafa Abd Soud

Mechanical Engineering Department, University of Technology, Baghdad.

ABSTRUCT

Rotating fan shaft system was investigated experimentally and theoretically to study its dynamic performance. The type of oil used for the bearing was taken in consideration during the experimental program .Three types of oil were used, SAE 40, SAE 50 and degraded oil. During the experiments, the fan blades stagger angle was changed through angles (20°, 30°, 40°, and 50°). The shaft rotational speed also changed in the range of (0-3000 rpm). All these parameters have investigated for two cases (balanced and unbalanced fan). The performance parameters of the fan were found experimentally by measuring the fan, volume flow rate, Reynolds and Strouhal numbers, efficiency and pressure head. Analytical part was also represented to prepare the prediction of fan system dynamic performance. The aerodynamic forces and moments of each blade were also predicted to obtain the rotor dynamic future. Experimentally and theoretically the critical fan speed was obtained in the x and y direction for different lubricant oil viscosities and shaft rotational velocities for balanced and unbalanced fan. Analysis of the vibrational response gave important information about the dynamic performance of fan rotating system. Acceptable agreement was found between analytical and experimental results.

الخلاصة

SAE 50   SAE 40

. 50°   40°   30°   20°

3000

)   Y   X

(
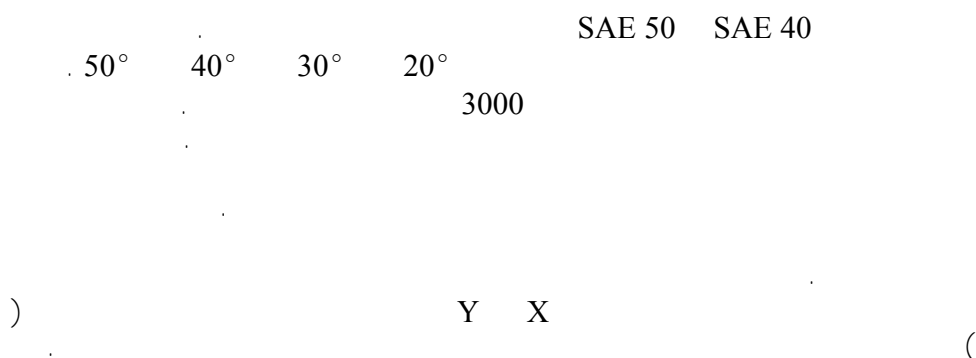
Dr. Assim H Yousif
Dr. Muawafak A Tawfik
Dr. wafa Abd Soud

INTRODUCTION

In the design study of turbo-machinery, performance and rotor dynamic considerations are often in compromise. The rotor performance usually desires to maximize the volume flow rate and the pressure, and minimize the fluid energy losses, though a machine of limited size and weight. This generally suggests high shaft speed, and multiple stages. All of these features tend to create rotor dynamic problems. The goal of increasing the efficiency of machines is essential for their development. Engineers and Scientists work to reach ways and method to guide the designers to develop new designs to reach this goal. They develop machine designs in order to prevent the operations errors and to predict them early.

The characterization of these errors and their causes is essential in the maintenance process in order to prevent the unexpected failure in these machines. These predicted errors can be found by using simple measuring equipments for vibrations and also by analytical methods. The causes of these vibrations can be predicted and the pre-prevented solutions can be found, which in fact would decrease the cost and increase the efficiency, which is the goal, and these are crucial in industry. This research,deals with the prediction of these errors, in order to reach this goal a fan rotor bearing casing system has been built up and vibration measuring equipments have been used.

The vibration in this system can be due to one of the following variables or combinations of them:
1. Changing the stagger angles.
2. Degradation of oil used.
3. Changing revolution speed.

turbine or compressor blade tip or seal rub, while keeping tip clearance and seals as tight as possible to increase the efficiency. Avoiding rotor dynamic instability and avoiding torsion vibration

4. Unbalance in fan or rotor shaft (crack, failure and dirt).

In addition to that, in the current research numerical solution, used to create, develop and modify computer software to give the required results for the dynamic response for each system.

ROTOR DYNAMIC FUTURE

All fans generate some vibration. They continuously rotate and since nothing is perfect, cyclic forces must be generated .Its only when vibration reaches certain amplitude that may be call "bad". Vibration may just be an indicator of some problem with a mechanism, or it may be cause of other problem .High vibration can breakdown lubricants in the bearings and, in addition may cause metal fatigue in the bearings. Excessive vibration can cause fasteners to loosen or can cause fatigue failure of structurally loaded components. Also vibration can be transmit into adjacent areas and interfere with precision processes, or create an annoyance for people.

Thus, experimental and numerical results can be used to analyze the vibrating signal (amplitude), and to predict the causes of these vibrations. The design of successful and reliable turbomachine requires cooperation and compromises between the two descriptions. From a rotor dynamic standpoint of view, the successful design of a turbomachine involves [**Tohn,1988**]. Avoiding critical speeds, if possible and minimizing dynamic response at resonance, if the critical speed is traversed. Minimizing vibration and dynamic load transmitted to machine structure through out the operating speed range. Avoiding resonance or torsion instability of the drive train system.

EXPERAMENTAL SET- UP

The axial fan used in the test rig is usually used in airconditioning system and industry. The fan is of ten blades aerofoil section [NACA 0021], each blade span is (120.8) mm, root chord is (61.7) mm, tip cord of (46.1) mm, leading edge twist angle is (14°), trailing edge twist angle is (zero) °. The fan located close to the shaft end. The fan blades material is (AL–Cast–Alloy) of density (2650 kg/m3) and a young modules equal to 7600 kgf/mm^2 [**R.N.Peter, 1998**]and each blade weights (0.196kg) .The stagger angles of the blade can be changed during the test from (20° to 50°) by steps of (10°).The disk rotor diameter is (400 mm), maximum blade thickness is (5.15 mm),i.e. located at 20%, chord located from the leading edge. The fan duct diameter is (404.8 mm), thus the tip clearance is 2.4 mm according to the data given in [**L.Neuhaus, 2002**] .The tip clearance can be varied by exchanging the casing segments relationship between measured vibration and the spinning rotor. This information is important in determining position of balance weight.

ASSUMPTION

For the sake of analysis, the following assumptions are adopted:
1. Axial fluid flow is constant along the blade.
2. Aerodynamic forces which are cased by air flow act on the center line of the blade surface.
3. Assume incompressible fluid flow.
4. Coefficients of damping and stiffness are to be changed during the rotation speed in the journal bearing.

For the present purpose of investigation, the system can be reduced into two coupled beams. The shaft and the

using adjustable screw maintained on the outer diameter of the duct to take into account the unbalance effect of the fan during the experimental test. Figure (1) shows the fan photograph. According to [**S.L.Dixon, 1978**] which gave the power required calculation procedure a 1.5 kW motor is used to derive the fan.

The rotor system consists of a rotor shaft carrying the axial fan and two journal bearings. The bearings were selected according to the maximum rotor shaft speed (3000 rpm), using the information given in [**R.N.Peter, 1998**].The motor speed was controlled by using invertors.

Two accelerometer in the x and y directions were mounted on the journal bearing by means of epoxy resin so that the surfaces were kept flat and smooth where the sensor is located as in figure (2).
Laser tachometer with the SBS Portable Balancer is used to measure

casing are treated as a simply supported beam [**M.A.Tawfik, 1996**] rested between two bearing and supporting structure as shown in Figure (3).

SYSTEM STATE VECTOR
The state vector at any point in the system (Fan blade –Disk – Rotor –Bearing) is the state vector of the station (i). There are two state vectors, one to the left $[Z]_i^L$, and the other to the right $[Z]_i^R$ contains two displacement component (y) and (ϕ), that is the deflection and mode shape , also associated state with these displacements are internal force (V) and moment (M), i.e. shear force and bending moment respectively . The state vector $[Z]_i$ can be written as indicated in [**M.A.Tawfik, 1996**] and [**I.Wattar, 2000**].

Dr. Assim H Yousif
Dr. Muawafak A Tawfik
Dr. wafa Abd Soud

$$\{Z\}_i = \{Z_S \; X_S \; Y_S \; \phi_{ZS} \; \phi_{XS} \; \phi_{YS} \; M_{ZS}$$

$$M_{XS} \; M_{YS} \; V_{ZS} \; V_{XS} \; V_{YS} \; Z_C \; X_C \; Y_C \; \phi_{ZC}$$

$$\phi_{XC} \; \phi_{YC} \; M_{ZC} \; M_{XC} \; M_{YC} \; V_{ZC} \; V_{XC} \; V_{YC} \; 1 \}$$

$$(1)$$

Where X, Y and Z represent the deflection in x, y and z respectively,

ϕ_{ZS} is the torsion angle about Z-axis, 4

ϕ_{XS}, ϕ_{YS} are the components of the mode shape in x, y axis,

M_Z is the torsion moment about Z-axis, M_X and M_Y are the bending moment about x and y axis'

V_Z is the axial force in Z-direction,

V_X and V_Y are the shear force in x and y directions, and subscripts C and S are indicated casing and rotor respectively.

UNBALANCE FORCES

Unbalance forces is defined as the allowance for a circumferential change in its position. It is a kind of excitation for the system. The unbalance force component [**M.A.Tawfik, 1996**and **Barth, 1976**] according to Figure (4) may be written as;

$$\Omega^2 U_y = \Omega^2 U^*_y \cos\Omega t - \Omega^2 U^*_x \sin\Omega t$$

$$(2)$$

$$\Omega^2 U_x = \Omega^2 U^*_x \cos\Omega t + \Omega^2 U^*_y \sin\Omega t$$

$$(3)$$

While as a complex function

$$\Omega^2 \overline{U}_y = \Omega^2 U^*_y + j\Omega^2 U^*_x \qquad (4)$$

$$\Omega^2 \overline{U}_x = \Omega^2 U^*_x - j\Omega^2 U^*_y \qquad (5)$$

POINT MATRIX (MASS ELEMENT MATRIX):

There are four cases for the point matrix. These cases cover all the possible arrangement at any station along the system as shown in figure (5)and they overall used to analyze the theoretical solution .

1- Lumped mass at the station (i):

a- lumped mass on rotor and casing [**M.A.Tawfik, 1978**]

b- Lumped mass on rotor and imaginary lumped mass on casing.

2- Bearing station

3- Pulley at the shaft and lumped mass on the casing.

4- Branch of fan blade.

There are two kinds of point matrix one where there are two real masses of casing and shaft as in Figure (6) and another one where there is imaginary part at the casing and real part in shaft's mass as in Figure (7). For the case(2)(bearing station)take the equilibrium of journal bearing in X and Y-direction then find the deflection ,slop, shear force and bending moment for this case as in figure (8).

Where

$$[QQ] = [GG][W]^{-1}[HH]$$

$$[DD] = [GG][W]^{-1}[RR]$$

$$[D]_{2\times 2} = [ss] - [RR][W]^{-1}[RR] \quad,$$

and $[Q]_{2\times 2} = [RR][W]^{-1}[HH] - [RR]$

Where

$$[GG] = \begin{bmatrix} K_{YY} + j\Omega_Y c_{YY} & K_{YX} + j\Omega_X c_{YX} \\ K_{XY} + j\Omega_Y c_{XY} & K_{XX} + j\Omega_X c_{XX} \end{bmatrix}$$

Where

$$[ss] = \begin{bmatrix} -\Omega^2 m_c + k_{cyy} + j\Omega c_{cyy} + Z_{yy} & k_{cyx} + j\Omega c_{cyx} \\ k_{cxy} + j\Omega c_{cxy} & -\Omega^2 m_c + k_{cxx} + j\Omega c_{cxx} + Z_{xx} \end{bmatrix}$$

where

$$[W]=\begin{bmatrix} -\Omega^2 m_p + k_{cyy} + k_{yy} + j\Omega c_{cyy} & k_{cyx} + k_{yx} + j\Omega c_{cyx} + j\Omega c_{yx} \\ k_{CXY} + k_{xy} + j\Omega c_{CXY} + j\Omega c_{xy} & -\Omega^2 m_p + k_{cxx} + k_{xx} + j\Omega c_{cxx} + j\Omega c_{xx} \end{bmatrix}$$

$$[HH]=\begin{bmatrix} -\Omega^2 m_p + k_{cyy} + j\Omega c_{cyy} & k_{cyx} + j\Omega c_{cyx} \\ k_{cxy} + j\Omega c_{cxy} & -\Omega^2 m_p - k_{cxx} + j\Omega c_{cxx} \end{bmatrix}$$

$$[RR]=\begin{bmatrix} k_{cyy} + j\Omega c_{cyy} & k_{cyx} + j\Omega c_{cyx} \\ k_{CXY} + j\Omega c_{cxy} & k_{cxx} + j\Omega c_{cxx} \end{bmatrix}$$

In case (4)The point matrix take in to consideration the effect of branch because of the dynamic load and gyroscope moment effect on the brunch system (moving blade)and the difference between the magnitudes properties of mass element (i).For the point matrix in the direction of the system will be as shown in figure (9).

COMPUTER PROGRAM CODE

A computer program written in FORTRAN 77 has been developed to embrace the theoretical work. The program adopted Figure (3) as a lumped masses distributed uniformly with circular shapes, negligible weight, having rigidity equal to the actual systems rigidity. The program takes into consideration the effect of, gyroscopic moment, shear force, moment of inertia for rotor and casing, Stiffness and damping coefficients of journal bearing and the Branch of the fan blade. To minimize the error and to enhance the accuracy of the results, non- dimensional terms are implemented.

The fan blade branch and journal bearing system have been reduced to a single matrix for the purpose of the solution .The rotor shaft has been divided in to (33) stations of masses and (32) of massless sections .The program has the ability to find the deflection, mode shape, shear force and moment for each station along the shaft and casing for a rang of speed (0-3000) rpm

The program was developed for the rotor, casing and branch system .In order to evaluate the final matrix, the point matrices are multiplied by the field matrices and boundary conditions are applied for the system to find the state vector in three dimensions along the system for every rotating speed and for different stagger angle and different oil viscosity in the journal bearing.

Performance Characteristic of the Fan

Results were obtained for a range of flow rate and various stagger angels of the fan blade at three different kinematics viscosity of oil used in bearing system, so that, the fan performance data could be generated. Sample of the fan performance characteristics is illustrated in Figure (10) as plots of qualitative performance curve for a typical fan stagger angle [40º] and for lubricant oil SAE 40 (Kinematics Viscosity =140 c.s), the efficiency curve leans more to the right; the head tends to decrease with flow rate increasing. The fan efficiency drops off rapidly for volume flow rate higher than that at the best efficiency point. The net head curve also decreases continuously with flow rate, although there are some wiggles. If the fan operated below its maximum efficiency point, the flow might be noisy and unstable which indicates that the fan may be oversized (large than necessary) [**Franklyn, 2002**]. For this reason it is usually best to run a fan at, or slightly above its maximum efficiency point.

In the duct fan,   a vortex shedding will appear in the flow down stream of the fan in addition to unsteady flow which can be represented by non-dimensional group, Strouhal number(St). Figure (11) shows a non-dimensional numbers, Reynolds number (Re) and (St) of the duct fan.

Dr. Assim H Yousif
Dr. Muawafak A Tawfik
Dr. wafa Abd Soud

(St) represents the characteristic dimension of the body (D) times the system frequency of vibrations (f) divided by the fluid free stream velocity (U∞). For axial fluid flow, the characteristic dimension taken as the outer diameter of the fan [**McGraw-Hill, 2006**], also the Re based on the outer diameter of the fan [**Franklyn, 2002**]. It can be seen from this figure, that at low stagger angle [20° low flow rate], the shedding frequency is fluctuating on the fan system ,due to the generation of forces on the fan structure .The vortex will be existed down stream of the fan [**Yunus, 2006**], and increased as the rotor speed increased .On the other hand, when using degraded oil (kinematics viscosity =117 c.s) at stagger angle equals (40º) and (50°) the value of strouhal no. is relatively high. At the stagger angle (30º), the vibration is at low values (St=0.5) and sharply increase to higher values (St=1.4) at Re=1.5x105. As Re increase the fluctuation behaviors of St and appeared to be more stable ranging between 1.32 and1.5. However, the St would seem to be higher at stagger angle (40°) and increase as the oil's viscosity increases, but at angle (50º), the vibration still be exist. However, these fluctuations are less than that for stagger angle (20°), but it is still high and become higher when using degraded oil. Due to swirl fluid downstream of the duct fan which leads to waste of kinetic energy and a high level of turbulence; this wasted kinetic energy partially reduced the level of the turbulence by using stator.

AMPLITUDE IN (X) AND (Y) DIRECTION:

Theoretical and experimental amplitude in X and Y directions for different system rotating speed, stagger angle and viscosity are indicated in figure (12). The remarkable point raised from this

Figure is that the natural frequency occurs at the same speed in x and y directions and the amplitude in the x-direction higher than its values in the y-direction for the first appear of the natural frequency. At some rotating speed natural frequency appears in the x directions and disappears in the y direction. Also it can be seen that the amplitude in x and y decreased when stagger angle is increase. The behavior of the theoretical work is the same in the x and y directions with slight differences. The amplitude of vibration in the x-direction decreases as the stagger angle increases. The closeness between experimental and theoretical results are acceptable (0-19.2%). The difference in values of x and y directions amplitude demonstrate the difference in stiffness coefficients. While Figure (13) shows that many natural frequencies occurred with high viscosity figure of oil in journal bearing for the same range of rotor speed. Also some natural frequencies appear in x and disappear in y directions.

Figure (14) shows that the amplitude in x and y directions decreased as the stagger angle increased. Figures (15) and (16) show a comparison between the experimental and theoretical work for x and y amplitudes versus rotor speed for different stagger angle and oil viscosity. The main conclusion raised from these results is that the experimental and the theoretical results are close to each other except at stagger angle 40˚.

EFFECT OF UNBALANCE FORCE ON THE VIBRATION ANALYSIS

Two masses of (m1=8 gm, m2=16 gm) are replaced at a radius of 62 mm from the fan hub center line, to measure the effect of unbalance masses on the system response of the vibration at bearing station(21).
Figure (17) shows the amplitude in x-direction .It can be seen that the amplitude

of vibration at balance force is small in magnitude and increases when the unbalance forces are increased. The maximum amplitudes in all the cases, Figure (18), occurred at a rotor speed (1339 rpm).The maximum amplitude appears at stagger angle 20º which is equal to (3.25x10-4) and decrease as the stagger angel is increased. When the rotor speed approaches 1700 rpm, the amplitude of vibration appears with large magnitude, but less than that for rotor speed of (1339)rpm .While in y- direction, as shown in figure(18), the amplitude is less in magnitude, but also it is maximum at (1339 rpm), approximately equal to $1x10^{-4}$m . The amplitude increases as the unbalance force increases. However Figure (18) shows that the modulus of the amplitudes increases drastically at and grater than the rotor speed (1700 rpm). These results indicated that the effects of unbalance forces are highly dangerous on the fan system operations and this effect may damage the system.

CONCLOSION REMARKES

Strouhal and Reynolds numbers represents clearly the flow and system frequency characteristics. Vibration response measurements and prediction yield great deal of information concerning any faults within rotating machines. The identification of common mass unbalance by vibration analysis is very well developed and can be performed in many ways. The experimental and the theoretical results are agreed well except one case. The natural frequency occurred in all cases approximately at the same speed in x and y directions.

REFRENCES

Barth & Zsolcsa , K.Paranabesh "Effect of Damping on the Lateral Critical Speed of Rotor-
Bearing System" J. of Engineering of Industry V.93 .No. 2,pp(505- 513),May 1976.

Franklyn Kelecy "Study Demonstrates that Simulation can Accurately Predict Fan Performance
"Journal Articles By Fluent Software Users. JA 108, pp(1-4),2002.

I, Wattar, W.Hafez, Z.Gao "Model Based Diagnosis of Chaotic Vibration signals", ABB
Automatically Cleveland State University, OH.2000

L. Neuhaus and W. Neise "Active Flow Control to Improve the Aerodynamic and Acoustic Performance of Axial Turbo machines" American Institute of Aeronautics and Astronautics, Inc., AIAA, 2948 June 2002.

M. A. Tawfik "Lateral vibration of Branch Systems in Particular Vertical Machines "M.s.c.
Thesis, Cranfield Institute of Technology 1978.

M.A.Tawfik;"The effect of Misalignment on the dynamic Performance of the Crank Shaft
Bearing System in a Diesel Engine ", PhD Thesis, Mechanical Engineering, University
of Technology, Baghdad, October 1996.

McGraw-Hill, "Strouhal Number", Dictionary of Scientific and Technical Term, 2006.

R.N. Peter Childs, "Mechanical Design" John Wily & Sons, Inc. N.Y., Toronto, p16, 1998.

S.L. Dixon, "Fluid Mechanics,
   Thermodynamics and
   Turbomachinery", 3ed edition, 1978.

Tohn M.Vance "Rotor Dynamic of
Turbomachinary" John Wiley and sons.Inc,

1988.

Yunus A.C. Engel, John M.Cimbala "Fluid
Mechanics; Fundamentals and Applications
"Mc
   GRAW Hill, International Edition
,2006

SYMBOLS	DEFINITION	UNITS
[P]	Point matrix	....
[F]	Field matrix	....
Re	Reynolds number based on fan diameter	$\dfrac{\rho U_\infty D_f}{\mu}$
St	Strouhal number	$\dfrac{f\,D_f}{U_\infty}$
U_x , U_y	Unbalanced forces	kg m
Ω	Angular speed	rad/s
T	Time	s
[U]	Combined element matrix	....
U^*x,y	Unbalance force in x &y directions	kg m
U_∞	Stream velocity	m/s
U	Absolute velocity	m/s
Vz	Axial force in z direction	N
Vx,Vy	Shear force in x &y	N
W	Applied load on bearing	N
W_1	Relative velocity	m/s
X,Y,Z	Deflection in x,y and z direction	m
$[z\ ]$	State vector at the left of mass	....
$[z]^r$	State vector at the right of mass	....
Z_f	Number of Blade	....
x^*,y^*	Relative motion in x &y	Mm
Ω	Rotational speed	rpm

191

Fig.1 Fan Duct System Test Rig assembly

Hollow shaft

Iron disk

Accelerometer in Y-direction

Accelerometer in X-direction

Bronze Bush
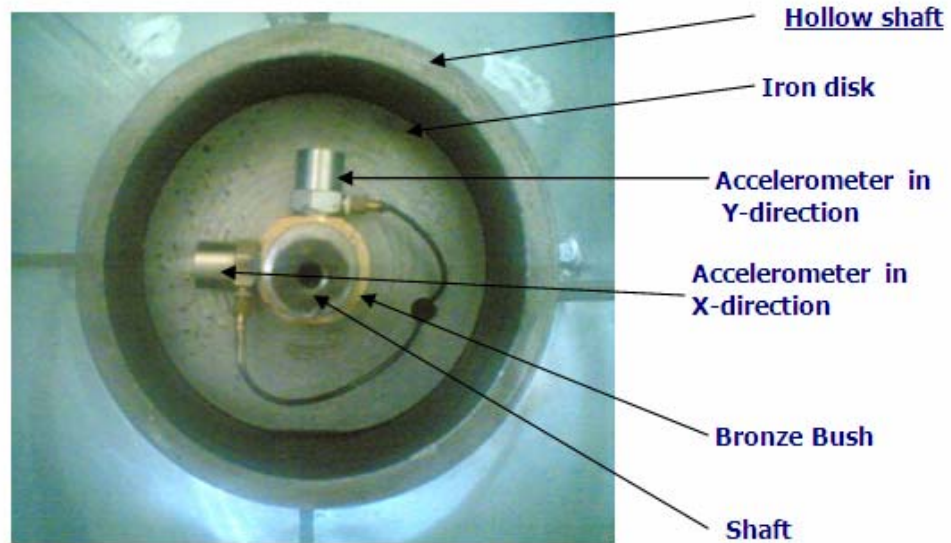
Shaft

Fig.(2) Two accelerometers mounted on the Bush bearing .

Dr. Assim H Yousif
Dr. Muawafak A Tawfik
Dr. wafa Abd Soud
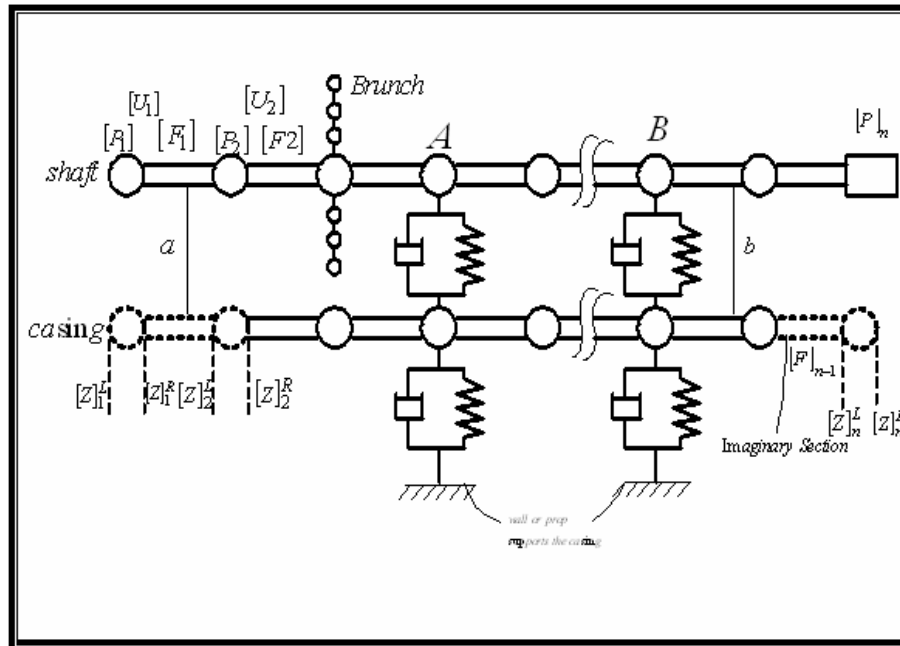
Fig. (3)   Mathematical model of horizontal machine, having shaft and casing and indexing of the stations and the corresponding shaft and casing element
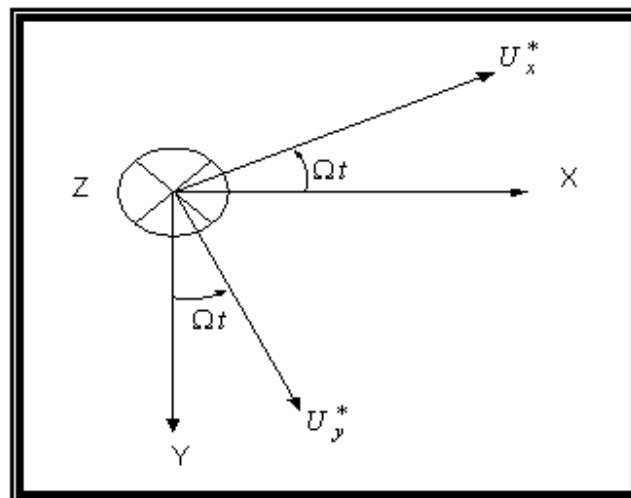
Fig. (4) Unbalance Force Component

Fig. (5) General Form of Point Matrix of Rotor Casing System.
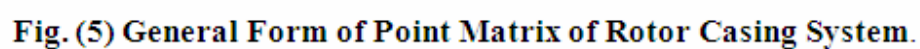
Fig.(6) Point matrix of real masses in shaft and casing .

Dr. Assim H Yousif
Dr. Muawafak A Tawfik
Dr. wafa Abd Soud

Fig(7)point matrix of real mass of shaft and imaginary part of casing

Fig.(8) Point matrix of case (2) Bearing at station considered

195

$$
\begin{bmatrix} Z \\ X \\ Y \\ \hline \phi_Z \\ \phi_X \\ \phi_Y \\ \hline V_Z \\ V_X \\ V_Y \\ \hline M_Z \\ M_X \\ M_Y \\ \hline 1 \end{bmatrix}^{R}_{i}
=
\begin{bmatrix}
[I] & \vdots & [0] & \vdots & [0] & \vdots & [0] & & 0 \\
 & & & & & & & & 0 \\
 & & & & & & & & 0 \\
\hline
 & & & & 8 & & & & 0 \\
[0] & \vdots & [I] & \vdots & [0] & \vdots & [0] & & 0 \\
 & & & & & & & & 0 \\
\hline
 & & & & [I] & \vdots & [0] & & \\
[R_s] - \sum \left[U_{PV} \cdot U^{-1}_{VV} \right] & & & & & & & & [R_s] - \sum \left[U_P - U_{PV} \cdot U^{-1}_{VV} \cdot U_V \right] \\
 & & & & [0] & \vdots & [I] & & \\
\hline
0\ 0\ 0\ 0\ 0\ 0 & \vdots & 0\ 0\ 0 & \vdots & 0\ 0\ 0 & \vdots & & & 1
\end{bmatrix}
\begin{bmatrix} \overline{Z} \\ \overline{X} \\ \overline{Y} \\ \hline \overline{\phi}_Z \\ \overline{\phi}_X \\ \overline{\phi}_Y \\ \hline \overline{V}_Z \\ \overline{V}_X \\ \overline{V}_Y \\ \hline \overline{M}_Z \\ \overline{M}_X \\ \overline{M}_Y \\ \hline 1 \end{bmatrix}_{i}^{L}
$$

Fig. (9) Point matrix of the brunch system.
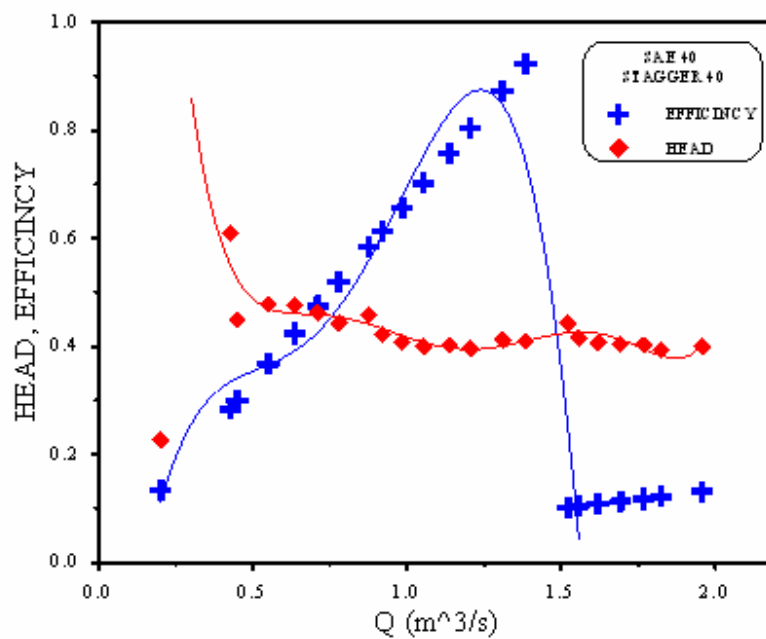
Fig.10 fan system performance

Dr. Assim H Yousif
Dr. Muawafak A Tawfik
Dr. wafa Abd Soud
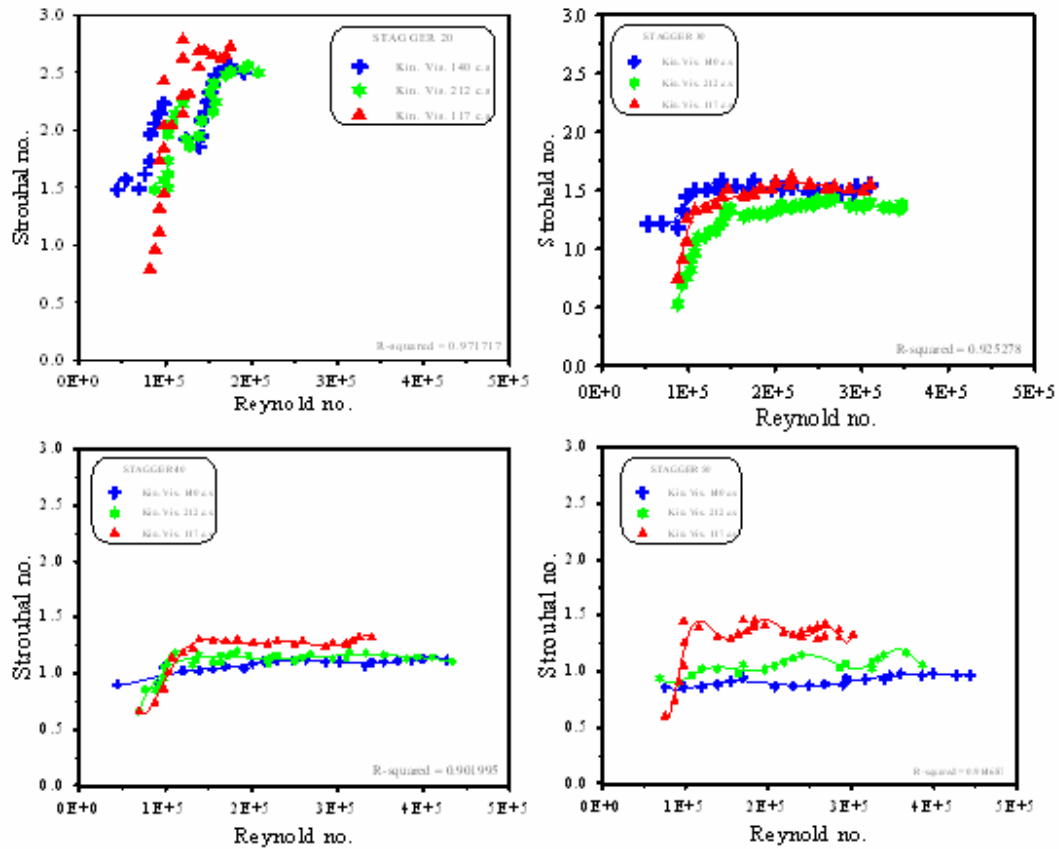
Fig. (11) St Verses Re for various oil kinematics viscosity and fan blade stagger angle.
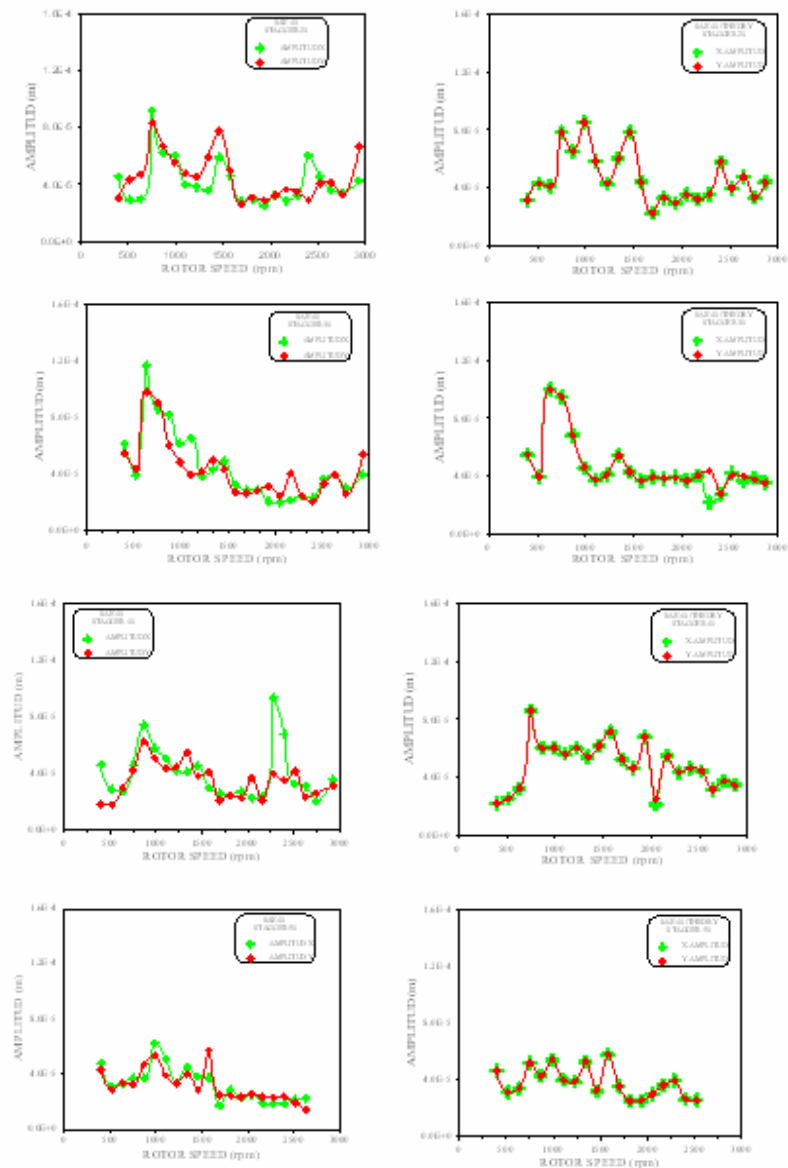
Experiment   Theory
Fig.12 Experimental and Theoretical Amplitude in X and Y Direction versus Rotor
Speed for SAE 40 Kin. Vis.=140 c.s.

Dr. Assim H Yousif
Dr. Muawafak A Tawfik
Dr. wafa Abd Soud
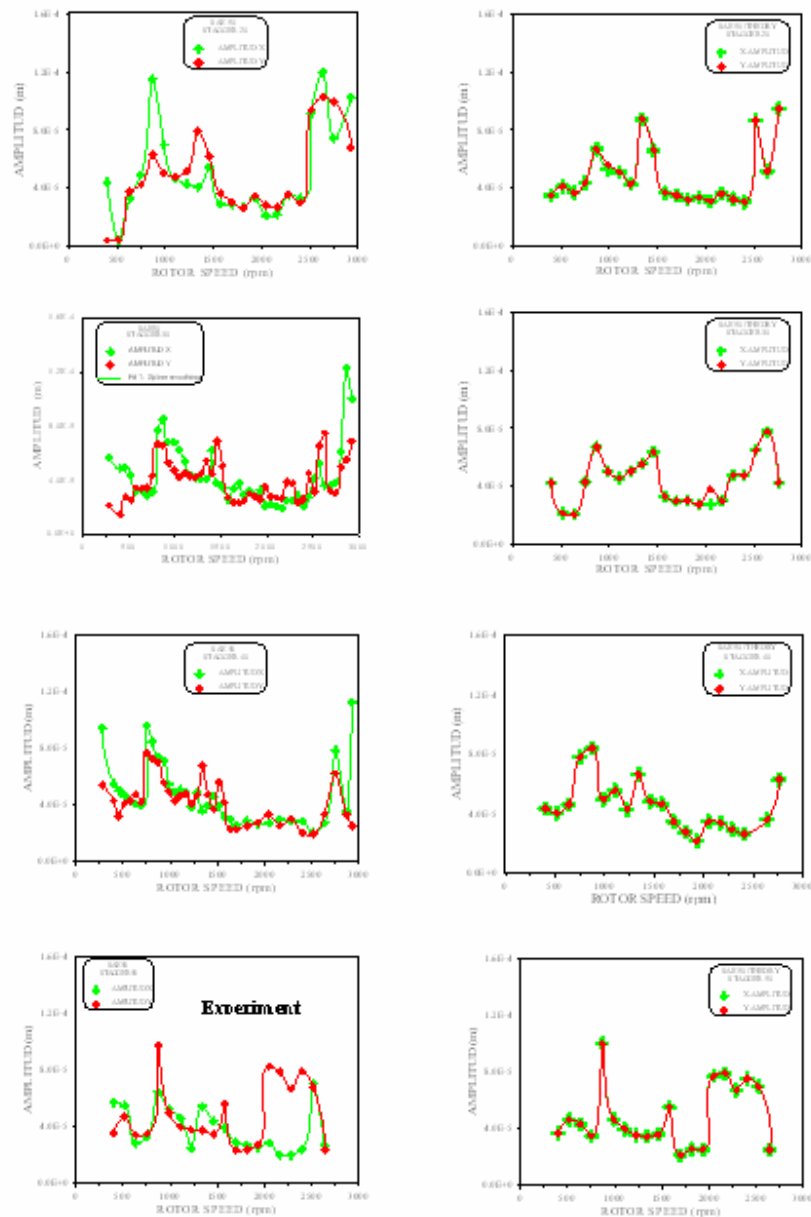
Experiment   Theory

Fig.13 Experimental and Theoretical Amplitude in X and Y Direction versus Rotor
Speed for SAE 50 Kin. Vis.=212 c.s.

199
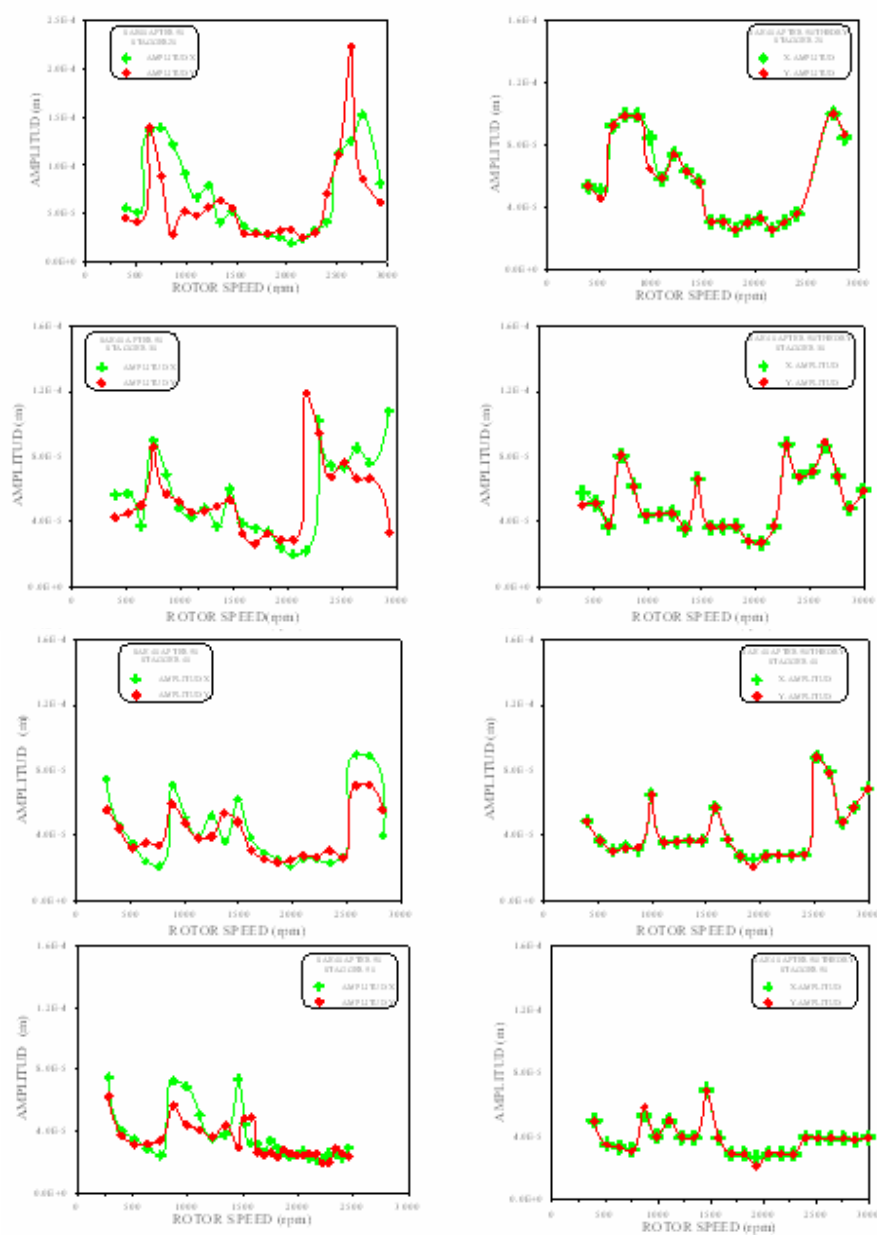
Fig.14 Experimental and Theoretical Amplitude in X and Y Direction versus Rotor
Speed for Degraded Oil SAE 40 Kin. Vis.=117 c.s.
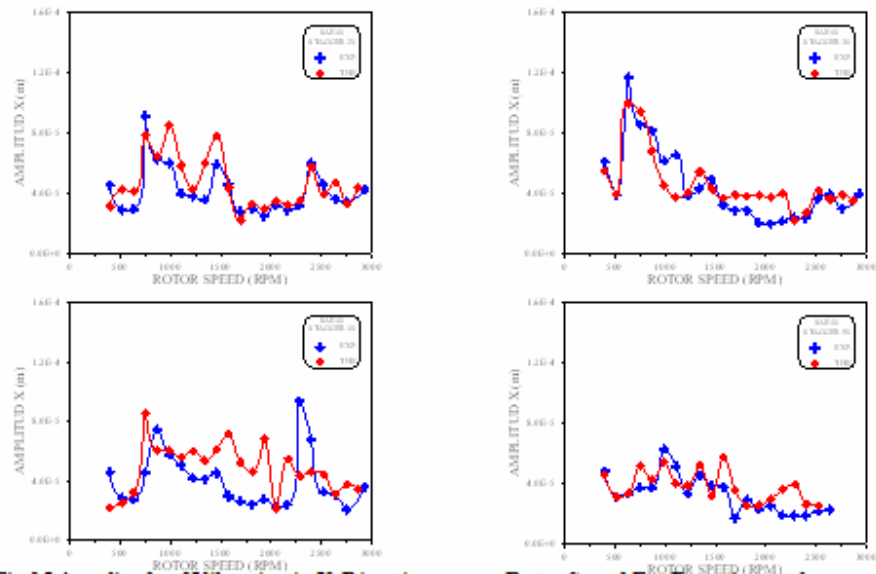
Fig.15 Amplitude of Vibration in X-Direction versus Rotor Speed For Experimental and Theoretical work for Different values of Stagger Angle and for Constant value of Viscosity SAE 40
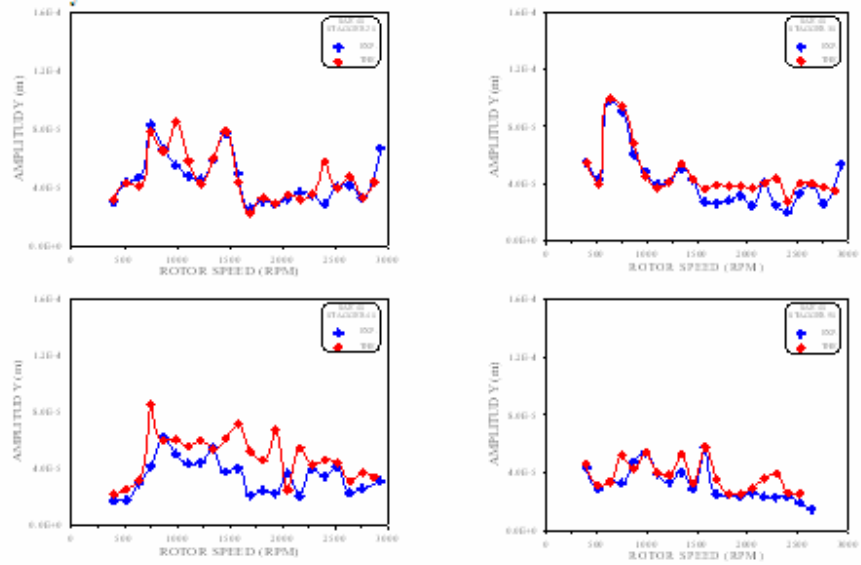
Fig.16 Amplitude of Vibration in Y-Direction versus Rotor Speed For Experimental and Theoretical work for Different values of Stagger Angle and for Constant value of Viscosity SAE 40

201
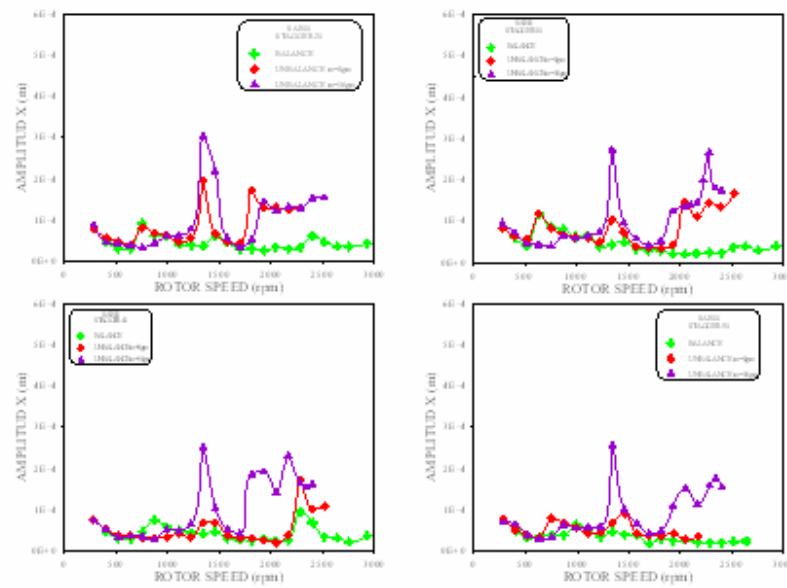
Fig. 17 Amplitude of Vibration in X-Direction versus Rotor Speed at Different Unbalance Force and Stagger Angle for SAE 40(Kin. Vis.=140 c.s.)
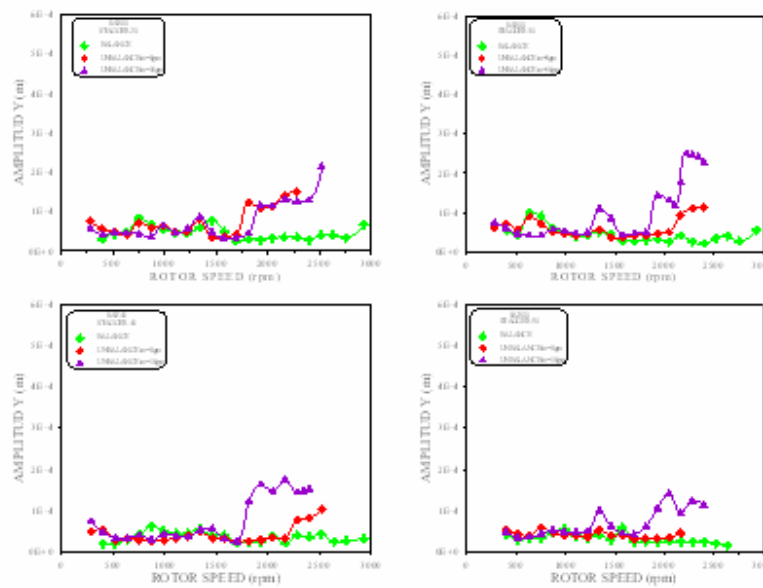
Fig. 18 Amplitude of Vibration in Y-Direction versus Rotor Speed At Different Unbalance Force and Stagger Angle for SAE 40 (Kin. Vis.=140 c.s.)

202

EXPERIMENTAL INVESTIGATION OF INDIVIDUAL EVACUATED TUBE HEAT PIPE SOLAR WATER HEATING SYSTEMS

Khalid A. Joudi and Hassan N. S. Al-Joboory
Department of Mechanical Engineering, College of Engineering, University of Baghdad, Baghdad, Iraq.

ABSTRACT

The work involves outdoor experimental testing of ten individual evacuated tube heat pipe solar water heating systems with heat pipes of three diameter groups of 16, 22 and 28.5 mm. The first and third groups had evaporator lengths of 1150, 1300 and 1550 mm. The second group had an additional length of 1800 mm. all heat pipes were of fixed condenser length of 200 mm. Ethanol at 50% fill charge ratio of the evaporator volume was used as the heat pipes working fluid. Each heat pipe condenser section was inserted in a storage tank and the evaporator section inserted into an evacuated glass tube of the Owens- Illinois type. The combined heat pipe and evacuated glass tube form an active solar collector of a unique design. The resulting ten solar water heating systems were tested outdoors under the meteorological conditions of Baghdad, Iraq. Experiments were carried out with no load, intermittent and continuous load conditions. Some tests, at no load, were carried out with and without reflectors. The overall system efficiency was found to improve with load conditions by a maximum of 55%. The system employing an 1800 mm evaporator length and 22 mm heat pipe (HP7) showed the best performance by higher water temperatures, overall useful energy gain and efficiency at various load conditions. System performance was predicted theoretically using electrical analogy derived from an energy balance. An agreement of within 14% was obtained between theoretical and experimental values.

الخلاصة

يتضمن البحث فحصا تجريبيا بالخارج لعشر منظومـات تسخين ميـاه بالطاقة الشمسيه ذات الأنبوب الحراري في الأنبوب المفرغ تستخدم أنابيب حرارية بثلاث أقطـار هي 16 و22 و28.5 ملم. تكونت مجموعتي الأنابيب ذات القطـرين الأول والثالث من أنابيب بأطوال مبخر 1150 و1300 و 1550 ملم بينما شملت المجموعـة الثانيـة طـولا اضـافيا هو 1800 ملم. كانت جميع الأنابيب بطول مكثف ثابت يبلغ 200 ملم. شحنت جميع الأنابيب الحراريـه بالايثانول كمـائع شغل بنسبة شحن بلغت 50% من حجم المبخر. تم إدخال المكثف لكل أنبوب حراري في خزان مـاء وادخل المبخر في أنبوب زجاجي مفرغ من نوع أوينز- ألينويز وأصبحت الوظيفة المركبـة الناتجة من ذلك تكون لاقط شمسي فعـال ذو تصميم فريد. كانت المنظومات الناتجة عشرة منظومات فردية ذات أنبوب حراري في الأنبوب المفرغ لتسخين المـاء بالطاقة الشمسية والتي تم فحصها تجريبيا في الظروف الجوية لمدينة بغداد. أجريت التجـارب على هذه المنظومـات بدون حمل وبحمل متقطع وحمل مستمر. كما أجريت بعض التجارب بدون حمل مع سطح عاكس وبدونه. وقد تحصل أفضل أداء من المنظومـة ذات الأنبوب الحراري HP7 بطول مبخر 1800 ملم وقطر 22 ملم من بين المنظومـات العشر والذي تمثل بدرجات حرارة مـاء سـاخن أعلى وتخزين طاقة حرارية كلية وكفاءة أعلى مع جميع أشكال التحميل. تبين من خلال البحث أن الكفاءة الكلية للمنظومـات الشمسية تحسنت مع التحميل بمقدار أقصاه 55%. تم القيام بتحليل نظري للمنظومـة الشمسـية باستخدام منظومـة مقاومـات كهربائية مناظرة متأتية من الاتزان الحراري للمنظومـة الشمسية وعند مقارنـة الأداء العملي مـع هذه الاستنتاجات النظريـة حصل توافق جيد بحدود 14% بين القيم النظرية والقيم العملية.

Keywords: Solar heat pipe; Evacuated tube heat pipe solar collector; Heat pipe solar water heater

INTRODUCTION

Heat pipes are being used in solar collectors as the heat absorbing component for their rapid response to solar radiation changes [Bairamov and Toiliev 1982], freeze tolerance [Radhwan et.al 1990], eliminating corrosion problems and thermal diode benefit. They permit the collection of solar energy at low solar radiation levels of 140 W/m^2 vs. 250 W/m^2 for flat plate collectors [Ward and Ward 1979]. Heat pipe absorbers have been suggested for flat plate solar collectors and evacuated tube collectors [Ortabasi and Buehl 1980], where high rates of heat are transferred from the absorber (evaporator section) to the heat- rejecting end (condenser section) at a very small temperature difference.

The incorporation of heat pipes with conventional flat plate and evacuated tube solar collectors has been investigated by many workers [Bairamov and Toiliev 1982, Akyurt 1984, Hammad 1995, Chun et.al 1999, Nada et.al 2004, Sivaraman and Mohan 2005, Hussein 1997, Walker et.al 2004, Ng et.al 2000, Praene et.al 2005 and Mahdy 2005] However, only a limited number of works has been devoted to the utilization of the evacuated glass tube solar collectors. No works were cited involving a heat pipe within an Owens- Illinois evacuated tube serving as a thermosyphon solar water heating system.

The present work investigates experimentally the use of wickless heat pipes of various lengths and diameters within an Owens- Illinois evacuated tube to form a solar collector connected directly to a storage tank. Ten such solar water heating systems were tested outdoors for performance evaluation. Effects of heat pipe evaporator length and diameter on the performance were assessed.

THE SOLAR WATER HEATING SYSTEMS

Each solar water heating system consists of an evacuated glass tube, a heat pipe, a storage tank and a flat reflector, mounted on a stand and facing south. Ten individual heat pipe solar systems were built, each with the same evacuated glass tube but a different heat pipe. **Fig. 1** shows four individual systems ready for simultaneous testing. Details of heat pipes HP1- HP10 and design specifications of the ten systems are given in **Table 1**. Ethanol was chosen as the heat pipe working fluid for all systems, with a fill charge ratio of 50% of the evaporator volume. The evaporator section of the heat pipe was placed inside the evacuated glass tube, whereas the condenser section was situated in the water storage tank. The evacuated glass tubes were all Owens- Illinois type, model 47-58-1800-YCF. 1 mm thick aluminum reflectors were positioned behind the evacuated glass tubes for better reflection [Kreider and Kreith 1981]. The capacity of the storage water tanks was within the recommended range of 7.25 liters [Kreider and Kreith 1981, Kreider and Kreith 1975]. One side of the tank was cut at 45° to facilitate receiving the heat pipe condenser into the tank. The inlet and outlet tubes to the storage tank were drilled for temperature sensors. A 3 mm air-vent tube was provided at the top of the tank. The temperature distribution along the height of the storage water was measured by three thermocouples within a 5 mm diameter probe. The heat pipe evaporator section was aligned at the center line of the evacuated glass tube. The solar water heating systems were inclined at an angle of 45° for winter operation in Baghdad (33.3^o N).

Temperatures at various locations of each heat pipe solar system (inlet and outlet storage water, evacuated tube surfaces, heat pipe evaporator surface and ambient) were measured by calibrated copper- constantan thermocouples connected to a digital readout. The mean tank temperature was taken as the average of the three temperature readings. The load water flow

rate was measured by a calibrated Rotameter. The outdoor experiments were carried out in April, May, June, July, August and September of 2008 on sunny days. Test data were considered constant for a period of time of half an hour for an operating period from 8:00 a.m. until 16:00 p.m. Also, data was recorded for a one hour period from 16:00 p.m. till 24:00 p.m. Systems incorporating heat pipes HP3, HP7 and HP10 were operated at different weather conditions and systems incorporating heat pipes HP1, HP2 and HP3 were operated with and without reflectors and at various hot water storage capacities. All individual systems were subjected to three load conditions; these are no- load, intermittent load, and continuous load. The experiments with no load condition were carried out with three storage capacities of 5.25 ℓ, 6.25 ℓ, and 7.25 ℓ. Intermittent loading experiments were carried out with three hot water removal quantities of 0.5 ℓ, 0.75 ℓ, and 1 ℓ for five minuets at the beginning of every hour from 10:00 a.m. to 14:00 p.m. Continuous loading tests were carried out with seven values of hot water withdrawal rates of 0.5, 1, 2, 3, 4, 5, and 6 ℓ/ hr. Each withdrawal process continued from 8:00 a.m. to 18:00 p.m.

The overall collected heat is determined from the measurements of storage tank temperatures at the start and end of the operating period from 8:00 a.m. till 18:00 p.m. by;

$$Q_o = M_t c_w (T_{mf} - T_{ms}) \qquad (1)$$

The daily overall or bulk efficiency of the system was then calculated from;

$$\eta_o = \frac{M_t c_w (T_{mf} - T_{ms})}{\int_0^t A_a I(t)dt} \qquad (2)$$

With load conditions, the overall heat collected was estimated from the equation;

$$Q_o = M_t c_w (T_{mf} - T_{ms}) + \int_0^t \dot{m}_l c_w (T_{lo} - T_{li})dt \qquad (3)$$

This equation was further simplified to the following form;

$$Q_o = M_t c_w (T_{mf} - T_{ms}) + M_l c_w (T_{mo} - T_{mi}) \qquad (4)$$

Where; $M_l = \sum \dot{m}_l^i \Delta t^i$, and

$$(T_{mo} - T_{mi}) = \sum_{i=1}^k \dot{m}_l^i (T_{lo}^i - T_{li}^i)\Delta t^i \Big/ \sum \dot{m}_l^i \Delta t^i$$

Where k is the number of time intervals, Δt^i, during the loading period, and Whereas, the overall or bulk system efficiency was calculated from the equation;

$$\eta_o = \frac{M_t c_w (T_{mf} - T_{ms}) + M_l c_w (T_{lo} - T_{li})}{\int_0^t A_a I(t)dt} \qquad (5)$$

The solar radiation intensity was calculated using the ASHRAE clear sky model [Farber and Morrison 1977].

RESULTS AND DISCUSSION

Performance curves are generally represented by the variation of the mean water temperature in the tank, the daily overall useful heat gain and the overall (bulk) efficiency of the systems. **Fig. 2** shows a typical variation of the mean tank temperature (T_m) with time for different storage capacities for solar system incorporating heat pipe HP7. The variation of T_m is similar in all systems. The mean tank temperature increases with time, reaches its maximum value at the period between 14:00 p.m. and 16:00 p.m., and then decreases slightly. **Fig. 2** also shows the effect on T_m of the storage capacity. Higher values of T_m are obtained with smaller storage capacity. T_m reached 75.6 °C, 82.4 °C and 89.5 °C with storage

capacities of 7.25 ℓ, 6.25 ℓ and 5.25 ℓ respectively. Reduced quantities of stored heat are obtained with decreased storage capacities due to the increased heat losses from the storage tank, resulting in reduced bulk efficiency. The overall stored heat and overall efficiency increased with storage capacity from 713 kJ and 20% to 1358 kJ and 54.1%, as shown in **Figs. 3 and 4** for various solar systems. The mean tank temperature is observed to increase with systems of longer evaporator heat pipes for the 22 mm diameter group as shown in **Fig. 5**. An increase from 1150 mm to 1800 mm in the evaporator length resulted in an increase of 3.4 ^{o}C to 10.3 ^{o}C in the maximum value of T_m. A similar observation was concluded for systems incorporating heat pipes of the same evaporator length but different diameters, as shown in **Fig. 6**. Higher temperatures are obtained with systems of larger heat pipe diameters. An increase from 16 mm to 28.5 mm in the heat pipe diameter resulted in an increase of 8.7 ^{o}C to 12.4 ^{o}C in the maximum value of T_m due to the increased radiative heat transfer attained by the increased heat pipe evaporator surface area. The effect of reflectors on the mean tank temperature at no load conditions is shown in **Fig. 7** with heat pipe HP3. The presence of reflectors increased the maximum mean tank temperature by 6.5 ^{o}C to 16 ^{o}C, accompanied with an increase in the overall stored heat by 1.7% to 17.4% and the overall efficiency by 1.8% to 14.7%, as shown in **Fig. 8**. These results agree with those obtained in other works [Ward and Ward 1979, Mahdy 2005]. From the above results, it is concluded that increased mean tank temperatures are attained with decreased storage capacities. While increased overall stored energy and efficiency are attained with increased storage capacities for all individual heat pipe solar systems. Therefore, such systems perform better with increased storage capacities and with reflectors.

To study the effect of intermittent load conditions, a fixed quantity of hot water was withdrawn from the storage tank at the beginning of each hour during the period from 10:00 a.m. to 14:00 p.m. This pattern of loading was recommended by [Esen and Esen 2005] under cold climates of Turkey, which is found practical for Iraq. The amounts of water withdrawn were 0.5, 0.75 and 1 ℓ in a period of five minuets. **Fig. 9** shows the results for the system with heat pipe HP7. The trend of variation is similar in all systems. T_m increases gradually, drops suddenly with each hot water removal, increases slightly after the removal process and increases continuously after the last removal process until the end of operation period. The sudden drop in T_m with hot water removal is due to the entry of a corresponding amount of cold mains water into the storage tank. This drop in T_m depends on the system involved, the quantity of hot water removed and the supply water temperature. A temperature drop of 1.5 ^{o}C to 3.2 ^{o}C was observed after each withdrawal process. **Fig. 10** depicts a typical behavior of varying heat pipe evaporator length at equal diameters on the variation of T_m with hot water removal quantity of 0.75 ℓ. A higher T_m was attained by systems incorporating heat pipes of longer evaporators. An increase in the overall daily useful energy of within 2.7% to 23.4% was observed corresponding to increasing evaporator length from 1150 mm to 1800 mm. A difference of T_m value of the various systems undergoing the same loading quantity was within 0.1 ^{o}C to 3.6 ^{o}C. **Fig. 11** compares variation of T_m in systems with heat pipes of equal evaporator length but different diameters. Increased T_m was observed with increased heat pipe diameter. It is noticed in **Figs. 10 and 11** that T_m and the outlet temperature continued increasing in spite of the hot water removal. This indicates that the heat input to the storage tank is more than that withdrawn by the load water. T_m continued rising after the last hot water removal at 14:00 p.m. to the end of the operation period to reach 61.5 ^{o}C and 78.1 ^{o}C depending on system specifications. The daily total useful energy increased from 1830 kJ to 2850 kJ and the overall daily

efficiency of the systems from 55.7% to 83.9% for longer heat pipes and increased loading, as shown in **Figs. 12 and 13**. The solar system with heat pipe HP7 showed the best performance among the ten systems. A higher T_m value was attained by this system with higher overall daily useful energy and efficiency. In general, system performance increased with increased heat pipe evaporator lengths and diameters. The overall useful energy was more by 55% with loading.

The experimental systems were subjected to continuous loading at various hot water removal rates. Each water withdrawal process continued along the whole operation period from 8:00 a.m. to 18:00 p.m. The flow rates used were 0.5, 1, 2, 3, 4, 5 and 6 ℓ/ hr respectively. **Fig. 14** shows typical results of the variation of the mean tank temperature with the seven removal rates for the system with HP7. A remarkable decrease of the mean tank temperature with increased removal rate is observed. This is a normal behavior due to the continuous entry of corresponding amounts of cold mains water into the storage tank. As a result, the overall useful energy is affected by the hot water removal rate. The experimental systems showed increased overall useful energy and increased overall efficiency with increased hot water removal rate accompanied with a decrease in the mean tank temperature. **Fig. 15** shows a typical variation of T_m with varying heat pipe evaporator lengths at a diameter of 22 mm at a removal rate of 3 ℓ/ hr. Whereas, **Fig. 16** shows the effect of varying heat pipe diameter at equal evaporator lengths of 1150 mm on the variation of T_m at 5 ℓ/ hr continuous loading. Higher values of T_m were obtained by heat pipe systems of longer evaporators and larger diameters as before as well as improved daily overall useful energy gain and efficiency. An increase from 1150 mm to 1800 mm in heat pipe evaporator length resulted in an increase of 3.7% to 31.8% in the overall useful energy, while an increase from 16 mm to 28.5 mm in the heat pipe

diameter caused an increase of 6.7% to 11.6%. It was observed that with flow rates of 0.5 to 5 ℓ/ hr, the overall useful energy increased significantly with increased flow rates. However, a decrease was observed in the overall useful energy and the overall efficiency when removal quantities exceeded 5 ℓ/ hr, as shown in **Figs. 17 and 18**. This is thought to be due to the system being incapable of providing the required heat at these loading conditions. An optimum removal rate of 5 ℓ/ hr was concluded, at which best performance was obtained. It is also concluded that all experimental solar systems performed better with load conditions. Higher water temperatures were obtained with no load condition, while higher amounts of overall useful energy and efficiency were obtained with load conditions. This is typical with domestic solar hot water systems.

The solar system with heat pipe HP7 showed the best performance among the experimental systems with all load conditions. The trend of variation of the mean tank temperature with time in the present work is similar to that in several works [Akyurt 1984, Chun et.al 1999 and Noren 1981], as shown in **Fig. 19**. However, the peak values are different due to the differences in design specifications and operation conditions of each system. A comparison can be carried out meaningfully only for the overall efficiency of the present systems with those in the literature, as given in **Table 2**.

The performance of the present solar systems was predicted theoretically from electrical analogy derived from energy balance of the system components. The model is similar to models of two commercial evacuated tube heat pipe solar systems [Walker et.al 2004 and Ng et.al 2000]. The model [Al-Joboory 2009] assumes that all of the absorbed solar energy is transferred directly to the storage tank via the heat pipe action and neglects heat losses from the system components except the storage tank. Any heat accumulation in the evacuated glass tube

was neglected i.e. time lag is not evident in the model. The predicted overall useful energy is greater by 14%, 10% and 11.5% for no load, intermittent and continuous loading, as shown in **Fig. 20**.

CONCLUSIONS

1. The performance of the heat pipe hot water system is improved with increased heat pipe length and diameter.

2. Higher water temperatures are obtained with no load at lower storage water capacity while higher stored heat and overall efficiency with higher storage water capacity.

3. The best performance was obtained for the system employing heat pipe HP7.

REFERENCES

Akyurt M., Development of Heat Pipes For Solar Water Heaters, J. Solar Energy, v.32, n. 5, pp. 625- 631, 1984.

Al-Joboory H.N.S., Experimental Investigation of Evacuated Tube Heat Pipe Solar Water Systems, Ph.D. Thesis, Mechanical Engineering Department, College of Engineering, University of Baghdad, Baghdad, Iraq, 2009.

Bairamov R. and Toiliev K., Heat Pipes in Solar Collectors, in Advances in Heat Pipe Technology, edited by Reay, D. A., pp.47- 54, 1982.

Chun W, Kang Y. and Lee Y., An Experimental Study of the Utilization of Heat Pipes for Solar Water Heaters, Appl. Ther. Engng., v. 19, pp 807-817, 1999.

Esen M and Esen H., Experimental Investigation of a Two- Phase Closed Thermosyphon Solar Water Heater, J. Solar Energy, v.79, n. 5, pp. 459- 468, 2005.

Farber E. and Morrison C., Clear-Day Design Values of Solar Energy, ASHRAE GRP 170, Application of Solar Energy for Heating and Cooling of Buildings, ed. Jordon R. and Liu B., 1977.

Hammad M., Experimental Study of the Performance of a Solar Collector Cooled By Heat Pipes, Renewable Energy, v. 6, n. 1, pp. 11- 15, 1995.

Hussein H., Theoretical and Experimental Investigation of a Wickless Heat Pipe Flat Plate Solar Collector, Ph. D. thesis, Faculty of Engineering, Cairo University, Egypt, 1997.

Kreider J. and Kreith F., Solar Energy Handbook, McGraw- Hill Co., 1981.

Kreider J. and Kreith F., Solar Heating And Cooling Engineering, Practical Design and Economics, Hemisphere Publishing Corporation, 1975.

Mahdy M., Experimental Investigation of Low Heat Flux Heat Pipes With and Without Adiabatic Section For Solar Application, Ph. D. Thesis, Mech. Eng. Dept., College of Engineering, University of Baghdad, Baghdad, Iraq, 2005.

Nada S., El- Ghetany H., and Hussein H., Performance of a Two- Phase Closed Thermosyphon Solar Collector With a Shell and Tube Heat Exchanger, Applied Thermal Engineering, v. 24, issue 13, pp. 1959- 1968, 2004.

Ng K., Yap C. and Khor T., Outdoor Testing of Evacuated- Tube Heat Pipe Solar Collectors, J. Process and Mech. Engineering, v, 214, n. 1, pp.23- 30, 2000.

Noren W., Heat Pipe Flat Plate Collector With Temperature Regulation, Report SERIWA, No. 810/36/1, Sol. Energy, p. 32 Res. Inst., West Australia, 1981.

Ortabasi U., and Buehl W. M., An Internal Cusp Reflector For An Evacuated Tubular Heat Pipe Solar Thermal Collector, J. Solar Energy, v.25, pp. 67-78, 1980.

Praene J., Grade F., and Lucas F., Dynamic Modeling and Elements of Validation of Solar Evacuated Tube Collectors, 9th Int. IBPSA Conf., Montreal, Canada, 2005.

Radhwan M., Zaki G., and Jamil A., Refrigerant- Charged Integrated Solar Water Heater, Int. J. of Energy Research, v.14, pp. 421- 432, 1990.

Sivaraman B. and Mohan N., Experimental analysis of heat pipe solar collector with different L/ d_i ratio of heat pipe, J. Scientific and Industrial research, v. 64, n. 9, pp. 698- 701, 2005.

Walker A., Mahjouri F. And Stiteler R., Evacuated- Tube Heat Pipe Solar Collectors Applied to the Recirculation Loop in a Federal Building, NERL report NERL/ CP- 710- 36149, presented at the Solar 2004 Conf., Portland, Oregon, 2004.

Ward D., and Ward J., Design Considerations for Residential Solar Heating and Cooling Systems Utilizing Evacuated Tube Solar Collectors, J. Solar Energy, v.22, pp.113- 118, 1979.

NOMENCLATURE

A_a	Absorber surface area	m^2
c_w	Specific heat of water	$kJ/kg.^oC$
D	Heat pipe diameter	m
I_t	Solar Insolation	W/m^2
k	Number of time intervals	-----
L_{ev}	Heat pipe evaporator length	m
L_{co}	Heat pipe condenser length	m
$\dot{m}$	Mass flow rate	kg/s
M	Mass of water (tank, load)	kg
Q_o	Overall useful energy gain	kJ
t	Time	s
T	Temperature	^oC

Greek symbols

α	Absorptivity	-----
β	Inclination angle from the horizontal	Degree
Δ	Difference	-----
ε	Emissivity	-----
η_o	Overall efficiency	-----
τ	Transmissivity	-----

Subscripts

a	Ambient
b	Bulk
i	In
m	Mean
max	Maximum
mf	Final mean value
ms	Starting mean value
l	Load
o	Out
t	Tank

Table (1) Design specifications of the individual evacuated tube heat pipe solar water heating systems with heat pipes HP1- HP10.

Part	Item	Design Specifications									
Solar collector	Type	Evacuated tube heat pipe solar collector									
	Absorber area	0.265 m^2									
Heat pipe	Type	Gravity assisted wickless heat pipe without adiabatic section									
	Material	Copper									
	Code	HP1	HP2	HP3	HP4	HP5	HP6	HP7	HP8	HP9	HP10
	Diameter (mm)	16	16	16	22	22	22	22	28.5	28.5	28.5
	L_{ev} (mm)	1150	1300	1550	1150	1300	1550	1800	1150	1300	1550
	L_{co} (mm)	200									
	Working fluid	Ethanol									
Evacuated glass tube	Material	High quality borosilicate glass									
	Length	1800 mm									
	Outer tube	Φ 58 mm									
	Inner tube	Φ 47 mm									
	Glass thickness	1.6 mm									
	Vacuum	10^{-4} torr									
	Coating	Graded Aluminum Nitride/ Aluminum									
	Transmittance	0.93									
	Absorptance	> 95%									
	Emittance	7- 8% (at 80 ^{o}C)									
Flat reflector	Material	Aluminum sheet									
	Size	1800 mm× 400mm									
Storage tank	Material	Galvanized steel 0.8 mm thick									
	Capacity	7.25 ℓ (max.)									

Table (2) Comparison of the overall daily efficiency with various works.

Works	Load condition	Design specifications				$\eta_{Overall}$ %
		Collector type	L_{ev}	L_{co}	**Working fluid**	
Present work (individual heat pipe systems)	No load	Evacuated tube-heat pipe solar collector	1.8 (m)	0.2 (m)	Ethanol	54.12
	Intermittent load					83.9
	Continuous load					81.5
Mahdy [2005]	No load	Evacuated tube-heat pipe collector	1.2 (m)	0.2 (m)	Ethanol	48
	Continuous load				H_2O	61
Akyurt [1984]	No load	flat plate heat pipe collector	2.1 (m)	1.2 (m)	Ethanol	52
Noren [1981]	No load	flat plate heat pipe collector	2.1 (m)	1.2 (m)	Ethanol	49
Chun et al. [1999]	No load	flat plate heat pipe collector	1.7 (m)	0.2 (m)	Ethanol	45

Figure (1) A photograph of four different evacuated tube heat pipe solar water heating
systems with instrumentation.
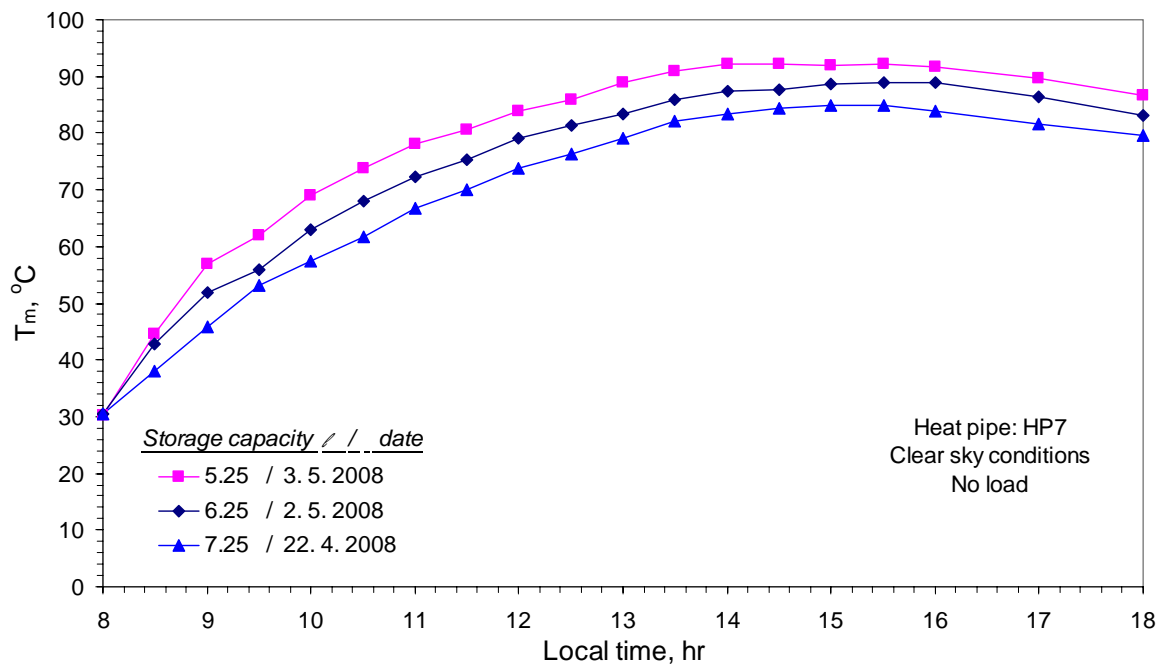
Figure (2) Variation of the mean tank temperature at various storage capacities.
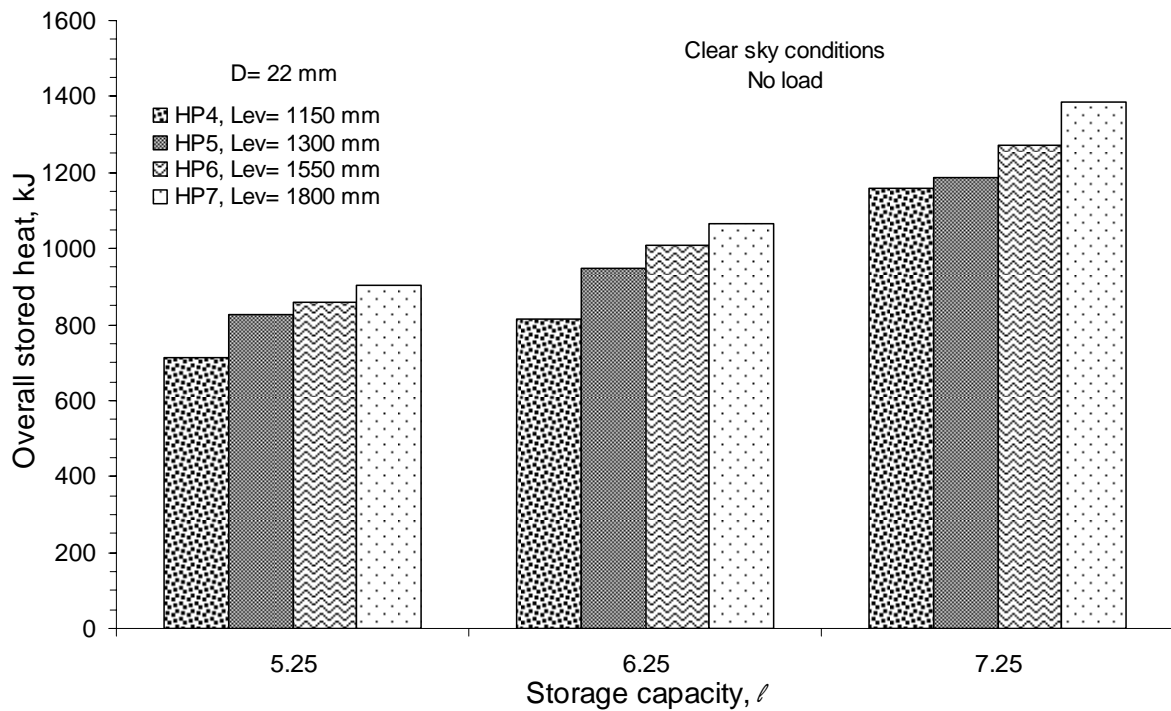
Figure (3) Effect of the storage capacity on the daily overall stored heat.
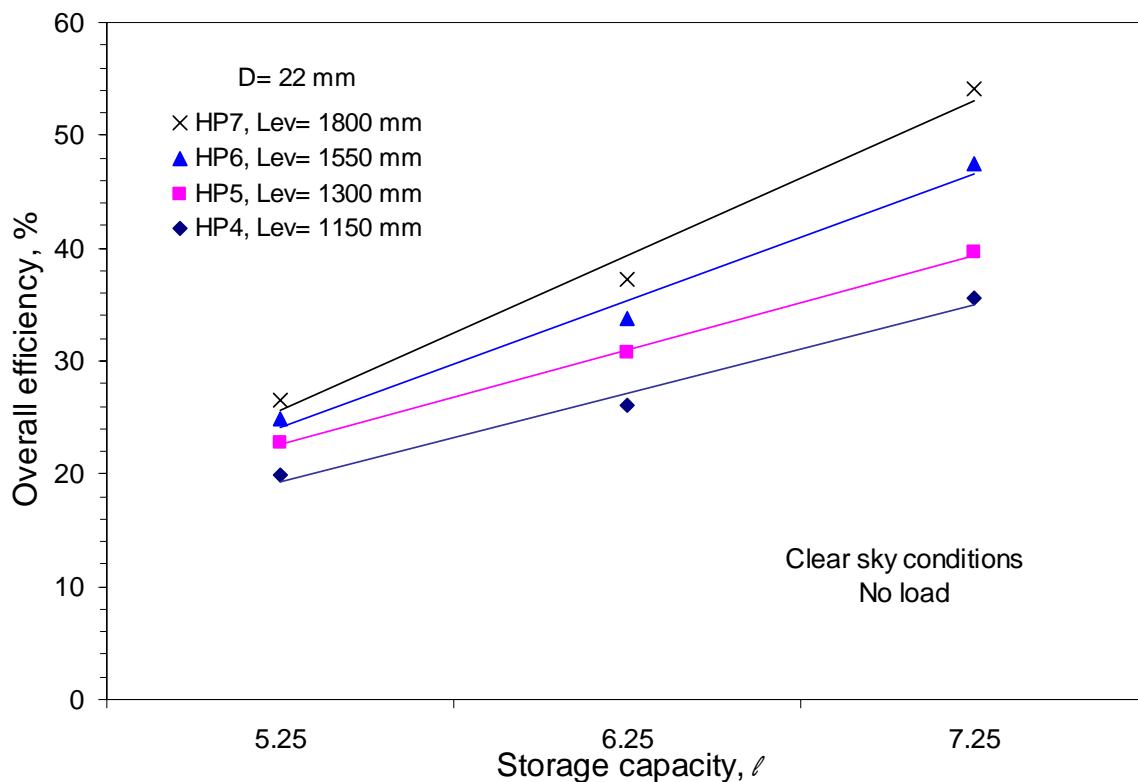
Figure (4) Effect of the storage capacity on the daily overall efficiency.
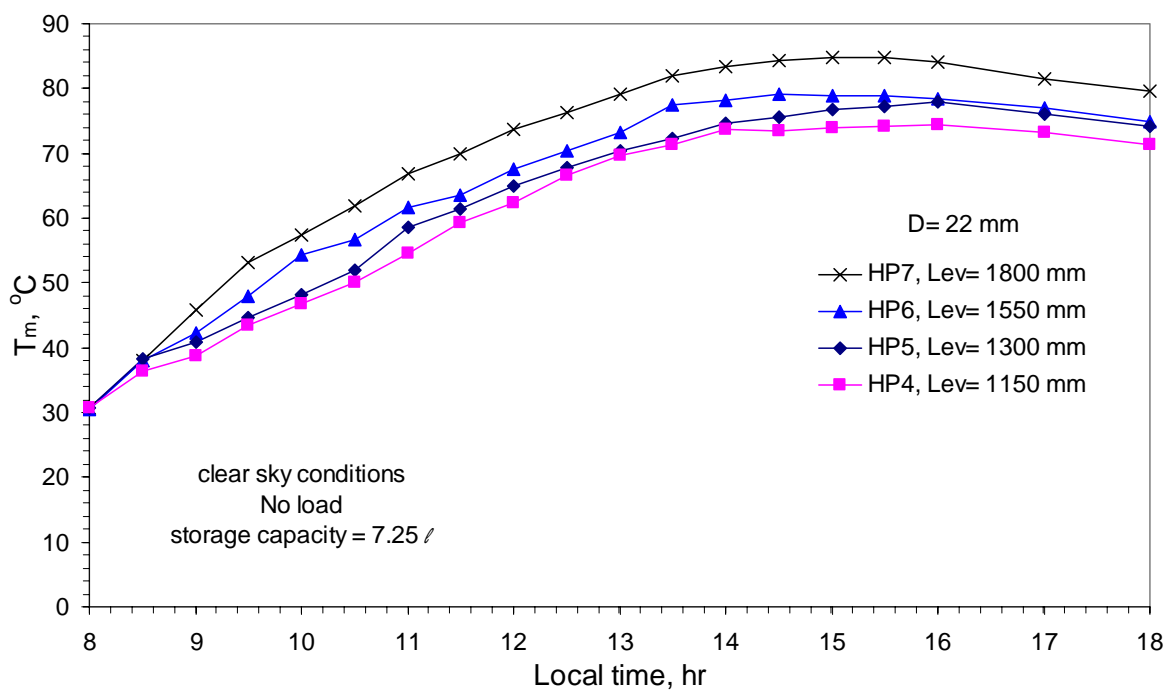
Figure (5) Variation of the mean tank temperature with different evaporator lengths.
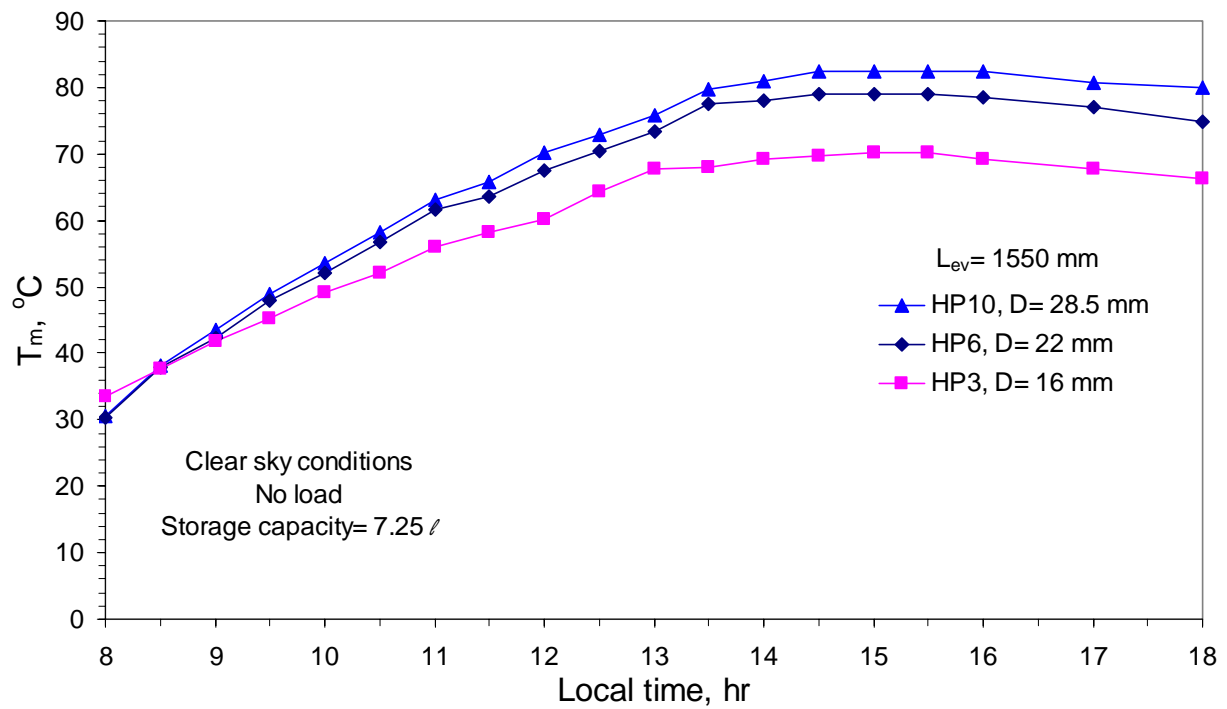
Figure (6) Variation of the mean tank temperature with different diameter heat pipes.
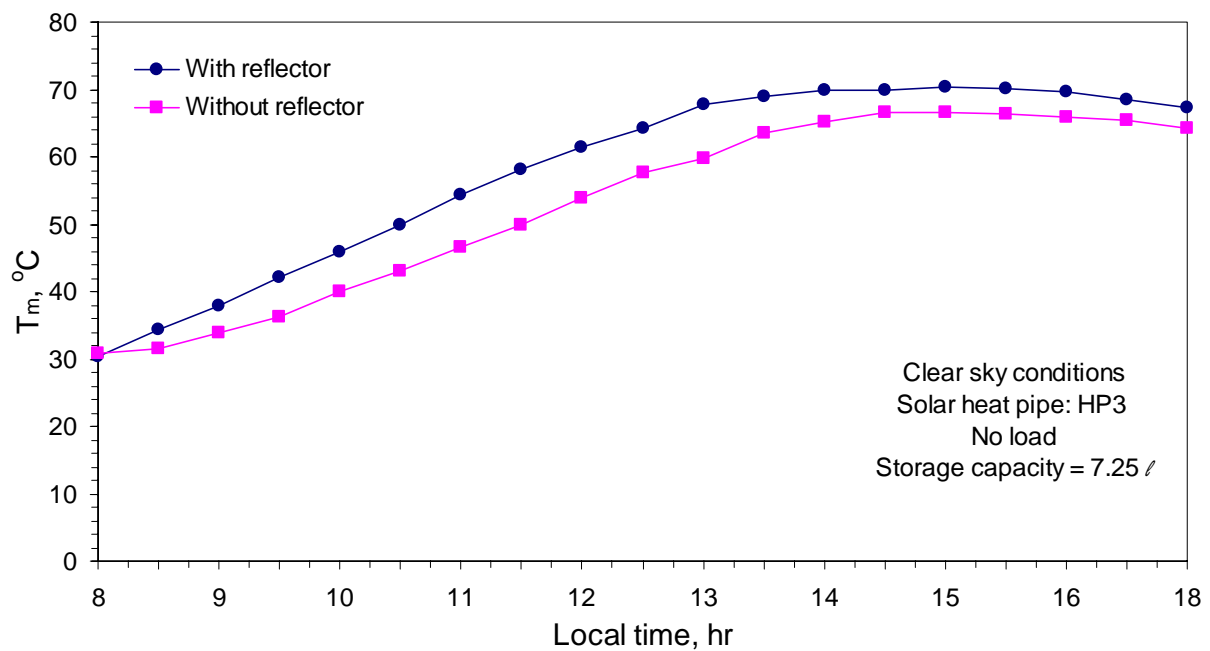
Figure (7) Effect of reflectors on the mean tank temperature.
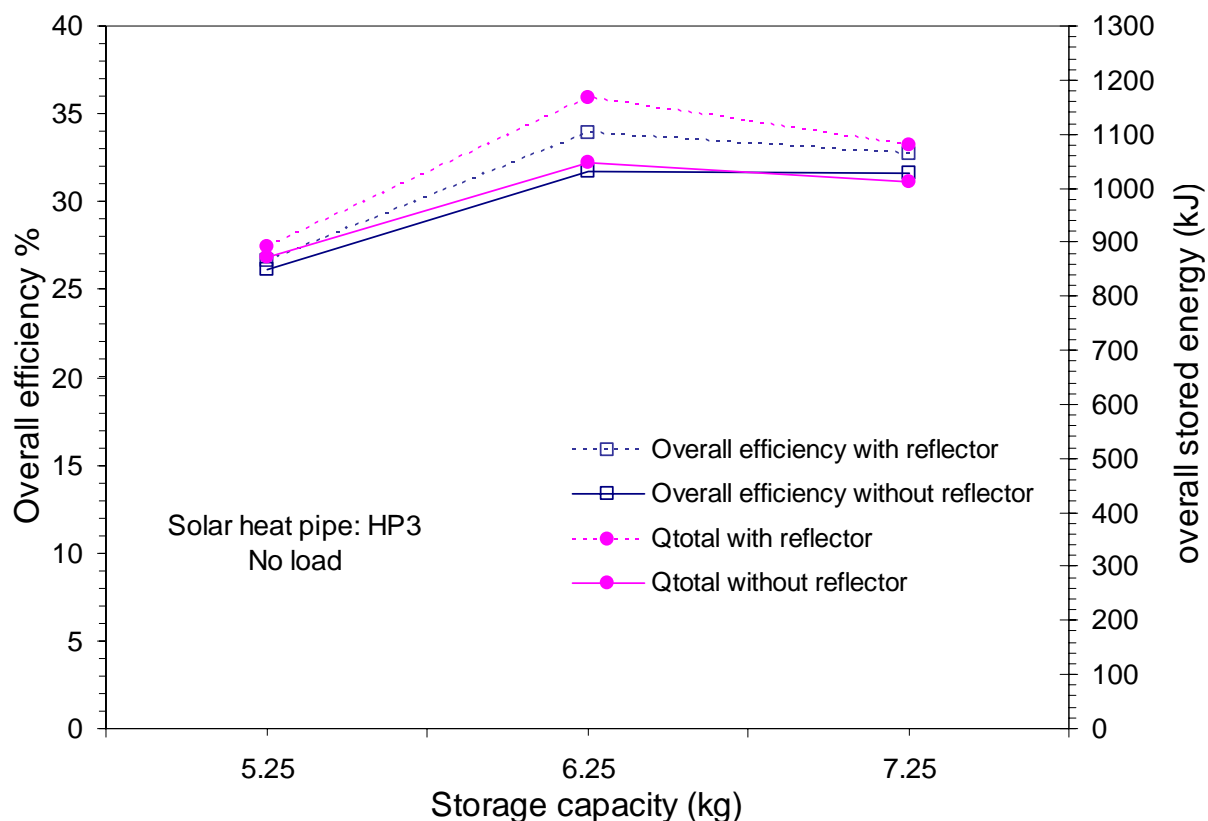
Figure (8) Effect of reflectors on the overall stored energy and efficiency at different storage capacities.
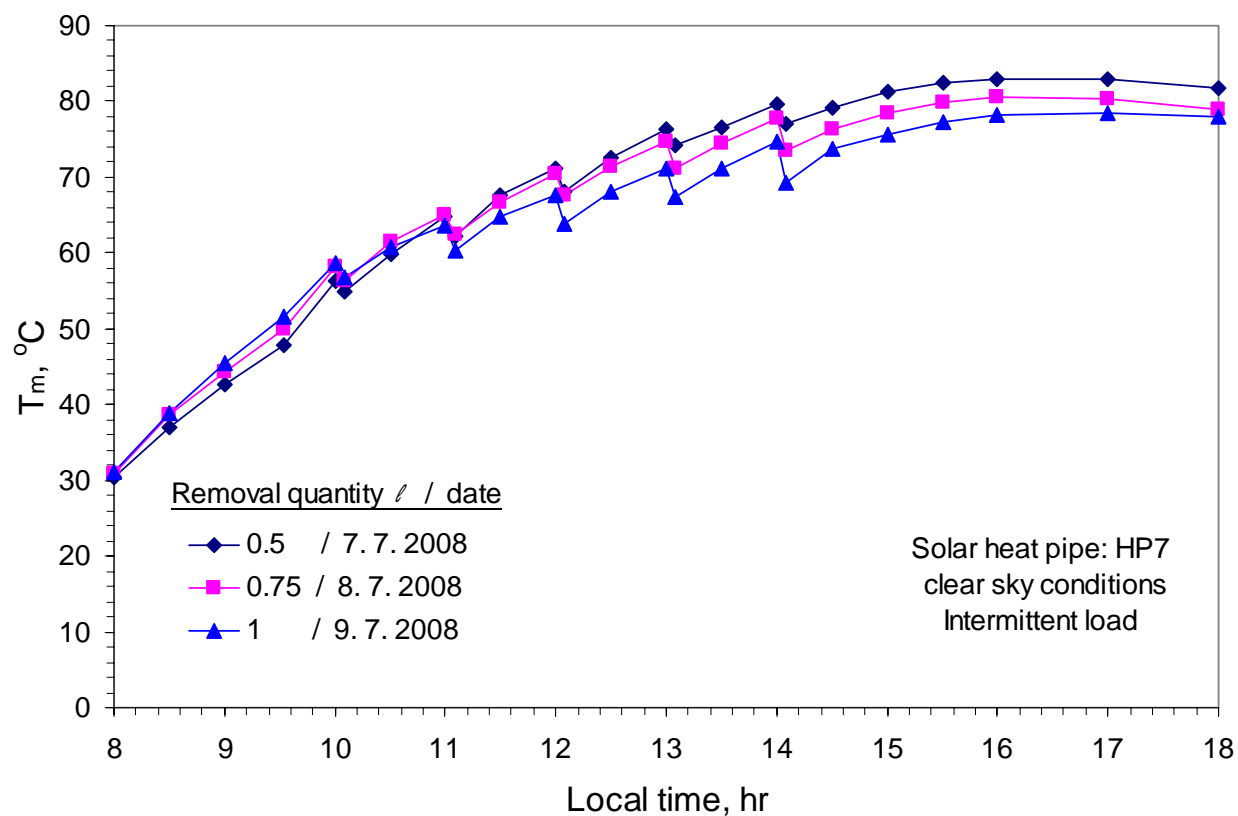
Figure (9) Effect of intermittent loading on T_m for solar system with heat pipe HP7.
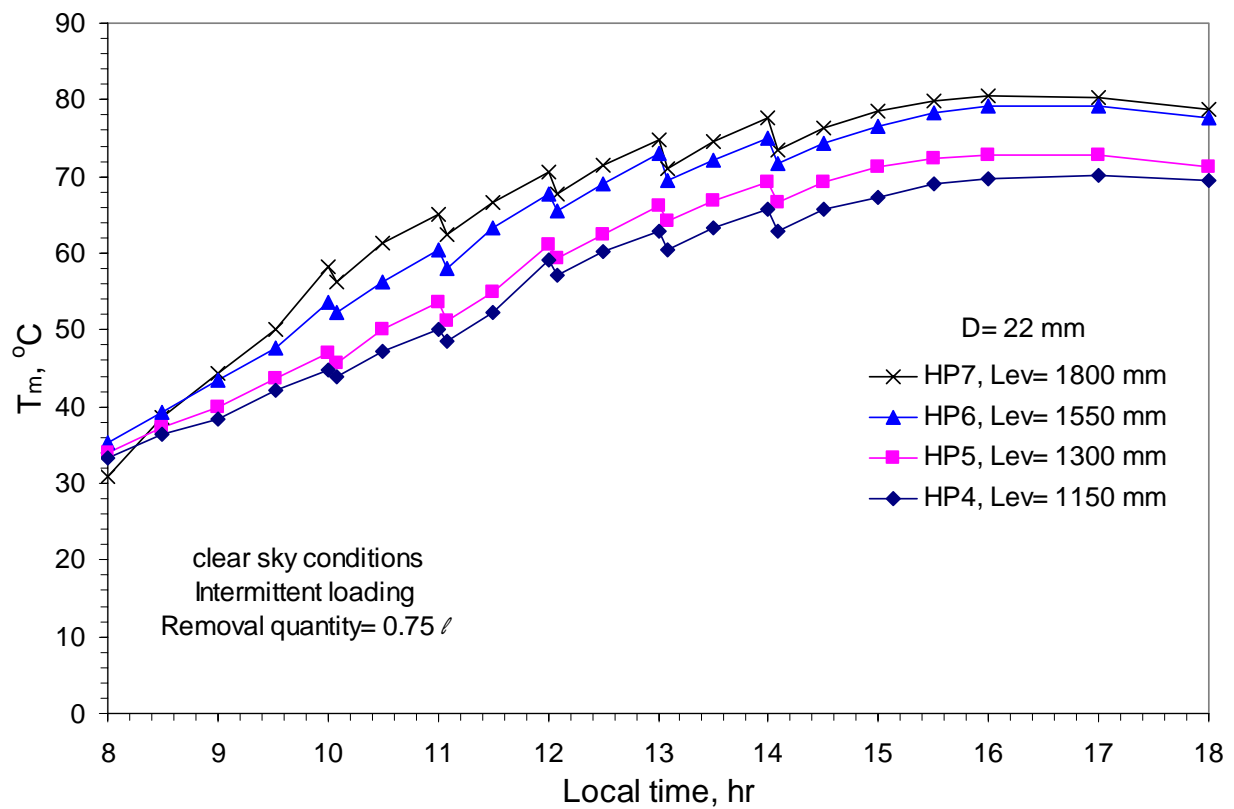
Figure (10) Effect of intermittent loading for the 22 mm diameter heat pipe systems on T_m.
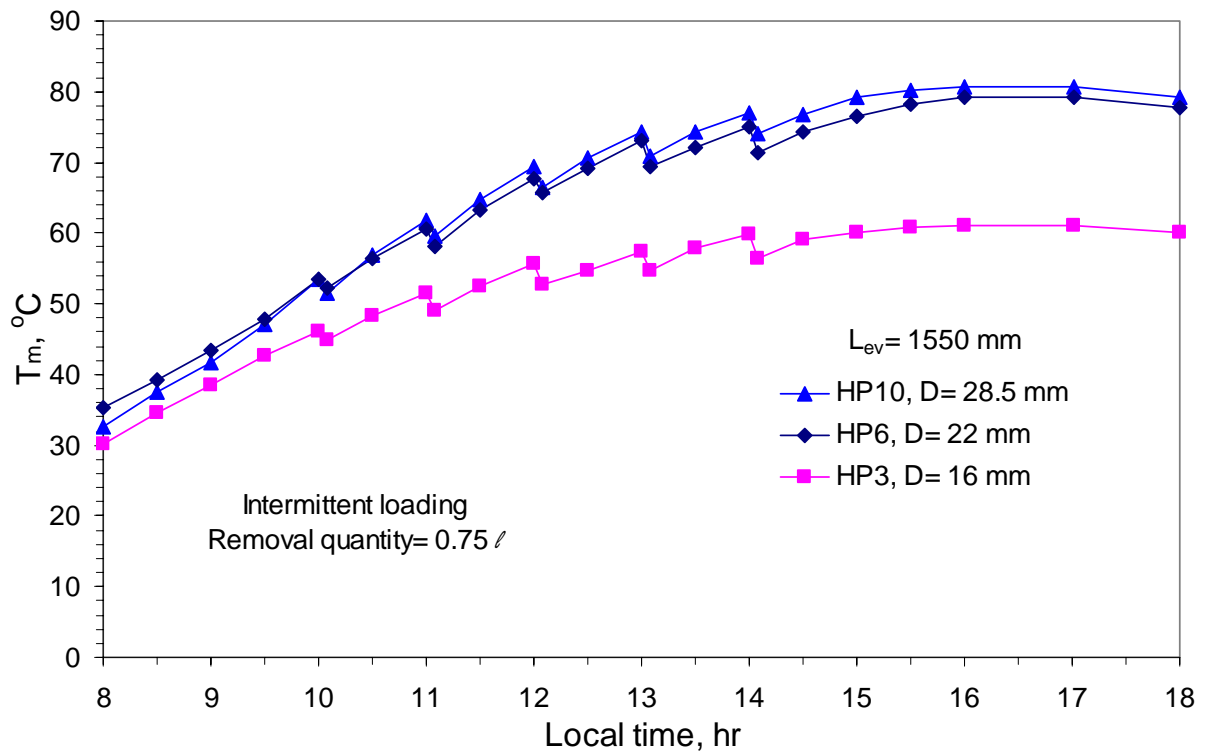
Figure (11) Effect of the heat pipe diameter with intermittent loading for systems with 1550 mm evaporator heat pipes.

217
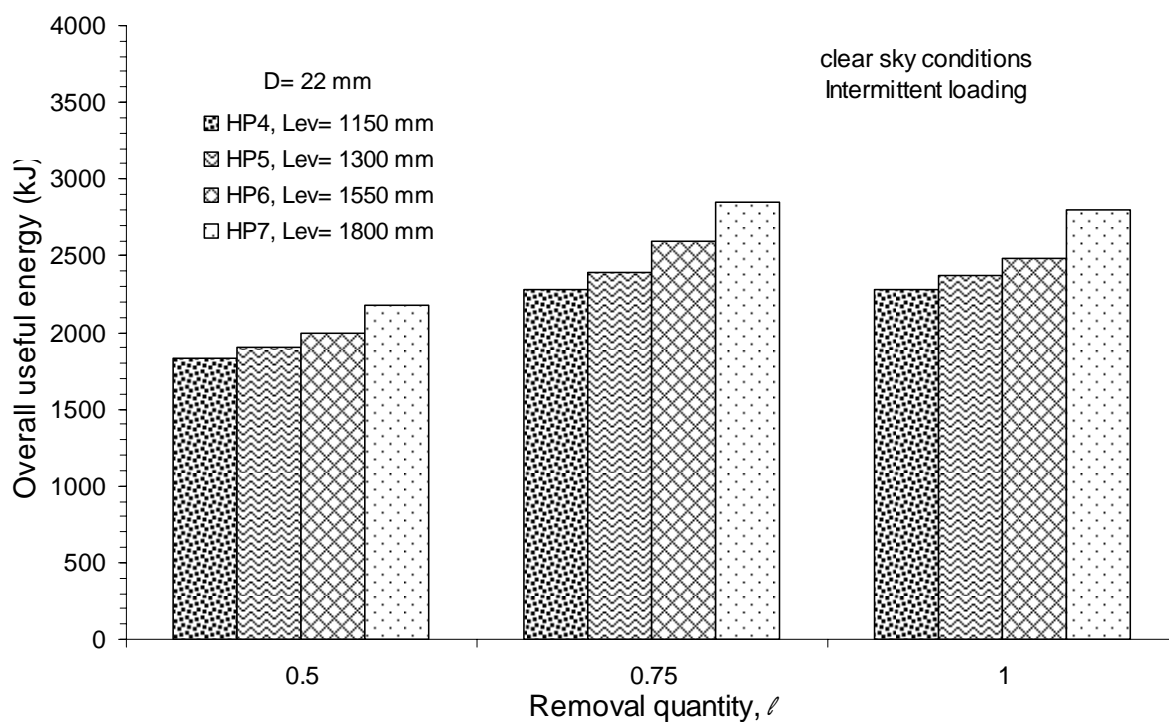
Figure (12) Effect of the heat pipe evaporator length, at 22 mm diameter, on the overall useful
energy at various loading conditions.
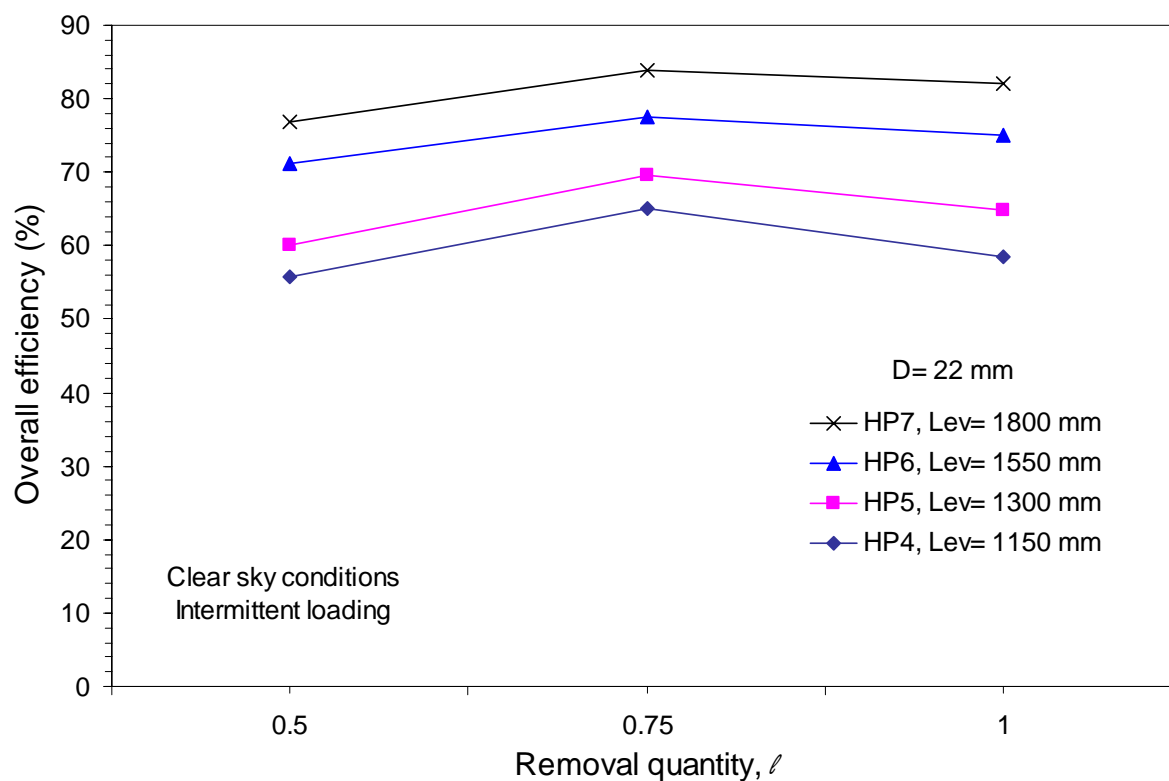
Figure (13) Effect of the heat pipe evaporator length, at 22 mm diameter, on the overall
efficiency at various loading conditions.
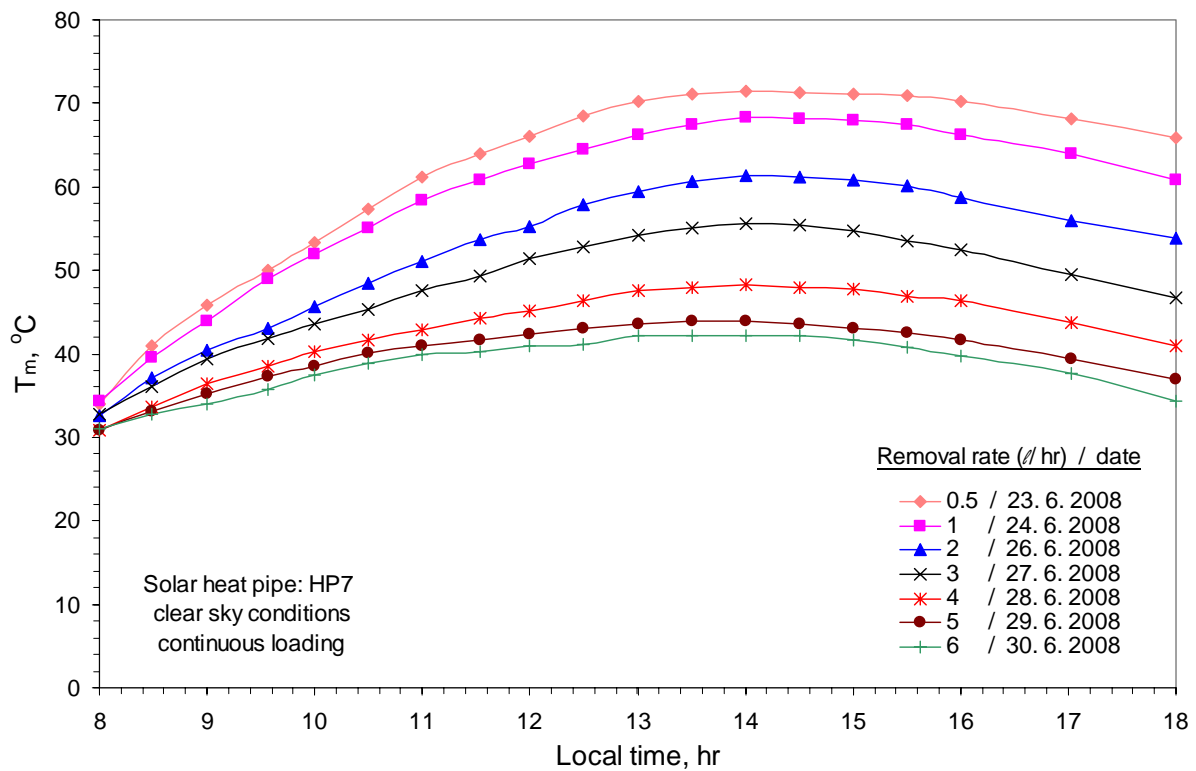
Figure (14) The effect of continuous loading on the mean tank temperature.
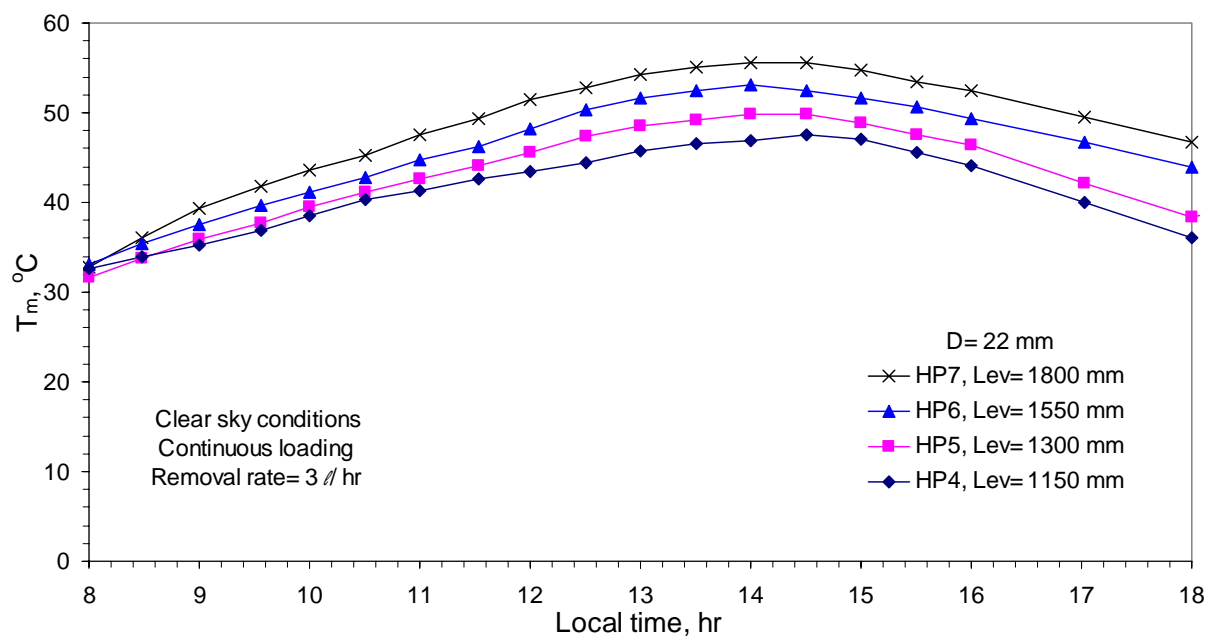
Figure (15) Mean tank temperature variation with various heat pipe evaporator lengths at continuous loading.
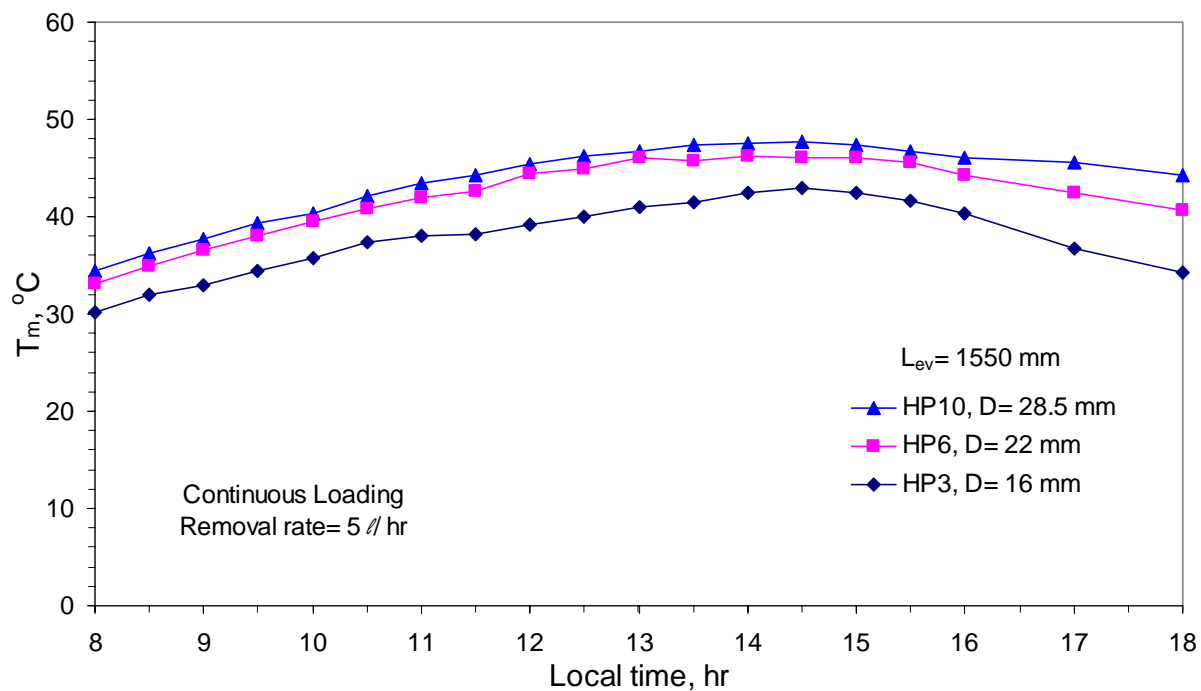
Figure (16) Effect of heat pipe diameter on the mean tank temperature variation at a removal rate of 5 ℓ/ hr.
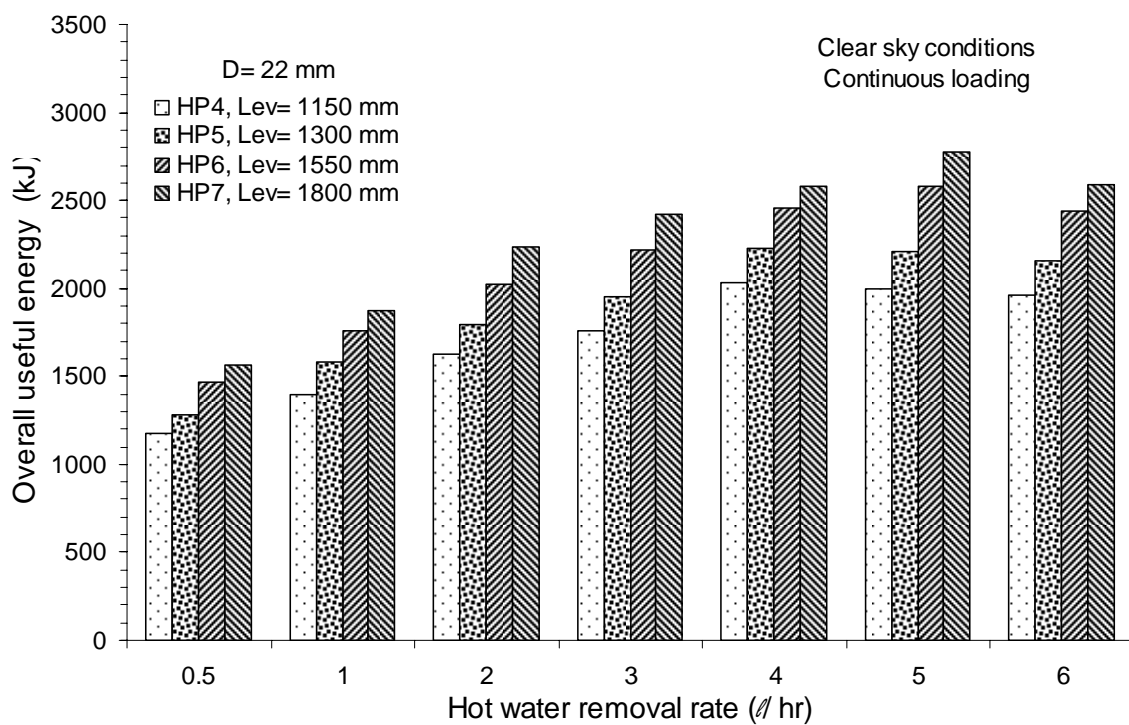
Figure (17) Effect of the heat pipe evaporator length, at 22 mm diameter, on the overall useful energy at various removal rates.
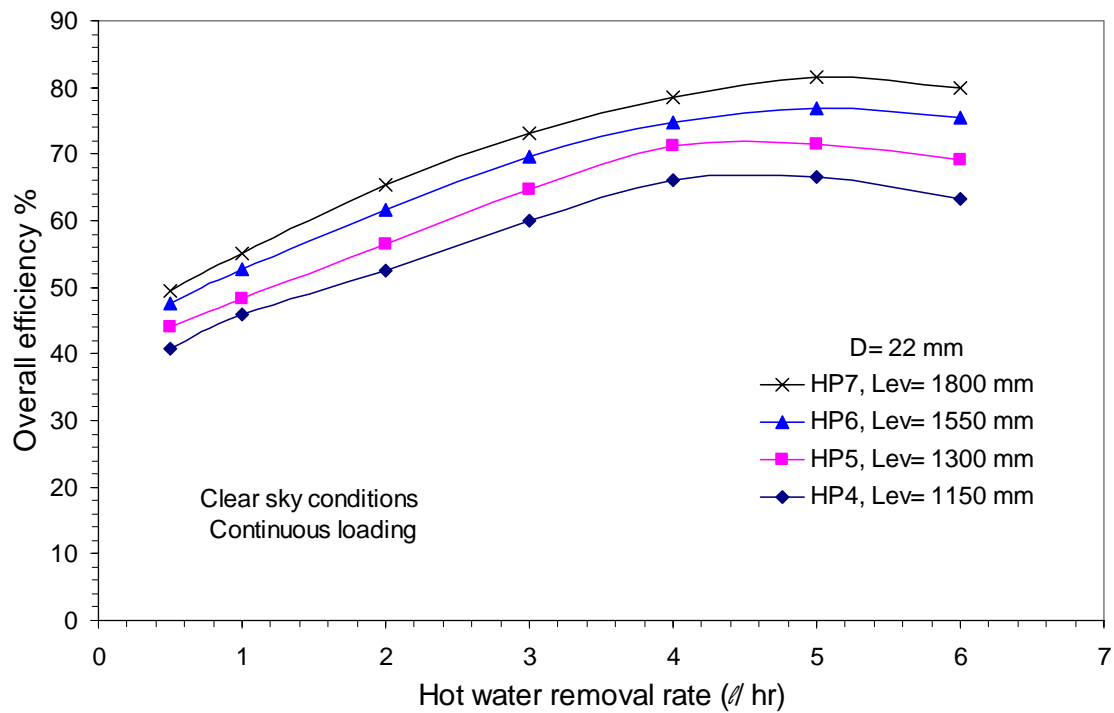
Figure (18) Effect of the heat pipe evaporator length, at 22 mm diameter, on the overall efficiency at various removal rates.
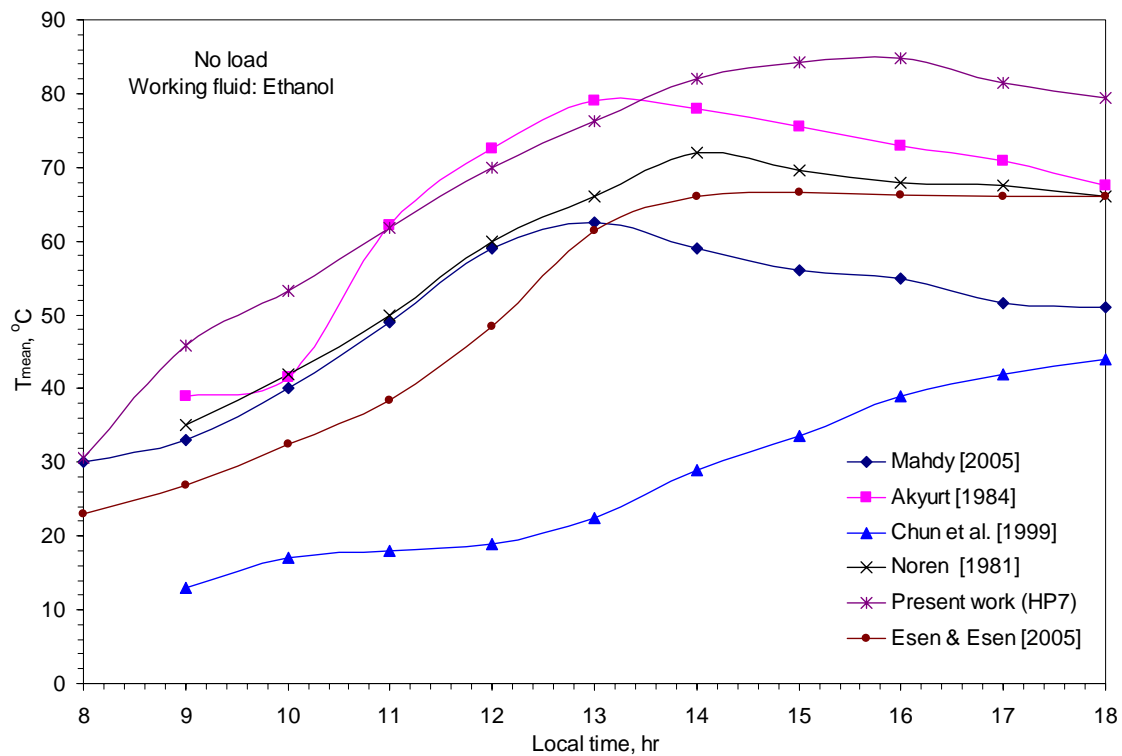
Figure (19) Comparison of the mean tank temperature variation with various works.

221
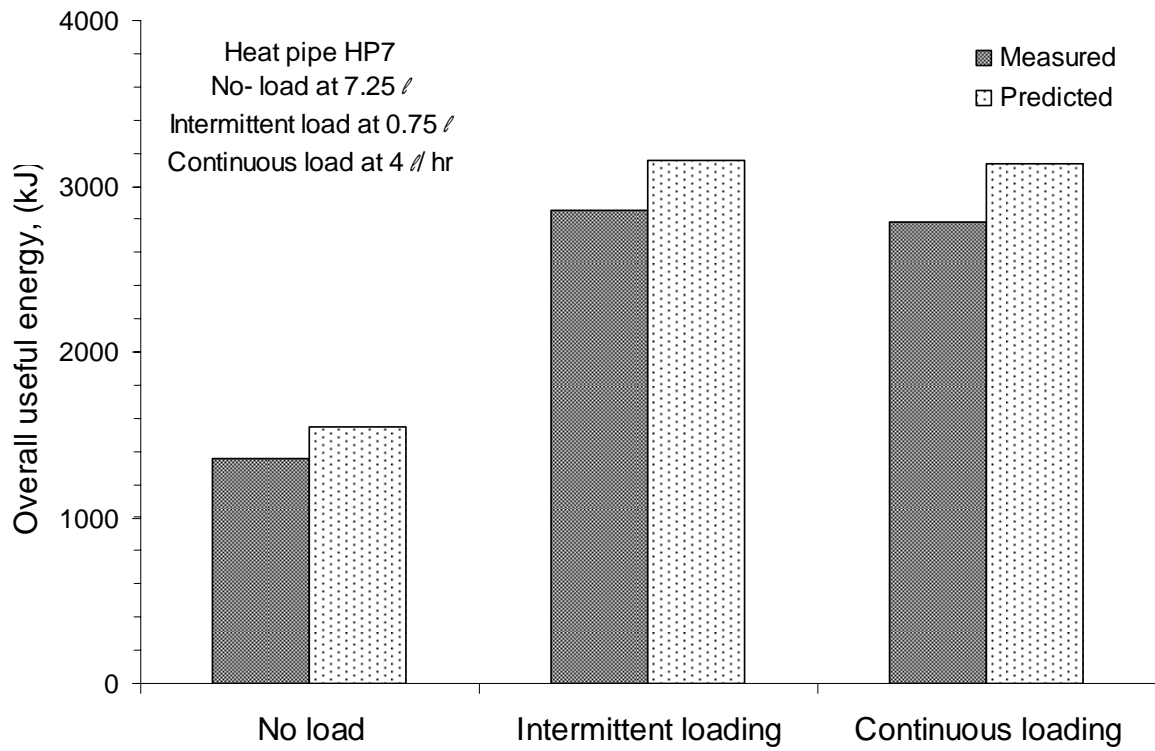
Figure (20) Comparison of measured and predicted overall useful energy.

Natural Convection Heat Transfer from a Plane Wall to Thermally Stratified Environment

Prof. Dr. Ihsan Y. Hussain
Department of Mechanical Engineering
University of Baghdad
E-mail: dr.ihsanyahya1@yahoo.com

Naseem K. Ali
Department of Mechanical Engineering
University of Baghdad
E-mail: alokaili@yahoo.com

The effect of linear thermal stratification in stable stationary ambient fluid on free convective flow of a viscous incompressible fluid along a plane wall is numerically investigated in the present work. The governing equations of continuity, momentum and energy are solved numerically using finite difference method with Alternating Direct implicit Scheme. The velocity, temperature distributions and the Nusselt number are discussed numerically for various values of physical parameters and presented through graphs. ANSYS program also used to solve the problem. The results show that the effect of stratification parameter is marginalized with the increase in Prandtl number, and the increase in Grashof number does not practically vary the effect of stratification parameter.

Key words: Natural convection, Thermal Stratification, Linear, Boundary Layer,

Prof. Dr. Ihsan Y. Hussain
Naseem K. Ali

Natural Convection Heat Transfer from a Plane Wall to
Thermally Stratified Environment

Introduction

Convective heat transfer in thermally stratified ambient fluid occurs in many industrial applications and is an important aspect in the study of heat transfer. If stratification occurs, the fluid temperature is function of distance. Convection in such environment exists in lakes, oceans, nuclear reactors. The problem had been investigated by many researcher analytically and numerically, see for example (Cheesewright 1967), (Yang et al 1972), (Jaluria and Himasekhar 1983), (Kulkarni et al 1987), (Angirasa and Srinivasan 1992), (Pantokratoras 2003), (Saha and Hossain 2004), (Ahmed 2005), (Ishak et al 2008), (Deka and Neog 2009), (Singh et al 2010). Experimental works also had been reported; see (Tanny and Cohen 1998).Theoretical and experimental work had been investigated by (Chen and Eichhorn 1976). The present work investigates the problem numerically with wide range of stratification parameter for different kinds of fluids (air, water, and oil), different Grashof number and different inclination angle. To support the numerical solution the problem was solved also using ANSYS Program.

Formulation of the Problem

Consider the two dimensional thermal boundary layer flows natural convection heat transfer of an incompressible fluid along a plane wall immersed in a stable thermally stratified fluid. The coordinates system and the flow configuration are shown in figure 1. Using Boussinesq approximations, the following continuity, momentum and energy equations in nondimensional form for laminar flow adjacent to a plane wall are obtained;

$$\frac{\partial U}{\partial X} + \frac{\partial V}{\partial Y} = 0 \tag{1}$$

$$\frac{\partial U}{\partial t^*} + U\frac{\partial U}{\partial X} + v\frac{\partial U}{\partial Y} = \frac{1}{\sqrt{Gr}}\left(\frac{\partial^2 U}{\partial X^2} + \frac{\partial^2 U}{\partial Y^2}\right) + \theta \tag{2}$$

$$\frac{\partial V}{\partial t^*} + U\frac{\partial V}{\partial X} + v\frac{\partial V}{\partial Y} = \frac{1}{\sqrt{Gr}}\left(\frac{\partial^2 V}{\partial X^2} + \frac{\partial^2 V}{\partial Y^2}\right) + \theta \tan\varphi \tag{3}$$

$$\frac{\partial \theta}{\partial t^*} + U\frac{\partial \theta}{\partial X} + v\frac{\partial \theta}{\partial Y} = \frac{1}{Pr\sqrt{Gr}}\left(\frac{\partial^2 \theta}{\partial X^2} + \frac{\partial^2 \theta}{\partial Y^2}\right) - SU \tag{4}$$

where (Angirasa and Srinivasan 1992);

$$X = \frac{x}{L}, \quad Y = \frac{y}{L}, \quad U = \frac{u}{u_c}, \quad V = \frac{v}{u_c},$$

$$t^* = \frac{t \cdot u_c}{L}, \quad Pr = \frac{\mu c_p}{k},$$

$$u_c = \sqrt{g \cdot \cos\varphi \cdot \beta \Delta T_0 \cdot L},$$

$$\theta = \frac{T - T_{\infty,x}}{T_w - T_{\infty,0}} = \frac{\Delta T_1}{\Delta T_0}, \quad Gr = \frac{g \cdot \beta \cdot \cos\varphi \cdot L^3 \cdot \Delta T_0}{\vartheta^2},$$

$$\beta = -\left(\frac{1}{\rho}\right) \cdot \left(\frac{\partial \rho}{\partial T}\right)_P, \quad S = \frac{1}{\Delta T_0} \cdot \left(\frac{dT_{\infty,X}}{dx}\right)$$

The initial condition can be written in nondimensional form as follows:

$$U = 0, V = 0, \theta = 0 \quad \text{for all } X, Y \tag{5}$$

The boundary conditions in nondimensional form are:

$$U = 0, V = 0, \theta = \theta_w \quad \text{at } Y = 0 \text{ for all } X \tag{6}$$

$$U = 0, V = 0, \theta = 0 \quad \text{at } Y \to \infty \text{ for all } X \tag{7}$$

$$U = 0, V = 0, \Theta = 0 \qquad at\ Y \rightarrow \infty\ for\ X = 0$$
$$(8)$$

The local rate of heat transfer in term of the local Nusselt number at the plate is given by;

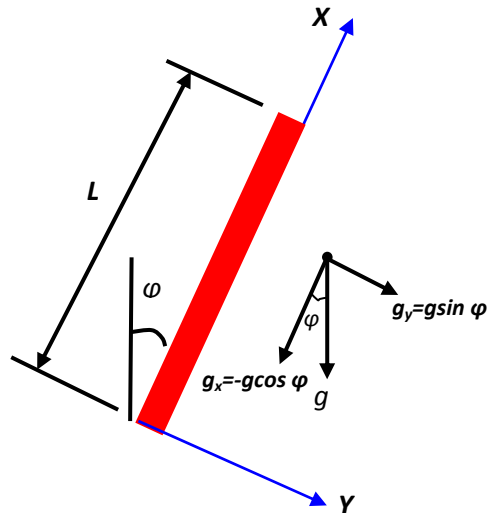$$Nu_X = -\frac{x}{\theta_w} \cdot \left(\frac{\partial\theta}{\partial Y}\right)_{Y=0} \qquad (9)$$

Figure1. Physical Model

Numerical Solution

Finite Difference Method is considered as efficient technique to solve the thermal problems; therefore it has been used in the present study. The Momentum and Energy equation are solved by Alternating Direction Implicit Scheme (ADI). Numerical results were first obtained to check for grid dependency. The results showed that no considerable difference in the results of suggested grid size after (51x51) and showed that no considerable different in the results of suggested transverse distance after (0.5). Therefore in the present study the grid size of (51x51) and transverse distance of (0.5) was used. The convergence of the solution to the steady state result for large time was obtained with a convergence criterion of (1×10^{-4}). This criterion was chosen after varying it over a wide range so that the steady state results were essentially independent of the chosen value. The mathematical model was solved by computer program which was written by Visual basic language to solve the momentum and energy equations and to calculate Nusselt number. The Tridiagonal system of equation was used to solve the matrix of dependent variables. Heat transfer process by natural convection in stratified media was also solved by Mechanical ANSYS Parametric Design Language (APDL). The FLUID 141 element is used which can solve model of transient or steady state fluid/thermal systems that involve fluid and/or non-fluid regions.

Results and Discussion

Theoretical investigation are done for three working fluids, air (Pr = 0.7), water (Pr = 6) and oil (Pr = 6400), three Grashof numbers (1E4, 1E5 and 1E6) and three angle (-30, 0 and 30) for wide range of thermal stratification (S = 0, 0.5, 1, 1.5, 2, 3, 4). Figure 2 shows the temperature profile for the different values of the stratification level at mid high wall plane (X = 0.5). The temperature profile decreases with increasing the stratification parameter. For the higher value of stratification, the ambient temperature exceeds the wall temperatures, which lead to negative temperature profile. The figures also show that the temperature profile equal to zero at (S = 2) because of the equalization between the wall and ambient temperature. A comparative study of figures 2 to 4 indicates that the effect of stratification parameter is marginalized with the increase in Prandtl number, as the separateness among the temperature profile reduces. Also for given value of Prandtl number the velocity and thermal boundary layer thickness are almost the same while with the increase in Prandtl number the boundary layer thickness reduces. Figure 5 shows that the temperature profile decreases with the increase in Prandtl

Prof. Dr. Ihsan Y. Hussain
Naseem K. Ali

Natural Convection Heat Transfer from a Plane Wall to
Thermally Stratified Environment

number. In addition, the reversal of temperature was found to be stronger at high Prandtl numbers and weaker at low numbers. It can be suitably remarked that the increase in Grashof number does not practically vary the effect of stratification factor on temperature profiles. Figures 6 show that with increase in Grashof number the fluid temperature deceases. This must happen because buoyancy force assists the flow by increasing fluid velocity and hence the heat is convected readily thereby reducing fluid temperature. Figure 7 illustrates the influence of the inclination angle (φ) on temperature profile for stratified media (S = 2), where observed that in addition to the influence of thermal stratification the temperature profile will be less effected by the inclination angle of the wall, this is considerably noted for high levels of thermal stratification, therefore the orientation marginalized the effect of the stratification parameter. Figure 8 shows that the velocity profile decreases with increasing the stratification parameter. It is understood, since the factor ($T_w - T_{\infty,x}$) reduces with the increase in stratification factor, thus buoyancy effect very close to the plate is marginalized thereby reducing the fluid velocity. A comparative study of figures 8 to 10 indicates that the effect of stratification parameter is marginalized with the increase in Prandtl number, as the separateness among the velocity profile reduces. Figure 11 shows that the velocity profile decreases with the increase in Prandtl number. At high Prandtl numbers there is a small reversal of flow while for low Prandtl numbers the flow reversal is much stronger. It can be suitably remarked that the increase in Grashof number does not practically vary the effect of stratification factor on velocity profiles. Figure 12 shows that with increase in Grashof number the fluid velocity increases. This is because the buoyancy force assists the flow

by increasing fluid velocity. Figure 13 shows that the velocity profile decreases with increasing the Grashof number. This phenomenon is clear at high Prandtl number which lowers fluid velocity. Figure 14 illustrates the influence of the inclination angle (φ) on velocity profile for stratified level (S = 2), where observed that in addition to the influence of thermal stratification the velocity profile will be less effected by the inclination angle of the wall, this is considerably noted for high levels of thermal stratification, therefore the orientation marginalized the effect of the stratification parameter. The effect of the stratification parameter is to reduce the Nusselt number. Nusselt number is equal to zero at any location of the plane wall when the wall temperature equal to ambient temperature. This equalization is result of stratification level. The figure 15 shows the deceases in Nusselt number with the stratification parameter because of the Nusselt number dependence on the temperature profile which decreased with increase in stratification parameter as mentioned above. As the Prandtl number increases the Nusselt number first deceases, then increases. An increase in Prandtl number is found to cause a decrease in thermal boundary layer thickness and an increase in the absolute value of the temperature gradient at the surface. In unstratified media the local Nusselt number for air is higher than for water and less than for oil as shown in figure 16. In stratified media, the Nusselt number has the same behavior of the unstratified environment. Nusselt number is dependent on many variables, one of these variables Grashof numbers which affects the heat transfer behavior from fluid to another. The fluids which have small Prandtl number, Nusselt number decreases with increasing the Grashof number. The reverse behavior is for fluids

which have large Prandtl number where the Nusselt number increases with increasing Grashof number as shown in figure 17.The Nusselt number has the same behavior in stratified and unstratified environment. Consider an inclined hot plate that makes an angle ($\varphi = 30$) from vertical wall plane. The difference between the buoyancy and gravity force acting on a unit volume of fluid in the boundary layer is always in the vertical direction. In the case of inclined plate, this force can be resolved into two components, the parallel force drive the flow along the plate and the normal force on the wall plane. The force that drives the motion is reduced; therefore the convection currents to be weaker and the rate of heat transfer to be lower relative to the vertical plane case. In the case ($\varphi = -30$) the opposite behavior is observed. The reason for this behavior is that the normal force component initiates upward motion in addition to the parallel motion along the wall plane, and thus the boundary layer breaks up and forms plumes. As result, the thickness of the boundary layer and thus the resistance to heat transfer decreases, and the rate of heat transfer increases relative to the vertical orientation. In the stratified media, the Nusselt number has the same behaviors of the unstratified media until temperature defect occurs, then the Nusselt number has the opposite behaviors as shown in figure 18.

ANSYS Analysis

Figures 19 to 21 show the temperature distribution for different stratification parameter. It is clear that in the thermal stratified environment, the fluid temperature increases with height and with stratification parameter. The domain have region with no heat transfer because of equalization between wall and fluid temperatures, the fluid above the equalization region have temperature more than wall temperature, therefore the temperature defect happens. Figures 22 to 24 show the velocity decreases with increase in stratification parameter and the reverse flow was happened in the media which have stratification parameter more than one. The figures 25 and 26 show visualization to fluid flow in thermal stratified media. The figures 27 to 29 show the heat transfer coefficient decrease with increase in stratification level.

Verification

To verify the results obtained for the present study, a comparison is made with the results achieved by previous studies. Temperature profile (figure 1) agrees with the results of Ahmed (2005) (numerical study) shown in figure 30 and Tanny and Cohen (1998) (experimental study) shown in figure 31. Velocity Profile (figure 8) agrees with the results of Angirasa and Srinivasan (1992) (numerical study) shown in figure 32 and Cheesewright (1967) (analytical study) shown in figure 33. The effect of Prandlt number on temperature Profile (figure 5) agrees with results of Singh et al (2010) (numerical study) shown in figure 34. Nusselt number (figure 15) agrees with the result of Ahmed (2005) shown in figure 35.

Conclusions

1. For constant wall temperature when the stratification parameter increases, the temperature profile steepens near the surface, the buoyancy level decrease and the maximum velocity decreases because of the decrease in buoyancy.
2. For constant wall temperature when the values of stratifications more than one, the local temperatures adjacent to the wall exceed the wall temperature in regions of

Prof. Dr. Ihsan Y. Hussain
Naseem K. Ali

Natural Convection Heat Transfer from a Plane Wall to
Thermally Stratified Environment

the top portion of the wall, which receives heat from the fluid, and a reverse flow will exist.

3. The effect of stratification parameter is marginalized with the increase in Prandtl number.

4. The reversal of temperature is strong at high Prandtl numbers and weaker at low numbers and the reversal of flow velocity is strong at low Prandtl numbers and weaker at high numbers.

5. The increase in Grashof number does not practically vary the effect of stratification on temperature and velocity profiles.

6. The local Nusselt number decreases when the stratification increases.

7. As Prandtl number increases the Nusselt number first decrease, then increase.

Nomenclature

Gr	Grashof number
g	gravitational Acceleration
L	characteristic length of the plane wall
Nu	Nusselt number
Pr	Prandtl number
S	thermal stratification parameter
T	temperature
t	time
t^*	non-dimensional time
u	velocity in x-direction
u_c	characteristic velocity
U	non-dimensional velocity in X-direction
v	velocity in y-direction
V	non-dimensional velocity in Y-direction

X	non-dimensional downstream coordinate
x	downstream coordinate
Y	non-dimensional horizontal space coordinate
y	horizontal space coordinate

Greek letters

α	thermal diffusivity
β	volumetric coefficient of thermal expansion
ʋ	kinematic viscosity
ρ	density
φ	angle of inclination
Θ	non-dimensional temperature

Superscript

∞	location away from the wall outside the boundary layer
∞, 0	location away from the wall at x = 0
∞, x	location away from the wall at any x
w	wall

References

Ahmed, T.E. (2005) "Transient natural convection heat transfer from a plane wall to a thermally stratified media" MSc. Thesis, University of Technology, Baghdad.

Angirasa, D. and Srinivasan, J. (1992) "Natural convection heat transfer from an isothermal vertical surface to a stable thermal stratified fluid" Journal of Heat Transfer Vol.114/917

Cheesewright, R. (1967) "Natural convection from a plane vertical surface in non-isothermal surroundings" Int. J. Heat and Mass Trans. Volume 10, Issue 12, Pages 1847-1859.

Chen, C.C and Eichhorn, R. (1976) "Natural convection from a vertical surface to a thermally stratified fluid" ASME Journal of Heat Transfer Vol.98, PP.446-451.

Deka, Rudra Kt and Neog, Bhaben Ch. (2009)" Unsteady natural convection flow past an accelerated vertical plate in a thermally stratified fluid" Theoret. Appl. Mech., Vol.36, No.4, PP. 261-274, Belgrade.

Isak, Anuar, Nazar, Roslinda and Pop, Ioan. (2008) "Mixed convection boundary layer flow adjacent to a vertical surface embedded in a stratified medium" Int. J. Heat and Mass Trans.vol. 51, PP. 3693-3695.

Jaluria, Y. (1980) "Natural convection heat and mass transfer" Pergamon Press.

Jaluria, Y. and Himasekhar, K. (1983) "buoyancy-induced two-dimensional vertical flows in a thermally stratified environment" Computers & Fluids Vol. 11, Issue 1, Page 39-49.

Kulkarni, A. K., Jacobs, H. R. and Hwang, J. J. (1987) " Similarity solution for natural convection flow over an isothermal vertical wall immersed in thermally stratified medium " Int. J. Heat and Mass Transfer Volume 30, Issue 4, PP 691-698

Pantokratoras, A. (2003) "A note on the Nusselt number adjacent to a vertical isothermal plate immersed in thermally stratified water at low temperatures" Int. J. Heat and Fluid Flow Vol. 32, Issue 2, Pages 278-281.

Saha, S.C, Hossain, M.A. (2004) " Natural convection flow with combined buoyancy effects due to thermal and mass diffusion in a thermally stratified media " Nonlinear Analysis: Modeling and Control, Vol. 9, No. 1, PP. 89–102.

Singh, Gurminder, Sharma, P.R and Chamkha, A.J. (2010) "Effect of thermally stratified ambient fluid on MHD convective flow along a moving non-isothermal vertical plate" international of Physical Science Vol.5 (3), PP.208-215.

Tanny, J. and Cohen, J. (1998) "The mean temperature field of a buoyancy induced boundary layer adjacent to a vertical plate immersed in a stratified medium" Int. J. Heat and Mass Transfer Volume 41, Issue 14, PP. 2125-2130.

Yang, K.T, Novotny, J.L and Cheng, Y.S. (1972) "Laminar free convection from a non-isothermal plate immersed in a temperature stratified medium" Int. j. Heat and Mass Transfer, Vol. 15, PP. 1097–1109.

Prof. Dr. Ihsan Y. Hussain
Naseem K. Ali

Natural Convection Heat Transfer from a Plane Wall to
Thermally Stratified Environment
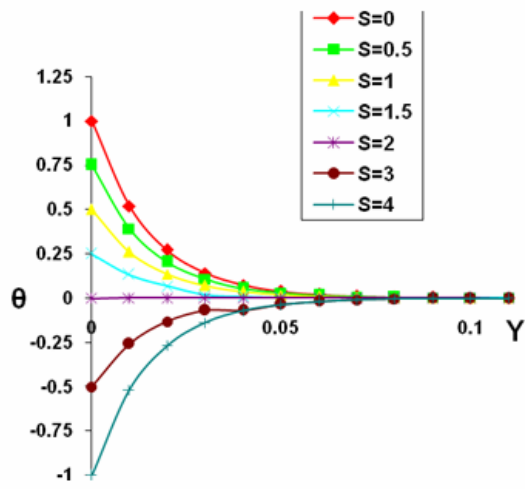
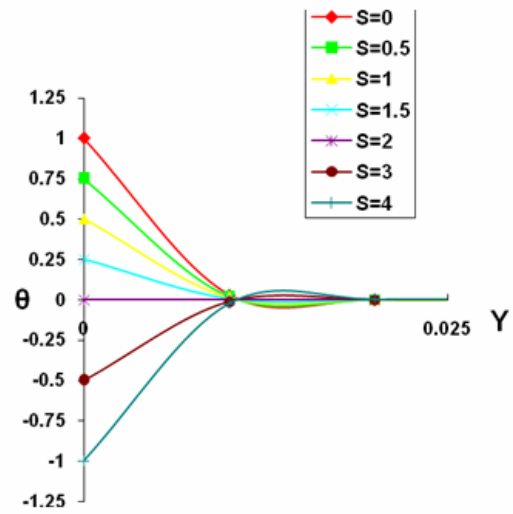**Figure 2.** Temperature profile for $Pr = 0.7$ and $Gr = 1E5$

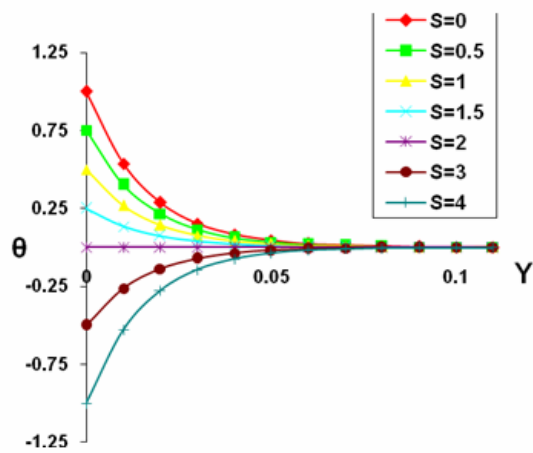**Figure 4.** Temperature profile for $Pr = 6400$ and $Gr = 1E5$

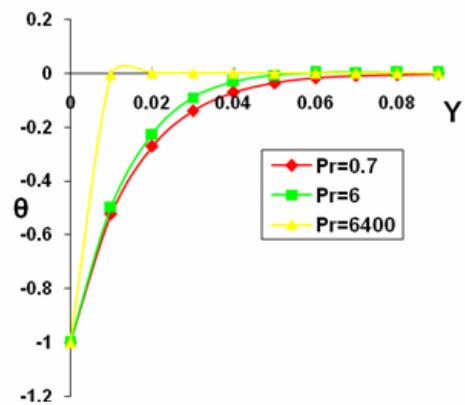**Figure 3.** Temperature profile for $Pr = 6$ and $Gr = 1E5$

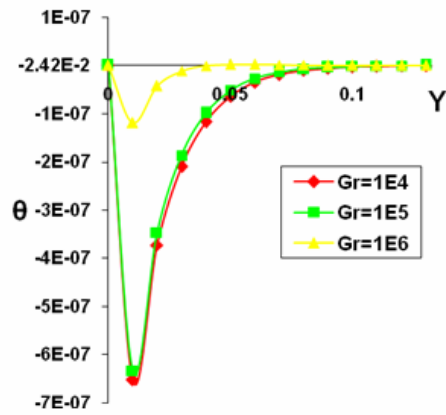**Figure 5.** Temperature profile for $S = 4$ and $Gr = 1E6$
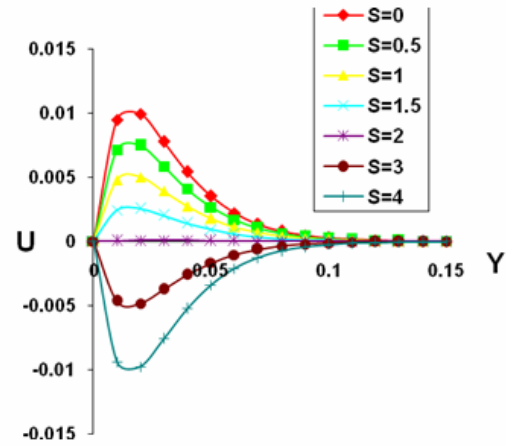
Figure 6. Temperature profile for Pr = 6400 and S = 2

Figure 8. Velocity profile for Pr = 0.7 and Gr =1E5
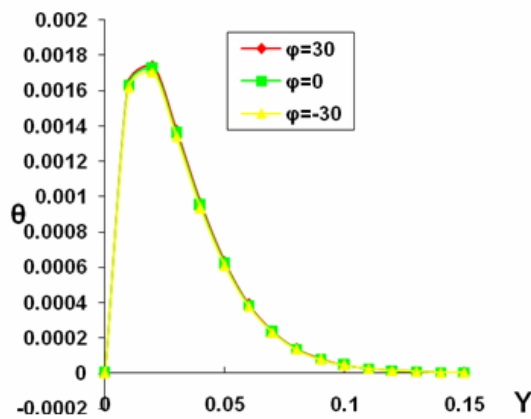
Figure 7. Temperature profile for Pr = 6 , Gr =1E5 and S = 2
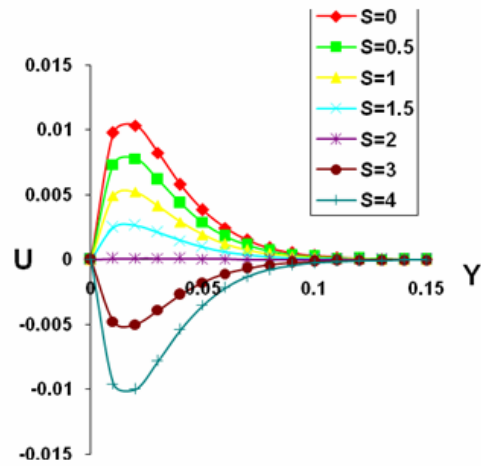
Figure 9. Velocity profile for Pr = 6 and Gr =1E5

Prof. Dr. Ihsan Y. Hussain
Naseem K. Ali

Natural Convection Heat Transfer from a Plane Wall to
Thermally Stratified Environment
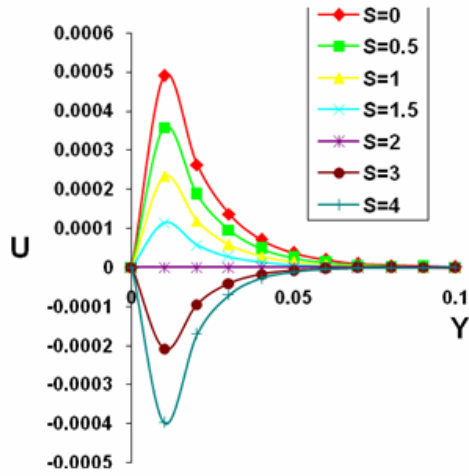
Figure 10. Velocity profile for Pr = 6400 and
Gr = 1E5
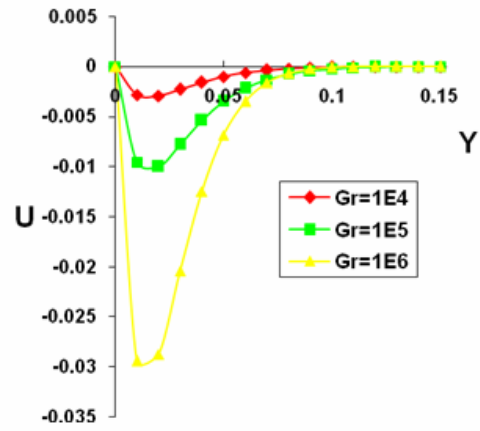
Figure 12. Velocity profile for Pr = 6
and S = 4
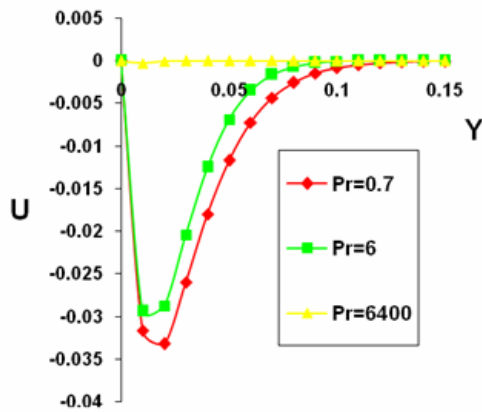
Figure 11. Velocity profile for S = 4 and
Gr = 1E6
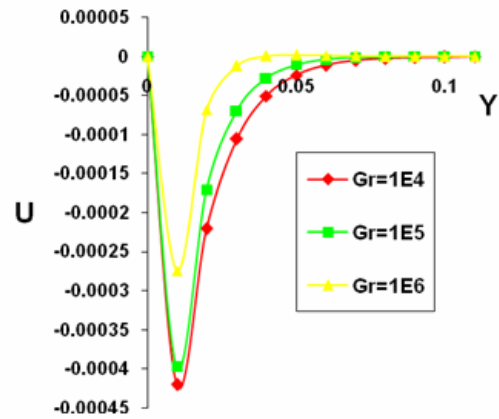
Figure 13. Velocity profile for Pr = 6400
and S = 4
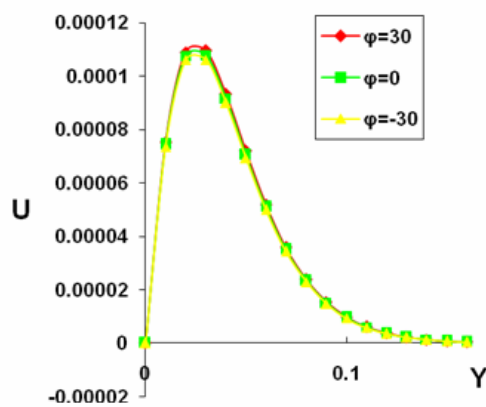
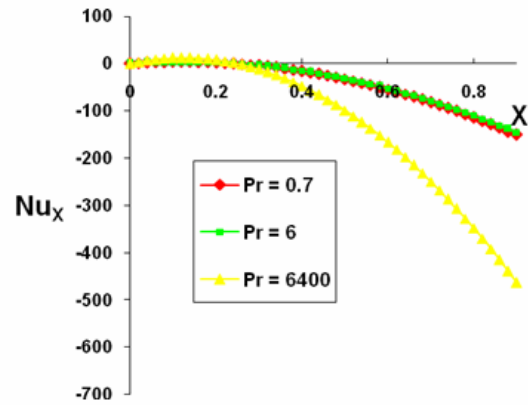**Figure 14.** Velocity profile for Pr = 6, S = 2 and Gr = 1E5

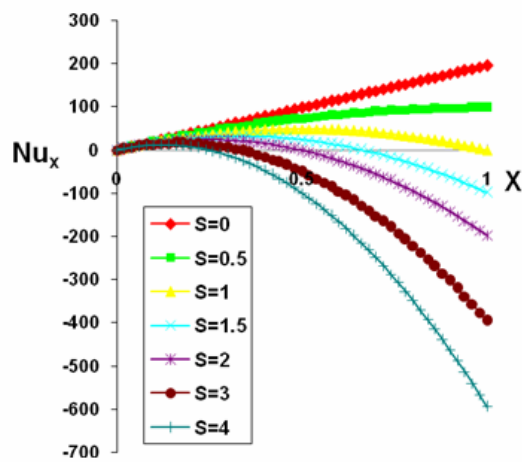
Figure 16. Local Nusselt number for S = 4 and Gr = 1E5

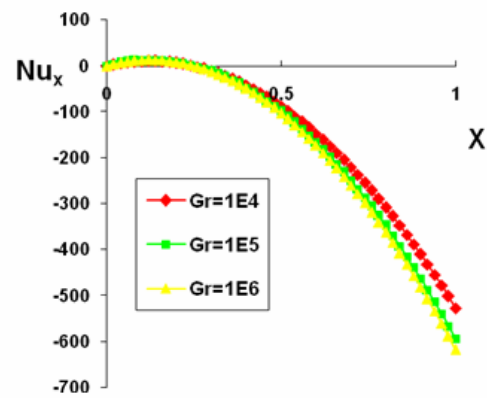**Figure 15.** Local Nusselt number for Pr = 6400 and Gr =1E5

Figure 17. Local Nusselt number for Pr = 6400 and S = 4

233

Prof. Dr. Ihsan Y. Hussain
Naseem K. Ali

Natural Convection Heat Transfer from a Plane Wall to
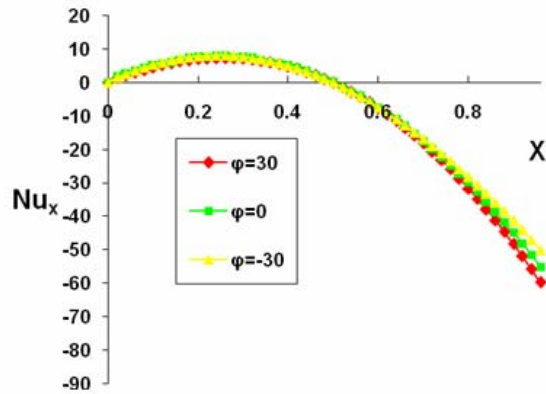Thermally Stratified Environment

Figure 18. Local Nusselt number for Pr = 6,
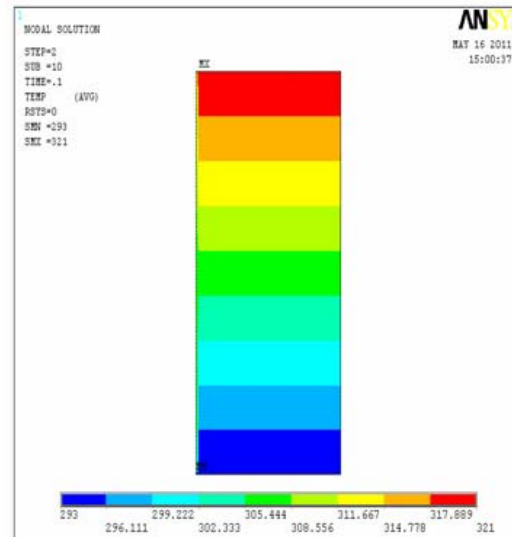S = 2 and Gr =1E5

Figure 20. Temperature distribution for
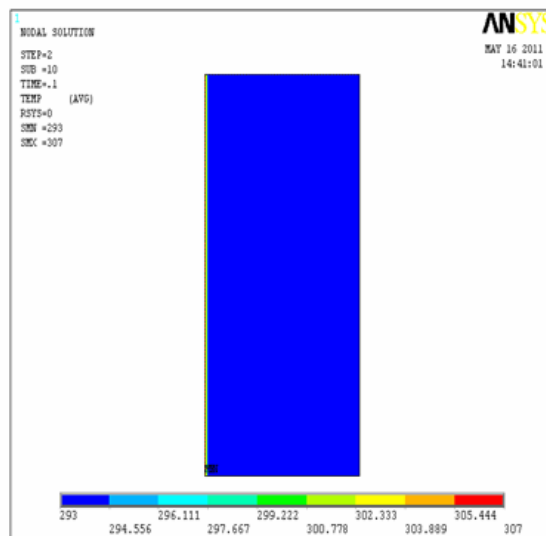Pr = 0.7 and S = 2

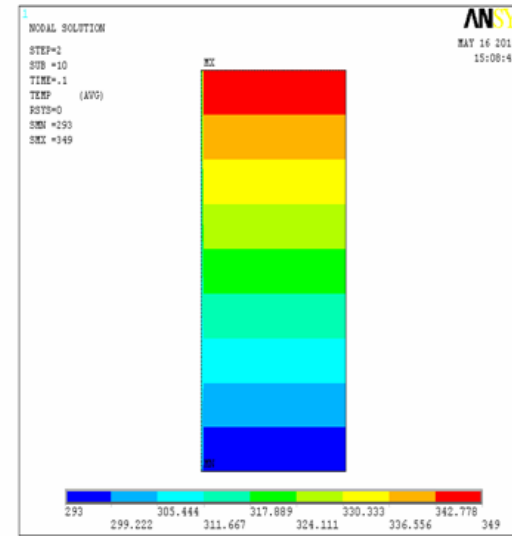**Figure 19.** Temperature distribution for Pr = 0.7
and S = 0

Figure 21. Temperature distribution for
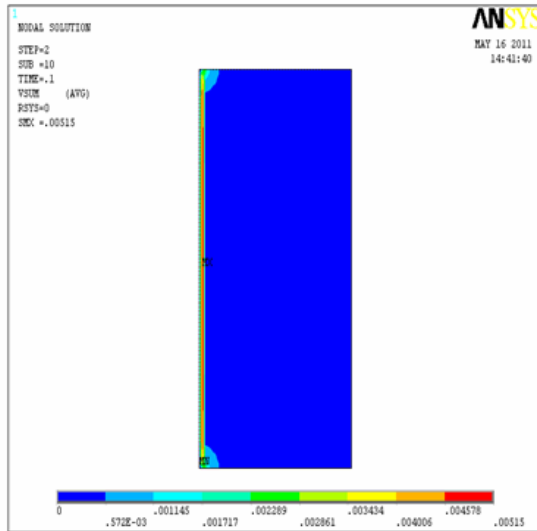Pr = 0.7 and S = 4

234

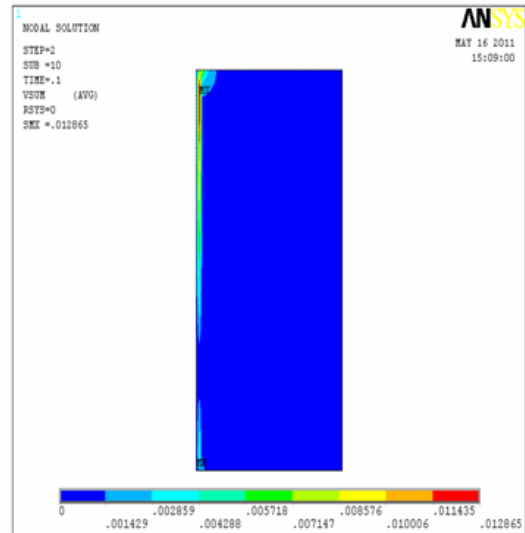**Figure 22.** Velocity distribution for Pr = 0.7 and S = 0

Figure 24. Velocity distribution for Pr = 0.7 and S = 4
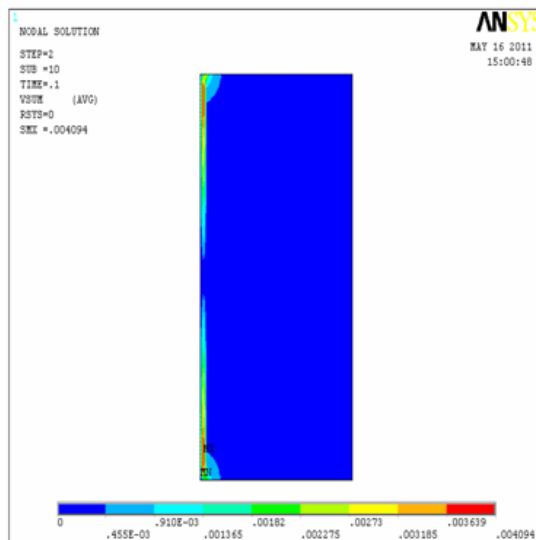
Figure 23. Velocity distribution for Pr = 0.7 and S = 2
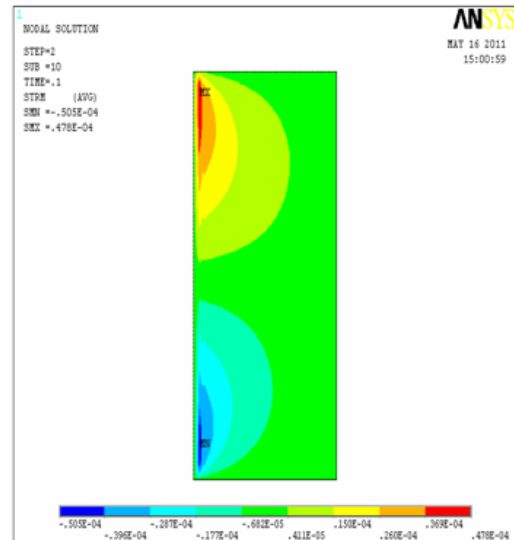
Figure 25. Stream function for Pr = 0.7 and S = 2

Prof. Dr. Ihsan Y. Hussain
Naseem K. Ali

Natural Convection Heat Transfer from a Plane Wall to
Thermally Stratified Environment
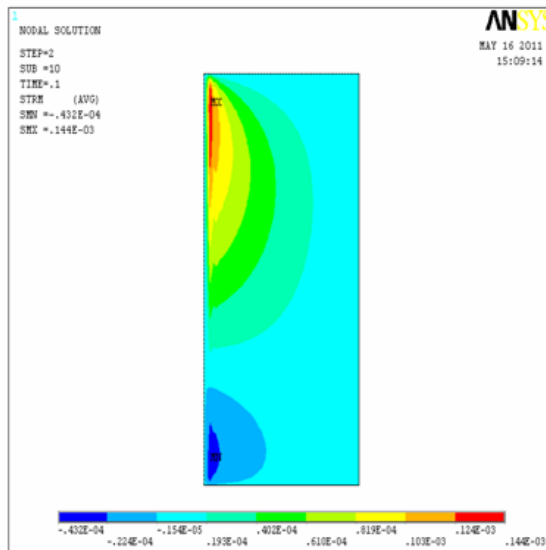
Figure 26. Stream function for Pr = 0.7 and
S = 4
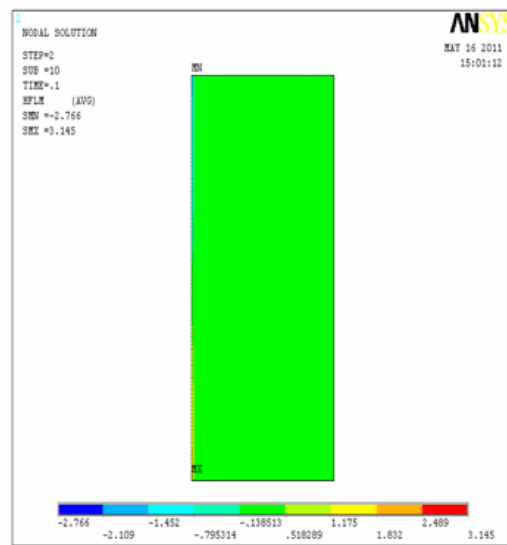
Figure 28. Heat transfer Coefficient for
Pr = 0.7 and S = 2
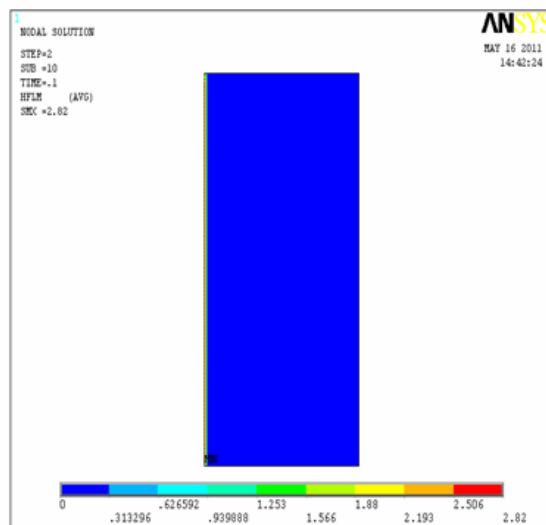
Figure 27. Heat transfer coefficient for Pr = 0.7
and S = 0
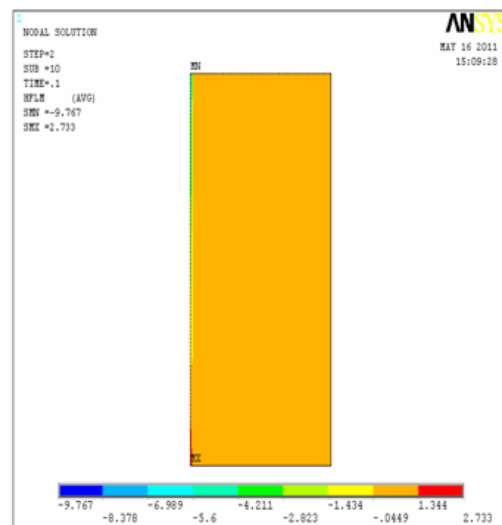
Figure 29. Heat transfer Coefficient for
Pr = 0.7 and S = 4
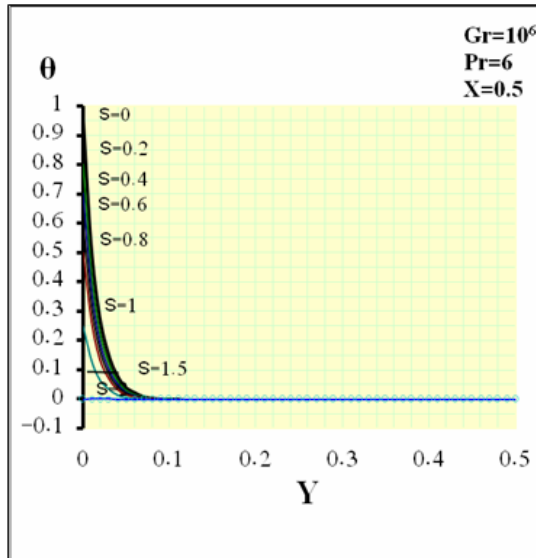
Figure 30. Temperature profile (Ahmed 2005)
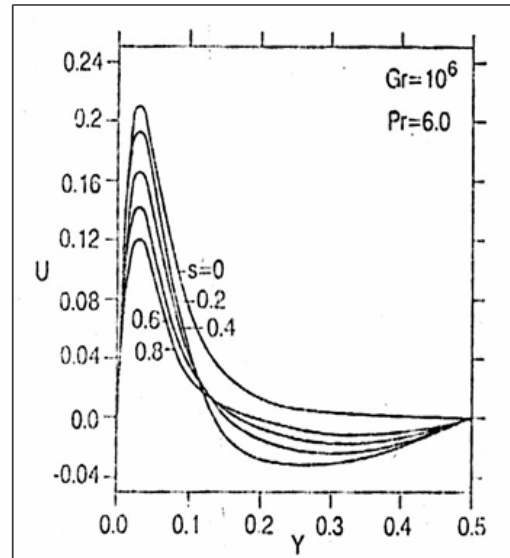
Figure 32. Velocity profile (Angirasa and Srinivasan 1992)
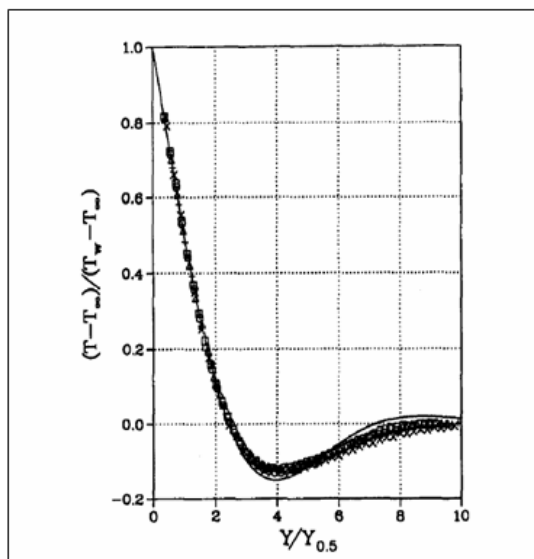
Figure 31. Temperature profile (Tanny and Cohen 1998)
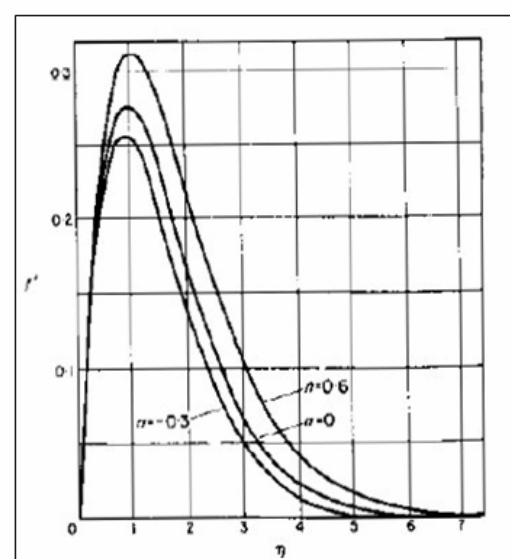
Figure 33. Velocity profile (Cheesewright 1967)

237

Prof. Dr. Ihsan Y. Hussain
Naseem K. Ali

Natural Convection Heat Transfer from a Plane Wall to
Thermally Stratified Environment
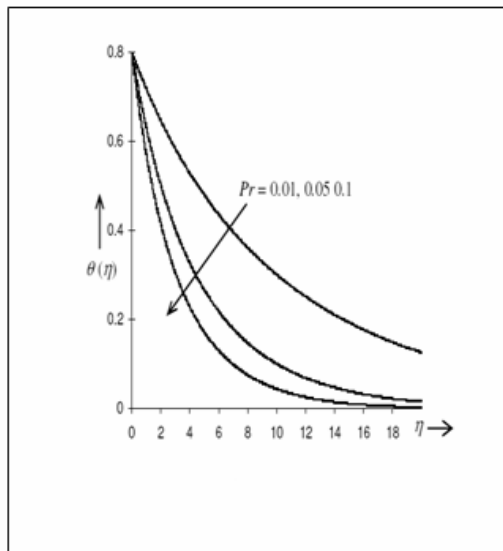
Figure 34. Effect Prandtl number (Singh et al 2010)
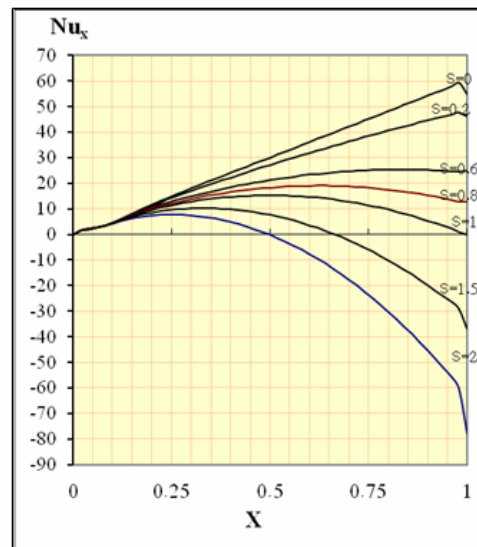
Figure 35. Nusselt number (Ahmed 2005)

System Identification Algorithm for Systems with Interval Coefficients

Mustaffa Mohammed Basil
M.SC. Control Engineering
Biomedical Engineering Department

Abstract

In this research a new system identification algorithm is presented for obtaining an optimal set of mathematical models for system with perturbed coefficients, then this algorithm is applied practically by an "On Line System Identification Circuit", based on real time speed response data of a permanent magnet DC motor. Such set of mathematical models represents the physical plant against all variation which may exist in its parameters, and forms a strong mathematical foundation for stability and performance analysis in control theory problems.

الخلاصة:

في هذا البحث تم تقديم طريقة جديدة لتعريف الأنظمة من أجل الحصول على المجموعة المثلى للنماذج الرياضية   للأنظمة التي تحتوي على معاملات غير ثابتة. تم تطبيق هذه الطريقة عمليا عن طريق منظومة لتعريف الأنظمة تعتمد على القراءات العملية للاستجابة الزمنية لسرعة المحرك التيار المستمر ذي المغناطيس الثابت. هذه المجموعة من النماذج الرياضية سوف تقوم بتمثيل الأنظمة الفيزياوية على الرغم من جميع التغييرات التي يمكن ان تحصل في معاملاتها العددية، و سوف تقوم بتكوين قاعدة رياضية قوية لمعالجة الأستقرارية و الأداء في منظومات السيطرة.

Keywords: system identification, interval coefficients, Sensitivity, uncertainty, transfer function.

1. Introduction:

In the controller design problem for any system, the basic goal is that the performance and stability characteristics meet certain specifications set by the designer; as a result this needs an accurate mathematical model for the system.

In the physical world, the process of obtaining accurate model is impossible, because input-output information and physical laws have never been complete. For example, ohm's law describes the relationship between current and voltage in the resistors, but it doesn't describe the effect of temperature, gravitational fields, or magnetic fields [1].

On the other hand all experimental data represent nonlinear functions between inputs and outputs, which in control analysis is not desirable because of the computational cost, so mostly these functions are linearized, and this linearization affect the accuracy of the model.

The general trend in the system identification theory is to model system with inaccuracy as a set of mathematical models, which represent all possible aspects of physical plants, so inaccuracy appears as sets of bounded range parameters. A system identification technique is presented in [2]; it is based on taking input-output data in frequency domain obtained from experimental test signals, and fitting these data to interval transfer function that contains complete frequency behavior with respect to frequency. In this paper alternative algorithm is presented to deal with input-output data obtained in time domain, this algorithm uses the sensitivity of functions to its parameters to estimate the range and weight of perturbation of each parameter.

2. Theory:

The problem of interval system identification can be formulated as follows: For any experimental set of data:

$D(t_i)$ for i = 1, 2, ..., N.

N: No. of data.

let $G_I(t)$ be the nominal function that represents these data, such that:

$$G_I(t) = a_1 f_1(t) + a_2 f_2(t) + ... + a_n f_n(t) \ (1)$$

n: number of parameters.

a_j : constant coeficients.

$f_j(t)$: function of time

for $j = 1, 2, ..., n.$

there is family of mathematical models:

$$\mathbf{G}(t) := \{G(t): \hat{a}_j \in [a_j - \omega_j \epsilon_j^-, a_j + \omega_j \epsilon_j^+]\}(2)$$

$$\bar{\omega} = [\omega_1 \quad \omega_2 \quad \omega_3 ... ... \omega_n]_{1 \times n}$$
$$\bar{\epsilon}^+ = [\epsilon_1^+ \quad \epsilon_2^+ \quad \epsilon_3^+ ... ... \epsilon_n^+]_{1 \times n}$$
$$\bar{\epsilon}^- = [\epsilon_1^- \quad \epsilon_2^- \quad \epsilon_3^- ... ... \epsilon_n^-]_{1 \times n}$$

ω_i : wight of perturbation.

ϵ_j^- : lower limit of perturbation.

ϵ_j^+ : upper limit of perturbation.

for $j = 1, 2, ..., n.$

That can represents all perturbation possibilities that occur for parameters. In any interval system identification, the basic requirements are [2]:

1. $\mathbf{G}(t)$ represents all experimental data.
2. $\|\bar{\epsilon}^+\|$ and $\|\bar{\epsilon}^-\|$ must be as small as possible.
3. $\bar{\omega}$ must be choosen so that the interval is tightly

   bounded around the parameter.

In this paper the procedure is divided into three parts. The first part include the identification of the nominal function $G_I(t)$, and this can be done by using Least Square Fit algorithm, then by using the sensitivity of function to parameters, the weight of perturbations for each parameter ω_i is calculated, finally the deflection of nominal function $G_I(t)$ from the experimental data is obtained as sets of bounded interval around parameters.

a) Nominal System Identification.
   For this task, the Least Square Fit algorithm is used, a brief description for this algorithm, that is the process of curve fitting for data set that contains a significant amount of noise and this can be done by minimizing the following function [3]:

$$S(a_1, a_2, ..., a_n) = \sum_{i=1}^{N} W_i^2 [D(t_i) - G_I(t_i)] \ (3)$$

where W_i is the weight of experimental data, optimal set of parametrs canbe obtained by solving the following equation:

$$\frac{\partial S}{\partial a_j} = 0 \quad j = 1,2,...,n \quad (4)$$

The above notation implies that we already have mathematical form of $G_I(t)$, usually from the theory related to experimental data, so the fitting process is exclusively for the parameters.

b) Weight Selection.

According to mathematical definition in (2), range of perturbation for each parameter is mainly dependant on $\bar{\omega}$, $\bar{\varepsilon}^-$ & $\bar{\varepsilon}^+$, so the problem of finding appropriate weight is considered in this part. Wight selection is extremely important for minimizing the family of models, by eliminating unnecessary members. Each parameter in the nominal function has its particular weight, which is defined as the average value of deflections which occur in nominal function at each time of experimental data, caused by small variation in that parameter.

First let define Δ_i, which represents the error between nominal function and experimental data.

$$\Delta_i = D(t_i) - G_I(t_i) \quad (5)$$
for $i = 1,2,...,N$.

Sensitivity of nominal function to particular parameter can be defined as:

$$S_{aj} = \frac{\partial G_I(t)}{\partial a_j} \quad (6)$$
for $j = 1,2,...,n$.

Now the participation of each parameter in the error between the nominal function and experimental data can be calculated from:

$$\Delta_{aij} = \Delta_i * \hat{S}_{aj} \quad (7)$$

$$\hat{S}_{aj} = \frac{S_{aj}}{\sum_{j=1}^{n} S_{aj}}$$

for $j = 1,2,...,n$.
for $i = 1,2,...,N$.

Δ_{aij}: Deflection in nominal function caused by variation in parameter (j) at each experimental data (i).

This relationship can be proved by the following simple argument:

Assume n dimensions space, where $G_I(t)$ of n parameters. The change in $G_I(t)$ can be approximated in term of the change in the n planes as follows:

$$\Delta = \sum_{j=1}^{n} \Delta_{aj} \quad (8)$$

Δ: change in $G_I(t)$.
Δ_{aj}: change in the jth plane.

lets assume that eq. (7) is valid and substitute it in eq. (8).

$$\Delta = \sum_{j=1}^{n} \Delta * \frac{S_{aj}}{\sum_{j=1}^{n} S_{aj}} \quad (9)$$

multiply both sides by $\left(\sum_{j=1}^{n} S_{aj}\right)$

$$\Delta * \sum_{j=1}^{n} S_{aj} = \Delta * \sum_{j=1}^{n} S_{aj}$$

since both sides are equal then eq. (7) is valid.

For mathematical simplicity, matrix notation will be used in calculation of weights, so first we construct $\hat{S}_a$ and $\bar{\Delta}$ which is respectively:

$$\hat{S}_a = \begin{bmatrix} S_{a11} & \cdots & S_{a1n} \\ \vdots & \ddots & \vdots \\ S_{aN1} & \cdots & S_{aNn} \end{bmatrix}_{N \times n}$$

$$\bar{\Delta} = \begin{bmatrix} \Delta_1 & \Delta_2 & \cdots & \Delta_{N-1} & \Delta_N \end{bmatrix}_{1 \times N}$$

The perturbation in nominal function which is defined as:

$$\hat{\Delta}_a = \begin{bmatrix} \hat{\Delta}_{a1} & \hat{\Delta}_{a2} & \hat{\Delta}_{a3} & \cdots & \cdots & \hat{\Delta}_{an} \end{bmatrix}_{1 \times n}$$

can be calculated as follows:
$$\hat{\Delta}_a = \bar{\Delta} * \hat{S}_a \quad (10)$$

Finally the weight of perturbation is:

$$\bar{\omega} = \frac{1}{N} * \hat{\Delta}_a \quad (11)$$

$$= [\omega_1 \quad \omega_2 \quad \omega_3 \dots \dots \omega_n]_{1 \times n}$$

c) Parameter Interval Identification.
In this part the range of parameter perturbation is calculated, and this can be done by solving the following equation for the variable ϵ_j at each time of experimental data:

$$D(t_i) = (a_1 + \omega_1 \epsilon_1) f_1(t_i) + (a_2 + \omega_2 \epsilon_2) f_2(t_i) + \dots + (a_n + \omega_n \epsilon_n) f_n(t_i) \quad (12)$$

The solution of above n variable can be estimated according to the following:

Lets define the ℓth range of perturbation in $\bar{\epsilon}$:

$$\bar{\epsilon} = \begin{cases} 0, & j \neq \ell \\ \hat{\epsilon}_\ell, & j = \ell \end{cases} \quad (13)$$

by substituting eq. (13)in(12),
this yields the following equation:

$$D(t_i) = a_1 f_1(t_i) + \dots + a_{\ell-1} f_{\ell-1}(t_i) + (a_\ell + \omega_\ell \hat{\epsilon}_\ell) f_\ell + a_{\ell+1} f_{\ell+1} + \dots + a_n f_n(t_i) (14)$$

Solving eq. (14) yields $\hat{\epsilon}_\ell$, which represents the maximum deflection in j^{th} parameter caused by the difference between experimental data and nominal function.

The actual value of deflection can be calculated by using the following equation:

$$\epsilon_\ell = \hat{\epsilon}_\ell * \frac{S_{a\ell}}{\sum_{j=1}^{n} S_{aj}} \quad (15)$$

This equation can be proved according to the following argument:
Consider the following triangle:
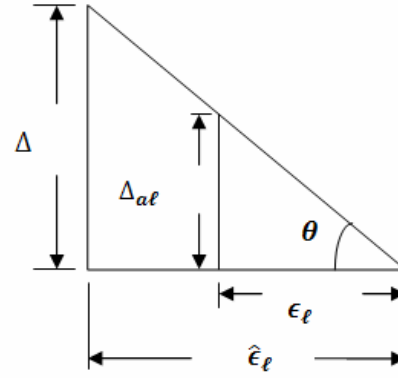
Fig. (1)

This triangle without losing generality represents the relationship between deflection in function and deflection in ℓ^{th} parameter, where:

$$\theta = \tan^{-1} S_{a\ell} \quad (16)$$

According to the triangle similarity:

$$\frac{\epsilon_\ell}{\hat{\epsilon}_\ell} = \frac{\Delta_{a\ell}}{\Delta} \quad (17)$$

and according to eq. (7):

$$\frac{\Delta_{a\ell}}{\Delta} = \frac{S_{a\ell}}{\sum_{j=1}^{n} S_{aj}} \quad (18)$$

By substituting eq. (17) in (18), it yields:

$$\epsilon_\ell = \hat{\epsilon}_\ell * \frac{S_{a\ell}}{\sum_{j=1}^{n} S_{aj}}$$

Now, for $(\ell = 1,2,\dots,n)$, we will have :

$$\bar{\epsilon} = [\epsilon_1 \quad \epsilon_2 \quad \epsilon_3 \dots \dots \epsilon_n]_{1 \times n}$$

for upper and lower range of perturbation
for parameters respectively

$$\epsilon_j^+ = \max_i \{0, \epsilon_i\}$$

$$\epsilon_j^- = \min_i \{0, \epsilon_i\}$$

3. Practical Application of Interval System Identification for DC motor

3.1. Mathematical Model of DC Motor [4,5,6]

242

The model of the motor shown in **Fig**. [2] based on the ideal permanent magnet DC-motor

Fig. [2], Permanent Magnet DC Motor

From **Fig** [2], J is the inertia of the rotor, B is the damping coefficient, ω_m is the motor speed (rpm), and $Em \,\&\, Im$ is the supply voltages and current respectively.

Now the torque generated by the motor T_m is:

$$T_m = K\,I_m \quad (19)$$

also

$$E_m = R_o \quad (20)$$

from Newton second law of motion

$$J\frac{d\omega_m}{dt} + B\,\omega_m = T_m \quad (21)$$
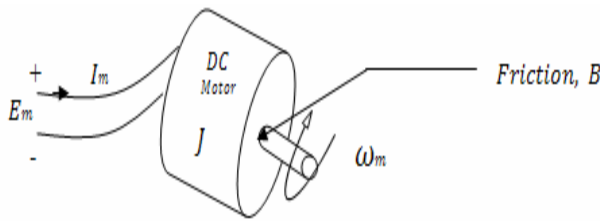
substitute eq. s (19) & (20) *into eq.* (21)

$$J\frac{d\omega_m}{dt} + B\,\omega_m = \frac{K\,E_m}{R_o} \quad (22)$$

by taking Laplace Transformation for eq. (22):

$$\frac{\omega_m(s)}{E_m(s)} = \frac{\dfrac{K}{R_o J}}{S + \dfrac{B}{J}} \quad (23)$$

Eq. (23) represents the transfer function for DC motor. By assuming that:

$$G(s) = \frac{\omega_m(s)}{E_m(s)}$$

and taking $\mathcal{L}^{-1}$ for both sides of eq(23) :

$$G(t) = a_1\,e^{-a_2 t} \quad (24)$$
$$a_1 = K/R_o J$$
$$a_2 = B/J$$

According to eq. (24), in order to find the response of motor speed as a function of time, there are some parameters needed to be found first, like K (motor constant), $B, J,\ \text{and}\ R_o$(motor's coil resistance), so motor static gain and time constant must be calculated, but this may be possible if the response of the motor speed can be found practically.

3.2. On Line System Identification Circuit
On Line System Identification Circuit is specially designed in this paper to collect data about DC motor speed response from initial condition till steady state, passing through transient state, this circuit is illustrated in the block diagram in **Fig**. [2].
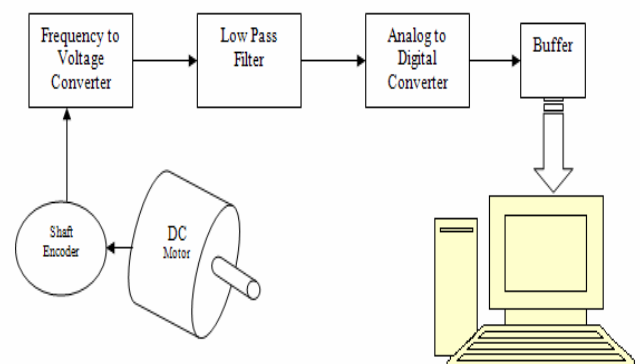

Fig. [3], On Line System Identification Circuit for DC Motor

According to the above block diagram, by using shaft encoder angular velocity first is converted to train of pulses, whose frequency is proportional directly to the angular velocity of motor; this train

of pulses then is converted to analogue voltage using Frequency to Voltage Converter Circuit, which implements LM331. The output voltage then is filtered by low pass filter, and converted to binary equivalent number by using ADC0804. The equivalent binary number is fed to the computer through parallel port LPT1 by a tri-state buffer 74LS245. As we can see from above description the process of reading velocities of DC motor by computer consists of successive sub processes, the synchronization and enabling of these sub processes is done by C++ program in that computer, after reading the data, the same program directly starts processing the algorithm presented in this paper and display the final result, which is the mathematical model of the motor plus the range and weight of perturbations of its parameters.

4. Results

For Hitachi permanent magnet DC motor (type D04A321E), the following results is obtained according to the three algorithm steps:

A) Nominal System Identification.

By using the Least Square Fit procedure, the transfer function can be obtained, and this transfer function can be verified by calculating it with an alternative way, since the static gain defined as the steady-state speed value relative to the supplied voltage value, and the time constant is the time by which the output of the system will reach 63% of its final value, then these two values can be found by matching the diagram in **Fig**.[4] to the practical response of system in **Fig**. [5], and the both approaches should have the same results which are:

$$G(S) = \frac{138.508386}{(S + 23.079689)}$$

$$a_1 = 138.508386$$

$$a_2 = 23.079689$$
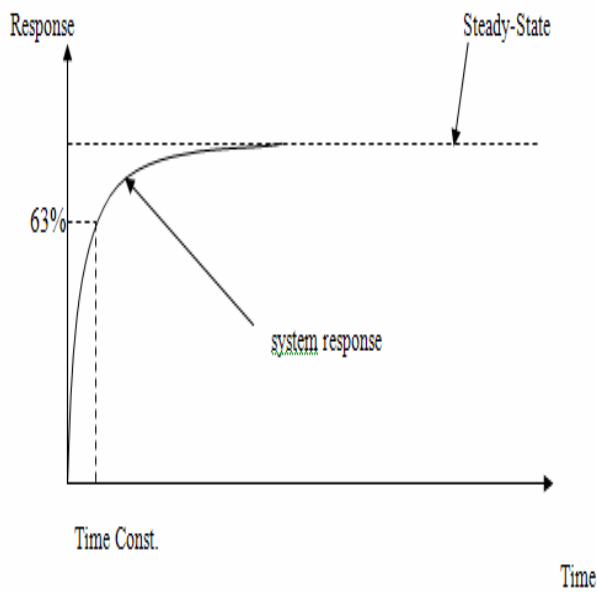
Fig. [4], Response of First Order System

$$\bar{\omega} = [\; \omega_{a1} \qquad\qquad \omega_{a2}]$$

$$= [0.115734 \quad 0.710374]$$

C) Parameter Interval Identification.
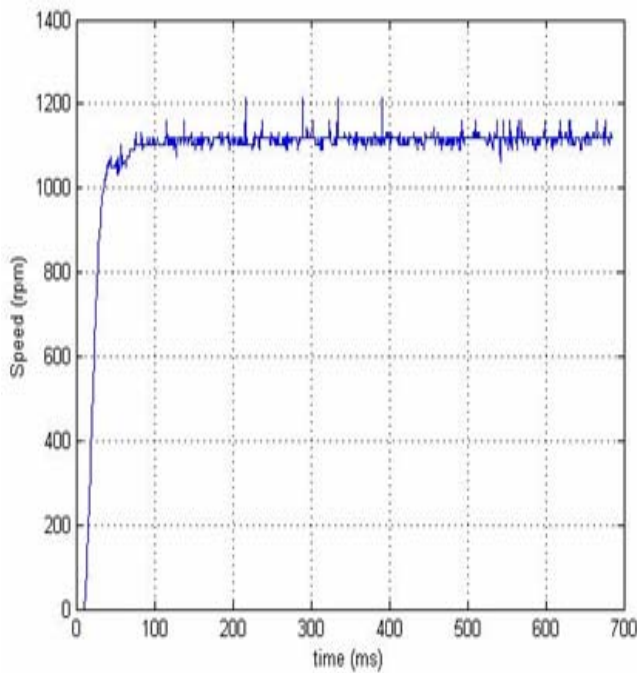
Fig [5], Practical Response for the DC Motor.

$$\bar{\epsilon}^{+} = [\; \epsilon_{a1}{}^{+} \qquad\qquad \epsilon_{a2}{}^{+}]$$

$$= [11.305207 \quad 1.777578]$$

$$\bar{\epsilon}^{-} = [\; \epsilon_{a1}{}^{-} \qquad\qquad \epsilon_{a2}{}^{-}]$$

$$= [17.177452 \quad 3.033393]$$

B) Weight Selection.

The flowchart for the program that was used to obtain the above result is shown in **Fig.** (6).

5. Conclusions

MagnetSynchronous Motor Drive System", University Of Puerto Rico Mayagüez Campus 2006.

1. The nominal function for the DC motor was derived using Least Square Fit method, which is an optimization technique, so the ranges of perturbation for parameters represent deviation between nominal function and experimental data, which are mainly caused by this optimization technique.

2. The assumption of linearity is also an important reason in forming the perturbation ranges.

3. The experiment for the DC motor speed response was carried without load, in case loaded motor a new ranges of perturbation will result, according to the amount of load.

According to above, all unexpected condition or incorrect assumption in practical field can be interpreted in term of ranges of perturbation, which will result a family of models. Members in the resulted family don't have the same stability and performance conditions, so this variety in characteristics must be taken in consideration.

References:

[1] R.S. Sanchez, "*Robust System Theory and Application*", John Wiley & sons (1998).

[2] S.P. Bhattacharyya, H. Chapellat, and L.H. Keel," *Robust Control Parametric Approach*", Prentice Hall (1995).

[3] J. Kivsalaas, "Numerical Method in Engineering", Cambridge University Press,(2010).

[4] Robert L. Woods and Kent L. Lawrence, "*Modeling and Simulation of Dynamic Systems*", Prentice Hall, (1997).

[5] T. J. E. Miller, *Fellow, IEEE*, Mircea Popescu, Calum Cossar, and Malcolm McGilp" *Performance Estimation of Interior Permanent-Magnet Brushless Motors Using the Voltage-Driven Flux-MMF Diagram"* IEEE Transactions On Magnetics, VOL. 42, NO. 7, JULY 2006.

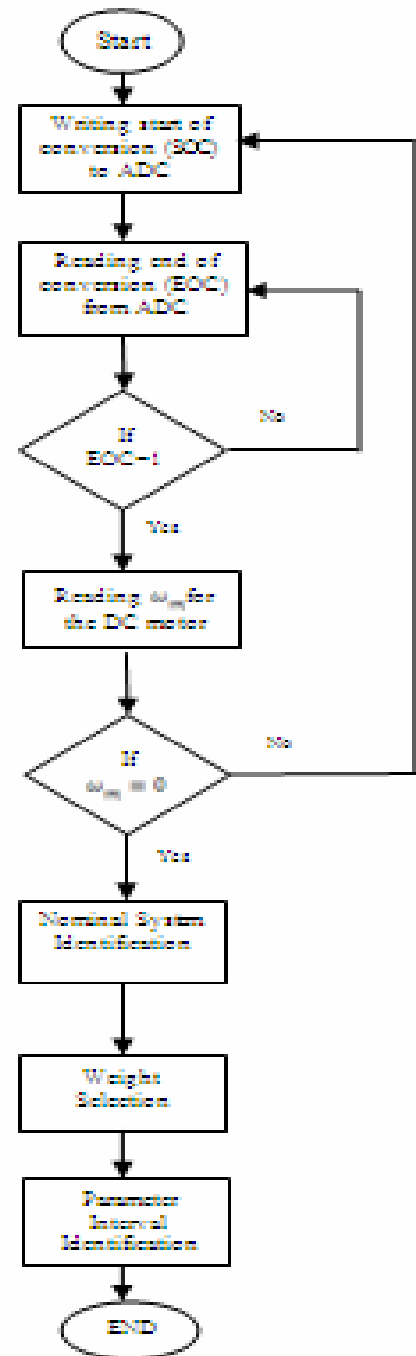[6] Enrique L. Carrillo Arroyo "*Modeling and Simulation of Permanent*

Fig. (6) Flowchart of the C++program.

Experimental Study For a Laminar Natural Convection Heat Transfer From an Isothermal Heated Square Plate With and Without Circular Hole

Asst. Prof. Dr. Ikhlase M. Fayed* & Asst. Lec. Wassan N. Matti**

ABSTRACT

An experimental investigation of natural convection heat transfer from an isothermal horizontal, vertical and inclined heated square flat plates with and without circular hole, were carried out in two cases, perforated plates without an impermeable adiabatic hole "open core" and perforated plates with an impermeable adiabatic hole "closed core" by adiabatic plug. The experiments covered the laminar region with a range of Rayleih number of $(1.11x10^6 \leq Ra_{Lo} \leq 4.39x10^6)$, at Prandtle number (Pr=0.7). Practical experiments have been done with variable inclination angles from horizon ($\Phi=0^o, 45^o, 90^o, 135^o$ and 180°), facing upward ($0^o \leq \Phi < 90^o$), and downward ($90^o \leq \Phi < 180^o$). The results showed that the temperature gradient increases while the thermal boundary layer thickness decreases when Grashof number and perforation ratio (m) increase . The temperature gradient for inclined position facing upward is less than facing downward, while the thermal boundary layer thickness is greater. The temperature gradient decreases while the thermal boundary layer thickness increases for perforated plates with an adiabatic core as compared with perforated plates without an adiabatic core. The value of average Nusselt number increases with increasing perforation ratio, and Grashof number for all specimens with and without an adiabatic core, also increases by increase in inclination of plates approaching the higher value at vertical position ($\Phi=90^o$), then decreases with increasing inclination of plates till horizontal position ($\Phi=180^o$). The average Nusselt number values for perforated plates with an adiabatic core are lower than for perforated plates without an adiabatic core for all perforation ratios. Maximum heat transfer rate occurs at perforated plate with perforation ratio of (m=0.1) without adiabatic core for vertical position ($\Phi=90^o$), at a range of Grashof number $(1.576x10^6 \leq Gr_{Lo} \leq 6.292x10^6)$, while the rate of heat transfer decreases with increasing perforation ratio for plates with and without adiabatic core for decrease in heat transfer rate area. The rate of heat transfer for perforated plates with circular hole is more than for perforated plates with square hole at the same perforation ratios (m=0.1,0.16,0.24 and 0.36). It found that the lack of core flow decreases the overall heat transfer rate by (6.477%) . There was a good agreement for the experimental present work results compared with other pervious results .

الخلاصة

يقدم البحث الحالي دراسة عملية لانتقال الحرارة بالحمل الحر من صفائح مربعة افقية وعمودية ومائلة عن الافق وذات ثقب دائري مسخنة بثبوت درجة الحرارة، لحالتي النماذج المثقبة بوجود سداد للثقب الدائري وعدم وجوده، ضمن منطقة الجريان الطباقي لرقم رالي ($1.11x10^6 \leq Ra_{Lo} \leq 4.39x10^6$)، عند رقم برانتدل Pr=0.7. اجريت التجارب العملية لمدى من زوايا الميل عن الافق ($\Phi=0^o, 45^o, 90^o, 135^o$&$180^o$) لوجه التسخين للأعلى وللأسفل. اظهرت النتائج ان انحدار درجات الحرارة يزداد فيما يقل سمك الطبقة المتاخمة الحرارية (δ) عند زيادة رقم كراشوف ونسبة التثقيب، فيكون انحدار درجات الحرارة للوضع المائل في حالة التسخين باتجاه الاعلى اقل من حالة التسخين باتجاه الاسفل بينما سمك الطبقة المتاخمة الحرارية اكبر ، كما ان انحدار درجات الحرارة يقل بينما يزداد سمك الطبقة المتاخمة الحرارية للصفائح المثقبة بوجود السداد عن عدم وجوده . تزداد قيمة متوسط رقم نسلت بزيادة رقم كراشوف وبنسبة التثقيب (m) بوجود وعدم وجود السداد، وتزداد قيمة متوسط رقم نسلت مع ازدياد الميلان في حالة التسخين الى الاعلى الى ان تصل اعظم قيمة لها عند الوضع العمودي ($\Phi=90^o$) ثم تقل بزيادة زاوية الميلان في حالة التسخين الى الاسفل وصولا الى الوضع الافقي ($\Phi=180^o$). لجميع نسب التثقيب تكون قيم متوسط رقم نسلت اقل للصفائح المثقبة بوجود السداد عن الصفائح المثقبة بدون وجود السداد. اقصى قيمة لكمية الحرارة المنتقلة تكون للصفيحة المثقبة بنسبة التثقيب (m=0.1) بدون وجود السداد في حالة الوضع العمودي ($\Phi=90^o$) لمدى رقم كراشوف ($1.57x10^6 \leq Gr_{Lo} \leq 6.292x10^6$)، وتقل كمية الحرارة المنتقلة بزيادة نسبة التثقيب بسبب النقصان الحاصل في مساحة سطح التبادل الحراري الذي يؤدي الى الانخفاض في معدل انتقال الحرارة للصفائح المثقبة بوجود وعدم وجود السداد .إن كمية الحرارة المنتقلة للصفائح المثقبة بثقب دائري اكبر من كمية الحرارة المنتقلة للصفائح المثقبة بثقب مربع لنفس نسب التثقيب (m=0.1,0.16,0.24,0.36). وكانت كمية الحرارة اللابعدية (Q) للنماذج المثقبة بوجود السداد للثقب تقل عن كمية الحرارة اللابعدية (Q) بدون وجوده بنسبة (6.477%). هناك توافق جيد للنتائج العملية للبحث الحالي مع نتائج بحوث سابقة .

Key Words: **Natural Convection, Square Plate With and Without Circular Hole, Facing Upward and Downward.**

*Dept. of Mech. Eng., University of Technology, Baghdad-Iraq.

Asst. Prof. Dr. Ikhlase M. Fayed
Asst. Lec. Wassan N. Matti

Experimental Study For a Laminar Natural Convection Heat Transfer
From an Isothermal Heated Square Plate With and Without Circular
Hole

INTRODUCTION

Decades ago have witnessed a great interest for the process of convection heat transfer from finite bodies such as (square surface) because of its wide spread application in many engineering and industrial applications, which include the heat flow from streaming radiant, cooling small electronic devices that have low power, air conditioning, warming systems in rooms, building walls, the natural convection enters in nuclear power applications for cooling objects surfaces that diffusion heat is generated in. It is also used in heat transfer resulting from chemical reactions, and in the environment, libratory devices, cooking, also natural convection can be found in engineering system such as heat exchange fin surfaces applications, electronic parts that have different shapes, electrical natural convection furnaces, heaters devices, and some load cell.

Natural Convection heat transfer from isothermal plates continues to be a topic of current research, and also a number of experimental and theoretical studies **[AL-Arabi & EL-Riedy (1976), Mustafa (2001), Aziz (2002), Robinson & Liburdy (1987) ,Pera &Gebhart (1973), Sahraoui et al. (1990)]** have been made in past to determine the natural convection heat transfer from heated isothermal plates hold in horizontal position, the convective flow situation is two dimensional and thus easier to study experimentally and theoretically. Two earliest studies **[Abd (2007)]** has been done theoretical study for a three-dimensional natural convection heat transfer from an isothermal horizontal , vertical and inclined heated square flat plates (with and without circle hole) which involved the numerical solution of the transient Navier-Stokes and energy equations by using Finite Different Method (F.D.M.), & **[Ali (2007)]** has been done experimental study for isothermal square flat plate (with and without square hole) with extension surface. The experiments covered the laminar region with a range of Rayleigh number of order of 10^6, and included the manufacturing of four square models of aluminum (10cm) length, (1cm)

thickness and perforation ratio (m=0.0,0.04,0.16&0.36) respectively with heater for each model for inclined position for square plate of constant temperature. Table (1) shows the results of previous studies.

The present experimental investigation aims to study the natural convection heat transfer from isothermal heated square plate, with and without circular hole, for different perforation ratio in two cases, perforator plates with and without adiabatic circular hole, and the effect of different inclination angle from horizon ($\Phi=0^o$, 45°, 90°, 135° and 180°), facing upward and downward, different ranges of Grashof number ($1.576\times10^6 \leq Gr \leq 6.292\times10^6$), then analysis the results to develop mathematical relationships that rely on the accounts (arithmetic) of natural convection taking into consideration the effect of inclination angles (Φ), perforation ratio (m) and heating levels.

EXPERIMENTAL APPARATUS

Manufacturing four specimens used as a heat exchange surfaces are made of aluminum sheets, having square shape with length and thickness (100mm and 10mm) respectively. A basic dimensions of the specimens are given in Table (2). The first specimen is a square shape, but the other specimens are perforated with circular hole at different perforated area (m=0.0,0.1,0.24 and 0.5) as shown in Figure (1). In order to measure the surface temperature homogeneity of the specimen, a copper-constantan type (T) thermocouples, embedded from the heated surface. The four specimens were drilled with a number of holes with diameter (2mm) and depth (9mm) from the bottom. The holes were distributed radialy with a pitch angle of 45° and radii (36, 40 and 45mm) for the specimens designated as 2-nd, 3-rd, and 4-th respectively. To heat up the heat exchange surfaces (specimens), an electric heaters are manufactured from nickrom (nickel-chromium alloy). In order to study the natural heat transfer for inclination angles from horizon ranging from (0° to 180°), the wooden extending surface which contains the heat exchange surfaces (specimens) have been installed on the apparatus bracket. It can be moved by moving

joints fitted between the extending surface and apparatus bracket, with the inclination angle could be controlled through the manual metal protractor, as shown in Figure (2).

A uniform temperature on the surface of the model was achieved by adjusting the electrical input power to the heating element . The specimen and heating element assembly were installed for the purpose of conducting the study with its own heater together with the wooden extending surface to ensure parallel flow at the specimen edges. The surface heat exchange (specimen) was isolated together with the heater from all sides, except the upper surface to reduce thermal losses. To minimize side effects of air currents room temperature in the process of natural heat transfer from heat exchange surfaces, the apparatus was placed in a room with dimensions (4m x 2m x 3m). In order to study the heat transfer by natural convection from the surface of a specimen, the surface air temperatures were measured by a thermocouple, which was installed in a holder with shape (⌐), to move the holder on the specimen surface in three dimensions (x, y, z), it is connected with three dimensional mechanisms. The steady state at heat exchange surface temperature is commonly reached within (4 to 5) hours. The voltage and current were recorded when reaching steady state, in order to calculate the power supplied. The temperatures over the heat exchange surface were recorded and for a small equal specified distances to the Z-axis perpendicular to each point of the measurement grid by the specified thermocouple sensing till reaching the space or ambient temperature in order to calculate the thermal boundary layer thickness (δ) until the difference between measured temperature and the ambient temperature was approximately (θ=0.02). The temperature distribution was measure at different ranges of Rayleigh number as shown in Table (3).

To calculate the local heat transfer coefficient by natural convection, a thermal balance was done as follows:

$$-k_f \frac{dT}{dz}\bigg|_{z=0} = h(T_w - T_\infty) \tag{1}$$

Rearranging equation (1), the local heat transfer coefficient on the heat exchange surface is obtained as follows:

$$h = \frac{-k_f \frac{dT}{dz}\bigg|_{z=0}}{(T_w - T_\infty)} \tag{2}$$

By integrating equation (2) along the plate area, the average heat transfer coefficient has been calculated as follows:

$$\bar{h} = \frac{1}{A} \int_A h\, .dA \tag{3}$$

The Local Nusselt number has been calculated from the following equation:

$$Nu_{L_o} = \frac{h.L_o}{k_f} \tag{4}$$

Substituting equation (2) into equation (4) yields:

$$Nu_{L_o} = \frac{-L_o \frac{dT}{dz}\bigg|_{z=o}}{(T_w - T_\infty)} \tag{5}$$

$$Z = \frac{z}{L_o} \tag{6}$$

$$\theta = \frac{T - T_\infty}{T_w - T_\infty} \tag{7}$$

$$Nu_{L_o} = -\frac{d\theta}{dZ}\bigg|_{z=o} \tag{8}$$

So the average Nusselt number can be calculated by integrating local Nusselt number over the heat exchange surface as follows:

$$\overline{Nu}_{L_o} = \frac{1}{A} \int_0^{L_o} \int_0^{L_o} \frac{d\theta}{dZ}\bigg|_{Z=0} .dx\,.dy \tag{9}$$

The thermal energy transferred by radiation can be calculated from the following equation:

$$Q_{Radiation} = F * \sigma * \varepsilon * A * (T_w^4 - T_a^4) \tag{10}$$

RESULT AND DISCUSSION

Temperature Distribution :- Figures (3) and (4-a-b) show the dimensionless

Asst. Prof. Dr. Ikhlase M. Fayed
Asst. Lec. Wassan N. Matti

Experimental Study For a Laminar Natural Convection Heat Transfer From an Isothermal Heated Square Plate With and Without Circular Hole

temperatures distribution at symmetry axes (X-axis and Y-axis), at the planes (Z-X and Z-Y), above the surface of square plate and circular perforated surface specimens with and without plug for inclination with horizontal ($\Phi=0^o, 45^o, 90^o, 135^o$, and 180°), for ($Gr_{Lo}=1.576 \times 10^6$, 3.546×10^6, 5.083×10^6, and 6.292×10^6). Temperature gradient in the upward heating state is lower than the case of downward heating. The adiabatic plug prevents the additional flow, that results decrease in the temperature gradient leads to decrease the quantity of the heat transferred. Generally for all inclination angles (Φ), increasing heating level, (increasing Grashof number (Gr_{Lo})) and perforation ratio (m) leads to increase the temperature gradient for the specimens.

Thermal Boundary Layer Thickness (δ):-
Figures (5) and (6-a-b) depict change of thermal boundary layer thickness above the surface of square plate and circular perforated surface specimens with and without plug above surface specimens in the (Z-Y) plane, for inclination angles from horizon ($\Phi=0^o, 45^o, 90^o, 135^o$, and 180°), at heating levels ($1.576 \times 10^6 \leq Gr_{Lo} \leq 6.292 \times 10^6$). In general, thickness of thermal boundary layer decreases with increasing (Gr_{Lo}), and perforation ratio (m) for all inclination angles. It is observed that the maximum thickness of thermal boundary layer is at the center and falls gradually toward the edges. This is attributed to the fluid molecules density which is greater above the edges compared with density of fluid molecules density above the center, which possesses the maximum temperature at the surface. This leads to raise the lower density hot molecules above the center at higher speed causing pressure rarefaction, then the adjacent molecules of higher density move from the outer edges in a horizontal moving to replace them. The flow at the edges is parallel to the surface and accelerates toward the center near to it, at which the fluid moves upwards in the shape of a plume, called thermal separation region at center, thermal separation occurs at center and the quantity of heat transfer is minimum, while it is maximum at the edges. The fluid rise near the specimen center results for making thermal boundary layer it is

maximum at the center in the horizontal position of specimen ($\Phi=0^o$), it is seen that the boundary layer thickness increases as compared with perforated specimens without plug, while the rate of heat transfer is reduced as a result of reduction of temperature gradient over perforated specimens surface in presence of plug (with no additional flow). In general thickness of thermal boundary layer decreases when (Gr_{Lo}) and perforation ratio increase for all inclination angles with the horizontal ($\Phi=0^o, 45^o, 90^o, 135^o$, and 180°), at four surface heating levels ($1.576 \times 10^6 \leq Gr_{Lo} \leq 6.292 \times 10^6$).

Effect Of Inclination Angle On The Average Nusselt Number:-
Figure (7-a-b) show the effect of inclination angle on the ($\overline{Nu}_{Lo}$) for the square specimen and circular perforated specimen with and without plug for inclination angles with the horizontal ($\Phi=0^o, 45^o, 90^o, 135^o$, and 180°) and for four surface heating levels ($1.576 \times 10^6 \leq Gr_{Lo} \leq 6.292 \times 10^6$). It is observed that, increases of the ($\overline{Nu}_{Lo}$) in the case of heating upward with increasing inclination angle from ($\Phi=0^o$) reaching the vertical position of specimens ($\Phi=90^o$), where is the maximum value of the ($\overline{Nu}_{Lo}$). With increasing inclination angle of downward heating reaching the horizontal position ($\Phi=180^o$) the value of the ($\overline{Nu}_{Lo}$) is gradual decrease. Also, there is an increase in values of ($\overline{Nu}_{Lo}$) with increasing (Gr_{Lo}) and perforation ratio, while decreasing values of ($\overline{Nu}_{Lo}$) for perforated specimens with plug compared to those without plug due to lower temperature gradient above the perforated specimens with plug.

Effect Of Perforation Ratio On The Average Nusselt Number:-
Figure (8-a-b) display the effect of perforation ratio on ($\overline{Nu}_{Lo}$) for the square specimen and circular perforated specimens with and without plug for inclination angles with the horizontal ($\Phi=0^o, 45^o, 90^o, 135^o$, and 180°), at surface heating levels ($1.576 \times 10^6 \leq Gr_{Lo} \leq 6.292 \times 10^6$). It is noticed an increases in the value of ($\overline{Nu}_{Lo}$) with increasing perforation ratio, but the increase for circular perforated specimens

without plug is greater than for perforated specimens with plug, because with hole the thermal separation region can be removed, which is formed at the centre of square specimen and gets nearer to the flow of boundary layer at the specimen outer edges, which increases ($\overline{Nu}_{Lo}$).

Mathematical Correlation Between The Average Nusselt Number And Rayleigh Number:-

Figure (9-a-b) for the square plate and circular perforated specimens with and without plug show a relationship, for upward and downward heating situation according to the following equation :

$$\overline{Nu}_{L_o} = C_1 (Ra.\sin\Phi)^{0.25}$$

………………………………………..…(11)

It is also observed the values of the constant (C_1) for perforated specimens without plug is more than for the perforated specimens with plug.

Figures (10) and (11) show the effect of perforation ratio in correlation between ($\overline{Nu}_{Lo}$) and (Ra_{Lo}) for perforated specimens with and without plug in the upward and downward heating situations for different inclination angles in accordance with the following equation:

$$\overline{Nu}_{L_o} = (C_2 + C_3 \times m)(Ra.\sin\Phi)^{0.25}$$

……………………………… (10)

The values of constants (C_2) and (C_3) in the upward heating case are lower than those in the downward heating case for the perforated specimens with and without plug.

Average Of Total Dimensionless Heat Transfer:-

Figure (12-a-b) display the effect of perforation ratio(m) on average dimensionless heat transfer at Grashof number ($Gr_{Lo}=1.576\times10^6, 3.546\times10^6, 5.083\times10^6$ and 6.292×10^6) for the square specimen and perforated specimens with and without plug. It is observed that the maximum heat transfer quantity is at perforation ratio (m=0.1), and gradually decreases with increasing perforation ratio (m=0.24 and 0.5), despite the increase in ($\overline{Nu}_{Lo}$), due to the decrease in the area of heat exchange, which leads to decrease in the rate of heat transfer. It is also observed the total heat transfer quantity to the

perforated plates with plug is lower than that transfer to the perforated plates without plug, by (6.477%) for all perforation ratios due to decreasing ($\overline{Nu}_{Lo}$) for perforated plates with plug from that for perforated plates without plug.

Choice Of Suitable Hole Shape:-

To investigate the perforated shape, and to determine the effect of most suitable hole shape on heat loss, a comparison has been done between quantity of heat transferred in the case of circular hole in present work with square hole as cited by [Ali, 2007] for the ratios of perforation are (m=0.1,0.16,0.24, and 0.36) for upward heating ($0^o<\Phi\leq90^o$) and downward heating ($90^o\leq\Phi<180^o$), at four heating levels, as shown in Figure (13-a-b). It is found that heat transferred in the case of circular hole is greater than the heat quantity in the case of square hole for the same perforation ratios. It founded there is no effect of square hole edges "corners" which represented stagnation flow region[AL-Arabi and EL-Riedy, 1976], this led to thermal loss in case of circular hole is greater than in case of square hole.

Comparison Of Present Results With Previously Published Results:-

There is agreement between results of present work for values of ($\overline{Nu}_{Lo}$) for horizontal square plate with its heated surface downward are shown in Figure (14) and for vertical position in Figure (15). And previous numerically published work by [Abd, 2007], and experimentally by [Ali, 2007] for horizontal square plates with their heated surface downwards, and in vertical position, also compared with previous numerical results for horizontal disc with heated surface downwards, and for heating in the vertical position with those by [Hassan, 2003]. Values of ($\overline{Nu}_{Lo}$) for inclined perforation square plate, with circular perforation, at perforation ratio (m=0.5) for both heating upward, shown in Figure (16) and heating downward shown in Figure (17) of present work with previous numerical work by [Abd, 2007], for an inclined square plate perforated with circular hole of perforation ratio (0.6), and with previous experimental work [Ali, 2007], for

Asst. Prof. Dr. Ikhlase M. Fayed
Asst. Lec. Wassan N. Matti

Experimental Study For a Laminar Natural Convection Heat Transfer
From an Isothermal Heated Square Plate With and Without Circular
Hole

an inclined square plate, perforated with square hole at perforation ratio (0.36) for upward and downward heating. There is good agreement in values of ($\overline{Nu}_{Lo}$) with results reported by [Abd, 2007], and the value of ($\overline{Nu}_{Lo}$) shows an increase, from the experimental results of [Ali, 2007], by (16.21%) for heating upwards, and by (18.74%) for heating downwards.

Conclusions:- The results show that for square specimen and specimens with circular hole without plug

1- The minimum temperature gradient and maximum thermal boundary layer thickness (δ) is above the centre of the square specimen in the horizontal position heated face upward ($\Phi=0^{o}$), while the gradient increases and thermal boundary layer thickness (δ) decreases when specimens are perforated.

2- The value of local Nusselt number (Nu_{Lo}) in the upward heating is less than in the downward heating, this leads to increase the quantity of heat transfer in the downward heating than in the upward heating. The maximum value of (Nu_{Lo}) is at the lower edge of inclined specimens in ($\Phi=90^{o}$).

3- Maximum value for the ($\overline{Nu}_{Lo}$) is in the vertical position ($\Phi=90^{o}$), and minimum value is in both horizontal position ($\Phi=0^{o}$,180°). The ($\overline{Nu}_{Lo}$) increases with increasing perforation ratio and heating level to reach its maximum value at perforation ratio (m=0.5) and ($Gr_{Lo}=6.292\times10^{6}$) in ($\Phi=90^{o}$).

4- Maximum heat transfer quantity is at perforation area ratio (m=0.1), and maximum heat transfer rate for square and perforated specimens is in the vertical position ($\Phi=90^{o}$) at all heating levels .

5- The realization of an empirical correlation for ($\overline{Nu}_{Lo}$) with term (Ra.sinΦ) and perforation ratio for square specimens having circular perforation with heated surface upwards without plug
{$\overline{Nu}_{Lo}$ =(0.599+0.407Xm)(Ra.sinΦ)$^{0.25}$ }, and its heated surface downwards {$\overline{Nu}_{Lo}$ =(0.634+0.333Xm)(Ra.sinΦ)$^{0.25}$ }.

6- The rate of heat transfer for circular hole is greater than for square hole for the same perforation ratio .

The results show for circular perforated specimens with plug

1- Decrease in temperature gradient and increase in the thermal boundary layer thickness (δ) occur in the perforated specimens with plug.

2- The values of local Nusselt number and quantity of heat transfer are lower than those without the plug.

3- The average Nusselt number for perforated specimens with plug is lower than without.

4- The quantity of heat transfer for perforated specimens with plug, is lower than that without plug by (6.477%) for all perforation ratios. The maximum values of the heat transfer is at the vertical position ($\Phi=90^{o}$) for all heating levels.

5- In order to formulate an empirical correlation for average Nusselt number ($\overline{Nu}_{Lo}$) with the expression (Ra.sinΦ) and perforation ratio for square specimens having circular hole with its heated surface upwards with plug {$\overline{Nu}_{Lo}$ =(0.544+0.287Xm)(Ra.sinΦ)$^{0.25}$}, and its heated surface downwards {$\overline{Nu}_{Lo}$ =(0.566+0.305Xm)(Ra.sinΦ)$^{0.25}$ }.

References

Abd Y. H. 2007
"Numerical Study For A Three Dimensional Laminar Natural Convection Heat Transfer From An Isothermal Heated Horizontal And Inclined Square Plate And With A Circle Hole".
Journal of Engineering Vol. 13, No.2,

AL-Arabi M. & EL-Riedy M. K.   1976
"Natural Convection Heat Transfer From Isothermal Horizontal Plates of Different Shapes".
Int. J.Heat & Mass Transfer . Vol. 19 , PP. 1399-1404.

Ali Th. H.   2007
"Experimental Study For A Three Dimensional Laminar Natural Convection Heat Transfer From An Isothermal Heated Square Plate".
M. Sc. Thesis Univ. Technology.

Aziz R. N. 2002
"Instructional System To Study Free Convection Heat Transfer from Isothermal Horizontal Square Flat Surfaces ".
M. Sc. Thesis Univ. Technology

Hassan A. K. 2003
"Prediction of Three Dimensional Natural Convection from Heated Disks and Rings at Constant Temperature ".
J. Eng. & Technology. Vol. 22, No.5, PP. 229

Robinson S. B. & Liburdy J. A. 1987
"Prediction of The Natural Convection Heat Transfer From A Horizontal Heated Disk".
Transactions of the ASME . Vol. 109 , PP. 906-911-248

Pera Luciano & Gebhart Benjamin 1973
"Natural Convection Boundary Layer Flow Over Horizontal And Slightly Inclined Surfaces".
Int.J. Heat & Mass Transfer . Vol. 16 , PP. 1131-1145.

Mustafa A. W. 2001
"Numerical and Experimental Study of Natural Convection Heat Transfer from Isothermal Horizontal Disks and Rings".
M. Sc. Thesis Univ. Technology

Sahraoui M. , Kaviany M. & Marshall H. 1990
"Natural Convection From Horizontal Disks And Rings " .
Transactions of the Asme . Vol. 112 , PP. 110-116

Asst. Prof. Dr. Ikhlase M. Fayed
Asst. Lec. Wassan N. Matti

Experimental Study For a Laminar Natural Convection Heat Transfer
From an Isothermal Heated Square Plate With and Without Circular
Hole

List Of Symbols

Nomenclature

Symbol	Definition	Unit
A	Total surface area	m^2
$C_1, C_2, C_3,$	Empirical constants of average Nusselt number with Rayleigh number correlation	------
D_o	Disc diameter	m
F	Shape factor	------
$\overline{h}$	Average heat transfer coefficient	$W/m^2.{}^oC$
h	Local heat transfer coefficient	$W/m^2.{}^oC$
k_f	Fluid Thermal conductivity at film temperature	$W/m.{}^oC$
L_i	Inner length for the square hole	m
L_o	Length of square side	m
L_p	Length of rectangular surface	m
m	Ratio of hole area to square plate area	------
q	Convective heat transfer rate calculated from local measurement method	W
Q	Dimensionless heat transfer rate by convection	------
$Q_{convcetion}$	Convection heat transfer rate calculated from energy balance method	W
$Q_{radiation}$	Radiation heat transfer rate from specimen surface	W
R^2	Correlation coefficient	------
T	Temperature	${}^oC$
T_∞	Ambient (atmospheric) temperature	${}^oC$
T_w	Heated surface temperature	${}^oC$
x,y,z	Normal coordinates	m

Dimensionless Group

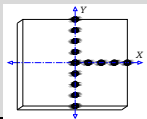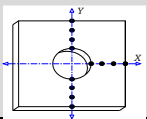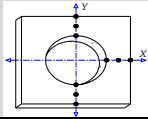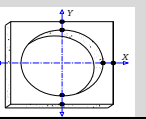|	
$Gr_{Do} = g\beta(T_w - T_\infty)D_o{}^3 / \upsilon^2$	Grashof number based on the outer diameter of disc or ring
$Gr_{Lo} = g\beta(T_w - T_\infty)L_o{}^3 / \upsilon^2$	Grashof number based on the side length of square plate
$Nu_{Lo} = h.L_o / k_f$	Local Nusselt number based on the side length of square plate
$\overline{Nu}_{Lo} = \overline{h}.L_o / k_f$	Average Nusselt number based on the side length of square plate
$\overline{Nu}_{Do} = \overline{h}.D_o / k_f$	Average Nusselt number based on the outer diameter of disc or ring
$\overline{Nu}_{Lo} = \overline{h}.L_o / k_f$	Average Nusselt number based on the side length of square plate
$\overline{Nu}_{Lo-Li} = \overline{h}.(L_o - Li) / k_f$	Average Nusselt number based on the difference between the length of square plate and hole length
$\overline{Nu}_{Lp} = \overline{h}.L_p / k_f$	Average Nusselt number based on the side length of rectangular plate
$Pr = \upsilon / \alpha$	Prandtl Number
$Ra_{Do} = Gr_{Do} \cdot P_r$	Rayleigh number based on outer diameter for disc or ring
$Ra_{Lo} = Gr_{Lo} \cdot P_r$	Rayleigh number based on the side length of square plate
$Ra_{Lp} = Gr_{Lp} \cdot P_r$	Rayleigh number based on the side length of rectangular plate

Greek Symbols

Φ	Angle of plate inclination from horizon	*degree*
σ	Stefan-Boltzman constant and it value 5.678×10^{-8}	W/m^2K^4
ε	Emissivity of heat exchange surface	------
θ	Dimensionless temperature	------
δ	Thickness of thermal boundary layer	*mm*

Table (1) the results of previous studies

Source	Type of Study	Plate Position	Geometric Figure	Characteristic Length	Dimensionless Equation	The Ranges
Pera & Gebhart (1973)	Experimental & Numerical	Horizontal & tilt $2o \leq \Phi \leq 6o$	Rectangle	L_p	upface heated $T_w=C$ $Nu_{Lp} = 0.394 Ra_{Lp}^{1/5} Pr^{1/20}$ $Nu_{Lp} = 0.656 Ra_{Lp}^{1/5} Pr^{1/20}$	$2.8x10^3 \leq Ra_{Lp} \leq 3x10^5$ $\Phi=0^o$ $4.8x10^3 \leq Ra_{Lp} \leq 3.5x10^5$ $2^o \leq \Phi \leq 6^o$ at $Pr = 0.72$
AL-Arabi & EL-Riedy (1976)	Experimental	Horizontal	Square, Circular & Rectangle	L_o D_o L_p	upface heated $\overline{Nu}_{Lo,Do,Lp} = 0.70 Ra_{Lo,Do,Lp}^{1/4}$ Laminar flow region ---- $\overline{Nu}_{Lo,Do,Lp} = 0.155 Ra_{Lo,Do,Lp}^{1/3}$ Turbulent flow region	$2x10^5 < Ra_{Lo,Do,Lp} < 4x10^7$ ---- $4x10^5 < Ra_{Lo,Do,Lp}$
Robinson & Liburdy (1987)	Experimental & Numerical	Horizontal	disk	D_o	$\overline{Nu}_{Do} = 0.602 Ra_{Do}^{1/5}$	$7.7x10^4 \leq Gr_{Do} \leq 1.2x10^5$ $10^4 \leq Gr_{Do} \leq 10^6$ Pr=0.72
Sahraoui et al. (1990)	Experimental & Numerical	Horizontal	disks & rings with and without adiabatic core	D_o	upface heated $\overline{Nu}_{Do} = 0.561 Ra_{Do}^{1/5} Pr^{0.085}$ ------ $\overline{Nu}_{Do} = 0.603 Ra_{Do}^{1/5} Pr^{0.085}$	$10 \leq Ra_{Do} \leq 1.25x10^5$ $0.1 \leq Pr \leq 10$
Mustafa (2001)	Experimental & Numerical	Horizontal	Disk & ring	D_o	upface heated $\overline{Nu}_{Do} = 0.95 Ra_{Do}^{0.192}$ ------ $\overline{Nu}_{Do} = (3r_2 + 0.95) Ra_{Do}^{0.192}$	$7x10^2 \leq Ra_{Do} \leq 7x10^6$ Pr=0.7 $r_2 = D_i / D_O$
Aziz (2002)	Experimental	Horizontal	square with and without square hole	L_o L_o-L_i	upface heated $\overline{Nu}_{Lo} = 0.73 Ra_{Lo}^{0.21}$ $\overline{Nu}_{Lo\text{-}Li} = 0.978 Ra_{Lo\text{-}Li}^{0.21}$	$10^6 < Ra_{Lo} < 4.5x10^6$ $4.18x10^5 < Ra_{Lo} < 1.73x10^6$ Pr=0.72
Abd (2007)	Numerical	Horizontal, vertical & tilt to the horizon	square with and without circular hole	L_o	upface heated $\overline{Nu}_{Lo} = 0.784 Ra_{Lo}^{1/5}$ $\overline{Nu}_{Lo} = (0.597 + 0.413 \ r_1)(Ra_{Lo}\sin\Phi)^{0.25}$ ------ downface heated $\overline{Nu}_{Lo} = 0.78 Ra_{Lo}^{1/5}$ $\overline{Nu}_{Lo} = (0.604 + 0.423 \ r_1)(Ra_{Lo}\sin\Phi)^{0.25}$	$7.2x10^2 \leq Ra_{Lo} \leq 3.6x10^4$ Pr = 0.72 $r_1 = a / Lo$
Ali (2007)	Experimental	Horizontal, vertical & tilt to the horizon	square with and without square hole	L_o	upface heated $\overline{Nu}_{Lo} = (0.584 + 0.222 m)(Ra_{Lo}\sin\Phi)^{0.25}$ ------ downface heated $\overline{Nu}_{Lo} = (0.606 + 0.267 m)(Ra_{Lo}\sin\Phi)^{0.25}$	$m = \dfrac{A_{hole}}{A_{square}}$ $10^6 \leq Ra_{Lo} \leq 3.96 X10^6$

Asst. Prof. Dr. Ikhlase M. Fayed
Asst. Lec. Wassan N. Matti

Experimental Study For a Laminar Natural Convection Heat Transfer
From an Isothermal Heated Square Plate With and Without Circular
Hole

Table (2) Basic dimensions of the specimens used in the laboratory experiments

Specimens arrangement		First Specimen	Second Specimen	Third Specimen	Fourth Specimen
Type		Square plate	Square plate with circular hole	Square plate with circular hole	Square plate with circular hole
Dimensions	**Thickness**	10mm	10mm	10mm	10mm
	External side length	100mm	100mm	100mm	100mm
	circular hole diameter	0 mm	36mm	56 mm	80mm
Area ratio (m)		m=0.00	m=0.10	m=0.24	m=0.50

Table(3) Grashof number(Gr_{Lo}) and Rayleigh number(Ra_{Lo}) ranges of the experiments

T_w (^oC)	40	60	80	100
T_{film} (K)	306.5	316.5	326.5	336.5
Gr_{Lo}	1.576×10^6	3.546×10^6	5.083×10^6	6.292×10^6
Ra_{Lo}	1.112×10^6	2.496×10^6	3.568×10^6	4.398×10^6
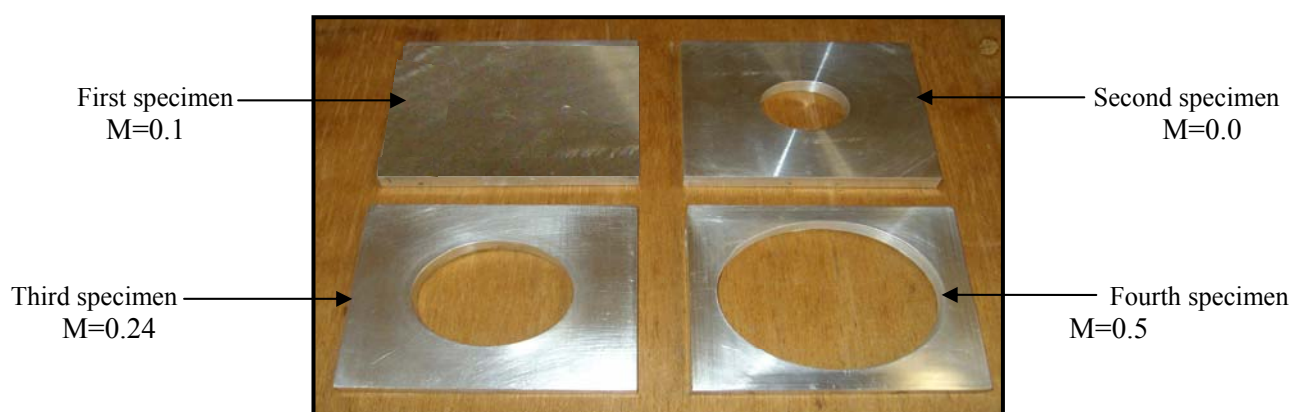
Figure (1) Specimens used in the experimental tests

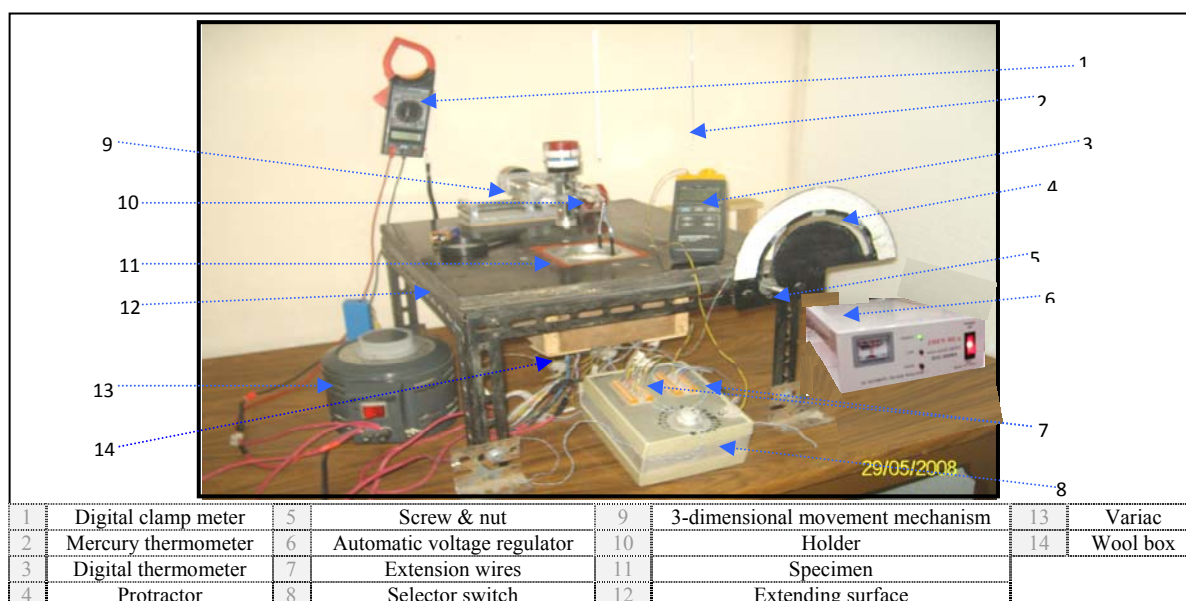| 1	Digital clamp meter	5	Screw & nut	9	3-dimensional movement mechanism	13	Variac
2	Mercury thermometer	6	Automatic voltage regulator	10	Holder	14	Wool box
3	Digital thermometer	7	Extension wires	11	Specimen		
4	Protractor	8	Selector switch	12	Extending surface		

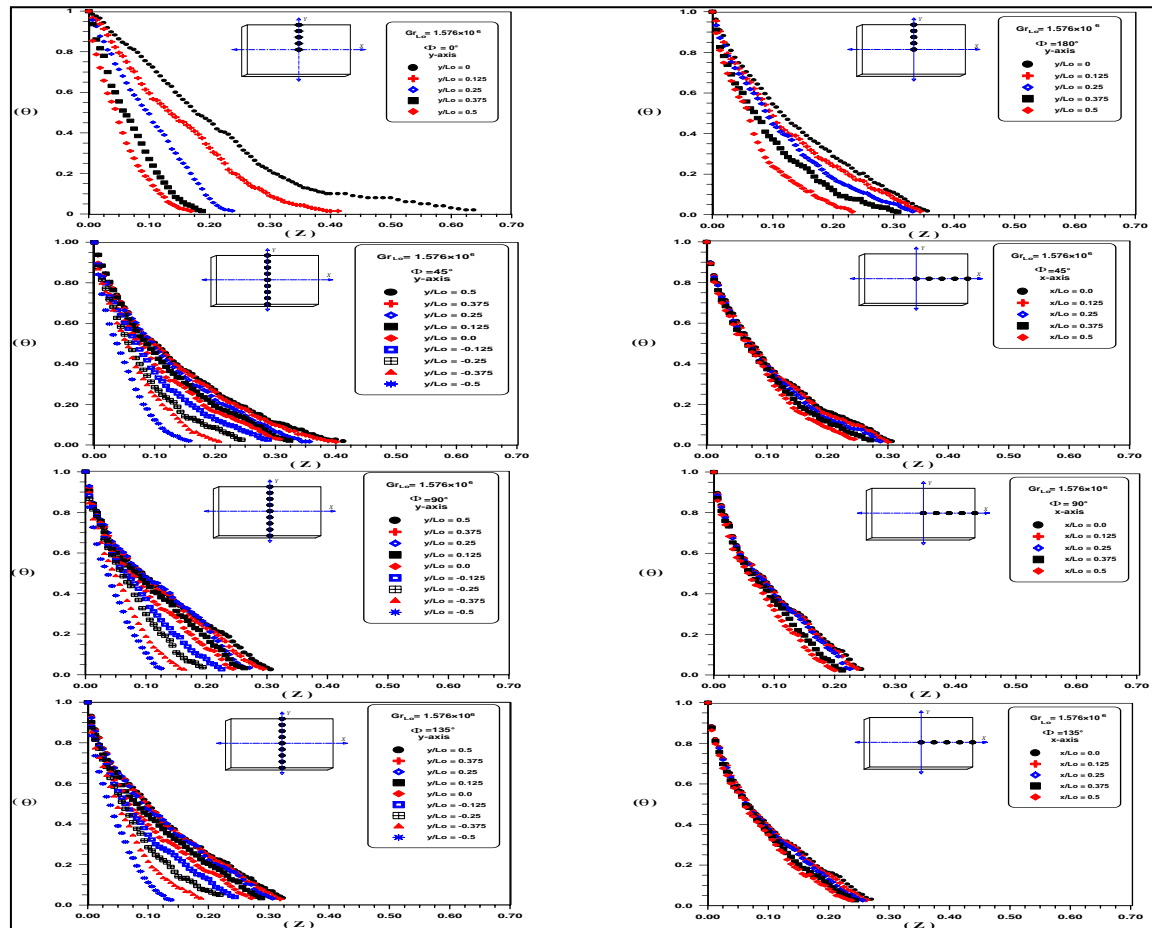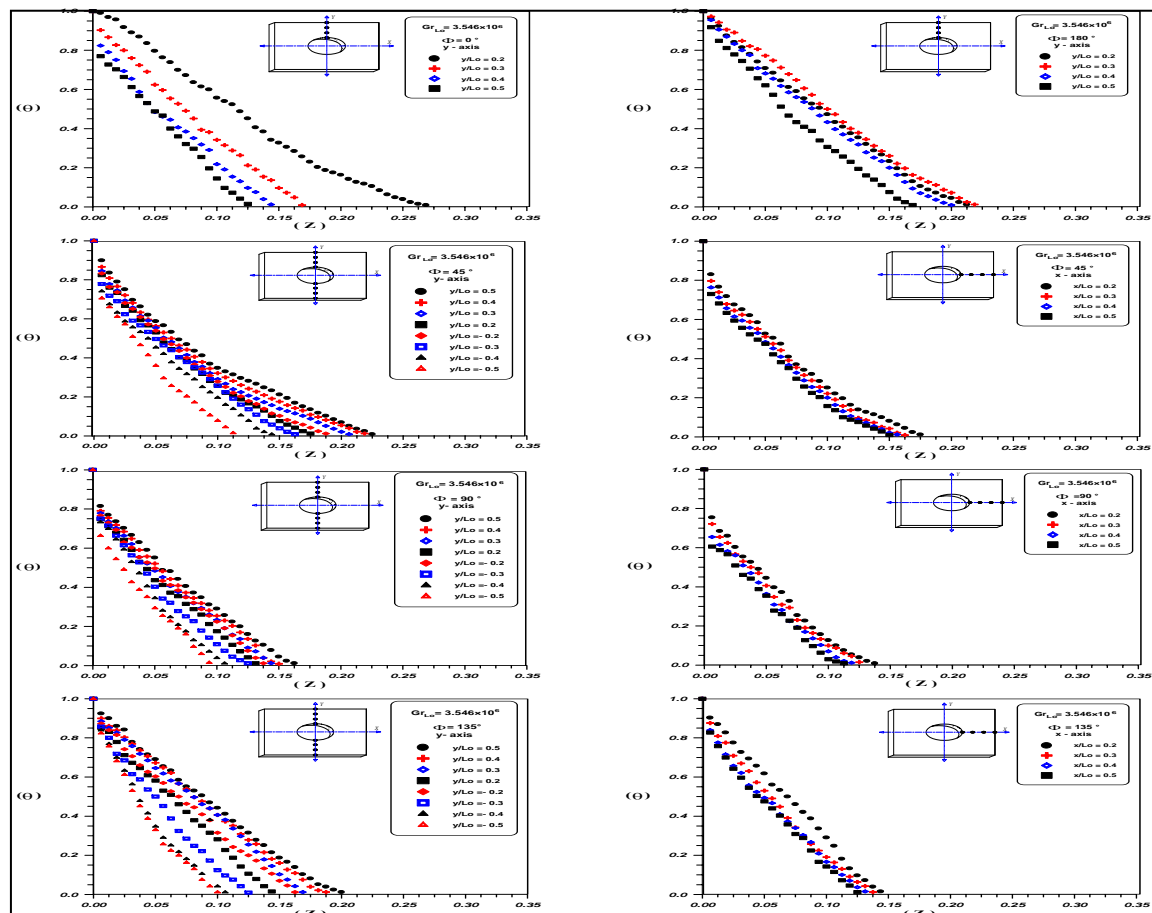**Figure (2) Test rig with measurement devices**

Figure (3)experimental temperature distribution over 1st specimen m=0.0 for Gr$_{L0}$=1.576X10^6

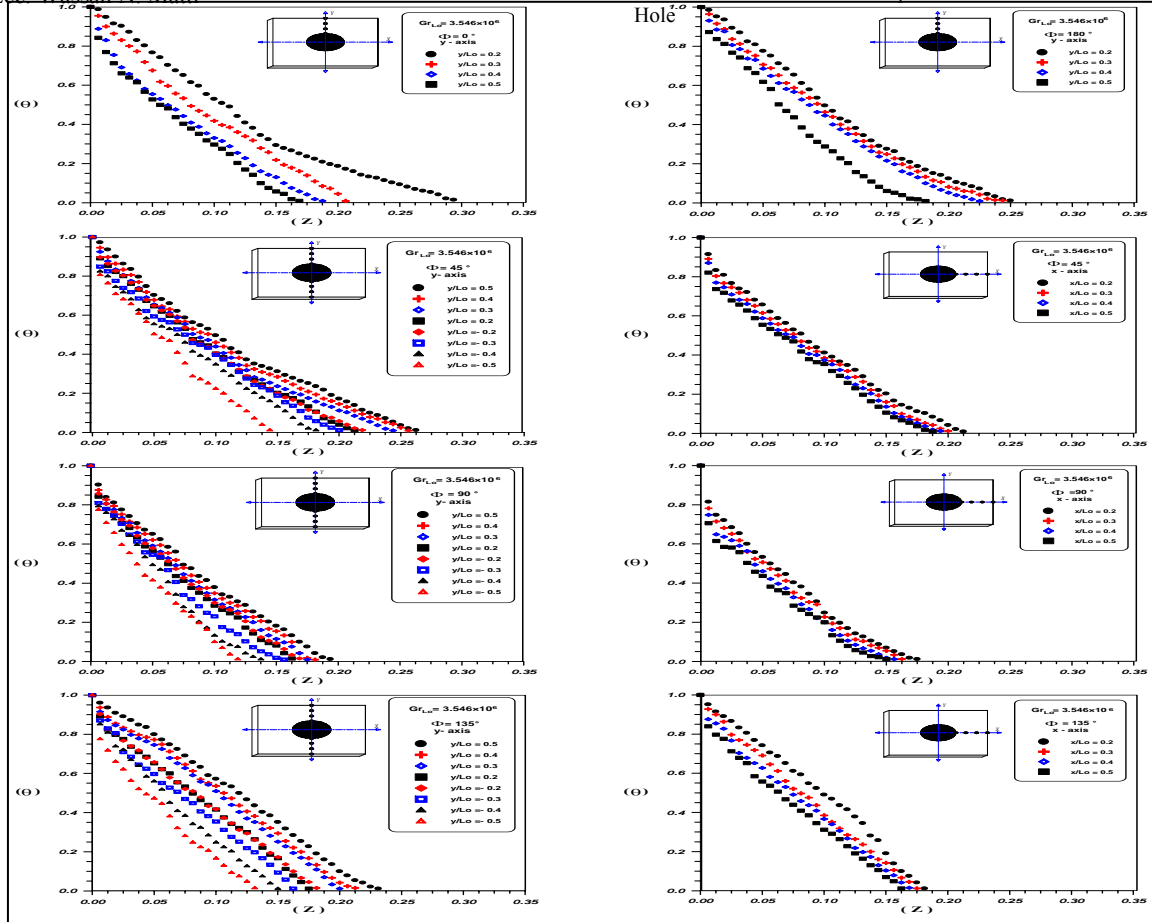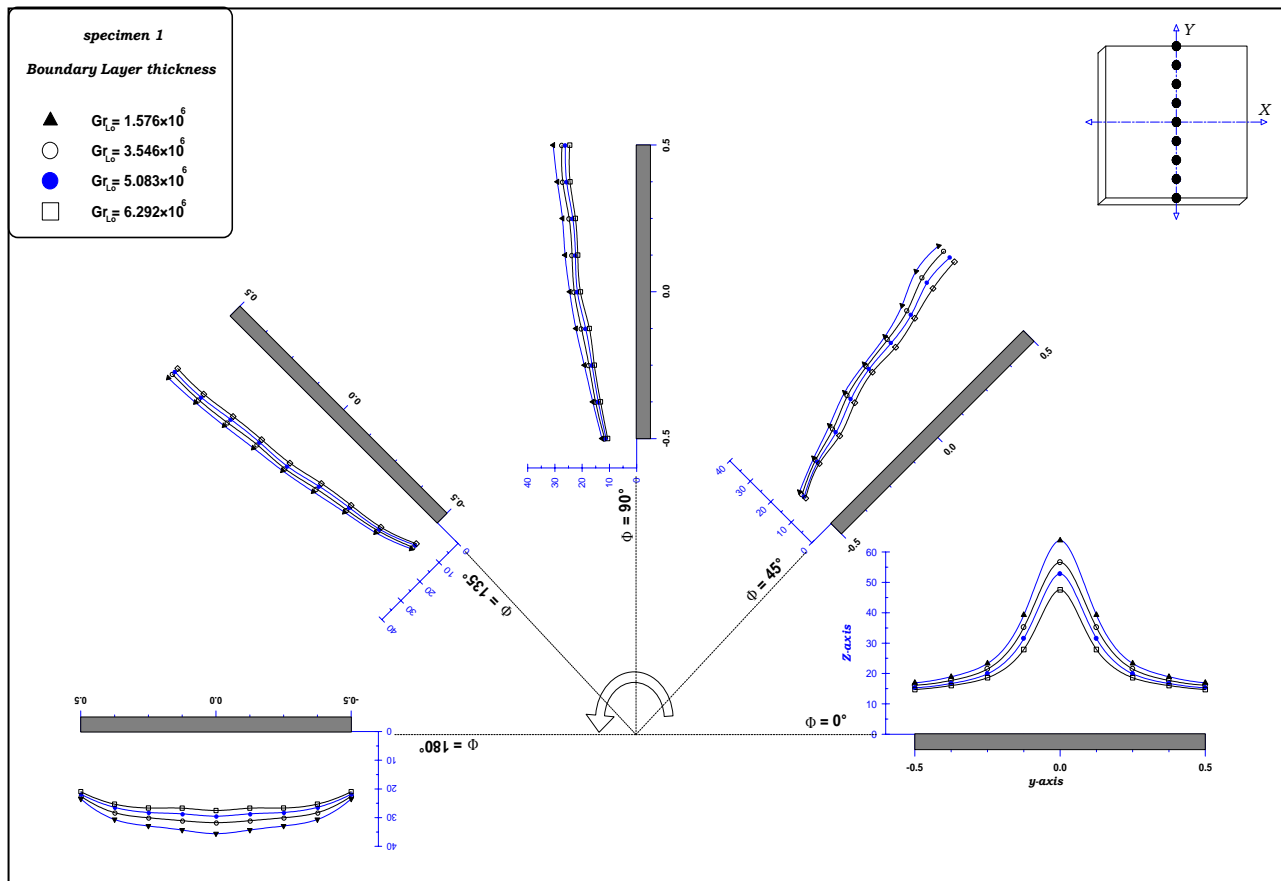**Figure(4-a) experimental temperature distribution over 2^{ed} specimen without plug m=0.1 for Gr$_{L0}$=3.546X10^6**

Asst. Prof. Dr. Ikhlase M. Fayed
Asst. Lec. Wassan N. Matti

Experimental Study For a Laminar Natural Convection Heat Transfer
From an Isothermal Heated Square Plate With and Without Circular Hole

Figure (4-b) experimental temperature distribution over 2ed specimen with plug m=0.1for
$Gr_{L0}=3.546X10^6$

Figure(5) boundary layer thickness over 1st specimen surface m=0.0 for
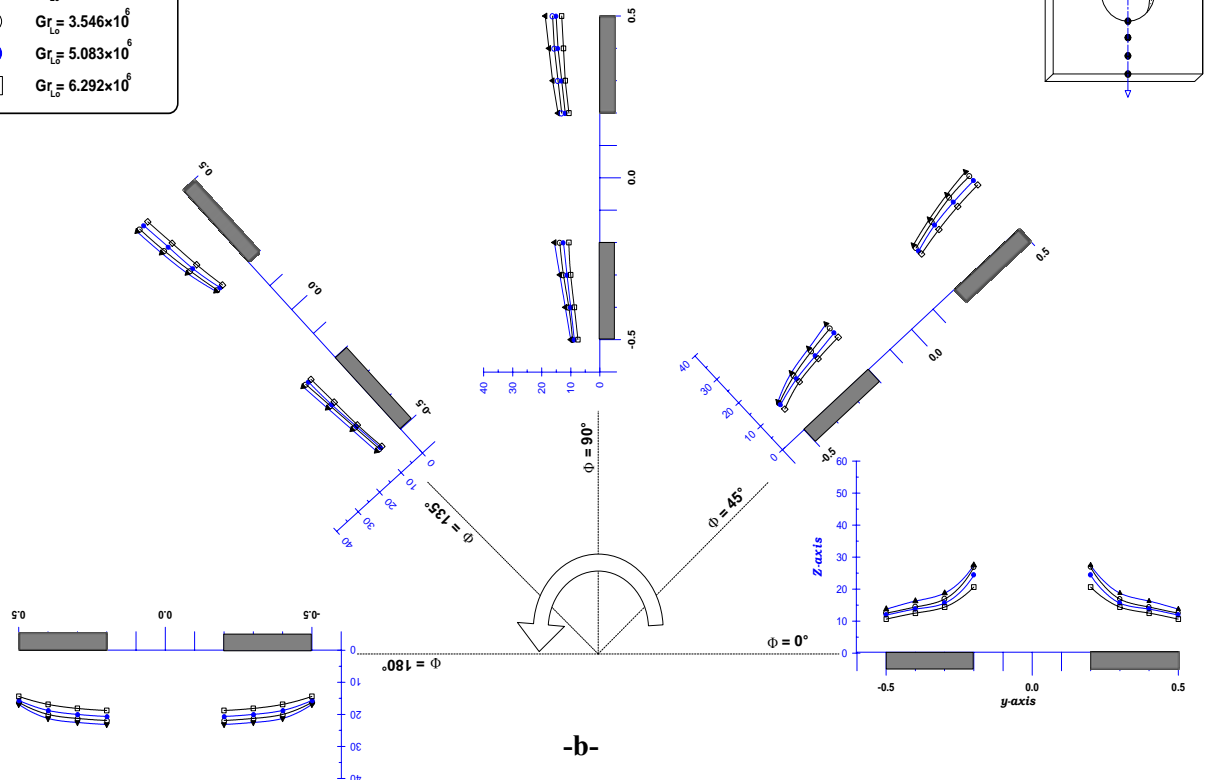**$(1.576x10^6 \leq Gr_{L0} \leq 6.292x10^6)$**

-a-

-b-
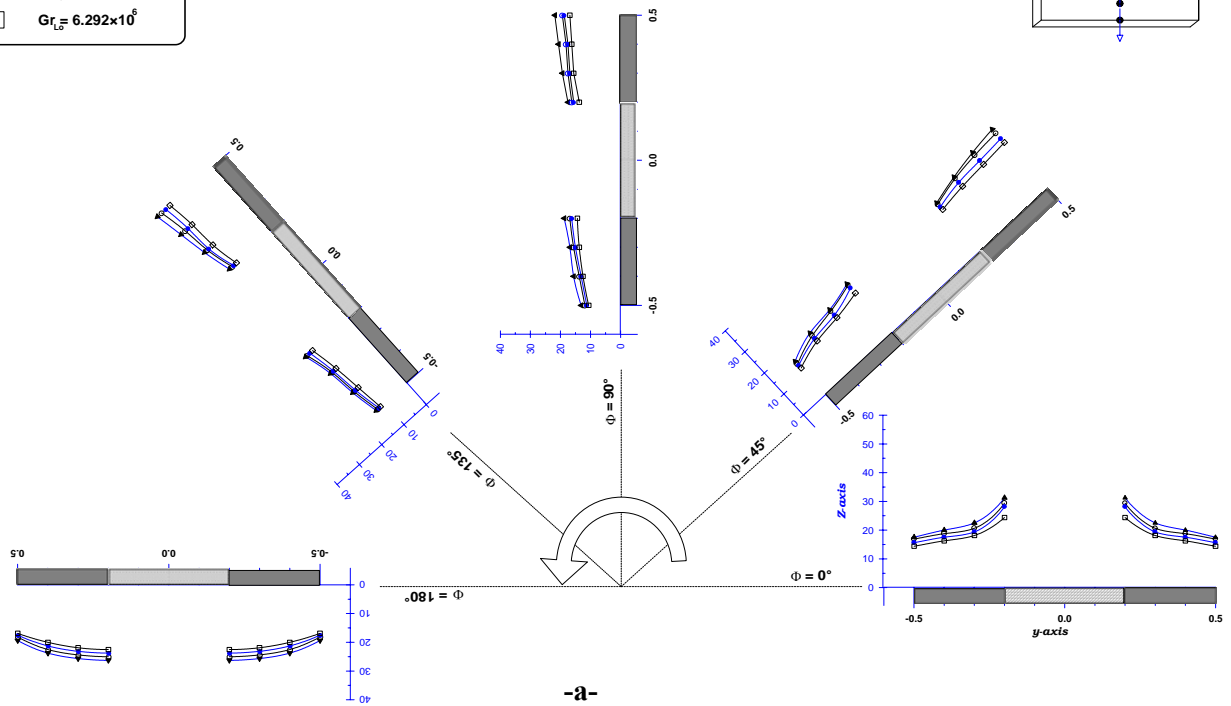
Figure(6) boundary layer thickness over 2^{ed} specimen surface m=0.1 for
$(1.576 \times 10^6 \leq Gr_{Lo} \leq 6.292 \times 10^6)$
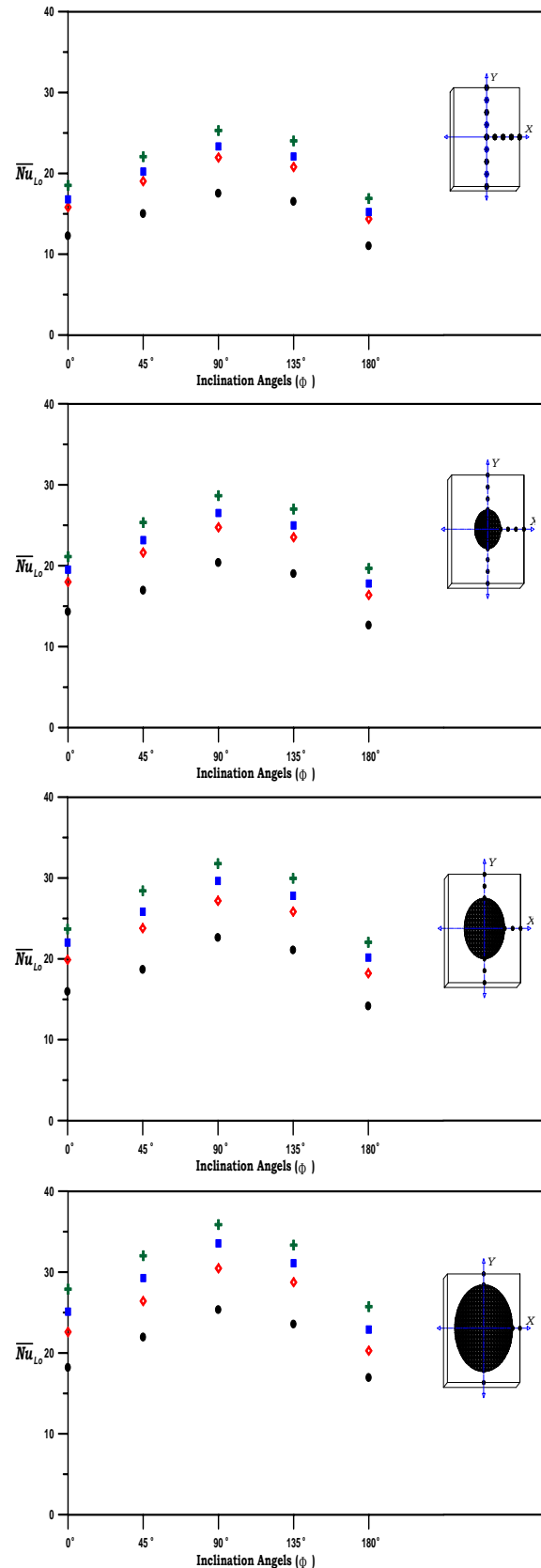-a- without plug (adiabatic core) for circular hole   -b- with plug (adiabatic core) for circular hole

Asst. Prof. Dr. Ikhlase M. Fayed
Asst. Lec. Wassan N. Matti

Experimental Study For a Laminar Natural Convection Heat Transfer
From an Isothermal Heated Square Plate With and Without Circular
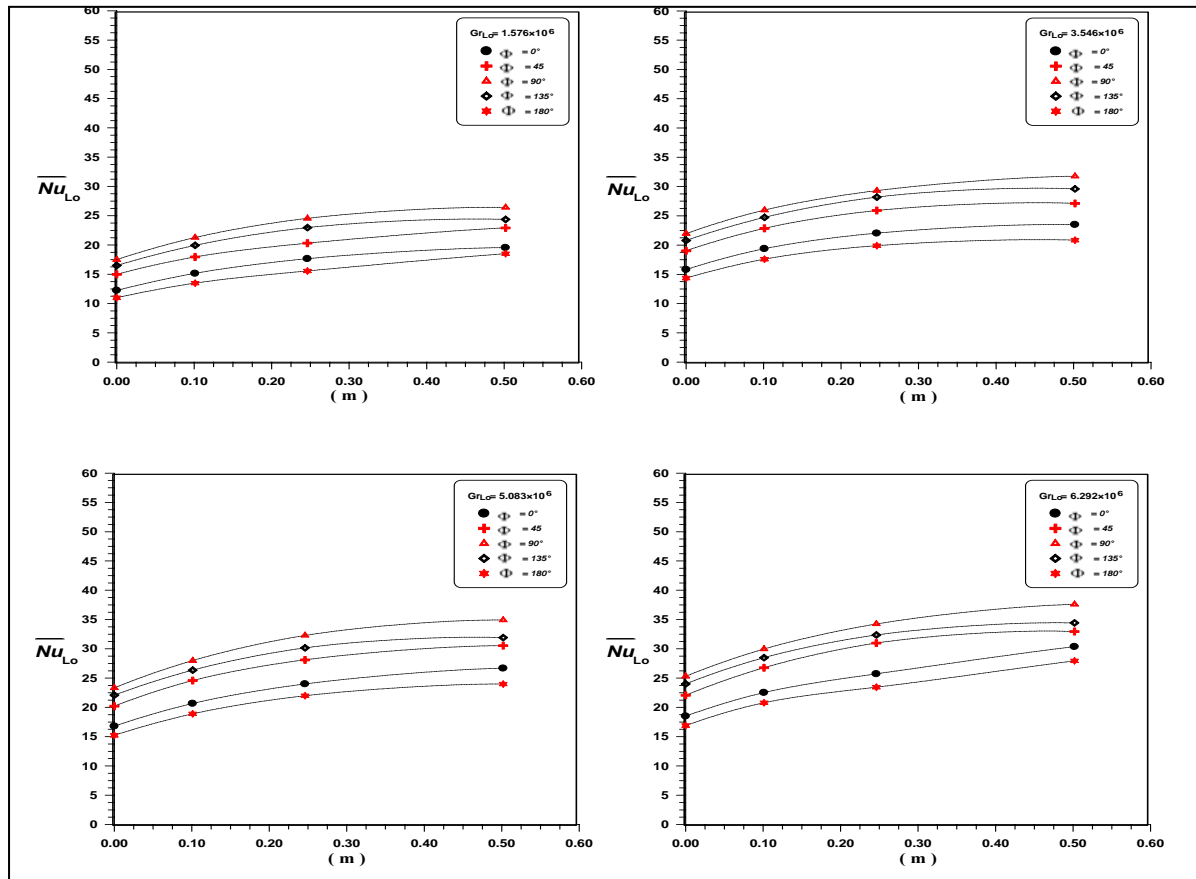Hole
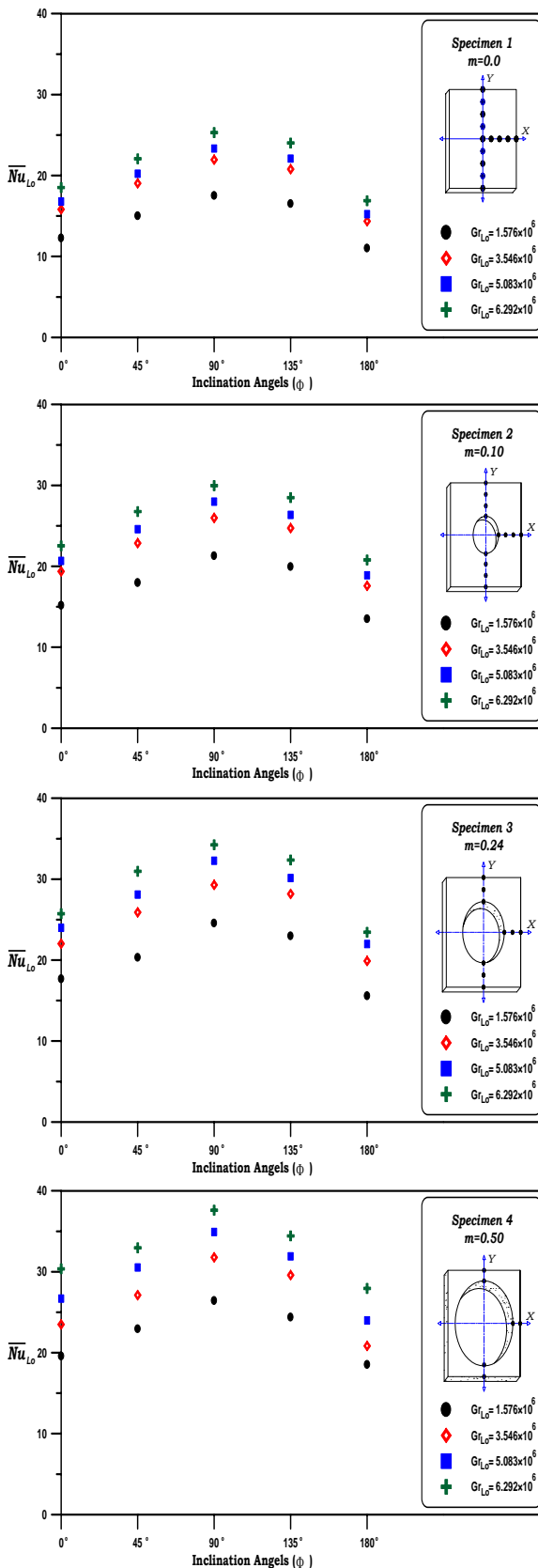
-a-

-b-

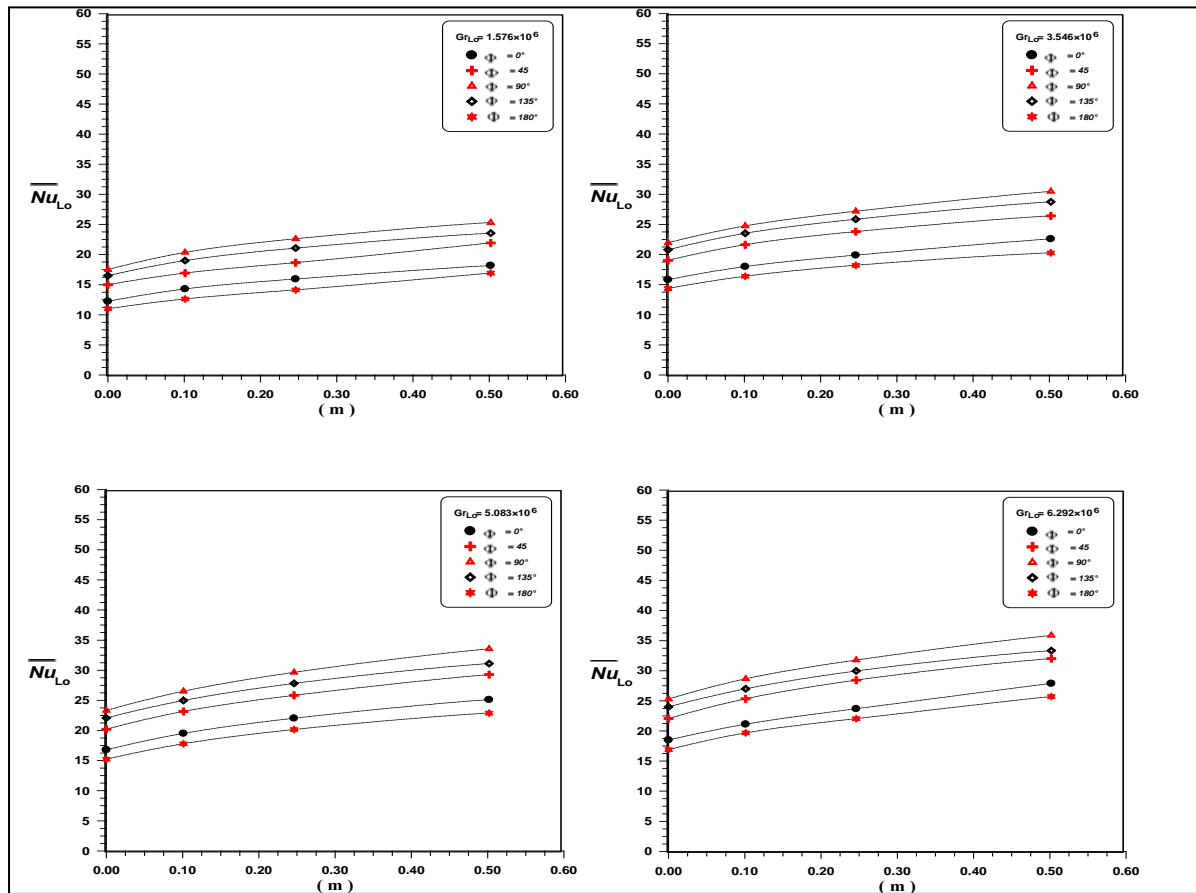Figure (7) the effect of inclination angle (Φ) from horizon on ($\overline{Nu}_{Lo}$)
-a- without plug (adiabatic core) for circular hole
-b- with plug (adiabatic core) for circular hole

-a-

-b-

) for four heating levels $\overline{Nu}_{Lo}$ **Figure (8) the effect of perforation ratio (m) on the (**
-a- without plug (adiabatic core) for circular hole
-b- with plug (adiabatic core) for circular hole

Asst. Prof. Dr. Ikhlase M. Fayed
Asst. Lec. Wassan N. Matti

Experimental Study For a Laminar Natural Convection Heat Transfer
From an Isothermal Heated Square Plate With and Without Circular
Hole

-a-

-b-
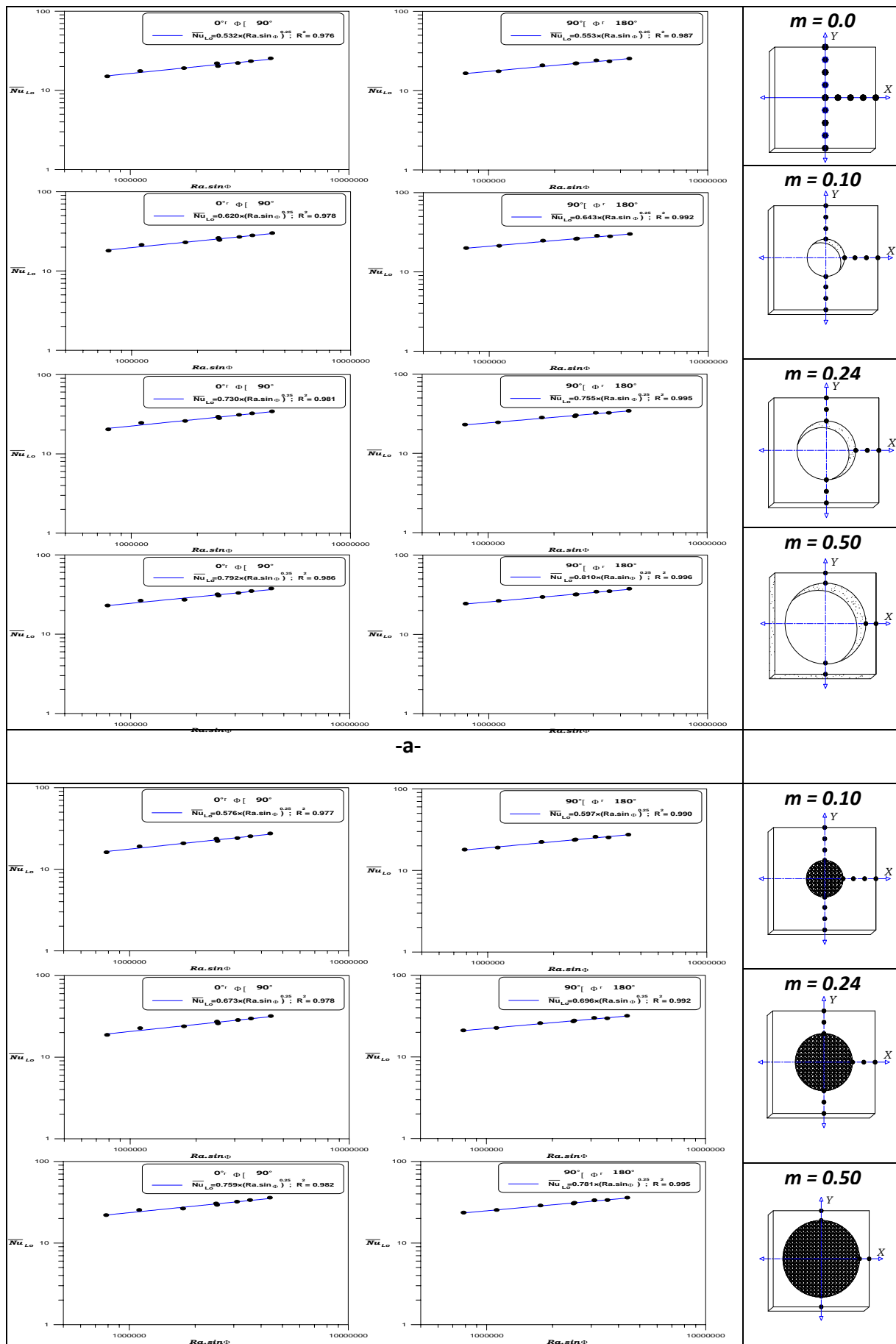
Figure (9) correlation between ($\overline{Nu}_{Lo}$) & (Ra$_{Lo}$) for specimens heating face upward & downward
-a- without plug (adiabatic core) for circular hole   -b- with plug (adiabatic core) for circular hole

Figure (10) ($\overline{Nu_{Lo}}$) as a function of Ra sin(Φ) & perforation ratio (m) for specimens without plug (adiabatic core) for circular hole
-a- upface heated
-b- downface heated

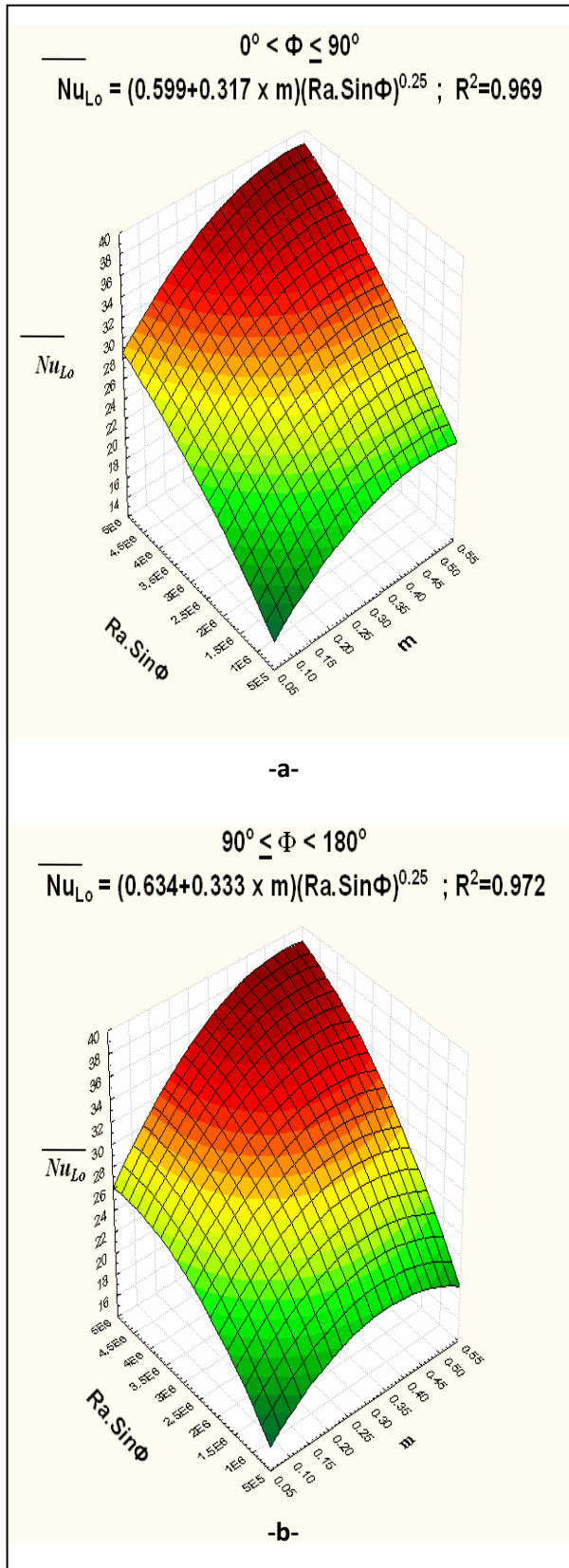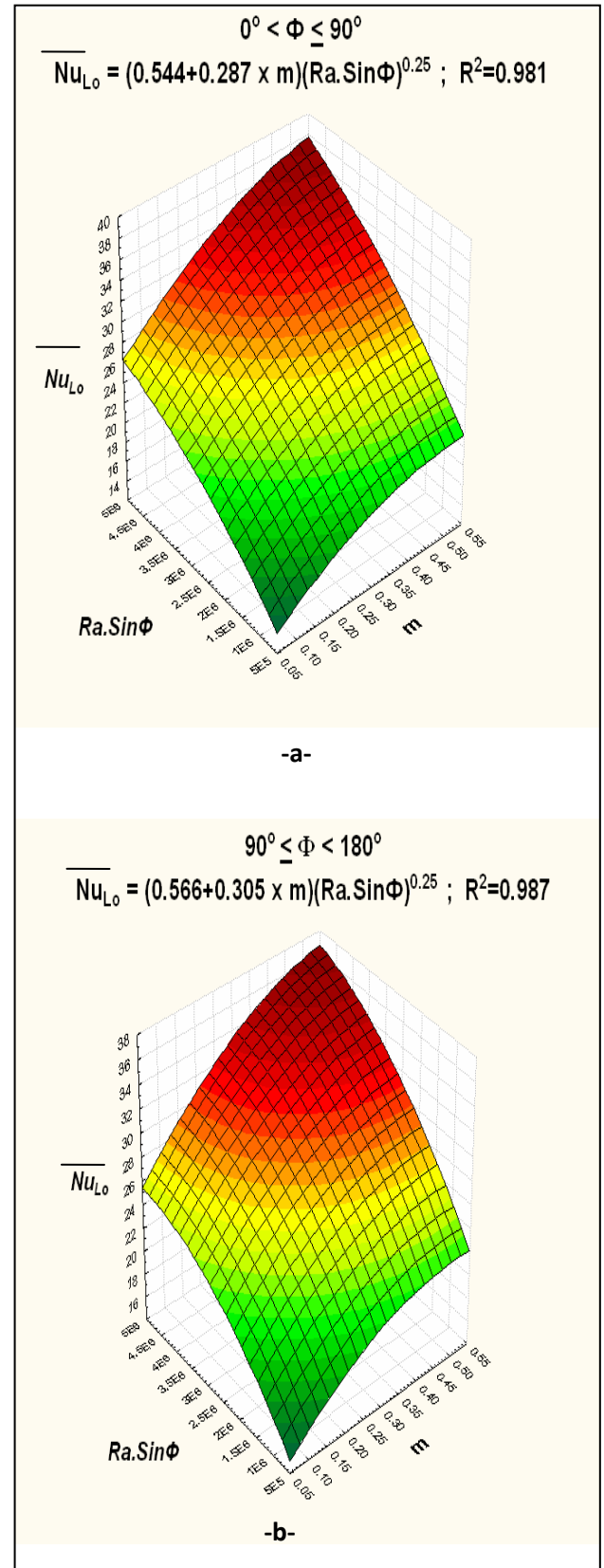**Figure (11)** ($\overline{Nu_{Lo}}$) as a function of Ra sin(Φ) & perforation ratio (m) for specimens with plug (adiabatic core) for circular hole
-a- upface heated
-b- downface heated

Asst. Prof. Dr. Ikhlase M. Fayed
Asst. Lec. Wassan N. Matti

Experimental Study For a Laminar Natural Convection Heat Transfer
From an Isothermal Heated Square Plate With and Without Circular
Hole
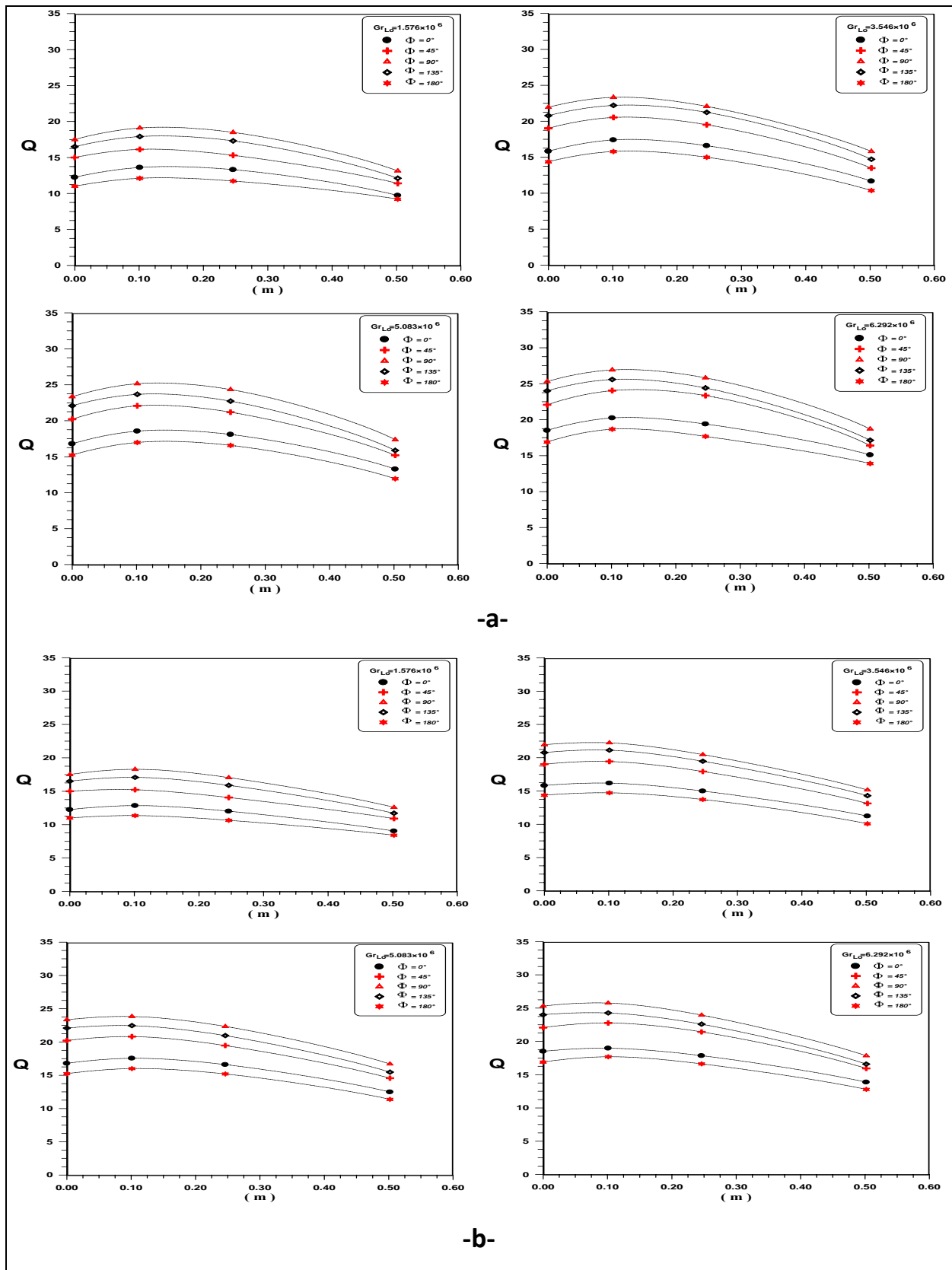
**Figure (12) the effect of perforation ratio (m) on the dimensionless heat transfer rate for
different heating levels
-a- without plug (adiabatic core) for circular hole
-b- with plug (adiabatic core) for circular hole**

Figure (13) effect hole shape on the dimensionless heat transfer rate for different heating levels and fore perforation ratio (m=0.1,0.16,0.24,0.36)
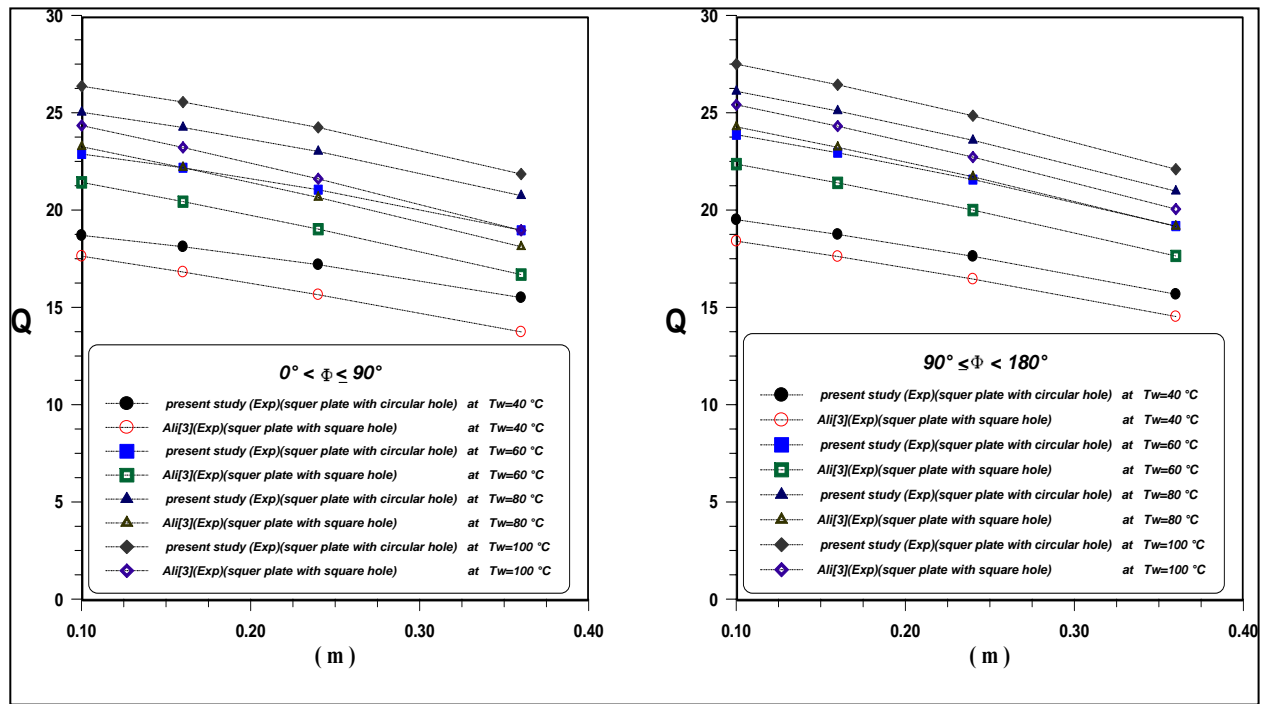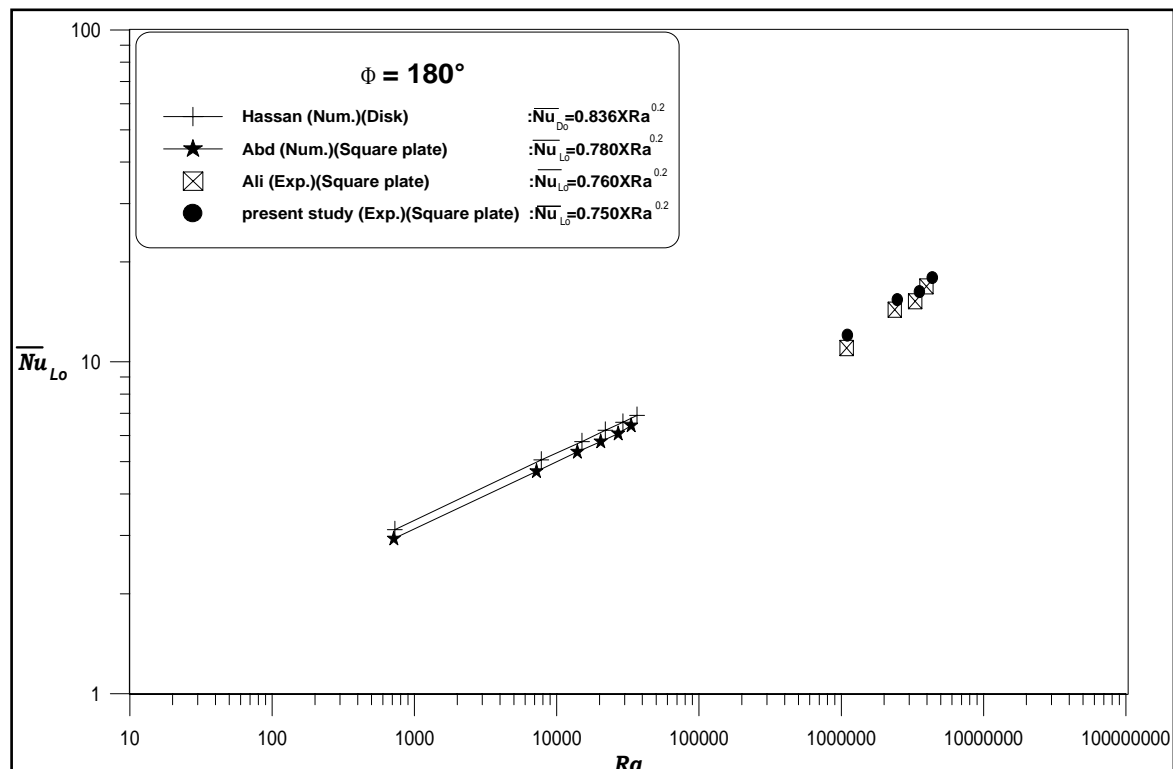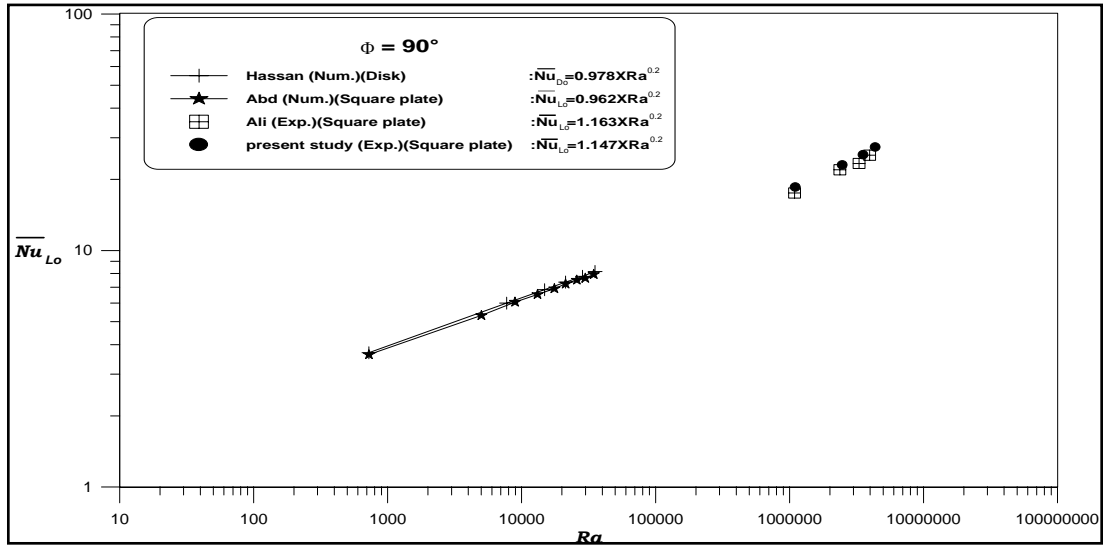**a- upface heated** **b- downface heated**

) number for present study horizontal square plate with $\overline{Nu}_{Lo}$ **Figure (14) comparison (experimental & numerical previous studies for horizontal square plates &disks at downface heated**

Asst. Prof. Dr. Ikhlase M. Fayed
Asst. Lec. Wassan N. Matti

Experimental Study For a Laminar Natural Convection Heat Transfer
From an Isothermal Heated Square Plate With and Without Circular
Hole

) number for present study at vertical position square plate $\overline{Nu}_{Lo}$ **Figure (15) comparison (**
with experimental & numerical previous studies for square plates &disks at vertical position
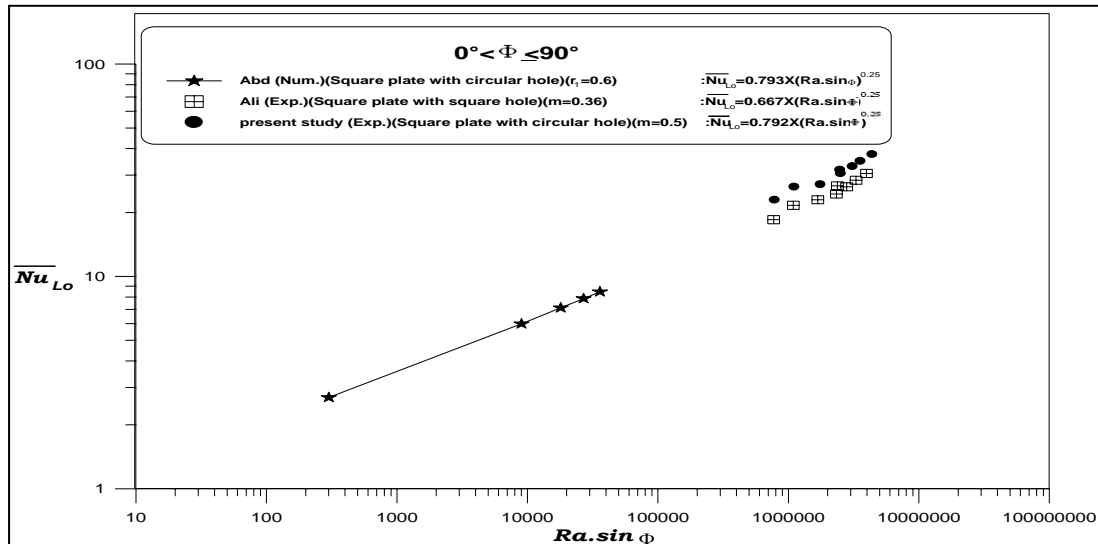
) number for present study perforate square plate with $\overline{Nu}_{Lo}$ **Figure (16) comparison (**
experimental & numerical previous studies for perforate square plates with circular, square hole
& ring at upface heated
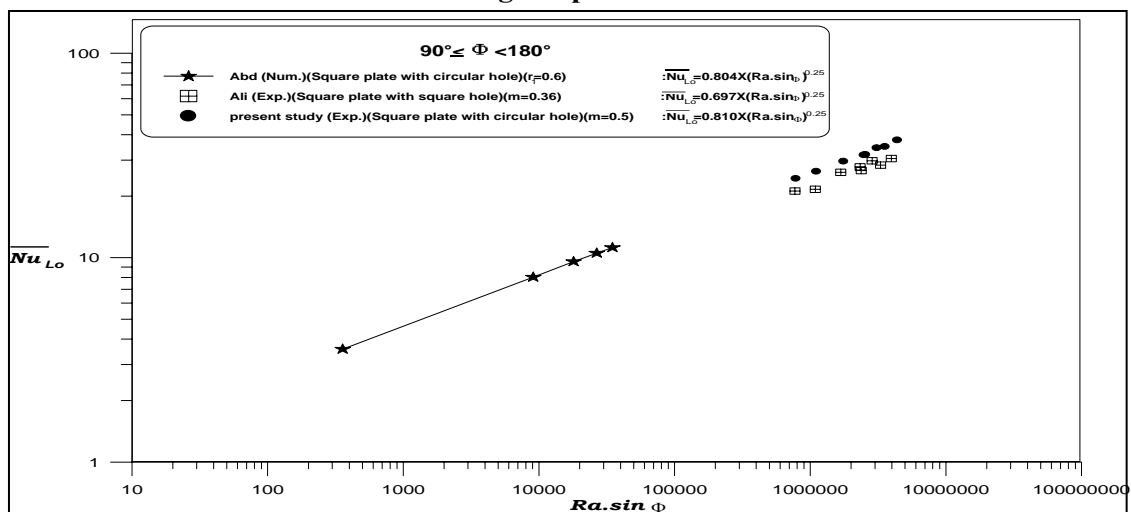
) number for present study perforate square plate with $\overline{Nu}_{Lo}$ **Figure (17) comparison (**
experimental & numerical previous studies for perforate square plates with circular,squar hole &
ring at downface heated

FREE VIBRATION ANALYSIS OF COMPOSITE LAMINATED PLATES USING HOST 12

Dr. Adnan N. Jameel   **Salam Ahmed Abed**
Mechanical Eng. Dep.   **Mechanical Eng. Dep.**
University of Baghdad   **University of Baghdad**

ABSTRACTE

This paper presents an application of a Higher Order Shear Deformation Theory (HOST 12) to problem of free vibration of simply supported symmetric and antisymmetric angle-ply composite laminated plates. The theoretical model HOST12 presented incorporates laminate deformations which account for the effects of transverse shear deformation, transverse normal strain/stress and a nonlinear variation of in-plane displacements with respect to the thickness coordinate – thus modeling the warping of transverse cross-sections more accurately and eliminating the need for shear correction coefficients. Solutions are obtained in closed-form using Navier's technique by solving the eigenvalue equation. Plates with varying number of layers, degrees of anisotropy and slenderness ratios are considered for analysis. The results compared with those from exact analysis and various theories from references.

للصفائح   (Higher Order Shear Deformation Theory (HOST 12))

الطبقية المركبة المتماثلة والغير متماثلة (ذات الألياف الغير متعامدة). النظرية المقدّمة HOST 12 تدمج تشويهات الطبقات التي تفسّر تأثيرات تشويه القصّ المستعرض، إجهاد طبيعي مستعرض / إجهاد و التوزيع اللاخطّي لأزاحات المستوي بالنسبة للسمك ـ هكذا تشكل تشويه المقاطع العرضية المستعرضة بدقة أكثر وتزيل الحاجة لمعاملات تصحيح القصّ. الحلول للمعادلات تضمنت الحل المضبوط للصفائح الطبقية المركبة (Navier Solution). أخذ بالأعتبار تأثير تنويع مواصفات الصفائح كعدد الطبقات ودرجة الأنتروبي ونسبة السمك الى العرض. النتائج قورنت مع حلول مضبوطة ونظريات متنوعة من مصادر متعددة.

Keywords: Free vibration; Higher order theory; Shear deformation; Angle-ply plates; Analytical solutions.

INTRODUCTION

Laminated composite plates and shells are finding extensive usage in the aeronautical and aerospace industries as well as in other fields of modern technology. It has been observed that the strength and deformation characteristics of such structural elements depend upon the fiber orientation, stacking sequence and the fiber content in addition to the strength and rigidities of the fiber and matrix material. Though symmetric and antisymmetric laminates are simple to analyze and design, some specific application of composite laminates requires the use of symmetric and antisymmetric laminates to fulfill certain design requirements. Symmetric and antisymmetric angle-ply laminates are the special form of symmetric and antisymmetric laminates and the associated theory offers some simplification in the analysis. The Classical Laminate Plate Theory (Reissner E. and Stavsky Y., 1961) which ignores the effect of transverse shear deformation becomes inadequate for the analysis of multilayer composites. The First Order Shear Deformation Theories (FSDTs) based on (Reissner E., 1945) and (Mindlin RD., 1951) assume linear in-plane stresses and displacements respectively through the laminate thickness. Since FSDTs account for layerwise constant states of transverse shear stress, shear correction coefficients are needed to rectify the unrealistic variation of the shear strain/stress through the thickness. In order to overcome the limitations of FSDTs, higher

order shear deformation theories (HSDTs) that involve higher order terms in the Taylor's expansions of the displacement in the thickness coordinate were developed. (Hildebrand et al., 1949) were the first to introduce this approach to derive improved theories of plates and shells. Using the higher order theory of (Reddy, 1984) free vibration analysis of isotropic, orthotropic and laminated plates was carried out by (Reddy and Phan, 1985). A generalized Levy-type solution in conjunction with the closed form solution was developed for the bending, buckling and vibration of antisymmetric angle-ply laminated plates by A. (Khdeir A., 1989). The exact solutions were obtained for the classical Kirchhoff theory and the numerical results were compared with their counterparts using the first order transverse shear deformation theory. The comparisons showed that the results obtained within the classical laminated theory could be significantly inaccurate. A selective review of the various analytical and numerical methods used for the stress analysis of laminated composite and sandwich plates was presented by (Kant and Swaminathan, 2001). Using the higher order refined theories already reported in the literature by (Kant, 1982), (Pandya and Kant, 1988) and (Kant and Manjunatha, 1988), analytical formulations, solutions and comparison of numerical results for the buckling, free vibration and stress analyses of cross-ply composite and sandwich plates were presented by (Kant and Swaminathan, 2002).

Recently the theoretical formulations and solutions for the static analysis of antisymmetric angle-ply laminated composite and sandwich plates using various higher order refined computational models were presented by (Swaminathan and Ragounadin, 2004), (Swaminathan et al., 2006) and (Swaminathan and Patil, 2008).

THEORETICAL FORMULATION

Higher Order Shear Deformation Theory (HSDT 12)

For the first time, derived the equation of motion based on higher-order shear deformation theory (HOST 12) in the present study.

The assumptions of a higher order plate theory can also be used within equivalent single layer formulation from (Swaminathan and Patil, 2008):

$$u(x,y,z,t) = u_o(x,y,t) + z\theta_x(x,y,t)$$
$$+ z^2 u_o^*(x,y,t) + z^3 \theta_x^*(x,y,t)$$
$$v(x,y,z,t) = v_o(x,y,t) + z\theta_y(x,y,t)$$
$$+ z^2 v_o^*(x,y,t) + z^3 \theta_y^*(x,y,t) \quad (1)$$
$$w(x,y,z,t) = w_o(x,y,t) + z\theta_z(x,y,t)$$
$$+ z^2 w_o^*(x,y,t) + z^3 \theta_z^*(x,y,t)$$

1. The plate may be moderately thick.
2. The in-plane displacement u (x, y, z, t) and v (x, y, z, t) are cubic functions of z.
3. The transverse displacement w (x, y, z, t)of any point (x, y) cubic functions of z.
4. The transverse shear stress σ_{XZ}, σ_{YZ} are parabolic in z.

5. The in-plane stresses σ_X, σ_Y and τ_{XY} are cubic functions of z.
6. The normal to the mid-surface before deformation are straight, but not necessarily remaining normal to the mid-surface after deformation.
7. The transverse normal strain σ_Z is not zero.

The parameters u_o, v_o are the in-plane displacements and w_o is the transverse displacement of a point (x, y) on the middle plane. The functions θ_x, θ_y are rotations of the normal to the middle plane about *y* and *x* axes respectively. The parameters u_o^*, v_o^*, w_o^*, $\theta_x^*, \theta_y^*, \theta_z^*$ and θ_z are the higher-order terms in the Taylor's series expansion and they represent higher-order transverse cross sectional deformation modes. This is done by taking into account the parabolic variation of transverse shear stresses through the thickness of the plate (Swaminathan and Patil, 2008).

The strain components will be derived, based on the displacement, as:

$$\begin{Bmatrix} \varepsilon_x \\ \varepsilon_y \\ \varepsilon_z \\ \gamma_{xy} \end{Bmatrix} = \begin{Bmatrix} \varepsilon_{xo} \\ \varepsilon_{yo} \\ \varepsilon_{zo} \\ \varepsilon_{xyo} \end{Bmatrix} + z \begin{Bmatrix} \kappa_x \\ \kappa_y \\ \kappa_z^* \\ \kappa_{xy} \end{Bmatrix} + z^2 \begin{Bmatrix} \varepsilon_{xo}^* \\ \varepsilon_{yo}^* \\ \varepsilon_{zo}^* \\ \varepsilon_{xyo}^* \end{Bmatrix} + z^3 \begin{Bmatrix} \kappa_x^* \\ \kappa_y^* \\ 0 \\ \kappa_{xy}^* \end{Bmatrix}$$

$$\begin{Bmatrix} \gamma_{yz} \\ \gamma_{xz} \end{Bmatrix} = \begin{Bmatrix} \varphi_y \\ \varphi_x \end{Bmatrix} + z \begin{Bmatrix} \kappa_{yz} \\ \kappa_{xz} \end{Bmatrix} + z^2 \begin{Bmatrix} \varphi_y^* \\ \varphi_x^* \end{Bmatrix} + z^3 \begin{Bmatrix} \kappa_{yz}^* \\ \kappa_{xz}^* \end{Bmatrix} \quad (2)$$

where:

$$\begin{Bmatrix} \varepsilon_{xo} \\ \varepsilon_{yo} \\ \varepsilon_{xyo} \end{Bmatrix} = \begin{Bmatrix} \dfrac{\partial u_o}{\partial x} \\ \dfrac{\partial v_o}{\partial y} \\ \dfrac{\partial u_o}{\partial y} + \dfrac{\partial v_o}{\partial x} \end{Bmatrix}$$

$$\begin{Bmatrix} \varepsilon_{xo}^* \\ \varepsilon_{yo}^* \\ \varepsilon_{xyo}^* \end{Bmatrix} = \begin{Bmatrix} \dfrac{\partial u_o^*}{\partial x} \\ \dfrac{\partial v_o^*}{\partial y} \\ \dfrac{\partial u_o^*}{\partial y} + \dfrac{\partial v_o^*}{\partial x} \end{Bmatrix}$$

$$\begin{Bmatrix} \varepsilon_{zo} \\ \varepsilon_{zo}^* \end{Bmatrix} = \begin{Bmatrix} \theta_z \\ 3\theta_z^* \end{Bmatrix}$$

$$\begin{Bmatrix} \kappa_x \\ \kappa_y \\ \kappa_z^* \\ \kappa_{xy} \end{Bmatrix} = \begin{Bmatrix} \dfrac{\partial \theta_x}{\partial x} \\ \dfrac{\partial \theta_y}{\partial y} \\ 2w_o^* \\ \dfrac{\partial \theta_x}{\partial y} + \dfrac{\partial \theta_y}{\partial x} \end{Bmatrix} \qquad (3)$$

$$\begin{Bmatrix} \kappa_x^* \\ \kappa_y^* \\ \kappa_{xy}^* \end{Bmatrix} = \begin{Bmatrix} \dfrac{\partial \theta_x^*}{\partial x} \\ \dfrac{\partial \theta_y^*}{\partial y} \\ \dfrac{\partial \theta_x^*}{\partial y} + \dfrac{\partial \theta_y^*}{\partial x} \end{Bmatrix}$$

$$\begin{Bmatrix} \kappa_{xz} \\ \kappa_{yz} \end{Bmatrix} = \begin{Bmatrix} 2u_o^* + \dfrac{\partial \theta_z}{\partial x} \\ 2v_o^* + \dfrac{\partial \theta_z}{\partial y} \end{Bmatrix}$$

$$\begin{Bmatrix} \kappa_{xz}^* \\ \kappa_{yz}^* \end{Bmatrix} = \begin{Bmatrix} \dfrac{\partial \theta_z^*}{\partial x} \\ \dfrac{\partial \theta_z^*}{\partial y} \end{Bmatrix}$$

$$\begin{Bmatrix} \phi_x \\ \phi_x^* \\ \phi_y \\ \phi_y^* \end{Bmatrix} = \begin{Bmatrix} \theta_x + \dfrac{\partial w_o}{\partial x} \\ 3\theta_x^* + \dfrac{\partial w_o^*}{\partial x} \\ \theta_y + \dfrac{\partial w_o}{\partial y} \\ 3\theta_y^* + \dfrac{\partial w_o^*}{\partial y} \end{Bmatrix}$$

Substituting eq. (2) in the stress- strain relation of the lamina, the constitutive relations for any layer in the (x, y) can be expressed in the form:

$$\begin{Bmatrix} \sigma_x \\ \sigma_y \\ \sigma_z \\ \tau_{xy} \\ \tau_{yz} \\ \tau_{xz} \end{Bmatrix}_k = \begin{bmatrix} \overline{Q}_{11} & \overline{Q}_{12} & \overline{Q}_{13} & \overline{Q}_{14} & 0 & 0 \\ & \overline{Q}_{22} & \overline{Q}_{23} & \overline{Q}_{24} & 0 & 0 \\ & & \overline{Q}_{33} & \overline{Q}_{34} & 0 & 0 \\ & & & \overline{Q}_{44} & 0 & 0 \\ & Symmetric & & & \overline{Q}_{55} & \overline{Q}_{56} \\ & & & & & \overline{Q}_{66} \end{bmatrix}_k$$

$$\begin{Bmatrix} \varepsilon_{xo} \\ \varepsilon_{yo} \\ \varepsilon_{zo} \\ \varepsilon_{xyo} \\ \phi_y \\ \phi_x \end{Bmatrix} + z \begin{Bmatrix} \kappa_x \\ \kappa_y \\ \kappa_z^* \\ \kappa_{xy} \\ \kappa_{yz} \\ \kappa_{xz} \end{Bmatrix} + z^2 \begin{Bmatrix} \varepsilon_{xo}^* \\ \varepsilon_{yo}^* \\ \varepsilon_{zo}^* \\ \varepsilon_{xyo}^* \\ \phi_y^* \\ \phi_x^* \end{Bmatrix} + z^3 \begin{Bmatrix} \kappa_x^* \\ \kappa_y^* \\ 0 \\ \kappa_{xy}^* \\ \kappa_{yz}^* \\ \kappa_{xz}^* \end{Bmatrix} \qquad (4)$$

where $[\overline{Q}]$ from equ. $[\overline{Q}] = [T]^T [Q][T]$,

[Q] given by :

$Q_{11} = E_1(1 - v_{23}v_{32})/\Delta$

$Q_{12} = E_1(v_{12} - v_{31}v_{23})/\Delta$

$Q_{13} = E_1(v_{31} - v_{21}v_{32})/\Delta$

$Q_{23} = E_2(v_{32} - v_{12}v_{31})/\Delta$

$Q_{33} = E_3(1 - v_{31}v_{23})/\Delta$ $\qquad (5a)$

$Q_{44} = G_{12}$

$Q_{55} = G_{23}$

$Q_{66} = G_{13}$

where:

$\Delta = (1 - v_{12}v_{21} - v_{23}v_{32} - v_{31}v_{13} - 2v_{12}v_{23}v_{31})$ $\qquad (5b)$

And the transformation matrix [T] is given by the transformation equations:

$$\overline{Q}_{11} = Q_{11}c^4 + 2(Q_{12} + 2Q_{33})s^2c^2 + Q_{22}s^4 \qquad (5c)$$

$\overline{Q}_{12} = (Q_{11} + Q_{22} - 4Q_{33})s^2c^2$
$\qquad + Q_{12}(s^4 + c^4)$

$\overline{Q}_{13} = Q_{13}c^2 + Q_{23}s^2$

$\overline{Q}_{14} = (Q_{11} - Q_{12} - 2Q_{44}) sc^3$
$\qquad + (Q_{12} - Q_{22} + 2Q_{44})cs^3$

$\overline{Q}_{22} = Q_{11}s^4 + 2(Q_{12} + 2Q_{33})s^2c^2$
$\qquad + Q_{22}c^4$

$\overline{Q}_{23} = Q_{13}s^2 + Q_{23}c^2$

$\overline{Q}_{24} = (Q_{11} - Q_{12} - 2Q_{44})cs^3$
$\qquad + (Q_{12} - Q_{22} + 2Q_{44})sc^3$

$\overline{Q}_{33} = Q_{33}$

$\overline{Q}_{34} = (Q_{31} - Q_{32})cs$

$\overline{Q}_{44} = (Q_{11} - 2Q_{12} + Q_{22} - 2Q_{44})c^2 s^2 \qquad\qquad (5d)$
$\qquad + Q_{44} (c^4 + s^4)$

$\overline{Q}_{55} = Q_{55}s^2 + Q_{66}c^2$

$\overline{Q}_{56} = (Q_{66} - Q_{55})cs$

$\overline{Q}_{66} = Q_{55}s^2 + Q_{66}c^2$

All other elements of $[Q_{ij}]$ and $[\overline{Q}_{ij}]$ are zero.

The entire collection of forces and moments resultants for N-layered laminated are defined as:

$$
\begin{Bmatrix} N_x \\ N_y \\ N_z \\ N_{xy} \end{Bmatrix} = \int_{-h/2}^{h/2} \begin{Bmatrix} \sigma_x \\ \sigma_y \\ \sigma_z \\ \tau_{xy} \end{Bmatrix}_k dz \qquad\qquad (6a)
$$

$$
= \sum_{k=1}^{N} \begin{bmatrix} \overline{Q}_{11} & \overline{Q}_{12} & \overline{Q}_{13} & \overline{Q}_{14} \\ & \overline{Q}_{22} & \overline{Q}_{23} & \overline{Q}_{24} \\ & symmetric & \overline{Q}_{33} & \overline{Q}_{34} \\ & & & \overline{Q}_{44} \end{bmatrix}_k
$$

$$
\left\{ \int_{z_{k-1}}^{z_k} \begin{Bmatrix} \varepsilon_{xo} \\ \varepsilon_{yo} \\ \varepsilon_{zo} \\ \varepsilon_{xyo} \end{Bmatrix} dz + \int_{z_{k-1}}^{z_k} \begin{Bmatrix} \kappa_x \\ \kappa_y \\ \kappa_z^* \\ \kappa_{xy} \end{Bmatrix} z\, dz \right.
$$

$$
\left. + \int_{z_{k-1}}^{z_k} \begin{Bmatrix} \varepsilon_{xo}^* \\ \varepsilon_{yo}^* \\ \varepsilon_{zo}^* \\ \varepsilon_{xyo}^* \end{Bmatrix} z^2\, dz + \int_{z_{k-1}}^{z_k} \begin{Bmatrix} \kappa_x^* \\ \kappa_y^* \\ 0 \\ \kappa_{xy}^* \end{Bmatrix} z^3 dz \right\}
$$

$$
\begin{Bmatrix} N_x^* \\ N_y^* \\ N_z^* \\ N_{xy}^* \end{Bmatrix} = \int_{-h/2}^{h/2} \begin{Bmatrix} \sigma_x \\ \sigma_y \\ \sigma_z \\ \tau_{xy} \end{Bmatrix}_k z^2 dz
$$

$$
= \sum_{k=1}^{N} \begin{bmatrix} \overline{Q}_{11} & \overline{Q}_{12} & \overline{Q}_{13} & \overline{Q}_{14} \\ & \overline{Q}_{22} & \overline{Q}_{23} & \overline{Q}_{24} \\ & symmetric & \overline{Q}_{33} & \overline{Q}_{34} \\ & & & \overline{Q}_{44} \end{bmatrix}_k \qquad (6b)
$$

$$
\left\{ \int_{z_{k-1}}^{z_k} \begin{Bmatrix} \varepsilon_{xo} \\ \varepsilon_{yo} \\ \varepsilon_{zo} \\ \varepsilon_{xyo} \end{Bmatrix} z^2\, dz + \int_{z_{k-1}}^{z_k} \begin{Bmatrix} \kappa_x \\ \kappa_y \\ \kappa_z^* \\ \kappa_{xy} \end{Bmatrix} z^3\, dz \right.
$$

$$
\left. + \int_{z_{k-1}}^{z_k} \begin{Bmatrix} \varepsilon_{xo}^* \\ \varepsilon_{yo}^* \\ \varepsilon_{zo}^* \\ \varepsilon_{xyo}^* \end{Bmatrix} z^4\, dz + \int_{z_{k-1}}^{z_k} \begin{Bmatrix} \kappa_x^* \\ \kappa_y^* \\ 0 \\ \kappa_{xy}^* \end{Bmatrix} z^5 dz \right\}
$$

$$
\begin{Bmatrix} M_x \\ M_x \\ M_z^* \\ M_{xy} \end{Bmatrix} = \int_{-h/2}^{h/2} \begin{Bmatrix} \sigma_x \\ \sigma_y \\ \tau_{xy} \end{Bmatrix}_k z\, dz_k
$$

$$
= \sum_{k=1}^{N} \begin{bmatrix} \overline{Q}_{11} & \overline{Q}_{12} & \overline{Q}_{13} & \overline{Q}_{14} \\ & \overline{Q}_{22} & \overline{Q}_{23} & \overline{Q}_{24} \\ & symmetric & \overline{Q}_{33} & \overline{Q}_{34} \\ & & & \overline{Q}_{44} \end{bmatrix}_k \qquad (6c)
$$

$$
\left\{ \int_{z_{k-1}}^{z_k} \begin{Bmatrix} \varepsilon_{xo} \\ \varepsilon_{yo} \\ \varepsilon_{zo} \\ \varepsilon_{xyo} \end{Bmatrix} z\, dz + \int_{z_{k-1}}^{z_k} \begin{Bmatrix} \kappa_x \\ \kappa_y \\ \kappa_z^* \\ \kappa_{xy} \end{Bmatrix} z^2\, dz \right.
$$

$$
\left. + \int_{z_{k-1}}^{z_k} \begin{Bmatrix} \varepsilon_{xo}^* \\ \varepsilon_{yo}^* \\ \varepsilon_{zo}^* \\ \varepsilon_{xyo}^* \end{Bmatrix} z^3\, dz + \int_{z_{k-1}}^{z_k} \begin{Bmatrix} \kappa_x^* \\ \kappa_y^* \\ 0 \\ \kappa_{xy}^* \end{Bmatrix} z^4 dz \right\}
$$

$$\begin{Bmatrix} M_x^* \\ M_y^* \\ 0 \\ M_{xy}^* \end{Bmatrix} = \int_{-h/2}^{h/2} \begin{Bmatrix} \sigma_x \\ \sigma_y \\ \sigma_z \\ \tau_{xy} \end{Bmatrix}_k z^3 \, dz$$

$$= \sum_{k=1}^{N} \begin{bmatrix} \overline{Q}_{11} & \overline{Q}_{12} & \overline{Q}_{13} & \overline{Q}_{14} \\ & \overline{Q}_{22} & \overline{Q}_{23} & \overline{Q}_{24} \\ & symmetric & \overline{Q}_{33} & \overline{Q}_{34} \\ & & & \overline{Q}_{44} \end{bmatrix}_k$$

(6d)

$$\left\{ \int_{z_{k-1}}^{z_k} \begin{Bmatrix} \varepsilon_{xo} \\ \varepsilon_{yo} \\ \varepsilon_{zo} \\ \varepsilon_{xyo} \end{Bmatrix} z^3 \, dz + \int_{z_{k-1}}^{z_k} \begin{Bmatrix} \kappa_x \\ \kappa_y \\ \kappa_z^* \\ \kappa_{xy} \end{Bmatrix} z^4 \, dz \right.$$

$$\left. + \int_{z_{k-1}}^{z_k} \begin{Bmatrix} \varepsilon_{xo}^* \\ \varepsilon_{yo}^* \\ \varepsilon_{zo}^* \\ \varepsilon_{xyo}^* \end{Bmatrix} z^5 \, dz + \int_{z_{k-1}}^{z_k} \begin{Bmatrix} \kappa_x^* \\ \kappa_y^* \\ 0 \\ \kappa_{xy}^* \end{Bmatrix} z^6 \, dz \right\}$$

$$\begin{Bmatrix} Q_y \\ Q_x \end{Bmatrix} = \int_{-h/2}^{h/2} \begin{Bmatrix} \tau_{yz} \\ \tau_{xz} \end{Bmatrix}_k dz$$

$$= \sum_{k=1}^{N} \begin{bmatrix} \overline{Q}_{55} & \overline{Q}_{56} \\ \overline{Q}_{56} & \overline{Q}_{66} \end{bmatrix}_k$$

(6e)

$$\left\{ \int_{z_{K-1}}^{z_K} \begin{Bmatrix} \phi_y \\ \phi_x \end{Bmatrix} dz + \int_{z_{K-1}}^{z_K} \begin{Bmatrix} \kappa_{yz} \\ \kappa_{xz} \end{Bmatrix} z \, dz \right.$$

$$\left. + \int_{z_{K-1}}^{z_K} \begin{Bmatrix} \phi_y^* \\ \phi_x^* \end{Bmatrix} z^2 \, dz + \int_{z_{K-1}}^{z_K} \begin{Bmatrix} \kappa_{yz}^* \\ \kappa_{xy}^* \end{Bmatrix} z^3 \, dz \right\}$$

$$\begin{Bmatrix} Q_y^* \\ Q_x^* \end{Bmatrix} = \int_{-h/2}^{h/2} \begin{Bmatrix} \tau_{yz} \\ \tau_{xz} \end{Bmatrix}_k z^2 \, dz$$

$$= \sum_{k=1}^{N} \begin{bmatrix} \overline{Q}_{55} & \overline{Q}_{56} \\ \overline{Q}_{56} & \overline{Q}_{66} \end{bmatrix}_k$$

(6f)

$$\left\{ \int_{z_{K-1}}^{z_K} \begin{Bmatrix} \phi_y \\ \phi_x \end{Bmatrix} z^2 \, dz + \int_{z_{K-1}}^{z_K} \begin{Bmatrix} \kappa_{yz} \\ \kappa_{xz} \end{Bmatrix} z^3 \, dz \right.$$

$$\left. + \int_{z_{K-1}}^{z_K} \begin{Bmatrix} \phi_y^* \\ \phi_x^* \end{Bmatrix} z^4 \, dz + \int_{z_{K-1}}^{z_K} \begin{Bmatrix} \kappa_{yz}^* \\ \kappa_{xy}^* \end{Bmatrix} z^5 \, dz \right\}$$

$$\begin{Bmatrix} S_y \\ S_x \end{Bmatrix} = \int_{-h/2}^{h/2} \begin{Bmatrix} \tau_{yz} \\ \tau_{xz} \end{Bmatrix}_k z \, dz$$

$$= \sum_{k=1}^{N} \begin{bmatrix} \overline{Q}_{55} & \overline{Q}_{56} \\ \overline{Q}_{56} & \overline{Q}_{66} \end{bmatrix}_k$$

$$\left\{ \int_{z_{K-1}}^{z_K} \begin{Bmatrix} \phi_y \\ \phi_x \end{Bmatrix} z \, dz + \int_{z_{K-1}}^{z_K} \begin{Bmatrix} \kappa_{yz} \\ \kappa_{xz} \end{Bmatrix} z^2 \, dz \right.$$ (6g)

$$\left. + \int_{z_{K-1}}^{z_K} \begin{Bmatrix} \phi_y^* \\ \phi_x^* \end{Bmatrix} z^3 \, dz \right.$$

$$\left. + \int_{z_{K-1}}^{z_K} \begin{Bmatrix} \kappa_{yz}^* \\ \kappa_{xy}^* \end{Bmatrix} z^4 \, dz \right\}$$

$$\begin{Bmatrix} S_y^* \\ S_x^* \end{Bmatrix} = \int_{-h/2}^{h/2} \begin{Bmatrix} \tau_{yz} \\ \tau_{xz} \end{Bmatrix}_k z^3 \, dz$$

$$= \sum_{k=1}^{N} \begin{bmatrix} \overline{Q}_{55} & \overline{Q}_{56} \\ \overline{Q}_{56} & \overline{Q}_{66} \end{bmatrix}_k$$

(6h)

$$\left\{ \int_{z_{K-1}}^{z_K} \begin{Bmatrix} \phi_y \\ \phi_x \end{Bmatrix} z^3 \, dz + \int_{z_{K-1}}^{z_K} \begin{Bmatrix} \kappa_{yz} \\ \kappa_{xz} \end{Bmatrix} z^4 \, dz \right.$$

$$\left. + \int_{z_{K-1}}^{z_K} \begin{Bmatrix} \phi_y^* \\ \phi_x^* \end{Bmatrix} z^5 \, dz + \int_{z_{K-1}}^{z_K} \begin{Bmatrix} \kappa_{yz}^* \\ \kappa_{xy}^* \end{Bmatrix} z^6 \, dz \right\}$$

Laminate Constitutive Equations

$$
\begin{Bmatrix} N_x \\ N_y \\ N_z \\ N_{xy} \\ N_x^* \\ N_y^* \\ N_z^* \\ N_{xy}^* \\ M_x \\ M_y \\ M_z^* \\ M_{xy} \\ M_x^* \\ M_y^* \\ 0 \\ M_{xy}^* \end{Bmatrix}
=
\begin{bmatrix} [A_{ij}] & [B_{ij}] & [D_{ij}] & [E_{ij}] \\ & [D_{ij}] & [E_{ij}] & [F_{ij}] \\ & & [F_{ij}] & [G_{ij}] \\ SYM & & & [H_{ij}] \end{bmatrix}
\begin{Bmatrix} \varepsilon_x \\ \varepsilon_y \\ \varepsilon_{zo} \\ \varepsilon_{xyo} \\ \kappa_x \\ \kappa_y \\ \kappa_z^* \\ \kappa_{xy} \\ \varepsilon_{xo}^* \\ \varepsilon_{yo}^* \\ \varepsilon_{zo}^* \\ \varepsilon_{xyo}^* \\ \kappa_x^* \\ \kappa_y^* \\ 0 \\ \kappa_{xy}^* \end{Bmatrix}
\tag{7}
$$

$$
\begin{Bmatrix} Q_y \\ Q_x \\ Q_y^* \\ Q_x^* \\ S_y \\ S_x \\ S_y^* \\ S_x^* \end{Bmatrix}
=
\begin{bmatrix} [A_{ij}] & [B_{ij}] & [D_{ij}] & [E_{ij}] \\ & [D_{ij}] & [E_{ij}] & [F_{ij}] \\ & & [F_{ij}] & [G_{ij}] \\ SYM & & & [H_{ij}] \end{bmatrix}
\begin{Bmatrix} \phi_y \\ \phi_x \\ \kappa_{yz} \\ \kappa_{xz} \\ \phi_y^* \\ \phi_x^* \\ \kappa_{yz}^* \\ \kappa_{xz}^* \end{Bmatrix}
$$

where the overall laminate stiffnesses A_{ij}, B_{ij}, D_{ij}, E_{ij}, F_{ij}, G_{ij} and H_{ij} are:

$$
\left(A_{ij}, B_{ij}, D_{ij}, E_{ij}, F_{ij}, G_{ij}, H_{ij} \right)
= \int_{-h/2}^{h/2} \overline{Q}_{ij}^{(k)} \left(1, z, z^2, z^3, z^4, z^5, z^6 \right) dz
\tag{8}
$$

$$i, j = 1, 2, 3, 4, 5, 6, 7)$$

If A_{ij}, B_{ij}, etc, are written in terms of the ply stiffness $\overline{Q}_{ij}^{(k)}$ and the ply coordinates z_k and z_{k-1}, the following is obtained:

$$
\left(A_{ij}, B_{ij}, D_{ij}, E_{ij}, F_{ij}, G_{ij}, H_{ij} \right) =
\frac{1}{n} \sum_{k=1}^{N} \overline{Q}_{ij}^{(k)} \left(z_{k+1}^n - z_k^n \right)
\tag{9}
$$

$$(n = 1, 2, 3, 4, 5, 6, 7)$$

Differential Equations of Equilibrium of Laminated Plates

The equilibrium differential equations in terms of the moments and forces resultants for a plate are (Swaminathan and Patil, 2008):

$$N_{x,x} + N_{xy,y} = I_1\ddot{u}_0 + I_2\ddot{\theta}_x$$
$$+ I_3\ddot{u}_0^* + I_4\ddot{\theta}_x^*$$
$$N_{y,y} + N_{xy,x} = I_1\ddot{v}_0 + I_2\ddot{\theta}_y$$
$$+ I_3\ddot{v}_0^* + I_4\ddot{\theta}_y^*$$
$$Q_{x,x} + Q_{y,y} + P_z = I_1\ddot{w}_0 + I_2\ddot{\theta}_z$$
$$+ I_3\ddot{w}_0^* + I_4\ddot{\theta}_z^*$$
$$M_{x,x} + M_{xy,y} - Q_x = I_2\ddot{u}_0$$
$$+ I_3\ddot{\theta}_x + I_4\ddot{u}_0^* + I_5\ddot{\theta}_x^*$$
$$M_{y,y} + M_{xy,x} - Q_x = I_2\ddot{v}_0$$
$$+ I_3\ddot{\theta}_y + I_4\ddot{v}_0^* + I_5\ddot{\theta}_y^*$$
$$S_{x,x} + S_{y,y} - N_z + \frac{h}{2}(P_z) = I_2\ddot{w}_0$$
$$+ I_3\ddot{\theta}_z + I_4\ddot{w}_0^* + I_5\ddot{\theta}_z^*$$
$$N_{x,x}^* + N_{xy,y}^* - 2S_x = I_3\ddot{u}_0$$
$$+ I_4\ddot{\theta}_x + I_5\ddot{u}_0^* + I_6\ddot{\theta}_x^*$$
$$N_{y,y}^* + N_{xy,x}^* - 2S_y = I_3\ddot{v}_0$$
$$+ I_4\ddot{\theta}_y + I_5\ddot{v}_0^* + I_6\ddot{\theta}_y^*$$
$$Q_{x,x}^* + Q_{xy,y}^* - 2M_2^* + \frac{h^2}{4}(P_z) = I_3\ddot{w}_0$$
$$+ I_4\ddot{\theta}_z + I_5\ddot{w}_0^* + I_6\ddot{\theta}_z^*$$
$$M_{x,x}^* + M_{xy,y}^* - 3Q_x^* = I_4\ddot{u}_0$$
$$+ I_5\ddot{\theta}_x + I_6\ddot{u}_0^* + I_7\ddot{\theta}_x^*$$
$$M_{y,y}^* + M_{xy,x}^* - 3Q_y^* = I_4\ddot{v}_0 + I_5\ddot{\theta}_y$$
$$+ I_6\ddot{v}_0^* + I_7\ddot{\theta}_y^*$$
$$S_{x,x}^* + S_{y,y}^* - 3N_z^* + \frac{h^3}{8}(P_z) = I_4\ddot{w}_0 + I_5\ddot{\theta}_z$$
$$+ I_6\ddot{w}_0^* + I_7\ddot{\theta}_z^*$$

(10)

The following plate inertia can be introduced:

$$\left(I_1, I_2, I_3, I_4, I_5, I_6, I_7\right) =$$
$$\sum_{k=1}^{N} \int_{z_k}^{z_{k+1}} \rho^{(k)}\left(1, z, z^2, z^3, z^4, z^5, z^6\right)dz$$

(11)

If the material for all the layer is identical, that is if the density $\rho^{(k)}$ is the same for all k, then

$$I_2 = I_4 = I_6 = 0$$

(12)

Exact Solution for Simply Supported Rectangular Plates

The exact analytical solution of the differential eq. (1) *(HOST 12)* for a general laminate plate under arbitrary boundary conditions are impossible task. However, closed-form solution for 'simply-supported' rectangular plates is to be considered.

The following simply supported boundary conditions are assumed (see fig. 1).

B. C. of cross-ply laminated plate associated SS-1 :

At edges $x = 0$ and $x = a$:
$$v_0 = 0, \quad w_0 = 0, \quad \theta_y = 0, \quad \theta_z = 0, \quad M_x = 0,$$
$$v_0^* = 0, \quad w_0^* = 0, \quad \theta_y^* = 0, \quad \theta_z^* = 0, \quad M_x^* = 0,$$
$$N_x = 0, \quad N_x^* = 0.$$

At edges $y = 0$ and $y = b$:
$$u_0 = 0, \quad w_0 = 0, \quad \theta_x = 0, \quad \theta_z = 0, \quad M_y = 0,$$
$$u_0^* = 0, \quad w_0^* = 0, \quad \theta_x^* = 0, \quad \theta_z^* = 0, \quad M_y^* = 0,$$
$$N_y = 0, \quad N_y^* = 0.$$

(13a)

B. C. of angle-ply laminated plate associated SS-2 :

At edges $x = 0$ and $x = a$;
$$u_o = 0; \quad w_o = 0; \quad \theta_y = 0; \quad \theta_z = 0; \quad M_x = 0; \quad N_{xy} = 0;$$
$$u_o^* = 0; \quad w_o^* = 0; \quad \theta_y^* = 0; \quad \theta_z^* = 0; \quad M_x^* = 0; \quad N_{xy}^* = 0.$$

At edges $y = 0$ and $y = b$;
$$v_o = 0; \quad w_o = 0; \quad \theta_x = 0; \quad \theta_z = 0; \quad M_y = 0; \quad N_{xy} = 0;$$
$$v_o^* = 0; \quad w_o^* = 0; \quad \theta_x^* = 0; \quad \theta_z^* = 0; \quad M_y^* = 0; \quad N_{xy}^* = 0$$
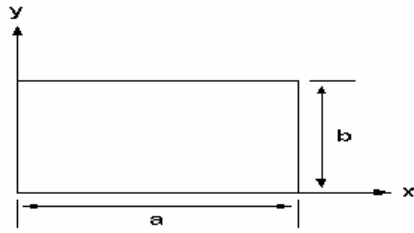
(13b)

Fig. 1 Geometry and the co-ordinate system of a rectangular plate of thickness h

Equation of Motion in Terms of Displacements HOST12

For the first time, the equations of motion to the HOST12 eq. (1) can be expressed in terms of displacements $\left(u_0, v_0, w_0, \theta_x, \theta_y, \theta_z, u_0^*, v_0^*, w_0^*, \theta_x^*, \theta_y^*, \theta_z^*\right)$ by Substituting eq. (6) into eq. (10) as in (Salam Ahmed A., 2008).

Free Vibration Solution by HOST12

The following form of solution satisfies the differential the equations of motion and the boundary condition eq. (13), when the applied load q (x, y, t) on the right hand side of the equations of motion is set to zero.

$$w_0 = \sum_{m,n=1}^{\infty} w_{0mn} \sin\alpha x \sin\beta y e^{i\omega_{mn}t},$$

$$w_0^* = \sum_{m,n=1}^{\infty} w_{0mn}^* \sin\alpha x \sin\beta y e^{i\omega_{mn}t},$$

$$\theta_x = \sum_{m,n=1}^{\infty} \theta_{xmn} \cos\alpha x \sin\beta y e^{i\omega_{mn}t},$$

$$\theta_x^* = \sum_{m,n=1}^{\infty} \theta_{xmn}^* \cos\alpha x \sin\beta y e^{i\omega_{mn}t},$$

$$\theta_y = \sum_{m,n=1}^{\infty} \theta_{ymn}^* \sin\alpha x \cos\beta y e^{i\omega_{mn}t},$$ (14a)

$$\theta_y^* = \sum_{m,n=1}^{\infty} \theta_{ymn}^* \sin\alpha x \cos\beta y e^{i\omega_{mn}t},$$

$$\theta_z = \sum_{m,n=1}^{\infty} \theta_{zmn} \sin\alpha x \sin\beta y e^{i\omega_{mn}t},$$

$$\theta_z^* = \sum_{m,n=1}^{\infty} \theta_{zmn}^* \sin\alpha x \sin\beta y e^{i\omega_{mn}t}$$

For antisymmetric cross-ply laminates:

$$u_0 = \sum_{m,n=1}^{\infty} u_{0mn} \cos\alpha x \sin\beta y e^{i\omega_{mn}t},$$

$$u_0^* = \sum_{m,n=1}^{\infty} u_{0mn}^* \cos\alpha x \sin\beta y e^{i\omega_{mn}t},$$ (14b)

$$v_0 = \sum_{m,n=1}^{\infty} v_{0mn} \sin\alpha x \cos\beta y e^{i\omega_{mn}t},$$

$$v_0^* = \sum_{m,n=1}^{\infty} v_{0mn}^* \sin\alpha x \cos\beta y e^{i\omega_{mn}t}$$

For antisymmetric angle-ply laminates:

$$u_0 = \sum_{m,n=1}^{\infty} u_{0mn} \sin\alpha x \cos\beta y e^{i\omega_{mn}t},$$

$$u_0^* = \sum_{m,n=1}^{\infty} u_{0mn}^* \sin\alpha x \cos\beta y e^{i\omega_{mn}t},$$ (14 c)

$$v_0 = \sum_{m,n=1}^{\infty} v_{0mn} \cos\alpha x \sin\beta y e^{i\omega_{mn}t},$$

$$v_0^* = \sum_{m,n=1}^{\infty} v_{0mn}^* \cos\alpha x \sin\beta y e^{i\omega_{mn}t},$$

By substituting eq. (14) into the equations of motion and expressing the a result in matrix form the following is obtained:

$$\left[[K] - w_{mn}^2 [M]\right]\{\Delta\} = \{0\}$$ (15)

The elements of the matrix [K] (*Stiffness Matrix*) [M] (*Mass Matrix*) are given in (Salam Ahmed A., 2008).

RESULT AND DISCUSSION

In the following, it is assumed that the material is fiber-reinforced and remains in the elastic range. The boundary conditions are SSSS, and the analytical procedure (HOST 12) is used in this work.

The material properties are :-
$E_2 = 6.92 \times 10^9$ N/m^2, $E_1 = 40E_2$,
$G_{12} = G_{13} = 0.5E_2$, $G_{23} = 0.6E_2$, $v_{12} = 0.25$

Dimensions of plate:

a=1 m ,   b=1 m   ,   h=0.02 m

Table 1 Effect of degree of orthotropy of individual layers on the fundamental frequency of simply supported symmetric square laminates: a/h=5, $\bar{\omega} = 10x\omega(\rho h^2 / E_2)^{\frac{1}{2}}$

No. of layers	Source	E1/E2				
		3	10	20	30	40
3	Exact	2.6474	3.2841	3.8241	4.1089	4.3006
	GTTR	2.6286	3.2679	3.7011	3.9456	4.1150
	Present HOST 12	2.5271	3.2197	3.6834	3.9442	4.1198
	% error*	4.54%	1.96%	4.99%	4.00%	4.20%
5	Exact	2.6587	3.4089	3.9792	4.3140	4.5374
	GTTR	2.6416	3.3802	3.9439	4.2809	4.5106
	Present HOST 12	2.5009	3.2913	3.8905	4.2476	4.4901
	% error	5.93%	3.44%	2.22%	1.53%	1.04%
7	Exact	2.6640	3.4432	4.0547	4.4210	4.6679
	GTTR	2.6460	3.4202	4.0310	4.4008	4.6533
	Present HOST 12	2.4508	3.2729	3.9204	4.3120	4.5780
	% error	8.00%	4.94%	3.31%	2.46%	1.92%

*Values in parenthesis the give percentage error for natural frequency with respect to exact solution mentioned above (Bose P. & Reddy J. N., 1998). GTTR (General Third Order Theory of Reddy) (Bose P. & Reddy J. N., 1998).
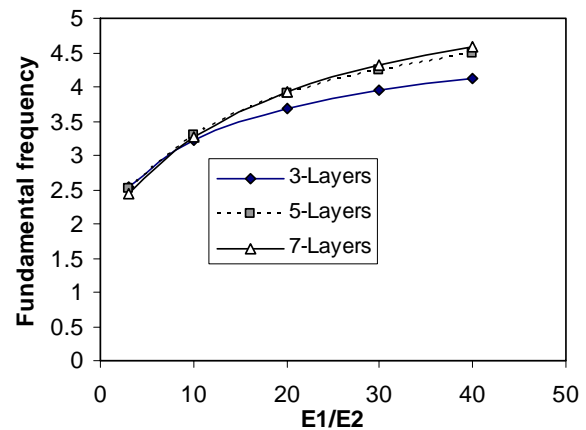
Fig. 2 Effect of degree of orthotropy of individual layers on the fundamental frequency of simply supported symmetric square laminates using (HOST 12):

a/h=5, $\bar{\omega} = 10x\omega(\rho h^2 / E_2)^{\frac{1}{2}}$

Table 2 shows analytical solutions of the variation of natural frequencies with respect to side-to-thickness ratio a/h for different E1/E2 ratio for two and four layered a simply supported antisymmetric angle-ply (45/-45/…) square laminated plate E1/E2 = open, E2 = E3, G12 = G13 = 0.6E2, G23 = 0.5E2, $\upsilon12 = \upsilon13 = \upsilon23 = 0.25$.

Table 2 Analytical effect of degree of orthotropy and (a/h) ratio of individual layers on the fundamental frequency $\overline{\omega} = (\omega\, a^2 / h) x \left(\rho / E_2\right)^{\frac{1}{2}}$

No. of layers	E_1/E_2	Source	a/h			
			2	4	10	100
2	3	GTTR	4.5312	6.1223	7.1056	7.3666
		HOST12	4.6159	6.2572	7.2879	7.5013
		Error %	1.87 %	2.20 %	2.56 %	1.82 %
	10	GTTR	4.9742	7.2647	8.9893	9.5123
		HOST12	5.0312	7.4041	9.1163	9.6453
		Error %	1.15 %	1.91 %	1.41 %	1.39 %
	20	GTTR	5.1817	8.0490	10.6412	11.5385
		HOST12	5.2725	8.1604	10.7724	11.6738
		Error %	1.75 %	1.38 %	1.23 %	1.17 %
	40	GTTR	5.3325	8.8426	12.9115	14.6668
		HOST12	5.3817	8.8933	13.0762	14.7414
		Error %	0.92 %	0.57 %	1.27 %	0.50 %
4	3	GTTR	4.6498	6.4597	7.6339	7.9545
		HOST12	4.7628	6.6133	7.8131	8.1412
		Error %	2.43 %	2.37 %	2.34 %	2.35 %
	10	GTTR	5.2061	8.3447	11.4116	12.5351
		HOST12	5.3307	8.4752	11.5777	12.6353
		Error %	2.40 %	1.56 %	1.45 %	0.79 %
	20	GTTR	5.4140	9.3306	14.4735	16.9927
		HOST12	5.5308	9.4927	14.6128	17.1034
		Error %	2.16 %	1.73 %	0.96 %	0.65 %
	40	GTTR	5.5674	10.0731	17.8773	23.4499
		HOST12	5.6147	10.1535	17.9268	23.5912
		Error %	0.85 %	0.80 %	0.30 %	0.60 %

*Values in parenthesis the give percentage error for natural frequency with respect to exact solution mentioned above (Swaminathan and Patil, 2008). GTTR (General Third Order Theory of Reddy) (Swaminathan and Patil, 2008).
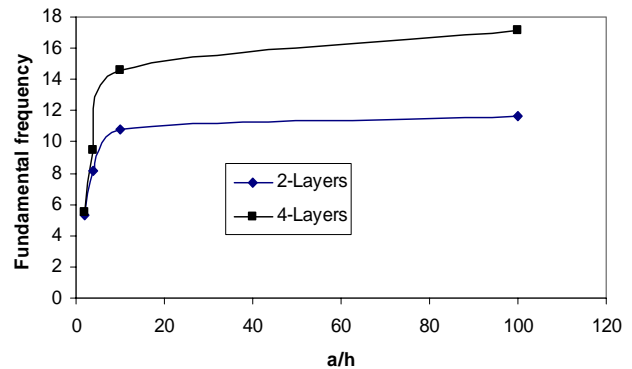
Fig. 3 Analytical effect of degree of (a/h) ratio of individual layers on the fundamental frequency using (HOST 12): $E_1/E_2 = 20$, $\overline{\omega} = (\omega\, a^2 / h) x \left(\rho / E_2\right)^{\frac{1}{2}}$
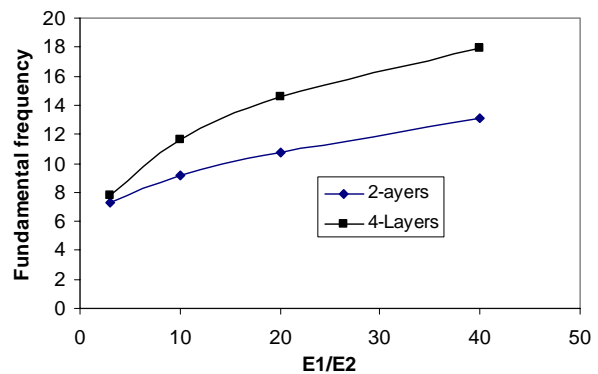
Fig. 4 Analytical effect of degree of orthotropy of individual layers on the fundamental frequency using (HOST 12): a/h=10, $\overline{\omega} = (\omega\, a^2 / h) x \left(\rho / E_2\right)^{\frac{1}{2}}$

It is also demonstrated that increasing the fundamental frequency with increases the degrees of orthotropy (E_1/E_2) for laminate plate due to the increase plate stiffness. The number of layers has different effects in laminated plates. As the span-to-thickness

ratio (a/h) increases, the fundamental frequency decreases, due to the decrease in the stiffness of the plate, but the factor of nondimensional is gives opposite relation.

CONCLUSIONS

1. Analytical formulations and solutions to the natural frequency analysis of simply supported antisymmetric angle-ply composite and sandwich plates hitherto not reported in the literature based on a higher order refined theory which takes in to account the effects of both transverse shear and transverse normal deformations are presented. The accuracy of the present computational model with 12 degrees of freedom in comparison to other higher order model with five degrees of freedom has been established.

2. The effect of degree of (a/h) ratio becomes more pronounced as the number of layers increases. Increasing the ratio (a/h) from (2 to 20) the natural frequency very increases and from (20 to 100) remains stable roughly for (E_1/E_2= 20).

3. The effect of degree of orthotropy (E1/E2) becomes more pronounced as the number of layers increases (for the same laminate thickness). Increasing the ratio (E1/E2) from (10 to 40) increases the natural frequency for (a/h = 5) and (a/h=10).

It has been concluded that for all the parameters considered Reddy's theory very much over predicts the natural frequency values both for the composite and sandwich plates.

REFERENCES

- Bose P. & Reddy J. N., 1998,"Analysis of Composite Plates Using Various Plate Theories. *Part 1*: Formulation and Analytical Solutions", J. Structural Engineering and Mechanics, Vol. 6, No. 6, 583-612,.

- Bose P.& Reddy J. N., 1998, "Analysis of Composite Plates Using Various Plate Theories. *Part 2*: Finite Element Model and Numerical Results", J. Structural Engineering and Mechanics, Vol. 6, No. 7, p.p. 727-746,.

- Hildebrand FB, Reissner E, Thomas GB., 1949, "Note on the foundations of the theory of small displacements of orthotropic shells", NACA TN-1833.

- Kant T., 1982, "Numerical analysis of thick plates. Comput Methods", Appl Mech Eng,31,1–18.

- Kant T., Manjunatha BS., 1988, "An unsymmetric FRC laminate C_ finite element model with twelve degrees of freedom per node", Eng Comput,5(3),300–8.

- Kant T., Swaminathan K., 2001, "Analytical solutions for free vibration of laminated composite and sandwich plates based on a higher order refined theory", Compos Struct,53(1),73–85.

- Kant T., Swaminathan K., 2002, "Analytical solutions for static analysis of laminated composite and sandwich plates based on a higher order refined theory", Compos Struct,56(4),329–44.

- Kant T., Mallikarjuna., 1989, "A higher order theory for free vibration of unsymmetrically laminated composite and sandwich plates – finite element evaluation", Comput Struct,32,1125–32.

- Kant T., Swaminathan K., 2001, "Estimation of transverse/interlaminar stresses in laminated composites – a selective review and survey of current developments", Compos Struct., 49(1), 65–75.

- Khdeir A. A., 1989, " Comparison between Shear Deformation and Kirchhoff Theories for Bending, Buckling and Vibration of Antisymmetric Angle-Ply Laminated Plates ", J. Composite Structures 13, 159-172.

- Mallikarjuna, Kant T., 1989, "Free vibration of symmetrically laminated plates using a higher order theory with finite element technique", Int J. Numer Methods Eng,28,1875–89.

- Mindlin RD., 1951, "Influence of rotary inertia and shear on flexural motions on isotropic, elastic plates", J Appl. Mech., 18,31–8.

- Pandya BN, Kant T., 1987, "A consistent refined theory for flexure of a symmetric laminate", Mech Res Commun,14,107–13.

- Pandya BN, Kant T., 1988, "Higher order shear deformable theories for flexure of sandwich plates – finite element evaluations", Int. J Solids Struct., 24(12), 1267–86.

- Reddy JN., 1984, "A simple higher-order theory for laminated composite plates", J Appl Mech., 51, 745–52.

- Reddy JN, Phan ND., 1985, "Stability and vibration of isotropic, orthotropic and laminated plates according to higher order shear deformation theory", J Sound Vib., 98(2), 157–70.

- Reissner E., 1945, "The effect of transverse shear deformation on the bending of elastic plates", J Appl. Mech., 12(2), 69–77.

- Reissner E, Stavsky Y., 1961, "Bending and stretching of certain types of heterogeneous aelotropic elastic plates", J Appl Mech., 28, 402–8.

- Salam Ahmed A., 2008, "Dynamic Analysis of Composite Laminated Plates", M. Sc, Thesis.

- Swaminathan K, Patil SS., 2007, "Higher order refined computational model with 12 degrees of freedom for the stress analysis of antisymmetric angle ply plates – analytical solutions. Compos Struct. 80, 595–608.

- Swaminathan K. & Patil S.S., 2008," Analytical solutions using a higher order refined computational model with 12 degrees of freedom for the free vibration analysis of antisymmetric angle-ply plates", Compos Struct. 82, 209–216.

‒

:ــــــــ

.

(   )   ( )

.

.

)   .

.(

The Effect of Spatial Organization on the Sustainability of the Neighborhood Unit in the Residential Environment

Abstract

Contemporary residential neighborhoods suffer from weak sustainability of urban residential environments as a result of the adoption of inefficient spatial organization at the neighborhood unit level. This resulted negative characteristics which affected the achievement of sustainable development plans for the residential environment that constitute the majority of the urban fabric of cities.

The physical affordances ,within the vocabulary of recent times,overcame the spiritual ones and affected the residential environment. Accordingly,the concept of space changed in contemporary residential areas through the dominance of the physical aspect (mass) on the symbolic aspect (space).The modern technology occupied an important level being one of the basic features of the era. Therefore, achieving sustainability at the urban level of the residential environment requires an efficient spatial organization which ensures the linking of urban space with the surroundings, and the new services together with the basic ones that need maintenance and rehabilitation.

The weak sustainability of the built residential environment constitutes the main research problem. This problem results from the inefficiency of space organization at the neighborhood unit level. The research aims to establish spatial organized mechanisms at the neighborhood unit level that would achieve sustainability through the investment of sustainable factors of traditional residential environment in the planning and design of modern neighborhood,as well as the adoption of human design strategies to raise the efficiency of spatial organization.The research stems for a hypothesis that states **(the efficient spatial organization at the neighborhood unit level produces a sustainable urban environment at the level of larger residential neighborhood).**

.1

:

.

1 .1   .

.1.1.1

(   )

(3- 2008) . ‫.‬ "John Elkington)

( )

‫":‬

.(6- 2006)

‫.‬ (Elkington1999 p.75)

‫.‬

1.1.3.

.(2- 2006) .

1. 1. 2

‫.‬

‫:‬

●

‫.‬

●

‫.‬

:.(79- -2006

‫:‬

‫.‬

‫:‬

●

‫.‬

‫:‬ 30 – 31 2006)

‫) .‬

‫.‬

-T.B.L)

1.1. 4 .

(Triple Bottomline .

20

.

.(2008-   ): .   (51-   2006 –   ).

:   :-

.

:   .   (Liddle)

Barton-)-   )

(2000,p7

(   )   :

.   •

.   •

•

•

5.1.1.   •

.   •

(   )

.

.   •

(Barton)

:   .

- (accessibility)

- (proimity)

- (functiona mix)   .

(Williams-)   :

(1

.

(2

.

(2008-).

(3

.   .

(4   ( )   .

(5

.

-   2006-   ).

(6

.(202

(7

.6.1.1.1

(.Williams&Barton ,2000,p8)

1-   :

(3.1.1   )

6 .1.1

.

.

:

( )

1- ـــــــــــــــــ :   .

ـــــــــــــــــ :

.

: (Baker&Steemer,2000,0)-p4) :ـ

.

:-   :-

.   .

:-   :-

.

)   .

.(

:-   :-

2- ـــــــــــــــــ :

(ـ)

(ـــــــــــــ)

(ـ ـ ـ

.

.   .

2- ــــــــــــــــــــــــ **: –**

.

.

.(Kim&Rigdon,1998A,p.27)

3– ـــــــــــــــــــــ ( ):

.

.

.

: –

.

1. – (–) (– .

.(1986 201).

. –: ـــــــــــــــــــــــــــــــ

.

2. .

.(142– 2006–).

- (600- 200)
.(3000-8000)

(164- 2010-).

- (–)
.(–)

1923

(Perry)

-

- .(5000)

-

)

(newurbanism –)

1927

.

(Mumford) .

.

(143- 2010-).

(5 – 10

.

1977

.

( )

(400 – 500)

:-

‒

.   .

‒:

.

‒

.

.   .

‒

(2009‒   )   .

:

. (144   ‒   )   .

.

.2

.1.2 :

.

(   ) .

.

(116-   -2010-   ).   .(1)   .

(   )

.

.

) –   –   –

(

. (73-   -1988-   ).

.

)

(.

.

(6-   -2004-   ).

.   .(2)

1.1.2

.

-      ).

(2009

.

.

.   (117-   -2010-   ) .(3)

.

.

2.1.2

(_____)   . (4)   (3)

(Lynch-1981-p115)

.

*

:

*

GridIron)

.(Pattern

.

(2009-   ).(4)

*   . (Lynch-p1981-p144-149)

*

)

(   )   (

.

(127   ) .

(   )   (

.

.

:

:

. maicroclimate

<u>:   **.1.2.2**</u>

*

:

•

.

•

.. （5).

2.2.
<u>:   </u>

.

(500-1000)

.(

•

.

•

)

30

●

.

●   (   )   (–   –   –   –)
                                                                        (

.

.(6)

2.2.2
:

-2   :

:

:

:   -1

●

.

.

●

.

●   .   ●

:

●   (–   –)

●

(–)   (–)

.

●

.

<u>3-</u>   <u>:</u>

‎-1

.(8) (7)‏

<u>3-</u>   <u>:</u>

‎*

)‏

(-Chen)   .

(2008

)‏

(‏

:‏

●   :

.

●   .   ●
                                                                            ●

.   ●
                                                                            ●

.

●   .

.

‎*   ●

.

‎-2

32

.

*

)   –

(–

.

.   .

- <u>المصادر</u>

*

- <u>المصادر باللغة العربية:</u>

-

–

.1986–

-    –

–

.

.2006

*

-

.

*

17–

.

2004/–21

.2004

-

.   –   .

-

*

ArchitectureModule:Indroduction to Sustainable Design, National Pollution Prevention Center for Higher Education,Michigan.USA.

- Lynch,Kevi:"Atheory of Good City Form";TheMIT press,Cambridge,Massachusetts,1981.

- –Williams,Kati,Barton,Elizabeth and JenkssMike,2000"Achieving Sustainable Urban Form".E&FN Span.

-

5-   -   -
                    7   2007.

•

                      -
                  2010.

•

            2
        1988.

•   .

            (–
2007   12–14

• –

        -
26   11–2008.

•

- -Barton,Hugh-1996.Sustainable Urban Design Quarterly,issue 57-Juauary 1996,Urban Design Group.

- Baker,Nick&Steemers,Koen,(2000),Energy and Environment in Architecture :aTechnical Design Guide , E&N Spon,London,UK.

- -Elkington,J,(1999),Triple Bottom Line Revolution:Reporting for the Third Millennium,Australian CPA,Vol.69.p75.

- Kim,Jong-Jin&Rigdon,Brenda (1998A)- Sustainable
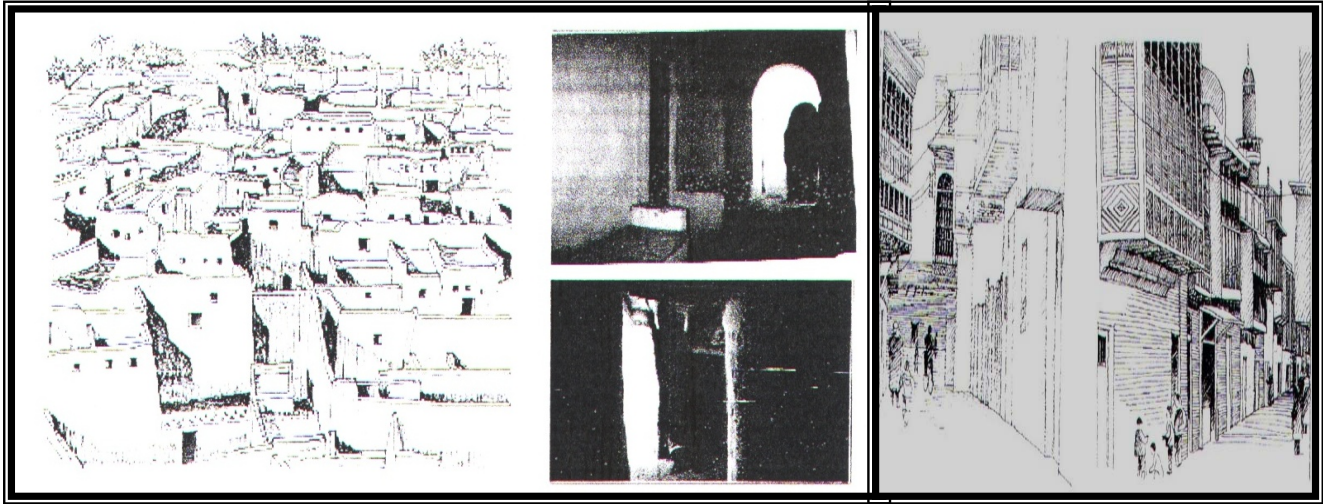
شكل (1) تجاور الوحدات السكنية وتظليل مسارات الحركة ذاتيا لتوفير بيئة مريحة للمشاة   –   (المصدر-الزبيدي-2006-ص48)
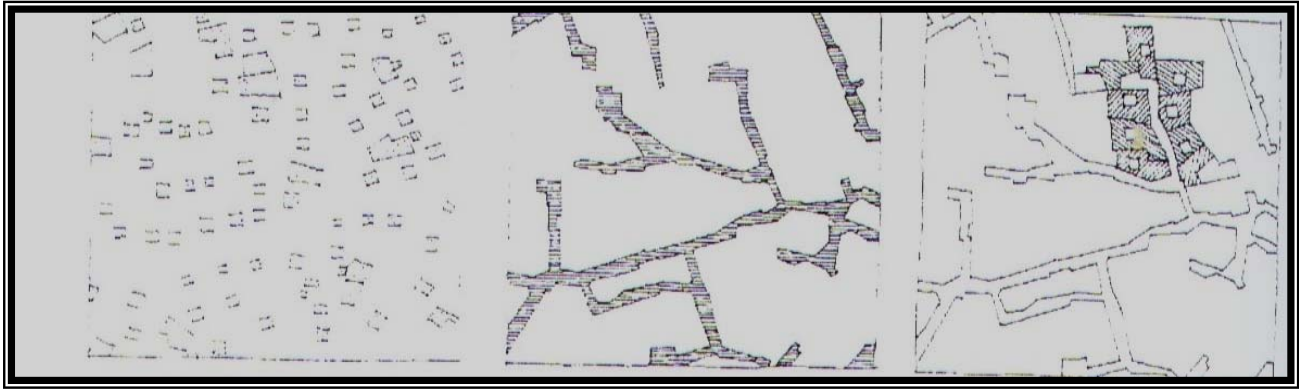

التنظيم الفضائي للفناءات الداخلية	الحركة مسدودة النها يةلمنع دخول	وحدة الجيرةتوفق مفهوم
وعلاقتها بعموم النسيج الحضري	الغرباءوالحفاظ على وحدة الجيرة	الاستدامة في النسيج الحضري
للتوظيف البيئي	في المدينة العربية	في المدينةالعربية

شكل(2) وحدة الجيرةومسارات الحركة و التنظيم الفضائي وفق مفهوم الاستدامة في المدينة العربية

المصدر:(الزبيدي،2006، ص-50)
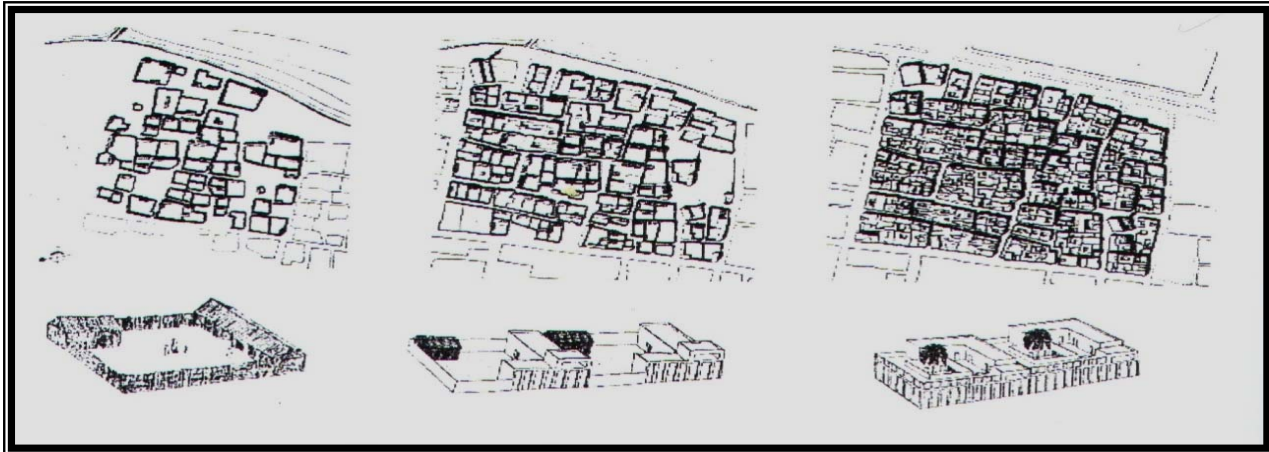
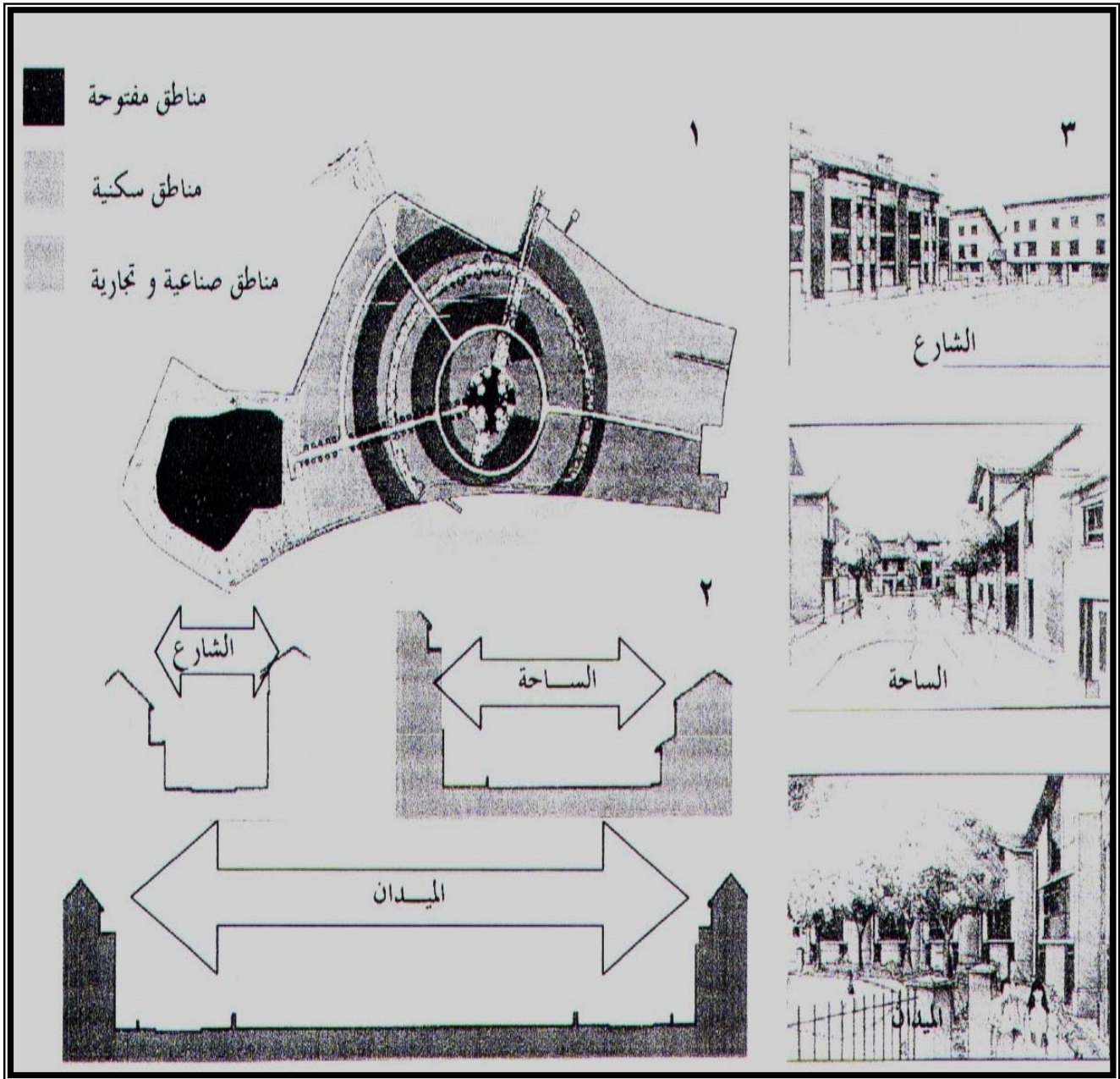**شكل(3) يوضح نمو وحدة الجيرة التقليدية والتدرج الهرمي للتنظيم الفضائي لها- وحدة الجيرة وحدة اجتماعية تراعي**
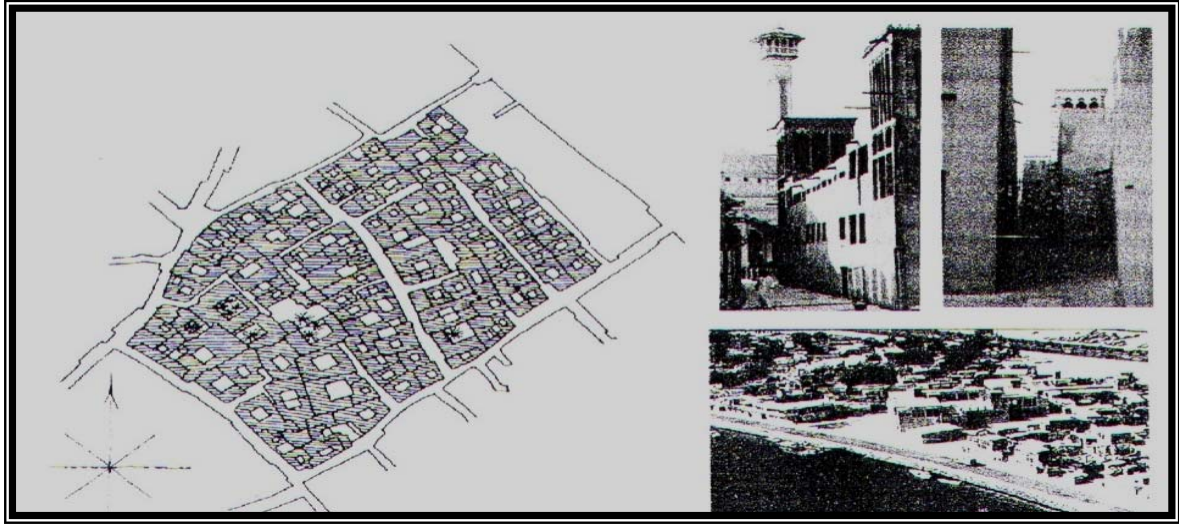
التجانس الاجتماعي بين افراد المجتمع الواحد ـ في الدوسر-مدينة الدمام المصدر(الاحبابي،2010،ص- 163)

شكل (4) التنظيم الفضا ئي المتضام والازقة المظللة في المدينة العربية التقليدية يساعد على تلطيف المؤثرات البيئية للمدينة (المصدر :الزبيدي-2006-ص 48)
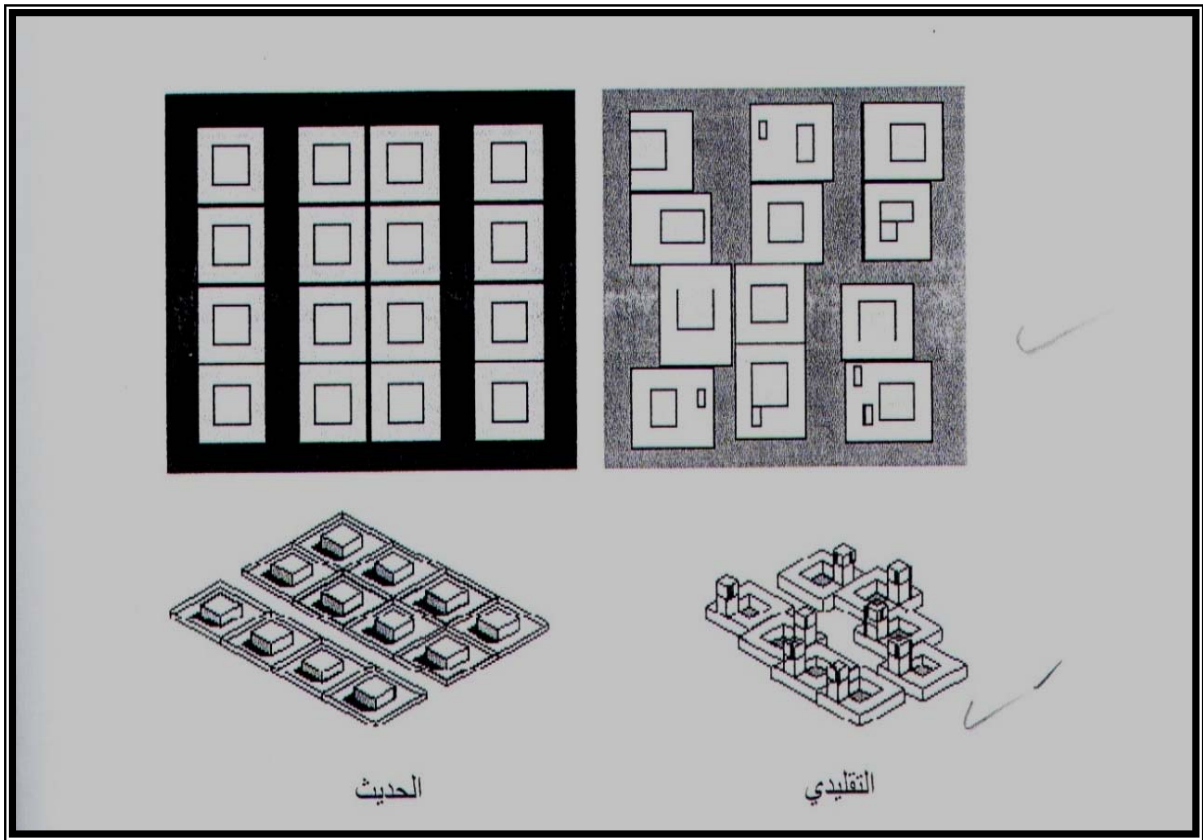

الحديث   التقليدي

شكل(5) يوضح التباين بين تصميم التنظيم الفضائي لوحة الجيرة التقليدية والحديثة (المعاصرة)

المصدر (الاحبا بي ،2010،ص-118)

|		
1- تعتمد الفكرة التصميميةعلى الفصل ما بين حركة السابلة و السيارات مع التأكيد عاى المناطق السكنية	2-التدرج في الخصوصيةودرجة الاحتوائية مابين الشارع ، الساحة ثم الميدان الذي يعتبر مركز التجمع والفعاليات العامة	3-تمثل الاماكن المفتوحة مناطق التجمع للسكان حيث تعتمدالفكرة التصميمية على حركة السابلة وخلق مناطق تتدرج في الاحتوائية

شكل (6) قرية شيروود للطاقة في المملكة المتحدة مثال على التطوير متعدد الاستخدام لوحدة الجيرة لتحقيق مبادئ الاستدامة البيئية،الاجتماعية والاقتصادية (المصدر: الزبيدي -2006-ص141)
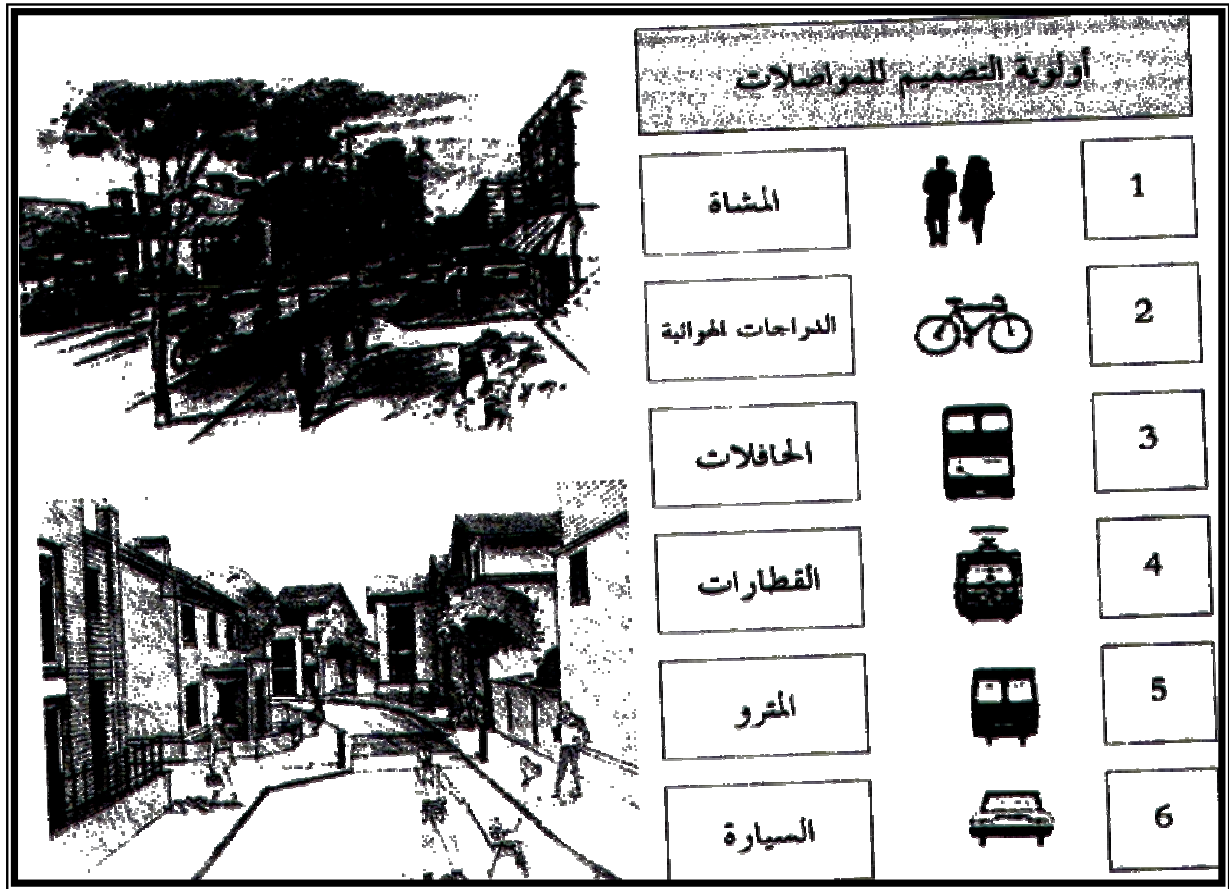
شكل(7) التصميم للمشاة ووسائط النقل الصديقة للبيئة في وحدة الجيرة المستدامة

(المصدر:الزبيدي-2006-ص 142)—
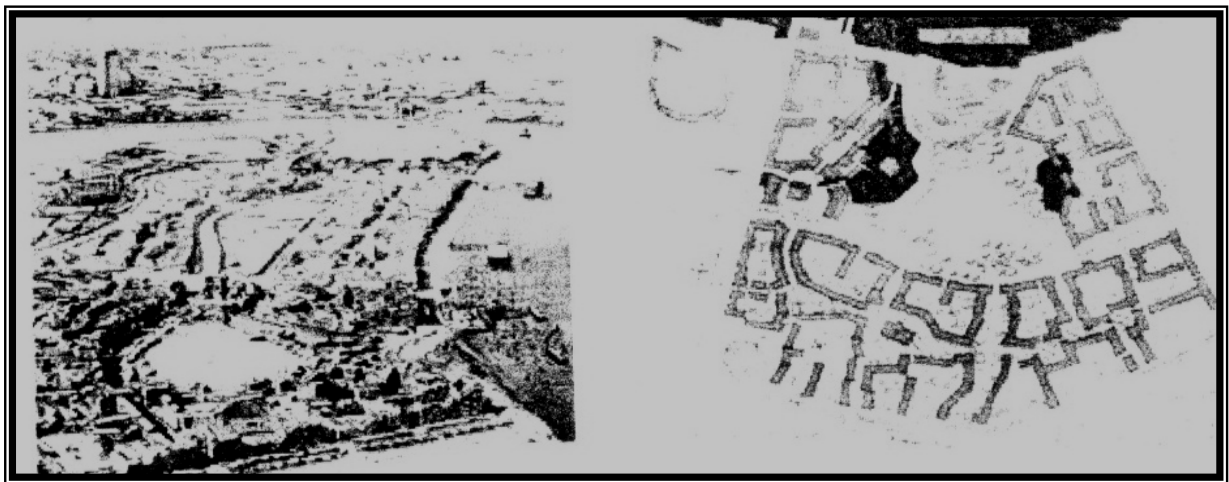
شكل (8) القرية الالفية والذي يعتمد التخطيط متعدد الاستخدام لاحياء التخطيط التقليدي بأ سلوب حديث-لندن

(المصدر:الزبيدي، 2006-ص176)